INVESTIGATIONS INTO SURFACE-CONFINED COVALENT ORGANIC FRAMEWORKS: TOWARDS DEVELOPING NOVEL ENANTIOSELECTIVE HETEROGENEOUS CATALYSTS

John Greenwood

A Thesis Submitted for the Degree of PhD
at the
University of St Andrews

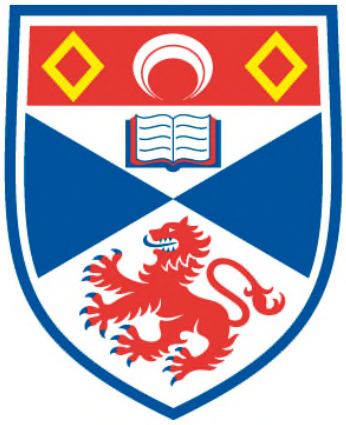

2013

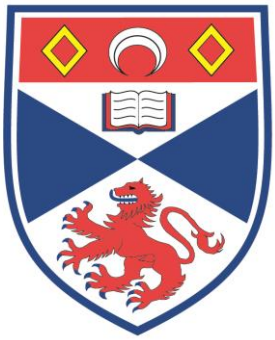

Investigations into Surface-Confined Covalent Organic Frameworks: Towards Developing Novel Enantioselective Heterogeneous Catalysts

John Greenwood

May 2013

A thesis submitted in accordance with the requirements of the University of St. Andrews for the degree of Doctor of Philosophy

Supervisor: Dr Chris Baddeley

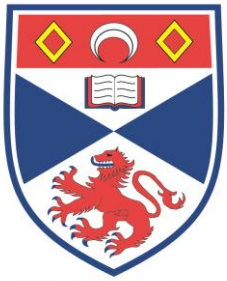

University
of
St Andrews

The Edinburgh and St Andrews
Research School of Chemistry

Declaration

1. Candidate's declarations:

I, John Greenwood, hereby certify that this thesis, which is approximately 50,000 words in length, has been written by me, that it is the record of work carried out by me and that it has not been submitted in any previous application for a higher degree. I was admitted as a research student in August, 2009 and as a candidate for the degree of Doctor of Philosophy in August, 2010; the higher study for which this is a record was carried out in the University of St Andrews between 2009 and 2013.

Date: Signature of candidate:

2. Supervisor's declaration:

I hereby certify that the candidate has fulfilled the conditions of the Resolution and Regulations appropriate for the degree of Doctor of Philosophy in the University of St Andrews and that the candidate is qualified to submit this thesis in application for that degree.

Date: Signature of supervisor:

3. Permission for electronic publication:

In submitting this thesis to the University of St Andrews I understand that I am giving permission for it to be made available for use in accordance with the regulations of the University Library for the time being in force, subject to any copyright vested in the work not being affected thereby. I also understand that the title and the abstract will be published, and that a copy of the work may be made and supplied to any bona fide library or research worker, that my thesis will be electronically accessible for personal or research use unless exempt by award of an embargo as requested below, and that the library has the right to migrate my thesis into new electronic forms as required to ensure continued access to the thesis. I have obtained any third-party copyright permissions that may be required in order to allow such access and migration, or have requested the appropriate embargo below.

The following is an agreed request by candidate and supervisor regarding the electronic publication of this thesis:

Embargo on all of both printed copy and electronic copy for the same fixed period of 2 years on the following grounds:

Publication would be commercially damaging to the researcher, or to the supervisor, or the

University; publication would preclude future publication.

Date:

Signature of candidate:

Signature of supervisor:

Acknowledgements

Firstly, I would like to take this opportunity to thank my supervisor, Dr Chris Baddeley. He has provided enormous support throughout my PhD. I am extremely grateful for his tireless encouragement and enthusiasm with regards to my research. If Carlsberg made PhD supervisors it would probably be Chris Baddeley.

I would like to thank Sean Jensen for teaching me the dark arts of STM. Dr Steve Francis and Dr Federico Grillo have provided a great deal of technical assistance and useful discussion for which I am very appreciative. Dr Herbert Früchtl performed the computational models throughout this project which has been crucial for my PhD; many thanks Herbert. I am thankful for the help from Dr Iain Smellie by providing useful suggestions. Thanks also to Professor Neville Richardson for the use of his UHV-STM, RAIRS and HREELS equipment. I would also like to thank EPSRC for the funding of my PhD.

Many thanks are owed to Dr Aoife Trant and Dr Tim Jones, who have been fantastic in providing help and encouragement during my time here, as well as being good drinking buddies.

I am also very grateful to the rest of the gang: Riho Green, Andrew Haire, Siddharth Jethwa, Alex Murdoch and Karen Wilson, for making my time here in St Andrews very enjoyable. Thanks for all the good times!

On a personal note, I would like to thank my friends at the University of St Andrews Karate club. Our nights out and time spent in training sessions and competitions provided a welcome relief to work and kept the insanity at bay, at the expense of a few bruises! Thanks also to Derek; our conversations every morning were a highlight of many days.

Enormous thanks to my family for their love and support throughout the years; especially to my mum, Collette, whose dedication and wisdom are the reason for where I am today.

Abstract

There is an increasing necessity for the pharmaceutical industry to develop enantiomerically pure drugs. Up till now, production of enantiomerically pure molecules has been provided by harvesting them from plants or utilising homogeneous catalysis and biocatalysis. None of these methods are efficient means of production, and attention is now being directed towards heterogeneous enantioselective catalysis as the preferred technique. This is on account of the high product yield and ease of separation of catalyst from the reaction mixture.

Over the past few decades, a great deal of research has been conducted into investigating the Ni catalysed hydrogenation of β-ketoesters and Pt catalysed hydrogenation of α-ketoesters. These are the most successful systems for enantioselective heterogeneous catalysis. However, they are unsuitable for industrial purposes due to the low thermal and mechanical stability of the modified surfaces.

The main goal throughout this project has been the investigation of surface-confined covalent reactions. The motivation of this research is to develop enantioselective heterogeneous catalysis; covalent networks are believed to infer the necessary thermal and chemical stability required to chirally modify catalytic surfaces for docking interactions with reactant species. Covalent organic frameworks (COFs) on surfaces hold potential for a number of chemical applications, and not just in the field of heterogeneous catalysis; for example in areas such as molecular electronics and templating.

List of Publications

(1) Jensen, S.; Greenwood, J.; Früchtl, H. A.; Baddeley, C. J. J. Phys. Chem. C 2011, 115, 8630-8636. 'STM Investigation on the Formation of Oligoamides on Au{111} by Surface-Confined Reactions of Melamine with Trimesoyl Chloride'

(2) Greenwood, J.; Früchtl, H. A.; Baddeley, C. J. J. Phys. Chem. C 2012, 116, 6685. 'Ordered Growth of Upright Melamine Species on Ni{111}: A Study with Scanning Tunnelling Microscopy and Reflection Absorption Infrared Spectroscopy'

(3) Greenwood, J.; Baddeley, C. J. Langmuir 2013, 29, 653-657. 'Formation of Imine Oligomers on Au under Ambient Conditions Investigated by STM'

(4) Greenwood, J.; Früchtl, H. A.; Baddeley, C. J. J. Phys. Chem. C 2013, 117, 4515-4520. 'Surface-Confined Reaction of Aliphatic Diamines with Aromatic Diisocyanates on Au{111} Leads to Ordered Oligomer Assemblies'

(5) Greenwood, J.; Früchtl, H. A.; Baddeley. 'Ordered Growth of Upright Melamine Species on Pd{111}' In Preparation.

Table of Contents

Chapter One: Introduction

1.1 Background

Catalysis is integral to the modern global economy. The significance is such that a considerable proportion of research is directed towards this scientific field. Large scale, industrially catalysed processes are dominated by heterogeneous catalysis, with selectivity considered as the prevailing issue to be explored in the 21st century.[1] A catalyst increases the rate of a chemical reaction by providing an alternative reaction mechanism of lower activation energy; after reaction, the catalyst is regenerated. Enantioselective catalysis involves the production of an excess of, or exclusively, a single enantiomer form over another. The number of surface science investigations into enantioselective catalysis has expanded enormously over recent years. This has, largely, been instigated by the need for the production of enantiomerically pure products in the pharmaceutical industry. In 2005, global sales of single enantiomer compounds reached $225 billion.[2] Chiral drugs comprise greater than half of the drugs approved worldwide, including many of the top selling drugs in the world. For example, among the top ten best-selling US

prescription small-molecule pharmaceuticals in 2009, six of these were single enantiomers, two were achiral, and only two were racemates.[3] Despite the importance of chiral molecules to the pharmaceutical industry, synthesis is performed using homogeneous catalysis. There are enormous economic benefits to developing heterogeneous enantioselective catalysis which would offer potentially improved product yields and easier product-catalyst separation relative to homogeneous catalysts.

The development of scanning tunnelling microscopy (STM) has been essential to recent advances in surface science, enabling visual representation of single chiral molecules. Consequently, STM has been crucial to advancing our fundamental understanding of interactions of chiral molecules with surfaces and processes such as chiral amplification and chiral recognition.[4] One of the main incentives for surface science investigations of chirality at surfaces is to provide an understanding of the surface chemistry of chiral catalysis, and to develop techniques for the logical design of chiral catalysts. STM is unequivocally the single most important analytical tool for surface scientists in this field.

1.2 Chirality

Molecules are chiral if they possess neither a mirror plane of symmetry nor a centre of inversion. The two mirror image forms of a chiral molecule are referred to as enantiomer pairs. Conventionally, an enantiomer contains a stereogenic centre which comprises a tetrahedral carbon atom connected to four *different* substituents. Enantiomer pairs can be differentiated by their capacity to rotate the plane of polarisation of a plane-polarised beam of light in either a clockwise or anticlockwise

direction, with such compounds designated as dextrorotary (D or (+)) and levorotary (L or (-)), respectively. The alternative (R), (S) convention for labelling chiral molecules according to their absolute stereochemistry is sometimes used.

It is well known that all proteins are consisted from (L) amino acids exclusively, and that DNA is constructed from only (R) sugar molecules, collectively referred to as biomolecular homochirality. As all DNA and protein molecules consist of exclusively chiral molecules, humans, consequently, are constructed from these very same constituents. Therefore, the effectiveness of pharmaceutical products depends greatly on their chirality.

The two enantiomeric forms of a drug can have varying degrees of differences in terms of their physiological effects. An example of which is the two enantiomeric forms of Ibuprofen, in which only the (S) enantiomer is biologically active, while the (R) enantiomer is biologically inactive. In contrast, for the case of Thalidomide – a drug used to treat morning sickness back in the late 1950s to early 1960s – only the (R) enantiomer is responsible for the desired effects, whereas the (S) enantiomer is teratogenic and resulted in birth defects. The latter example and many more reiterate the necessity for the production of enantiomerically pure drugs provided by the pharmaceutical industry.

If chiral compounds are synthesised from prochiral reagents, the inevitable result is a racemic mixture of products at equilibrium. This is due to the fact that enantiomer pairs possess identical Gibbs free energies. Since the physical properties of two enantiomers are the same, the production of exclusively one enantiomeric product is an extremely challenging requirement.[5]

In developing enantioselective catalysts, the main priority is to allow recognition of the stereochemistry of a reactant molecule and produce a product of a single enantiomer in excess, or, preferentially, exclusively one enantiomer. In so doing, the synthesis of a product is achieved with a minimisation of waste. This is in contrast to chiral resolution techniques, for which, when used on a racemic mixture, 50% of the starting materials are wasted, as well as the energy used for production.

The development of homogeneous enantioselective catalysis enabled the mass production of chirally pure compounds from prochiral reagents. These catalysts utilised bulky chiral ligands, complexed to a transition metal coordination centre; this resulted in a reagent adopting a specific geometry, and consequently the production of a single enantiomer compound. The Nobel Prize for Chemistry was awarded in 2001 to Knowles, Noyori, and Sharpless for their research into this work.[6] The award signifies the importance of homogeneously catalysed enantioselective reactions with regards to synthetic chemistry.

1.3 Heterogeneous Enantioselective Catalysis

Currently, enantioselective catalysis is the domain of homogeneous catalysis and bio-catalysis. However, there are numerous advantages to using heterogeneous catalysis for enantioselective reactions. Foremost of these is the ease and low cost of separation of the catalyst from the reaction mixture, as well as high product yields. Homogeneous catalysis does not allow for the isolation of the expensive enantioselective catalyst from the reaction mixture. Unfortunately, despite a great deal of research having been conducted over many decades, relatively few examples

of successful enantioselective heterogeneous catalysts exist on a laboratory scale, and the impact on industry is negligible.[5]

The two most researched asymmetric catalyst models are: nickel catalysts modified with tartaric acid (useful for β-functionalised ketones with enantiomeric excesses (ees) up to 98.6 %), and platinum catalysts modified with cinchona alkaloids and related modifiers (successful for α-functionalised ketones with ees up to 98%).[7] Addition of organic modifiers from solution to the metal nanoparticles is the critical process in bestowing enantioselectivity upon the catalyst. When the modifier is chiral, the reaction can be performed enantioselectively. There are very few combinations of a metal, a modifier and a substrate type that leads to good enantioselectivity, accounting for the limited number of examples in which this method of catalyst modification is applied.

1.3.1 Platinum Catalysed Hydrogenation of α-Ketoesters

There are essentially two fundamental mechanisms in which chirality can be bestowed. Either the surface is provided with chiral adsorption sites by the modifier itself, or the racemic surface becomes chiral when the modifier generates an excess of surface catalysing chiral kink sites via enantioselective etching of the step edges.

The importance of step-kink sites on metal surfaces has been of interest in recent years, and many surface science studies have been conducted to investigate the relevance of step-kink sites with regards to heterogeneous enantioselective chemical reactions. Cutting a metal single crystal with a small miscut angle leads to surfaces with a high Miller index plane; these types of surfaces are referred to as *vicinal*

surfaces. The coordination number of step and kink site atoms is less than those in the terraces; as such, the electronic structure differs and, therefore, so too does the chemical reactivity. Gellman and co-workers[8-10] were the first group to investigate the possibility of chiral structure of kink sites on vicinal metal surfaces. They studied the adsorption of chiral molecules on fcc-$\{643\}^{R}$ and $\{643\}^{S}$ surfaces. These two surfaces are mirror equivalent and non-superimposable. Attard et al.[11] provided experimental evidence of step sites inducing chirality by investigating the electro-oxidation of D- and L- glucose in aqueous sulphuric acid using platinum electrodes. The findings indicated a significant change to the voltammetry readings for when the electrode contained either R or S chiral kink sites, suggesting an enantiomeric preference for adsorption of the modifier at one particular chiral kink site. This work has not been confirmed by experimental evidence to show analogous behaviour for alkaloid adsorption on Pt with an excess of chiral sites, suggesting an alternative mechanism is occurring. A study by Lambert and Stephenson found that the intrinsically chiral kink sites of Pt$\{643\}^{R}$ neither favour nor disfavour the adsorption of either enantiomer of 1-napthyl ethylamine (NEA).[12]

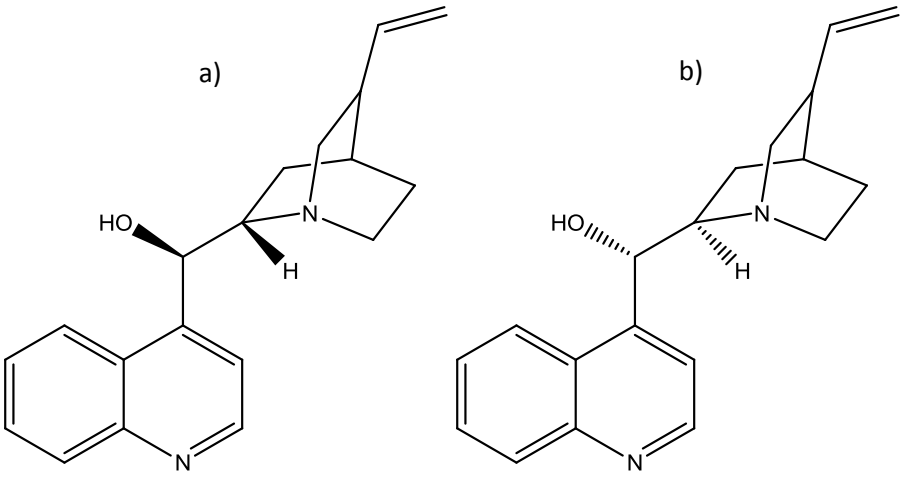

Figure 1.1: Chemical structures of (a) cinchonidine and (b) cinchonine.

Chiral alkaloids such as cinchonidine or cinchonine, shown in Figure 1.1, are the most widely used modifier species on platinum. Orito and co-workers[13] reported on the hydrogenation of methyl pyruvate, the simplest α-keto ester, to form R-methyl lactate on a Pt surface post modification with a chiral modifier, see Figure 1.2. A number of theories have been proposed in an effort to provide an explanation for the enantioselectivity of the Orito reaction.

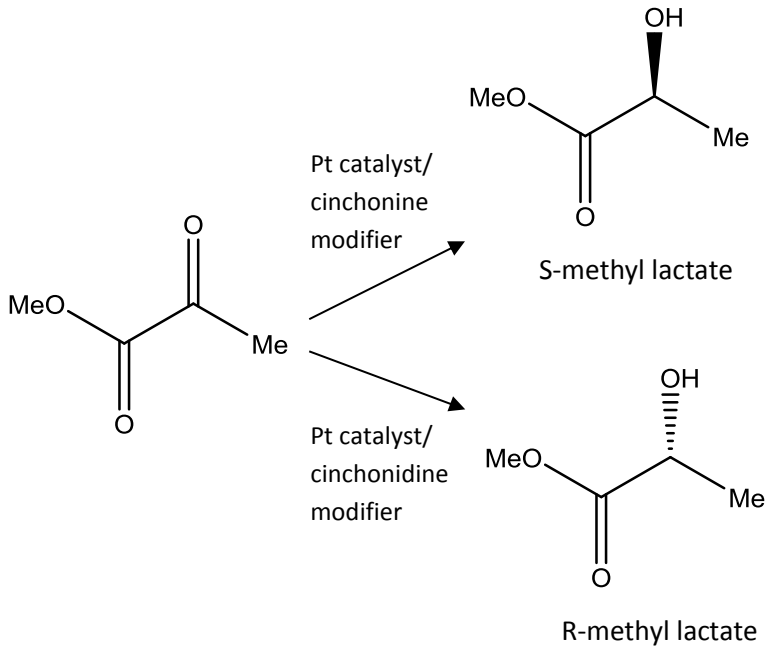

Figure 1.2: Reaction scheme of the Orito reaction between methyl pyruvate hydrogen on a modified Pt surface.

The Template Model proposed an ordered, porous arrangement of modifier molecules on the substrate surface.[14] In the model, the modifier aromatic rings adsorb parallel to the Pt surface, analogous to naphthalene adsorption on Pt forming an ordered arrangement.[15] This behaviour would result in the quinuclidine moiety pointing away from the surface, consequently creating a chiral environment with

which one face of the reactant molecule could interact with, accounting for the enantioselective behaviour observed.

Another interaction model, referred to as the Active Chiral Site Model, negates the requirement for an ordered arrangement of modifier. Instead, the chiral interaction between modifier and reactant is believed to be one-to-one in nature. There is an inherent rate enhancement for the hydrogenation of α-ketoester reagents on Pt post modification.[16] This has been explained as due to a stabilization of either a protonated modifier or reagent, allowing for H-bonding interactions between the modifier N atom of the quinuclidine moiety and the reagent ketone group.[17] Experimental evidence from LEED results has discredited the Template Model, indicating the chiral modifiers do not form an ordered array upon adsorption.[17] It is now widely accepted that the Template Model is unable to account for enantioselective behaviour of the Pt system. The chiral step-kink site behaviour shown by the groups of Gellman and Attard holds promise; however, this explanation does not account for the enantioselectivity imparted by alkaloid modification of Pt. The general consensus is that an Active Chiral Site Model is the correct way to describe the enantioselective behaviour of cinchona modified Pt catalysed hydrogenation reactions of α-ketoester reactants;[18-21] the main debate now is over the absolute structure of the modifier-reactant complex.

1.3.2 Nickel Catalysed Hydrogenation of β-Ketoesters

The hydrogenation reaction of β-ketoesters by chirally modified Ni catalysts is another extensively researched enantioselective system. Successful chiral modifiers include α-hydroxy carboxylic acids and α-amino acids. Tartaric acid, see Figure 1.4, is

the most studied modifier species for Ni catalysts. This area of work has been thoroughly studied by several prominent research groups in Japan over the past few decades. Work by Izumi and co-workers[22] found that optically active tartaric acid and its derivatives were observed to produce the highest enantiomeric excess of all the reagents, yielding ees of 95%. The adsorption of tartaric acid on Ni is corrosive, causing leaching of Ni into the modifying solution, the amount of which depends on the modifying conditions. Therefore, the modifier concentration, temperature, pH, and modifying time are all variables crucial to catalyst performance.[22]

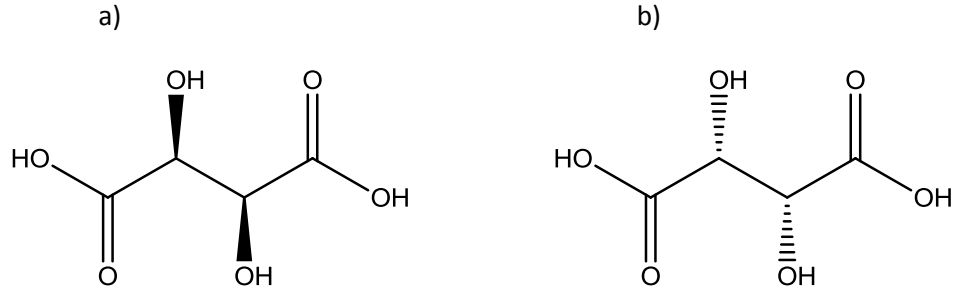

Figure 1.4: Chemical structure of: (a) (R, R)-tartaric acid, (b) (S, S)-tartaric acid.

The hydrogenation of methylacetoacetate (MAA) over (R, R)-tartaric acid modified Ni catalysts yields the product (R)-methyl-2-hydroxybutyrate (MHB) in excess; conversely, modification with (S, S)-tartaric acid yields the product of the opposite enantiomer, shown in Figure 1.5.[16]

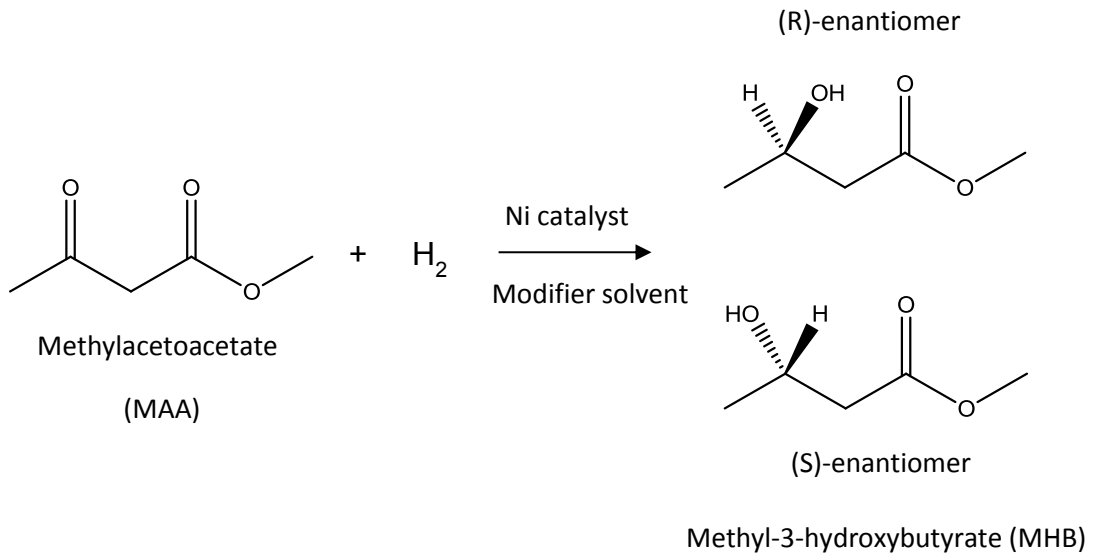

Figure 1.5: Schematic of the reaction between MAA and H_2 over a Ni modified catalysts surface to produce both enantiomers of MHB, adapted from reference [16].

Significant contributions to this field of research have been made by the groups of Sachtler,[23] Webb[16] and Keane.[24] A significant aspect of the fundamental spectroscopic evidence for the enantioselectivity of the catalytic process has been provided by Baddeley and Raval. Their initial work was on the adsorption of (R, R)-tartaric acid on Cu{110}, using LEED, STM and RAIRS as characterisation techniques.[25] Both STM and LEED indicated the formation of ordered networks; these were found to be sensitive to the adsorption temperature and adsorbate coverage.

It has been suggested that the adsorption environment of this species would allow for chiral channels, which is consistent with a Template Model type process of adsorption of reactants at the Cu surface within the channel pores. When the (S, S)-tartaric acid enantiomer is adsorbed, it forms the mirror image of the ordered (R, R)-tartaric acid ordered structure. STM images show ordered networks of both (R, R)

and (S, S)-tartaric acid and their corresponding overlayer structures. From this behaviour, the authors concluded that the adsorption of tartaric acid creates an extended chiral array on the entire Cu{110} surface, and not just a local chiral environment around the individual adsorbed species. It is worth noting that similar channels within networks were also observed for (S)-alanine adsorption on Cu{110}.[26] The main conclusions the authors made about tartaric acid adsorption on Cu{110} are, firstly, the adsorption geometry is controlled by the thermodynamic stability of the modifier-surface interaction. Second, the unit cell of the overlayer structure is most likely formed due to a dynamic hydrogen-bonding interaction between the adsorbed species, directing them into their adsorption sites.

The work by Raval and Baddeley on the adsorption of tartaric acid was a breakthrough in terms of understanding chiral modification, resulting in supramolecular assemblies of tartaric acid induced chirality, i.e. chirality spread across the entire surface. However, the fact that Cu is a poor hydrogenation catalyst limits the applicability of the findings. Therefore, Ni, which is an extremely effective hydrogenation catalyst, has been the focus of recent research in this field. For this reason, (R, R)-tartaric acid adsorption has been looked at on the Ni{110} surface.[27] The interaction between the tartaric acid molecules and the Ni atoms are more localised, reducing the lateral mobility and, consequently, no long-range ordered structures are formed on the surface.[5]

The most relevant surface planes in the face centred cubic (fcc) systems are the {100}, {110} and {111} low index planes. As the {111} surface is the most thermodynamically stable surface structure for fcc metals, the majority of the

research has been aimed on this particular surface. Since the {111} surface is the most stable, it is expected to be the dominant crystal face on Ni nanoparticles.

Chirally pure enantiomers of MHB are a useful building block for synthetic reactions in order to produce more complex organic molecules. Production of such organic molecules incorporating chiral functional groups is a key requirement in developing drugs for the pharmaceutical industry. Therefore, the enantioselective hydrogenation of MAA on Ni is an important reaction to be understood. Jones and Baddeley have provided extensive experimental evidence towards elucidating the fundamental interactions of the chiral modifier (R, R)-tartaric acid with the Ni{111} surface.[28] They have shown that the two-dimensional packing, molecular conformation and thermal stability of the modified surfaces are all closely linked, and critically dependent on sample temperature, flux rate of the modifier at the surface and the presence of coadsorbed species.

The asymmetric hydrogenation of methylacetoacetate (MAA), the simplest β-keto ester, to (R)-methyl-3-hydroxybutyrate (MHB) over (R, R)-tartaric acid or (S)-glutamic acid modified Ni catalysts are well studied examples of heterogeneous enantioselective catalysis. MAA exists as two tautomeric forms, either as the enol or ketone form, see Figure 1.6. Intermolecular hydrogen bonding between the hydroxyl and carbonyl group of the enol forms a six membered ring, stabilising this species. The Ni-catalysed hydrogenation of MAA is thought to proceed via the hydrogenation of either a C=O bond (i.e. the diketone form) or a C=C bond (i.e. the enol form).

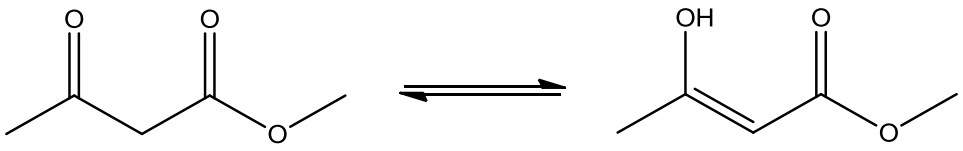

Methylacetoacetate (diketo form) Methylacetoacetate (enol form)

Figure 1.6: Schematic diagram showing the two tautomeric forms of MAA.

Adsorption of MAA on Ni{111} at 300 K occurs with a relatively high sticking probability.[29] However, surface bound species are unstable up to ~350 K, at which point they decompose to yield CO and H_2. IR data indicates that the vast majority of molecular species are in the diketo form on the Ni{111} surface. On a Ni{111} surface saturated with (R, R)-tartaric acid at 300 K, the sticking probability of MAA is extremely low. As described in their previous work,[28] Jones and Baddeley reported high coverage of the modifier results in a relatively strong intermolecular hydrogen bonding network, which uses up the available functional groups, therefore, none are free to bond with MAA.

At lower pre-coverage of (R, R)-tartaric acid, where the intermolecular hydrogen bonding network is disrupted by coadsorbed CO, adsorption of MAA does occur. This is likely helped by the fact that, analogous to (R, R)-tartaric acid,[28] MAA is capable of displacing CO from the Ni{111} surface. RAIRS data strongly implies that the MAA molecular conformation on the modified surface differs from that adsorbed on clean surface, with the plane of MAA more upright in the coadsorbed system.

Crucially, at no stage for individual adsorption of either (R, R)–tartaric acid or MAA on Ni{111} was such ordering observed. Jones and Baddeley believe MAA adsorption

occurs at the disordered phase of low coverage (R, R)–tartaric acid, in which adventitiously adsorbed CO has disrupted the intermolecular linkages. MAA thereby displaces CO upon adsorption, integrating into the tartrate phase. They concluded that, upon adsorption, MAA organises the surrounding tartrate species into a well-defined arrangement, as seen in the STM images.

For the low coverage phase of MAA and (R, R)-tartaric acid, all of the MAA molecules adopt the same orientation within the structure. Subsequent hydrogenation of this species would occur via attack of an adsorbed H-atom from below the MAA molecule, yielding a C-OH bond pointing away from the surface. The resulting molecule corresponds to (R)–methyl–3–hydroxybutyrate.[29] This is the observed product for MAA hydrogenation on (R, R)–tartaric acid modified Ni catalysts. If this model is the same under catalytic conditions, it would be evidence for the observed enantioselectivity. The second ordered structure observed corresponds to a higher coverage of MAA. The unit cell contains one tartrate species and two MAA species, which are of opposite mirror images to each other. Therefore, hydrogenation of both MAA species within the unit cell would result in a racemic product.

The fact that a wide range of β-keto esters display enantioselective hydrogenation,[7] including some with extremely bulky substituents, means that it is not possible for these molecules to be accommodated within the spaces of the ordered modifier structures on Ni{111}. On this basis, the authors proposed that for treatment of Ni with a tartrate solution there is a competitive adsorption process between the tartrate and solvent molecules for adsorption sites. Therefore, at sub-monolayer coverage of (R, R)-tartaric acid, the intermolecular interactions are disrupted by the

presence of solvent molecules, analogous to CO (ads) disruption in the UHV system, such that formation of an ordered (R, R)-tartaric acid adlayer is hindered. It is feasible then, once MAA is introduced, adsorption displaces solvent molecules and results in local ordering, as observed for the low coverage system of MAA on (R, R)-tartaric acid modified Ni{111}. The adsorption geometry of MAA would be controlled by the chirality of the neighbouring tartrate species. Provided the rate of hydrogenation of MAA is facile, this would result in a short lifetime of MAA bound to the surface. Consequently, this would agree with the authors' model of a low coverage (enantioselective) MAA system.

Previous experiments have confirmed the optimum modifier coverage, giving the greatest enantioselectivity, to be ~ 0.05 – 0.06 ML of modifier on the Ni catalyst surface.[30] It is well understood that the absolute coverage is important in the catalysis of MAA. In the absence of modifier, the achiral Ni catalysts produce a racemic mixture of products. However, too high a coverage of modifier hinders the adsorption capability of the reactant molecule; hence, a compromise is required between modifier coverage and bare metal surface. The low modifier coverage allows for available adsorption sites of MAA at the Ni surface, which interact enantioselectively with the adsorbed (R, R)-TA, and corroborates the experimental model put forward by Jones and Baddeley.[29]

The illustration in Figure 1.7 represents the hydrogenation of both enantiomorphs of MAA on a catalytic {111} surface. The result is the production of both enantiomers of MHB. Chiral modification allows only for the adsorption of one enantiomorph of MAA, and, therefore, subsequent hydrogenation produces a single enantiomer.

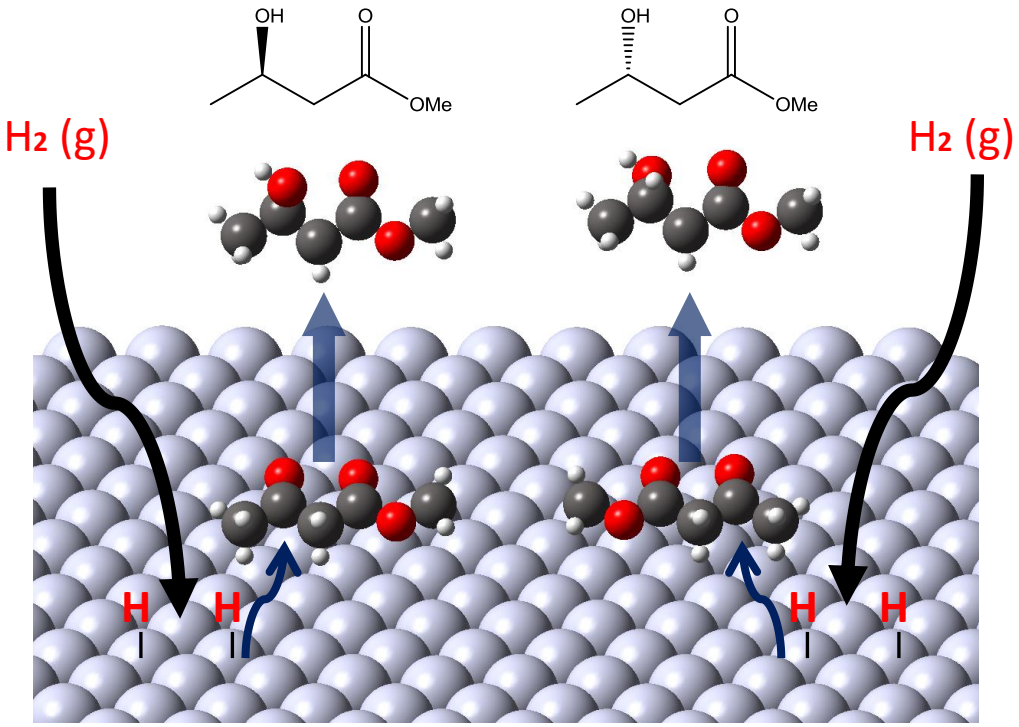

Figure 1.7: Illustration of the hydrogenation of methylacetoacetate (MAA) on a {111} vicinal surface, with both enantiofaces adsorbed to the surface. The result is the production of both enantiomers of methyl-3-hydroxybutyrate (MHB).

Variation of modifier coverage over time is an unwanted aspect for catalysis. Ideal coverage allows for a ratio of modifier to reactant species which results in the highest enantioselectivity along with the highest reaction turnover. Too high a coverage of modifier hinders adsorption of the reactant species, as observed for R,R-tartaric acid modification of Ni{111};[29] whereas, too low a coverage results in an excess of reactant to modifier, not allowing for enantioselective interactions to dominate. This underpins the motivation behind this project; that is, to develop a 2-D modifier porous network, coverage of which is independent of time and cannot be displaced by solvent or reactant species. Should the modifier network contain chiral functional groups, analogous to those of the modifier species discussed previously in this

section, subsequent docking interactions with reactant species in the network pore would result in enantioselective behaviour.

1.4 Hydrogen Bonded Networks

Supramolecular chemistry applied to two-dimensional assemblies on surfaces provides a significant method for forming surface nanostructures. With regards to chiral catalysis, and linking in with the previous section on chiral modifiers, supramolecular networks may allow for the formation of a heterogeneous enantioselective catalytic system via incorporation of chiral functional groups into the network reactants. Supramolecular chemistry has attracted a great deal of interest from research groups of late. It is not the aim of this Chapter to thoroughly review the extensive literature of supramolecular chemistry; however, this section will focus on an area relevant to chiral networks, that is, hydrogen bonded supramolecular systems.

Many structures have been realised by hydrogen-bonded self-assembled structures. These include rows,[31-34] clusters[35-37] and extended networks.[36, 38-41] One of the more promising approaches is that of Beton and co-workers, who have reported two-dimensional honeycomb networks stabilised by H-bonding on Ag – terminated Si and Au{111}.[41, 42] On both surfaces, their method was to mix two different reactants, melamine and perylene tetra-carboxylic di-imide (PTCDI), to yield a two-dimensional open honeycomb network that subsequently controls and templates new surface phases formed by deposited fullerene molecules. The authors chose melamine and PTCDI as the preferred reactants due to the fact that the hetero-intermolecular H-bonding is far stronger than the homo-intermolecular. The

melamine units form the vertices of the network while PTCDI forms the straight edges of the structure. The incorporation of PTCDI into the straight edges of the network is the key to the potential applications such modification of catalytic surfaces may hold. The reason for this is that the pore sizes are of an appropriate size to allow trapping of several large molecules. This contrasts with the behaviour of previous studies investigating hexagonal networks composed of a single molecular species.[36, 38-40]

Buck and co-workers[43] have demonstrated that the same PTCDI-melamine network can also be formed under ambient conditions at the liquid solid interface on Au/mica. They have used this system as a template for the precise creation of self-assembled monolayers (SAMs), imparting sufficient robustness for further processing. The melamine-PTCDI system is a versatile bimolecular network, which can be controlled by altering the side groups of the perylene ring to vary the pore size. Buck and co-workers have demonstrated different SAMs, consisting of: adamantane thiol, ω (4'-methylbiphenyl-4-yl) propane thiol and dodecane thiol; adamantane thiol is small and rigid with weak intermolecular interactions, while the latter two thiols show much stronger intermolecular interactions.

Upon formation of the SAM-network structure, the robustness is such, that, it was possible to process it further in a liquid environment with electrochemical deposition of Cu in the under-potential deposition (UPD) region.[43] The authors showed the growth of a monolayer of Cu between the Au surface and thiol molecules without disrupting the hybrid structure.

The system investigated by Buck and co-workers is a promising one due to the versatility of controlling pore size, as well as varying the SAMs; each enabling separate surface modification. This is also an important step in overcoming the necessity for top-down methods of nanofabrication, with SAM-network hybrids providing nanometre scale precision from a bottom-up approach, allowing for the option of metal deposition.

1.5 Covalent Organic Frameworks

The past decade has seen an enormous increase in the amount of research conducted into ordered two-dimensional arrays on a range of surfaces. Such research has utilised hydrogen bonded networks,[41, 44-49] van der Waals interactions[50, 51] and metal-organic coordination[45, 52] to create the desired nanostructures.

If porous covalent networks could be modified to incorporate chiral functional groups this would enable docking interactions of guest molecular species to occur. For example, reactant species such as MAA adsorbing in the pores of such covalent networks, the H-bonding interactions between the MAA and chiral functional groups could lead to a single adsorption geometry adopted by all of the MAA molecules, thus achieving a key requirement for enantioselective catalysis.

Non-covalent nanoporous supramolecular networks have been shown to be capable of hosting guest molecular species[32, 53-55] and are an important area of study for the understanding of enantioselective adsorption. However, with the desired end goal to produce catalysts for industrial scale production, the chemical and thermal stability of the aforementioned networks is insufficient to be viable for use in templating and catalysis. A possible solution lies in designing and fabricating two-

dimensional nanostructures on surfaces incorporating covalent linkages. The increased stability, both chemical and thermal, of covalently linked networks would enable them to be an economically feasible system for enantioselective heterogeneous catalysts. Only in recent years has research been conducted into developing networks of this type with the desire for creating extended, defined and periodic networks. The covalent linkages results in an inherently superior durability to the non-covalently linked analogues. However, the size and complexity of the organic reactants are limited by thermal decomposition in sublimation techniques, a necessary step for ultra-high vacuum deposition. The solution to this is to deposit smaller molecular precursors, which react with each other by forming covalent linkages whilst on the surface.

There has been a growing realisation in recent years that the fabrication of covalent organic networks (COFs) offers a route to structures with the required stability for practical applications. This area of surface chemistry has been the subject of a number of recent review articles,[56-59] highlighting the significance of this relatively new, but increasingly influential branch of nanotechnology research.

A range of covalent reactions have now been demonstrated on surfaces. The surface-confined polymerisation of organic adsorbates by covalent reactions is proving to be a versatile area of surface chemistry. Reactions have been shown to proceed with single component systems such as octylamine coupling to form trioctylamine[60] in which it is suggested that the Au{111} surface is a crucial component to the reaction mechanism. Also, the surface is vital to the mechanism of the radical coupling of tetra (mesityl) porphyrins on Cu{110}[61] and to the Ullmann

reaction for the coupling of diiodobenzene molecules in which the by-product is copper iodide.[62] A study on one-dimensional coordination polymers found that the Cu{111} surface provided adatoms necessary for the metal-organic polymers to form promoting interactions between the Cu atoms and the pyridyl groups of the porphyrin derivative building blocks.[63] There have been reports of surface-confined radical coupling reactions, including the thermally induced polymerisation of 1,3,5-tris(4-bromophenyl)-benzene[64] on Au{111}, as well as 1,3,4-tris(4-bromophenyl)-benzene on Cu{111} and Ag{110}[65] all via debromination. Multicomponent reaction systems are also well documented in the literature, including the thermally induced reaction between a fullerene/porphyrin binary nanostructure system on Ag{110}.[66] Other examples include condensation reactions between aldehydes and amines[67, 68], producing imine linkages, and the nucleophilic attack of amines at isocyanates,[69, 70] as well amines at acyl chlorides,[71, 72] to produce urea and amide linkages, respectively.

The approach to using radical coupling reactions in order to create covalently interlinked structures on surfaces has been successfully attempted on numerous occasions. The method is based on using small molecular building blocks, which make up the network constituents, with reactive side groups that react via radical coupling to form covalent bonds at predefined connection points. The first step consists of dissociating the substituent atoms by heating; thereafter, thermal diffusion of the monomer units allows the reaction to occur at the activated free radical group. The number of connection points on the molecule and their relative arrangement allows

for the control of the topology of the resulting structure, such as dimers, linear chains and two-dimensional arrays.

Grill et al.[73] studied the coupling reactions of tetra phenyl porphyrin (TPP) with a range of one, two and four Br substituents in the para position on the phenyl groups. As the reaction proceeds, the reacted phase of connected building blocks grows larger, resulting in reduced mobility and diffusion. Therefore, the growth is self-limiting and the number of networks on the surface decreases with increasing number *n* of bound molecules. The nanostructure topology corresponds precisely to the number and arrangement of Br substituents on the TPP building block. With only one Br substituent (Br TPP), the product is exclusively dimers because each building block provides only one reactive side. A porphyrin building block with two Br atoms in the trans geometry (*trans*-Br_2 TPP) leads to the formation of long, linear chains. The final design, with four Br substituents, one on each phenyl leg (Br_4 TPP), enables the fabrication of two dimensional networks. The formation of the networks is not a self-assembly process, because it is not reversible.

Polyimides are known to be chemically resistant, with a high decomposition temperature,[74, 75] hence, they hold potential for use as network materials for use in industrial catalysis. Richardson, Fasel and co-workers[76] have investigated the formation of polyimide films on Au{111} using low-temperature STM. They have shown that surface-confined imidisation of aromatic amines and anhydrides occurs above ~ 570 K, whose detailed structure can be altered from parallel linear strands to an extended, 2D connected, porous network by varying the amine reactant species. The authors noted the individual oligoamides can be altered to either PTCDA or DATP

by providing an excess of the appropriate species during deposition. The parallel oligomers are densely packed, stabilised by CH-O hydrogen bonds.

The imidisation between PTCDA and (2, 4, 6)-tris-(4)-aminophenyl-(1, 3, 5)-triazine (TAPT) has also been investigated by the authors.[77] TAPT is a three-fold symmetric triamine species, providing a three-way link for PTCDA molecules to react with. Compared to the network structure formed by the linear DAPT, the network is very porous, exhibiting an extended 2D connectivity.

A growing number of covalent organic frameworks on surfaces have been developed in ambient conditions. In many ways, these reactions provide a greater degree of complexity to systems studied in UHV. Extra factors have to be taken into account, such as solvent-surface interactions and possible atmospheric reactions with the reactants. The most common system studied is the reaction between an amine and aldehyde.[78-80] In addition, Beton et al.[81] investigated the radical dimerization of an organic precursor following annealing on Au in ambient conditions. Development of these systems is an important step for creating covalent networks that can hopefully be incorporated into catalytic systems which can tolerate the necessary environmental conditions.

1.6 Thesis Layout

The work undertaken during this project has focused on investigating surface-confined covalent reactions. A range of chemical reaction systems has been studied in an effort to ascertain the most effective nucleophile/electrophile combinations for covalent organic framework formation.

The initial results chapters are concerned with the catalytically active metal surfaces of Ni{111} and Pd{111}. Chapters 3 and 4 are both split into two parts. The first part looks in detail at the interaction between melamine, the nucleophile species, and the substrate, utilising a variety of experimental techniques. In addition, density functional theory calculations have been performed. The second part describes the interaction between melamine and the aldehyde reactant species.

The latter chapters use Au{111} as the substrate. Though Au is not catalytically active with regards to hydrogenation reactions, the inert nature allows for greater diffusion of the reactant species across the surface in order to react together. Chapter 5 is the only one to report on work carried out under ambient conditions. The same reaction system investigated in Chapters 3 and 4 is looked at on Au/mica over a period of three days.

Chapter 6 describes the reaction system between an amine and isocyanate. Two different structural isomers of the isocyanate species were used to create different structural topologies of the resultant polymers. The last system to be looked in Chapter 7 investigated the attempted reaction between cyanuric acid 1,4-phenylene diisocyanate. No reaction was observed in this case, but the co-deposition of the reactant species resulted in large domains of two porous phases after annealing. These hold promise for hosting guest molecular species in future studies.

1.7 References

[1] G.A. Somorjai, C.J. Kliewer, React. Kinet. Catal. Lett. 96 (2009) 191-208.
[2] G.-Q. Lin;, Q.-D. You;, J.-F. Cheng., Wiley and Sons Chapter 1 (2011) 23.
[3] V.P. Anum, *Pharmaceut*. *Technol*. **30**. (2006) 58-66.
[4] C.J. Baddeley, *Topics in Catalysis* 25 (2003) 1-4.
[5] C.J. Baddeley, G. Held, Elsevier Academic press. (2010).
[6] http://nobelprize.org/nobel_prizes/chemistry/laureates/2001/.
[7] M. Studer, H.U. Blaser, C. Exner, Adv. Synth. Catal. 345 (2003) 45-65.
[8] J.D. Horvath, A.J. Gellman, J. Am. Chem. Soc. 124 (2002) 2384-2392.
[9] J.D. Horvath, A.J. Gellman, J. Am. Chem. Soc. 123 (2001) 7953-7954.
[10] C.F. McFadden, P.S. Cremer, A.J. Gellman, Langmuir 12 (1996) 2483-2487.
[11] G.A. Attard, A. Ahmadi, J. Feliu, A. Rodes, E. Herrero, S. Blais, G. Jerkiewicz, J. Phys. Chem. B 103 (1999) 1381-1385.
[12] M.J. Stephenson, R.M. Lambert, J. Phys. Chem. B 105 (2001) 12832-12838.
[13] Y. Orito, S. Imai, S. Niwa, Nippon Kagaku Kaishi (1979) 1118-1120.
[14] I.M. Sutherland, A. Ibbotson, R.B. Moyes, P.B. Wells, J. Catal. 125 (1990) 77-88.
[15] J.L. Gland, G.A. Somorjai, Surface Science 38 (1973) 157-186.
[16] G. Webb, P.B. Wells, Catal. Today 12 (1992) 319-337.
[17] A.F. Carley, M.K. Rajumon, M.W. Roberts, P.B. Wells, J. Chem. Soc.-Faraday Trans. 91 (1995) 2167-2172.
[18] O. Schwalm, B. Minder, J. Weber, A. Baiker, Catal. Lett. 23 (1994) 271-279.
[19] J.M. Bonello, E.C.H. Sykes, R. Lindsay, F.J. Williams, A.K. Santra, R.M. Lambert, Surface Science 482 (2001) 207-214.
[20] J.M. Bonello, R.M. Lambert, Surface Science 498 (2002) 212-228.
[21] J.M. Bonello, F.J. Williams, R.M. Lambert, J. Am. Chem. Soc. 125 (2003) 2723-2729.
[22] Y. Izumi, Advances in Catalysis 32 (1983) 215-271.
[23] A. Hoek, W.M.H. Sachtler, J. Catal. 58 (1979) 276-286.
[24] M.A. Keane, Langmuir 13 (1997) 41-50.
[25] M.O. Lorenzo, C.J. Baddeley, C. Muryn, R. Raval, Nature 404 (2000) 376-379.
[26] M.O. Lorenzo, S. Haq, T. Bertrams, P. Murray, R. Raval, C.J. Baddeley, J. Phys. Chem. B 103 (1999) 10661-10669.
[27] V. Humblot, S. Haq, C. Muryn, R. Raval, J. Catal. 228 (2004) 130-140.
[28] T.E. Jones, C.J. Baddeley, Surface Science 513 (2002) 453-467.
[29] T.E. Jones, C.J. Baddeley, Surface Science 519 (2002) 237-249.
[30] M.A. Keane, G. Webb, J. Catal. 136 (1992) 1-15.
[31] J.V. Barth, J. Weckesser, C.Z. Cai, P. Gunter, L. Burgi, O. Jeandupeux, K. Kern, Angew. Chem.-Int. Edit. 39 (2000) 1230-+.
[32] D.L. Keeling, N.S. Oxtoby, C. Wilson, M.J. Humphry, N.R. Champness, P.H. Beton, Nano Lett. 3 (2003) 9-12.
[33] Q. Chen, D.J. Frankel, N.V. Richardson, Langmuir 18 (2002) 3219-3225.
[34] T. Yokoyama, S. Yokoyama, T. Kamikado, Y. Okuno, S. Mashiko, Nature 413 (2001) 619-621.
[35] M. Bohringer, K. Morgenstern, W.D. Schneider, R. Berndt, Angew. Chem.-Int. Edit. 38 (1999) 821-823.
[36] M. Furukawa, H. Tanaka, T. Kawai, Surface Science 445 (2000) 1-10.
[37] N. Lin, A. Dmitriev, J. Weckesser, J.V. Barth, K. Kern, Angew. Chem.-Int. Edit. 41 (2002) 4779-4783.
[38] S. Griessl, M. Lackinger, M. Edelwirth, M. Hietschold, W.M. Heckl, Single Mol. 3 (2002) 25-31.

[39] A. Dmitriev, N. Lin, J. Weckesser, J.V. Barth, K. Kern, J. Phys. Chem. B 106 (2002) 6907-6912.
[40] S. Berner, M. Brunner, L. Ramoino, H. Suzuki, H.J. Guntherodt, T.A. Jung, Chem. Phys. Lett. 348 (2001) 175-181.
[41] J.A. Theobald, N.S. Oxtoby, M.A. Phillips, N.R. Champness, P.H. Beton, Nature 424 (2003) 1029-1031.
[42] L.M.A. Perdigao, E.W. Perkins, J. Ma, P.A. Staniec, B.L. Rogers, N.R. Champness, P.H. Beton, J. Phys. Chem. B 110 (2006) 12539-12542.
[43] R. Madueno, M.T. Raisanen, C. Silien, M. Buck, Nature 454 (2008) 618-621.
[44] T. Kudernac, S. Lei, J.A.A.W. Elemans, S. De Feyter, Chemical Society Reviews 38 (2009) 402-421.
[45] J.V. Barth, Annu. Rev. Phys. Chem. 58 (2007) 375-407.
[46] S. De Feyter, F.C. De Schryver, J. Phys. Chem. B 109 (2005) 4290-4302.
[47] S. De Feyter, A. Miura, S. Yao, Z. Chen, F. Wurthner, P. Jonkheijm, A. Schenning, E.W. Meijer, F.C. De Schryver, Nano Lett. 5 (2005) 77-81.
[48] I. Cebula, C. Shen, M. Buck, Angewandte Chemie International Edition 49 (2010) 6220-6223.
[49] F. Silly, A.Q. Shaw, M.R. Castell, G.A.D. Briggs, M. Mura, N. Martsinovich, L. Kantorovich, J. Phys. Chem. C 112 (2008) 11476-11480.
[50] S. Furukawa, K. Tahara, F.C. De Schryver, M. Van der Auweraer, Y. Tobe, S. De Feyter, Angew. Chem.-Int. Edit. 46 (2007) 2831-2834.
[51] M.C. Blum, E. Cavar, M. Pivetta, F. Patthey, W.D. Schneider, Angew. Chem.-Int. Edit. 44 (2005) 5334-5337.
[52] S. Stepanow, M. Lingenfelder, A. Dmitriev, H. Spillmann, E. Delvigne, N. Lin, X.B. Deng, C.Z. Cai, J.V. Barth, K. Kern, Nat. Mater. 3 (2004) 229-233.
[53] S. Stepanow, M. Lingenfelder, A. Dmitriev, H. Spillman, E. Delvigne, N. Lin, X. Deng, C. Cai, J.V. Barth, K. Kern, Nat. Mater. 3 (2004) 229-233.
[54] J.V. Barth, J. Weckesser, G. Trimarchi, M. Vladimirova, A. De Vita, C.Z. Cai, H. Brune, P. Gunter, K. Kern, J. Am. Chem. Soc. 124 (2002) 7991-8000.
[55] J.A. Theobald, N.S. Oxtoby, N.R. Champness, P.H. Beton, T.J.S. Dennis, Langmuir 21 (2005) 2038-2041.
[56] A. Gourdon, Angew. Chem.-Int. Edit. 47 (2008) 6950-6953.
[57] G. Franc, A. Gourdon, Physical Chemistry Chemical Physics 13 (2011) 14283-14292.
[58] M. Lackinger, W.M. Heckl, J. Phys. D-Appl. Phys. 44 (2011).
[59] H. Liang, Y. He, Y.C. Ye, X.G. Xu, F. Cheng, W. Sun, X. Shao, Y.F. Wang, J.L. Li, K. Wu, Coord. Chem. Rev. 253 (2009) 2959-2979.
[60] S. Weigelt, J. Schnadt, A.K. Tuxen, F. Masini, C. Bombis, C. Busse, C. Isvoranu, E. Ataman, E. Laegsgaard, F. Besenbacher, T.R. Linderoth, J. Am. Chem. Soc. 130 (2008) 5388-+.
[61] M.I. Veld, P. Iavicoli, S. Haq, D.B. Amabilino, R. Raval, Chem. Commun. (2008) 1536-1538.
[62] J.A. Lipton-Duffin, O. Ivasenko, D.F. Perepichka, F. Rosei, Small 5 (2009) 592-597.
[63] D. Heim, D. Ecija, K. Seutert, W. Auwarter, C. Aurisicchio, C. Fabbro, D. Bonifazi, J.V. Barth, J. Am. Chem. Soc. 132 (2010) 6783-6790.
[64] M.O. Blunt, J.C. Russell, N.R. Champness, P.H. Beton, Chem. Commun. 46 (2010) 7157-7159.
[65] R. Gutzler, H. Walch, G. Eder, S. Kloft, W.M. Heckl, M. Lackinger, Chem. Commun. (2009) 4456-4458.
[66] F. Sedona, M. Di Marino, M. Sambi, T. Carofiglio, E. Lubian, M. Casarin, E. Tondello, ACS Nano 4 (2010) 5147-5154.

[67] S. Weigelt, C. Busse, C. Bombis, M.M. Knudsen, K.V. Gothelf, T. Strunskus, C. Woll, M. Dahlbom, B. Hammer, E. Laegsgaard, F. Besenbacher, T.R. Linderoth, Angew. Chem.-Int. Edit. 46 (2007) 9227-9230.
[68] S. Weigelt, C. Bombis, C. Busse, M.M. Knudsen, K.V. Gothelf, E. Laegsgaard, F. Besenbacher, T.R. Linderoth, ACS Nano 2 (2008) 651-660.
[69] S. Jensen, H. Fruchtl, C.J. Baddeley, J. Am. Chem. Soc. 131 (2009) 16706-16713.
[70] J. Greenwood, H.A. Fruchtl, C.J. Baddeley, The Journal of Physical Chemistry C 117 (2013) 4515-4520.
[71] C.H. Schmitz, J. Ikonomov, M. Sokolowski, J. Phys. Chem. C 113 (2009) 11984-11987.
[72] S. Jensen, J. Greenwood, H.A. Fruchtl, C.J. Baddeley, J. Phys. Chem. C 115 (2011) 8630-8636.
[73] L. Grill, M. Dyer, L. Lafferentz, M. Persson, M.V. Peters, S. Hecht, Nat. Nanotechnol. 2 (2007) 687-691.
[74] M.X. Ding, Prog. Polym. Sci. 32 (2007) 623-668.
[75] E. Halasa, Polimery 50 (2005) 20-28.
[76] M. Treier, N.V. Richardson, R. Fasel, J. Am. Chem. Soc. 130 (2008) 14054-+.
[77] M. Treier, R. Fasel, N.R. Champness, S. Argent, N.V. Richardson, Phys. Chem. Chem. Phys. 11 (2009) 1209-1214.
[78] Y. Li, J. Wan, K. Deng, X. Han, S. Lei, Y. Yang, Q. Zheng, Q. Zeng, C. Wang, The Journal of Physical Chemistry C 115 (2011) 6540-6544.
[79] R. Tanoue, R. Higuchi, N. Enoki, Y. Miyasato, S. Uemura, N. Kimizuka, A.Z. Stieg, J.K. Gimzewski, M. Kunitake, Acs Nano 5 (2011) 3923-3929.
[80] J. Greenwood, C.J. Baddeley, Langmuir 29 (2013) 653-657.
[81] J.C. Russell, M.O. Blunt, J.M. Garfitt, D.J. Scurr, M. Alexander, N.R. Champness, P.H. Beton, J. Am. Chem. Soc. 133 (2011) 4220-4223.

Chapter Two: Experimental Techniques

2.1 Ultra High Vacuum

A fundamental requirement for surface science research is maintaining a well-defined and clean surface. All surface science investigations involve probing the surface interface at an atomic or molecular level for the purpose of developing an insight into surface properties and reaction models. In order to maintain a clean surface for the duration of the experimental investigation the research must be conducted in an environment free of contamination. The rate of surface bombardment (Z), flux, incident upon the surface can be calculated from the *Hertz-Knudsen equation*, Equation 2.1.

$$Z = \frac{\mathrm{P}}{\sqrt{(2\pi \mathrm{mkT})}} \ \mathrm{cm^{-2}\,s^{-1}} \qquad \textbf{Equation 2.1}$$

P= ambient pressure (N cm^{-2}); m= atomic/molecular mass (kg $molecule^{-1}$); T= absolute temperature (K); and k= Boltzmann constant (J K^{-1}).

The rate of surface contamination is also a factor of the sticking probability S(θ) of the impinging molecules, where θ = surface coverage. A good indication of the necessity for a low pressure environment to avoid contamination can be gained by using an example. If one assumes a sticking probability of S(θ) = 1 for a contaminant species, general atomic species X with mass 32 amu, at 300 K and for a surface with atomic density of 10^{15} cm^{-2}. At an ambient pressure of 1 x 10^{-6} torr (1 torr = 7.5006 x 10^{-3} N m^{-2}), the flux of contaminant species (Z) = 3.58 x 10^{14} cm^{-2} s^{-1}. Since the sticking probability, S(θ), is equal to 1, every X species that strikes the surface is adsorbed. Therefore, the rate at which the surface becomes contaminated with a monolayer of X is equal to 0.358 monolayers s^{-1}. Hence, the time for 1 monolayer of contaminant sticking to the surface at 10^{-6} torr is 2.8 s. Therefore in order to prevent contamination of the surface, surface science investigations must be performed in the ultra-high vacuum (UHV) regime. This requires a pressure of below 10^{-9} torr, thereby providing enough time to perform experimental investigations without the surface becoming significantly contaminated.[1]

In addition to keeping the surface clean, UHV is required to perform electron spectroscopy of samples. The mean free path (the average distance travelled by a particle between collisions) of the electrons must be sufficiently large to avoid scattering with residual gas molecules. UHV provides a low enough pressure to perform electron spectroscopy studies, so that the electron beam is able to traverse the distance between the source, sample, and analyser without significant interference from background gas molecules.

2.2 Achieving UHV

Ultra-high vacuum chambers consist of a variety of pumps to attain the required pressure for surface science studies. Each class of pump is designed to operate within a specific pressure range; hence, since the pressure range from atmosphere to UHV is so large, no one pump can cover this, and numerous pumps are required to pump the entire pressure range.

Of the pumps used, they can be split into two categories: compression pumps and entrapment pumps. Compression pumps cover the first phase of pumping, removing relatively large quantities of gas, and, hence, are also classed under the term mass transfer pumps. Rotary pumps are used in conjunction with turbomolecular and/or diffusion pumps initially to attain a base pressure of 10^{-5} torr. Rotary pumps are placed on the exhaust of mass transfer pumps, removing the gas by means of a cyclical increasing and decreasing volume chamber, thereby maintaining a high pressure gradient between the inlet and outlet of the mass transfer pumps. Entrapment pumps consist of sorption pumps, cryopumps, ion pumps and titanium sublimation pumps (TSP). Of these, the latter two were used throughout this PhD project. These pumps cover the low pressure region and enable a pressure of 10^{-10} torr to be attained. TSP works by subliming Ti into the chamber from solid electrodes by passing a high current through them. Ti is reactive enough to interact with most residual gases, forming stable compounds; these compounds subsequently condense on the chamber walls, removing them from the background. Ion pumps ionise the residual gases in the vicinity of a high electric field. Once ionised, the positively charged particles are collected and embedded in the cathode of the ion pump.

Each time the vacuum chamber is pumped down from atmosphere, it must be baked out to remove adsorbed molecules on the chamber walls; otherwise, these adsorbed molecules would provide a constant source of contaminant to the background pressure. Typically, the bake-out temperature is approximately 150°C. For this reason, all of the component materials of the UHV chamber must be able to withstand these conditions. Stainless steel is the material of choice for UHV chambers. Different sections of UHV chambers are connected with flanges sealed with oxygen free, high conductivity (OFHC) Cu gaskets. Flanges comprise of a 'knife-edge', which, when compressed against the malleable Cu gasket, provides a vacuum seal. Metals for the internal components of UHV systems are chosen for their low outgassing properties to minimise the background pressure; these include: tungsten, molybdenum and tantalum.[2]

2.3 Sample Preparation

Single crystal metal surfaces are cleaned by argon ion bombardment. A high energy beam of ionised argon atoms (500-1500 eV) incident upon the single crystal sample imparts kinetic energy on the surface, physically removing impurities and desorbing them into the chamber. This process is designated 'sputtering'. The sputtering process leaves a damaged and rough surface. Annealing the sample to a sufficiently high temperature allows the surface atoms to rapidly diffuse and reform the thermodynamically stable miller index plane surface. Repeated cycles of sputtering and annealing are required, the number of cycles required depends on the reactivity, and, hence, level of contamination present, of the sample. For highly reactive surfaces, such as Ni and Pd, annealing in a high oxygen background pressure (10^{-6}

torr) is usually required, in addition to sputtering-anneal cycles, in order to oxidise carbon contamination on the surface.

2.4 Electron Spectroscopy

2.4.1 Auger Electron Spectroscopy (AES)

Pierre Auger discovered the β-emission of electrons by ionising a gas with X-rays in 1923.[3] The ionisation process can also be initiated by photons or electrons; the latter is referred to as the Auger process. The emitted electrons are known as 'Auger electrons', and this is the basis for Auger electron spectroscopy (AES). AES is a workhorse technique for the surface specific elemental analysis of single crystal samples for the first - tenth atomic layer.

The Auger electrons emitted via electron bombardment are constituents of the secondary electron spectrum, possessing specific energies allowing elemental identification. The process works as follows: an incident electron (or photon) ionises a core electron, electron 1. This creates a hole, or electron vacancy, in the core level which can be filled by the downward transition of an electron from a higher energy level, electron 2. The energy transition of electron 2, the 'down' electron, releases a photon of energy specific to the quantum of energy ΔE between the two respective energy levels. This photon of energy, hν, can escape as X-ray fluorescence. Alternatively, the energy released can be transferred to a third electron, electron 3, which is designated as the Auger electron and possesses a kinetic energy as given by Equation 2.2.

$$E_{kin} = (E_K - E_{L1}) - (E_{L\,2,3} - \phi) \qquad \textbf{Equation 2.2}$$

Where E_K is the binding energy of the core level electron 1; E_{L1} is the binding energy of electron 2. $E_{L\ 2,\ 3}$ is the binding energy of electron 3; ϕ is the work function of the analyser. The term in the first parenthesis represents the available energy to the Auger electron from the 'down' electron. The term in the second parenthesis represents the minimum energy required to initiate emission from the atom. Figure 2.1 represents an illustration of the Auger process.

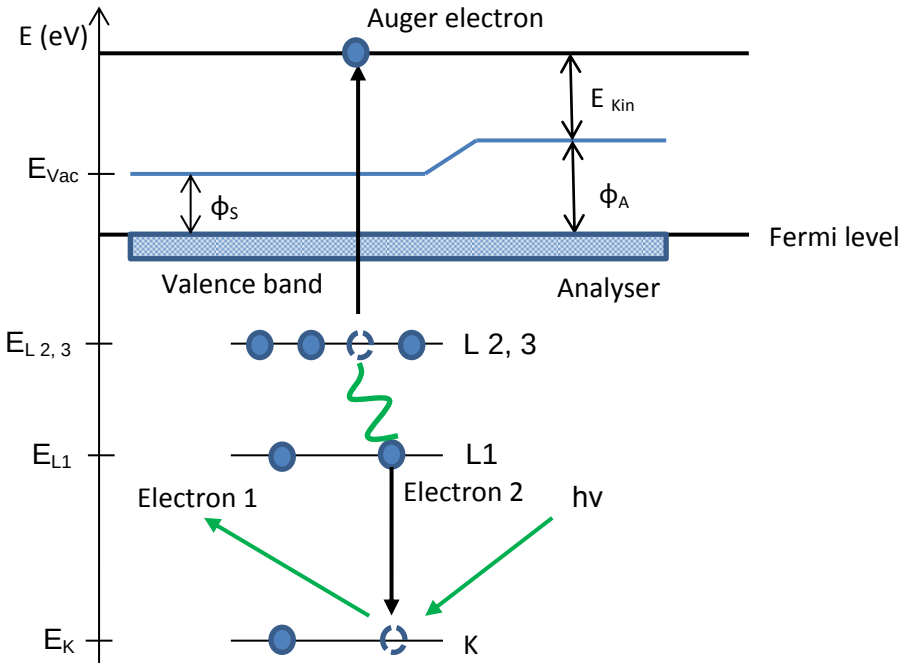

Figure 2.1: Illustration of the Auger process: ϕ_S and ϕ_A are the work functions of the sample and analyser respectively. E_{kin} is the kinetic energy of the Auger electron.

The crucial characteristic with regards to AES is that the kinetic energy of the Auger electron is independent of the incident particle energy which initiates electron emission, except for the requirement that the incident particle energy must be sufficiently high enough to ionise a core level electron. The energy transferred to the emitted Auger electron is only a factor of the internal atomic energy level transition.

Hence, a quantum of energy is transferred to the Auger electron specific to the energy levels of the atom in question, allowing for elemental identification.

In the Auger process, a minimum of three electrons is required; hence, only elements with $Z \geq 3$ are detectable with this technique. As the atomic number increases, the number of electronic energy levels also increases; the complexity of which grows, due to the greater number of possible electronic transitions. The probability of X-ray fluorescence is higher than Auger emission for higher atomic number elements; therefore, the Auger process is most sensitive for low atomic number elements. Typically, Auger electron spectra are differentiated, providing greater sensitivity to the Auger peaks. The majority of emitted electrons are secondary electrons; these are electrons which have undergone multiple energy loss processes. The differentiation of the electron energy distributions allows for a clearer identification of the Auger peaks superimposed on the large secondary electron background spectrum. The integral of the Auger peaks provides information on the elemental concentration of the corresponding surface species.

2.4.2 Low Energy Electron Diffraction (LEED)

A crucial necessity for surface scientists is to have the ability to determine the long range surface structure and periodicity of single crystal metal surfaces. The technique of choice for surface structure analysis is provided by the diffraction of low energy electrons. The theory of electron diffraction was first postulated in 1924 by Louis de Broglie, for which he received the Nobel Prize for Physics in 1929,[4] creating a new field of physics known as wave-mechanics. This demonstrated the wavelike behaviour of particles, given by the expression in Equation 2.3.

$$\lambda = \frac{h}{mv} \equiv \frac{h}{p}$$ **Equation 2.3**

Where λ is the electron wavelength, h is Planck's constant, m is the electron mass, v is the electron velocity and p is the electron momentum. Experimental confirmation for the wavelike behaviour of particles came in 1927 when Davisson and Germer observed a diffraction pattern with an angular dependence of intensity of electrons backscattered from a crystalline nickel sample.[5] The de Broglie expression of matter waves proves that the wavelength is inversely proportional to the linear momentum of a particle, and, also, the frequency is directly proportional to the kinetic energy of the particle.

The inelastic mean free path (IMFP) is defined as: the total distance, including elastic scattering events that an electron can travel with a probability of 1/*e* of not undergoing an inelastic scattering event, where *e* is the electric charge of an electron. Electrons will lose energy through interactions such as plasmon- and phonon excitations in addition to electron- electron interactions.[1] Incident electrons in the energy range 20-1000 eV possess inelastic mean free paths of ~ 5-20 Å;[6] therefore, the stated energy range is designated as the surface sensitive energy regime, with electrons providing diffraction information on the top atomic layers of a surface. Electrons within the stated energy range possess de Broglie wavelengths of comparable orders of magnitude to the interatomic spacing between surface atoms. Consequently, electron diffraction occurs from periodic atomic arrangements.

Low energy electron diffraction (LEED) analysis incorporates the de Broglie properties of electrons to act as an excellent experimental probe of surface structure and the

structure of ordered adsorbate overlayers. The experimental setup is such that an electron gun fires a monochromatic beam of electrons incident to an electrically conducting sample. The electron gun filament is made from either the low work function material lanthanum hexaboride (LaB_6) or tungsten. Electron emission occurs via thermionic emission of the cathode filament, upon which the emitted electrons are accelerated by a potential difference. An array of electrostatic lenses within the filament focuses the electrons into a parallel beam directed towards the sample. The sample must be grounded to earth to prevent charging. Diffracted electrons pass through retardation grids which ensure only electrons scattered elastically pass through. The elastically scattered electrons are then accelerated towards a fluorescent phosphor-coated screen. Figure 2.2 shows a diagram of the apparatus setup. Electrons striking the phosphor screen produce a diffraction pattern representative of the crystalline structure of the sample surface.

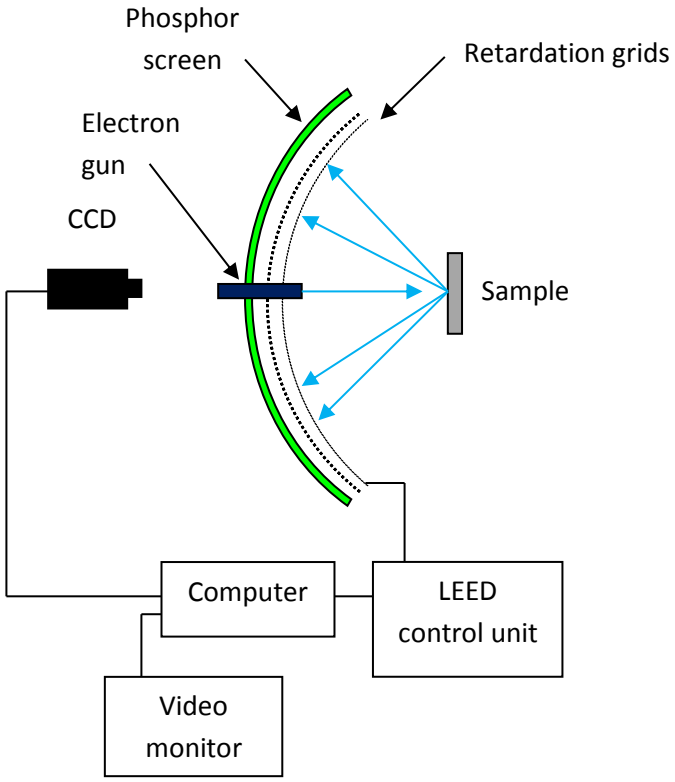

Figure 2.2: Schematic illustration of the LEED apparatus, adapted from reference [6].

Electrons diffracted from the surface undergo constructive interference between the electron waves. This only occurs under the condition of the path length difference being equal to an integer value of wavelengths. Expressions for the path length difference and the condition for constructive interference are given in Equations 2.2 and 2.3, respectively.

$$\Delta_a = a \sin \theta_a \qquad \textbf{Equation 2.2}$$

$$\Delta_a = n \lambda \qquad \textbf{Equation 2.3}$$

Where Δ_a is the path length difference, 'a' is the lattice separation, θ_a is the scattering angle and λ is the electron wavelength.

Equation 2.2 states, that, for constant values of wavelength, λ, and lattice spacing, a, only specific values of θ_a enable the conditions for constructive interference to be met, corresponding to integer values. Hence, discrete diffracted beams will be seen at particular angles.[6] For fixed values of λ, as 'a' increases, θ_a will decrease, resulting in the diffracted beams becoming more closely spaced. This relationship leads to the observed LEED pattern representing the reciprocal lattice of the real space structure.

LEED analysis can be utilised in two ways: 1) The qualitative approach provides information on the surface structure periodicity. It also allows an exact definition of the two dimensional periodicity of an overlayer structure relative to the substrate, providing details of the unit cell size and rotational alignment. 2) The quantitative approach analyses variations in the diffraction pattern spot intensities as a function of incident electron beam energy. This produces I-V curves, providing information on the type of adsorption site occupied by adsorbates, as well as the bond lengths and bond angles. I-V curves are generated by comparison of experimental data with theoretical curves.

2.5 Scanning Tunnelling Microscopy (STM)

The most important event in recent years for the development of surface science studies has been the introduction of scanning probe microscopy. Gert Binnig and Heinrich Röhrer, whilst working at the IBM research facility in Zürich, invented the

scanning tunnelling microscope (STM) in 1982.[7-9] The scientists were awarded the Nobel Prize for Physics in 1986.[10] The short space of time for the awarding by the Nobel Prize committee is a testament to the clear breakthrough STM provided in terms of the molecular investigation of surface structure.

Unlike other electron microscopy techniques, the use of a point probe tip does not require lenses; as such, STM images are very resolved, producing no distortions due to aberration. The distance between the tip apex and sample is comparable or smaller than the electron wavelength, $d \leq \lambda$; this is referred to as the 'near-field' regime. Consequently, diffraction does not limit the achievable spatial resolution.[11] STM is a versatile technique, used not only in ultra-high vacuum conditions but, also, in ambient conditions and in solution, and at variable temperatures between near zero degrees Kelvin and hundreds of degrees Kelvin. The fact that STM can also be operated in air and liquids, since there are no free electrons involved, is another advantage it holds over electron microscopy and surface analytical techniques.[11]

A basic setup of scanning tunnelling microscopy is represented in Figure 2.3. An atomically sharp, conductive tip, usually W or Pt/Ir wire, is positioned within a few nanometres of a conducting surface which is connected electronically to the STM controls. A potential difference of a few millivolts is applied between the tip and the sample. Depending on the potential difference bias, electrons either flow from the tip to the sample or vice versa, lowering their potential energy in doing so. This behaviour is not in line with classical physics, which dictates that electrons are bound within the solid and must overcome the sample work function, Φ, to escape. Electrons pass through the vacuum gap between the tip and sample by a quantum

mechanical process known as electron tunnelling. This avoids the necessity for electrons to acquire sufficient kinetic energy to overcome the work function. The current produced by electron tunnelling is small but measurable. The true value of STM lies in the exponential dependence of tunnelling current magnitude on the tip-sample separation distance, represented in Equation 2.4.

$$I(s) = C \exp(-s \sqrt{\Phi}) \qquad \textbf{Equation 2.4}$$

Where I is the tunnelling current, s is the tip-sample separation, and Φ the sample work function. C is a constant. Therefore, scanning a section of the sample surface and measuring the tunnelling current magnitude provides a topographical representation of the surface. Atomic resolution is possible, with good resolution considered to be 0.1 nm lateral resolution and 0.01 nm depth resolution.[6] The sample stage is vibrationally isolated in order to obtain high resolution images.

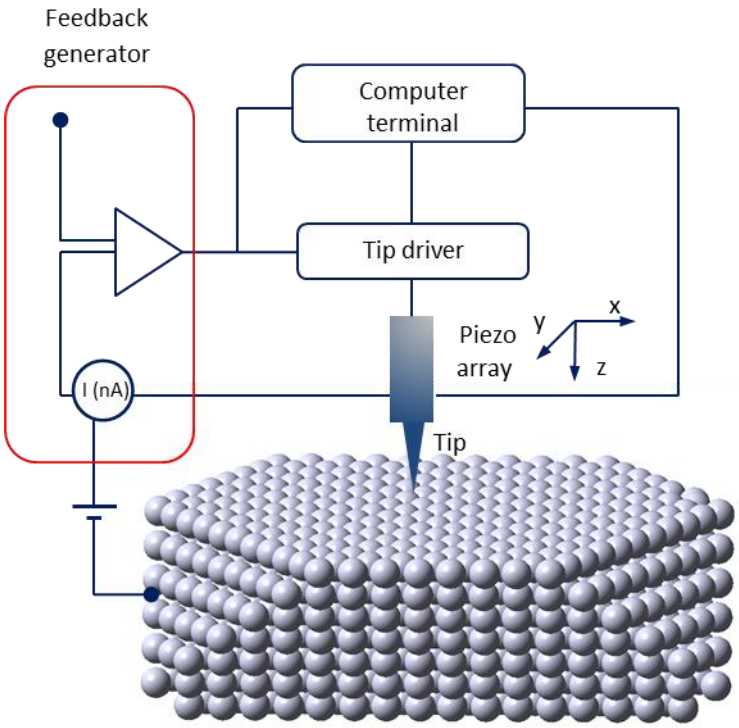

Figure 2.3: Illustration of the experimental set-up used for STM.

The STM probe is mounted on a set of piezoelectric ceramic actuators; the standard material is PZT (lead zirconium titanate). This allows the tip to be moved in three dimensions. High voltage amplifiers are required to polarize the actuators to produce the desired effect.[12] This polarization can be lost gradually after long use. Therefore, the calibration of actuators has to be repeated regularly.[12] The atomic spacing of the Si(111)-7 x 7 surface is typically used as a calibration reference of the x-y piezo actuators in UHV conditions. The step height value is used for calibration in the z direction. For ambient STM, highly oriented pyrolytic graphite (HOPG) atomic spacing is the calibration reference.

Scanning the tip in constant height mode results in increases in current from tunnelling electrons corresponding to protrusions on the surface, be these atomic corrugations or steps on the surface etc., due to a lowering in the tip-surface distance. In this mode, the x-y plane is used to scan across the surface whilst maintaining a constant value for the z-direction. Another mode of scanning can also be employed, known as constant current mode. In this case, the tip can move in the z-direction as well in order to maintain a constant current value. A topographical representation of the surface is then presented by plotting the measurements of the variations in the z-piezo voltage against the lateral position of the tip. Constant height mode is the preferred method for atomically flat surfaces, enabling rapid scanning without the risk of tip-surface collisions. Constant current mode is preferred for relatively rough surfaces, since the tip height needs to be adjusted continually to avoid collisions.

The tunnelling current (I_t) is in the range of pico-amps (pA) to nano-amps (nA) and is measured with a preamplifier.[12] This signal is the input of the feedback loop and is compared to I_o, which is designed to keep the tunnelling current constant during x-y scanning.[12] The output signal is amplified and connected to the z-piezo actuator. Tip separation is adjusted to maintain a constant via expansion or contraction of the z-piezo electric actuator.

To elaborate further on the quantum mechanical tunnelling process of STM, the wavelike properties of electrons need to be discussed in greater detail. The simplistic one-dimensional tunnelling of an impinging electron of mass m and energy E on a rectangular potential barrier can be used to describe the process. Electrons travel as free waves through the metallic bulk of both the STM-tip and sample. As they approach the surface they are reflected by the change in density of positive charge, scattering back into the bulk. However, the electrons overspill out into the vacuum for two reasons: First, the potential does not fall away immediately, but obeys a Coulomb dependence. Also, the electrons can tunnel into the vacuum since the potential does not go to infinity. This gives a finite electron density in the vacuum above the surface, leaving this region negatively charged. If two metals are brought close enough together (in this case the STM-tip and sample surface), the electron wave functions of those tunnelling out of the surface and STM-tip can overlap, hence tunnelling of electrons can occur between two metals. This is represented in the diagram in Figure 2.4, where d is the wave displacement, V is the potential barrier height and ψ is the wave function.

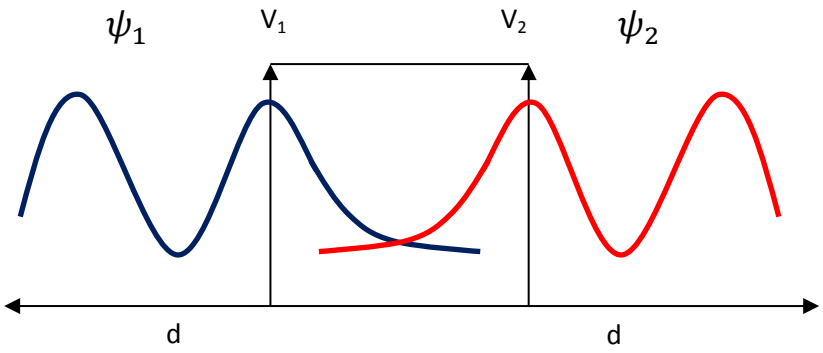

Figure 2.4: Illustration of two wave functions overlapping across a one-dimensional barrier, adapted from reference [11].

Interpretation of the STM images requires an understanding of the mechanism for the flow of electrons between the tip and surface. The work function of a metal is represented by Equation 2.5. One can consider the two metals as being two sets of electron energy levels, with the highest occupied energy level known as the *Fermi level*.[6] The difference in the work functions of the two metals represents the difference in the Fermi level energies, represented by Equation 2.6.

$$\Phi = E_{vac} - E_f \qquad \textbf{Equation 2.5}$$

$$\Phi_c = E_f{}^L - E_f{}^R \qquad \textbf{Equation 2.6}$$

By adjusting the potential difference between the two metals one can control the direction of current flow, as well as the amount. If the right-hand metal is biased positively relative to the left-hand metal, this lowers the Fermi energy level, $E_f{}^R$, by an energy equal to *e*U, where *e* is the elemental electric charge and U is the potential difference. In this case, the electrons tunnel from the Fermi level of the left-hand metal into unoccupied states of the right-hand metal. A negatively biased tip results in electron tunnelling from the occupied states of the tip to the unoccupied states of the sample. In contrast, a positively biased tip results in electrons tunnelling from the

occupied states of the sample to the unoccupied states of the tip. An important point is that STM images the electronic states of the sample, or the local density of states (LDOS). Changing the bias voltage results in imaging of either local occupied or unoccupied states of the sample; in terms of adsorbed molecular species, this is an invaluable phenomenon since this corresponds to imaging the HOMO and LUMO orbitals, respectively. The atoms themselves are not imaged, but as the electronic states correlate closely with atomic position it is therefore a good approximation to consider STM images in terms of atomic positions.[1]

2.6 Temperature Programmed Desorption (TPD)

Temperature programmed desorption is a useful technique for probing the desorption energies and kinetics of single molecular species on surfaces in ultra-high vacuum. The procedure begins by dosing the single crystal for a specified time and pressure. The crystal is then moved to face a mass spectrometer; a quadrupole mass spectrometer (QMS) is the standard equipment employed. A pre-determined, linear temperature ramp is applied to the sample. Subsequent desorption is monitored as a function of temperature. A QMS has the advantage of mass-selectively measuring the pressure rise; therefore, it determines whether multiple products are formed and discriminates against background gases.[1]

Upon the application of a temperature ramp, the rate of desorption may be expressed as:

$$-\frac{d\theta}{dt} = k_d N^m \qquad \textbf{Equation 2.7}$$

Where θ is the adsorbate surface coverage, k_d is the rate constant for the desorption process, and m is the order of reaction.[6]

Desorption is an activated process. The rate constant (k_d) obeys an Arrhenius dependency, which is expressed as:

$$k_d = A \exp\left(\frac{-E_d}{RT}\right) \qquad \textbf{Equation 2.8}$$

where E_d is the activation energy for desorption and A is a pre-exponential factor. Although E_d increases exponentially with temperature, a maximum is observed because the surface coverage simultaneously decreases.[6]

We can make the assumption

$$\frac{d\,\theta}{d\,t} = \frac{d\,\theta}{d\,T} \times \frac{d\,T}{d\,t} = \frac{d\,\theta}{d\,T}\beta \qquad \textbf{Equation 2.9}$$

where $\beta = \frac{d\,T}{d\,t}$ (the heating rate)

A general expression for the thermal desorption peak maximum (T_{max}), E_d and θ is given by:

$$\frac{E_d}{RT^2 max} = \frac{A}{\beta} m\,\theta^{m-1} \exp\left(\frac{-E_d}{RTmax}\right) \qquad \textbf{Equation 2.10}$$

For *zero-order desorption*, m = 0; hence, Equation 2.10 can be expressed as:

$$-\frac{d\,\theta}{d\,t} = \frac{A}{\beta} \exp\left(\frac{-E_d}{RT}\right) \qquad \textbf{Equation 2.11}$$

Multilayer systems generally obey zero-order desorption kinetics. Multilayer peaks appear at a lower desorption temperature relative to the monolayer. Multilayers of molecules tend to be physisorbed to the surface via van der Waals interactions which

are weaker than the covalent bonds often formed by molecules bound directly to metal surfaces.

First-order desorption is the result when the rate of desorption is dependent on only a single desorbing species coverage. In this case m = 1, and is expressed as:

$$-\frac{\mathrm{d}\,\theta}{\mathrm{d}\,t} = \frac{A\,\theta}{\beta}\exp\left(\frac{-\mathrm{E_d}}{RT}\right) \qquad \textbf{Equation 2.12}$$

Second-order desorption, m = 2, is observed when two species recombine on the surface prior to desorption. This results in T_{max} being dependent on θ for a second-ordered process. When θ increases, T_{max} is observed to decrease for a fixed value of E_d.[6]

First-order desorption leads to asymmetric peaks, and second-order desorption leads to symmetric peaks. These generalisations only apply if A and E_d are coverage independent. Lateral interactions between adsorbed molecules can occur, especially at high coverage. These interactions are typically repulsive in nature, and result in a lowering of E_d, and the desorption temperature.

2.7 Vibrational Spectroscopy

Vibrational spectroscopy is another way of identifying chemical species adsorbed on a surface, as well as which chemical groups of the molecule binds to the surface, how strongly it is bound and which orientation it adopts. Variations in vibrational frequencies can also be analysed to determine changes in the bonding interactions. There are three main techniques used: reflection-absorption infrared spectroscopy, electron energy loss spectroscopy and Raman spectroscopy.

An N-atom molecule in the gas phase has 3N degrees of freedom, specified by three coordinates which can be given independently of each other. If the molecule moves through space without changing shape (pure translation) then three coordinates are needed to describe that motion (using the centre of gravity of the molecule as the Cartesian axes origin). The rotation of the molecule can be described by three perpendicular axes, again needing three coordinates to describe them. Therefore, there are 3N-6 degrees of freedom for vibration motions. Total degrees of freedom are 3N, translation: 3, rotation: 3, and vibration: 3N-6.[13]

If the molecule is linear, then there is no rotation about the bond axis, so rotation requires one less degree of freedom and linear molecules have 3N-5 different internal vibrations. For both linear and non-linear molecules (with the exception of cyclic molecules) N-1 of the vibrations will be bond stretching vibrations, since a molecule with N atoms has N-1 bonds. An N-atom molecule on a surface contributes additional 3N degrees of freedom to the solid. Upon adsorption of a molecule, the vibrational modes of the molecule are retained. Depending on the strength of the adsorbate-substrate bonding interaction, the adsorbed molecule may or may not freely translate or rotate.[13]

In the case of chemisorbed atoms, vibrational frequencies are exhibited in the range 200-800 cm^{-1} (1 meV = 8.065 cm^{-1}). Chemisorbed molecules are the area most relevant to this project, with the majority of vibrations of functional groups within chemisorbates occurring above 800 cm^{-1}.

2.7.1 Reflection Absorption Infrared Spectroscopy (RAIRS)

RAIRS shall be the focus of the vibrational spectra techniques in this section. It is a highly complementary technique to those already discussed in this Chapter, and provides specific information on bond types and molecular orientation. Figure 2.5 shows an experimental set-up for a UHV RAIRS experiment. The technique does not require UHV conditions, and can be applied to ambient and solution-based environments. The analysis by infrared radiation is non-destructive. Since most surfaces used for surface science studies are opaque to IR radiation, the reflection mode analysis is incorporated. The surface is irradiated by IR light; vibrational frequencies of an adsorbate species matching the IR frequency absorb the IR radiation, hence reducing the intensity of the reflected IR beam. Examination of the reduced intensities in the IR spectrum provides details of the vibrational frequencies.

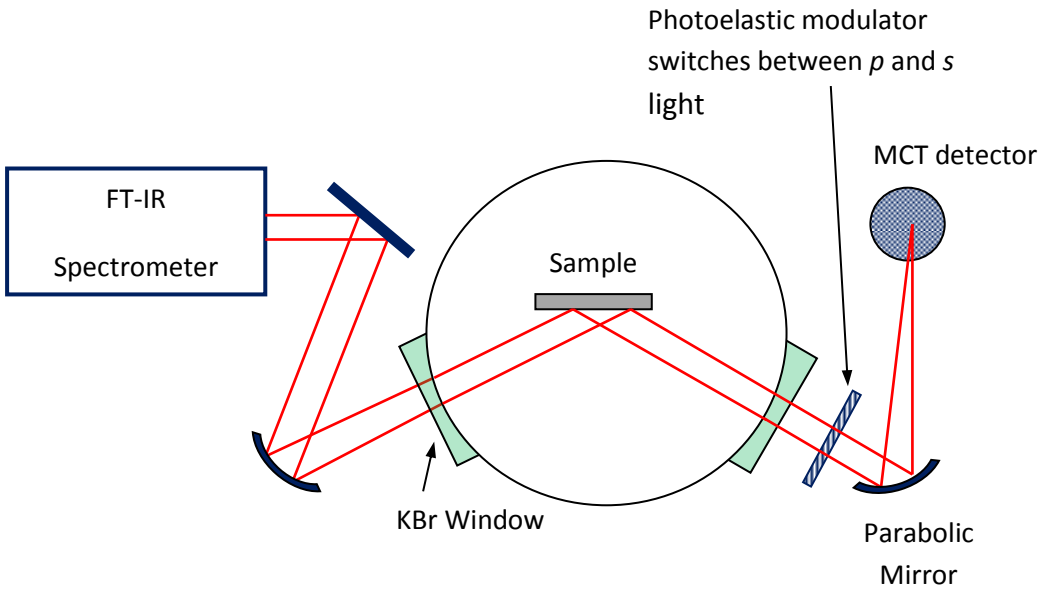

Figure 2.5: Experimental apparatus used for RAIRS experiments.

The detector in most cases is a mercury cadmium telluride (MCT) photoconductive semiconductor (detection range 5000-800 cm^{-1}).[6] Detecting vibrational frequencies < 800 cm^{-1} is not reliable because of the insensitivity of the detector in this range. However, a major advantage of IR spectroscopy is its high resolution of 1 cm^{-1} or less. Due to the much smaller number of atoms/molecules at the surface as compared to the bulk (typically 10^{14} cm^{-2} as opposed to 10^{21} cm^{-3}), absorption is generally quite weak.

Considering the electric fields produced by the reflection of radiation at a bare metal surface; s-polarisation denotes the field is polarised perpendicular to the plane of incidence (which means it is parallel to the surface), p-polarisation denotes the field is polarised parallel to the plane of incidence (see Figure 2.6). E_s^i and E_p^i refer to the s and p components, respectively, of the electric field vectors of the incident beam; while E_s^r and E_p^r refer to the reflected beam. The phase of the s-polarised radiation changes by nearly 180°, and, since the reflection coefficient is almost 100%, the relevant field from the s-component is practically zero at the surface. However, at grazing incidence the resultant field for the p-component is nearly twice the value for the incident ray, perpendicular to the surface.

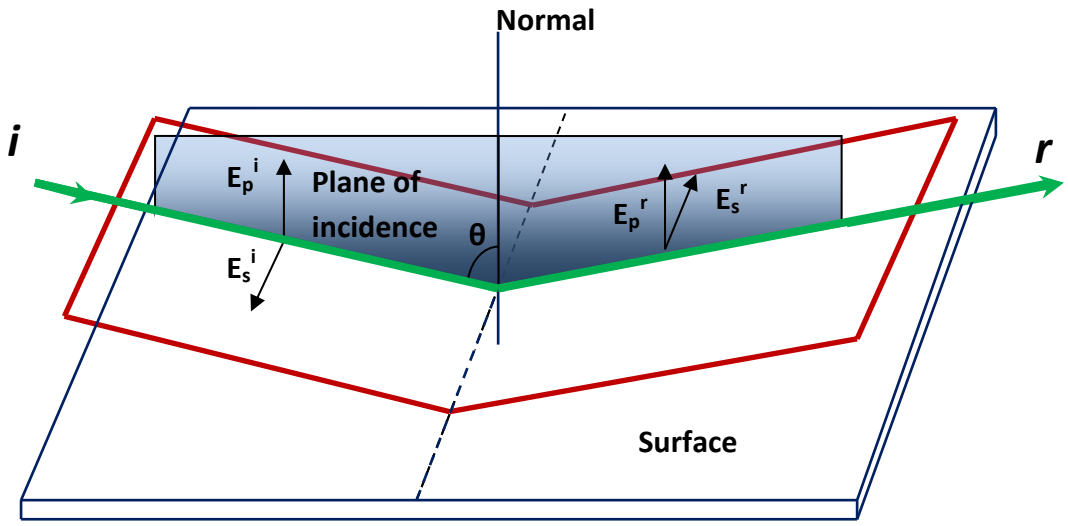

Figure 2.6: Reflection geometry showing the s and p components of the electric fields.

Only the perpendicular component of the p-polarised radiation can interact strongly with a dynamic dipole which is also normal to the surface. This is referred to as the metal-surface selection rule: *only molecular vibrations which have components of the dynamic dipole moments perpendicular to the metal surface will have measurable intensities*. A dipole moment in front of a metallic surface will create an image dipole moment in the metal surface. A molecule that adsorbs on a metal surface and has a dipole moment in one direction will create the opposite image dipole moment in the surface, see Figure 2.7. This is on account of the response of the valence electrons present in the surface to the molecular dipole. These two dipole moments cancel each other out, and the mode is consequently IR inactive at the surface. However, a molecule showing a dipole moment change perpendicular to the surface has its dipole moment enhanced by the image dipole.

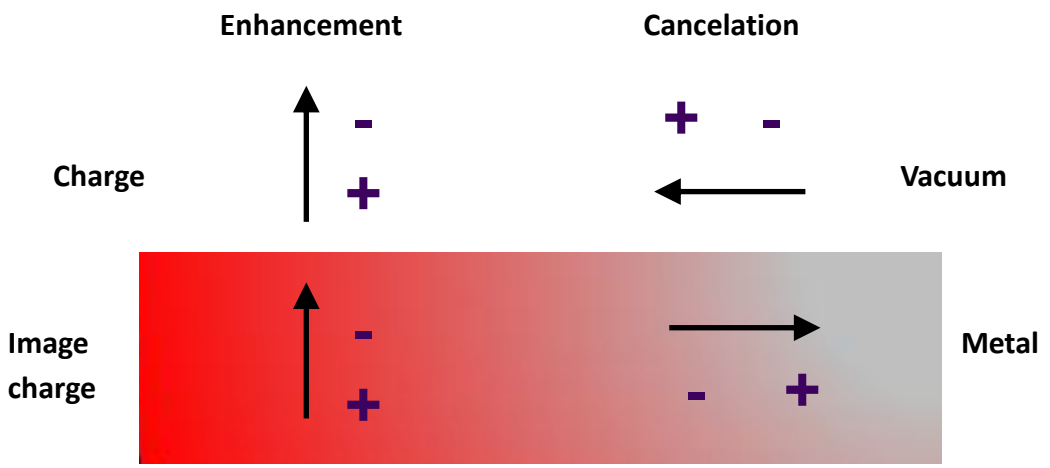

Figure 2.7: Illustration of the image dipoles for a molecule adsorbed perpendicular and parallel to the surface.

The selection rule has an important consequence for the required angle of incidence of IR light. A change in dipole moment during vibration can only interact with the electric field, *if the electric field and the direction of dipole moment change are parallel to each other.*

The intensity of the electric field at the surface is the sum of the incoming and reflected fields. Since s-polarised light undergoes a nearly 180° phase change at the surface, its intensity is virtually zero. On the other hand, p-polarised light has less of a phase change, which actually leads to enhancement at the surface. In addition, the shallower the incidence angle, the greater the proportion of p-polarised light and the area covered by the beam becomes larger, so that the ideal incidence angle to maximise IR absorption is approximately 85°. This is one reason why RAIRS experiments are conducted at grazing incidence. As well as this, utilising grazing incidence geometry increases the path length of the IR beam at the surface, hence increasing the sensitivity for very thin layers of adsorbate.[6]

A significant problem for using RAIRS is that IR active species in the gas/solution phase can absorb IR radiation and hence interfere with the signal, H_2O and CO_2 for example. Any reduction in signal intensity is a major concern for IR analysis of surface species due to the already weak signal. However, the surface selection rule can be used to our advantage in this case; p-polarised light is absorbed by the surface species *and* gas phase species, whereas s-polarised is *only* adsorbed by gas phase species. Polarisation-modulation (PM)-RAIRS works by subtracting the contribution of s-polarised light from the IR signal, therefore any attenuation in the IR spectrum is on account of p-polarised light absorbed by surface species and gas/solution phase species. Calibration of the set-up allows the absorption due to the solvent to be removed from the overall signal intensity, $I_p - I_s$, where I is the intensity, hence subtracting the effect of solvent absorption. This technique removes the effects of background interference on the IR beam that is detected.

2.7.2 High Resolution Electron Energy Loss Spectroscopy (HREELS)

Ibach and co-workers developed the method of high resolution electron energy loss spectroscopy (HREELS) in the early 1970s.[14] The method works by exciting atomic or molecular vibrations at the surface interface with a monochromatic electron beam.[15] The electron beam must have an energy spread of < 10 meV since the quantised vibrations have energies in the range between hundredths and tenths of an electron volt.[6] Typical electron beam energies are of between 1 and 10 eV. HREELS was the first surface science technique to probe the vibrational structure of sub-monolayer adsorbates, even those with relatively weak dynamic dipole moments. Advances in IR methods have caught up with this ability; however, the

main advantage HREELS holds over RAIRS is the capability to analyse vibrational modes below 1000 cm^{-1}, which are typically associated with substrate-adsorbate atom stretches.

Single crystal surfaces are essential for HREELS, since the energy of the scattered electrons are broadened from an ill-defined surface scattering potential, as is the case with a polycrystalline surface. The best energy resolution achievable with HREELS is 30-40 cm^{-1}, measured as the full width at half maximum (FWHM) height of the elastically scattered peak. This resolution is poor in comparison with RAIRS, but is sufficient for vibrational analysis of single crystal surface samples. An illustration of the experimental setup for HREELS is shown in Figure 2.8. The requirement of low energy electrons determines this is solely a high vacuum technique.

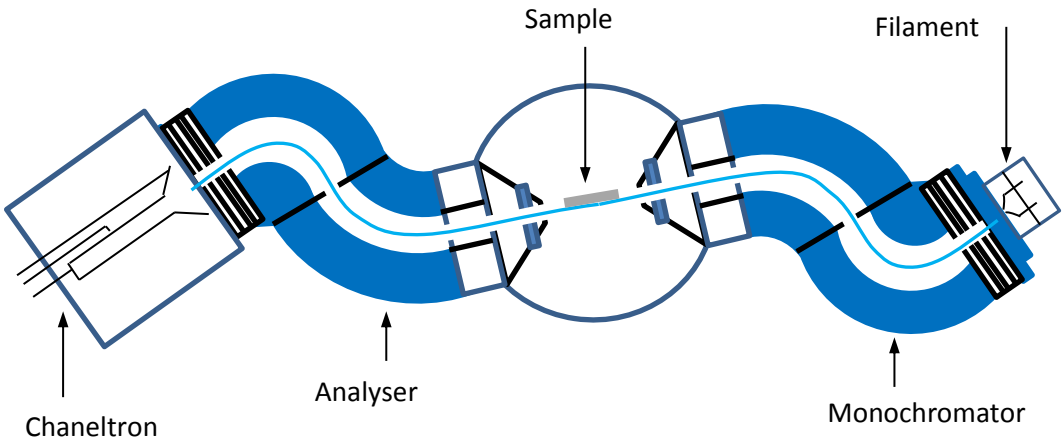

Figure 2.8: Schematic diagram of the HREELS experimental setup.

Another advantage HREELS has over RAIRS is the potential to probe vibrational modes by two types of scattering events: *Dipole scattering* is analogous to the photon interaction of RAIRS, in that only vibrational modes with a component of the

dynamic dipole moment perpendicular to the surface are detectable, see Figure 2.7. Minimal energy losses occur, therefore the momentum vector, *k*, of the electron has approximately the same amplitude for the incident and scattered electron, and the net vector direction remains the same.[16] The majority of electrons are scattered in the specular direction. The electric field of the incident electron interacts with the varying electric field of a composite of the molecular and image dipole. The interaction is relatively long-range, with the Coulombic energy transfer occurring with the electron 100-200 Å above the surface.[16] *Impact scattering* is the second mechanism by which vibrational excitation may occur. The incident electrons interact with the surface atomic potentials, modulated at vibrational frequencies over a short range. Impact scattering allows both parallel and perpendicular vibrations, with respect to the surface, and possessing an accompanying dipole moment, to be excited and analysed. This mode of scattering results in a loss of momentum with regards to the electrons, hence the angle of incidence is no longer equal to the angle of reflectance. As such, impact scattering events can be distinguished from dipole scattering vibrations by monitoring in the off-specular direction. By monitoring in the off-specular direction, the dipole forbidden modes of the intense dipole scattered events signals are absent from the spectrum, which would otherwise overwhelm the weak signal of the impact scattered vibrations.

2.8 References

[1] K. Kolasinski, Surface Science: Foundations of Catalysis and Nanoscience. Second edition. Wiley (2008).
[2] A. Chambers, R.K. Fitch, B.S. Halliday, Institute of Physics publishing (1998).
[3] P. Auger, *J. Phys. Radium* **6** (1925) 205.
[4] http://nobelprize.org/nobel_prizes/physics/laureates/1929/.
[5] C. Davisson, H.L. Germer, Nature **119** (1927) 558-560.
[6] G. Attard, C. Barnes, OUP, Oxford (1998).
[7] G. Binnig, H. Rohrer, C. Gerber, E. Weibel, *Applied Physics Letters* **40** (1982) 178.
[8] G. Binnig, H. Rohrer, C. Gerber, E. Weibel, Phys. Rev. Lett. **49** (1982) 57.
[9] G. Binnig, H. Rohrer, *Surface Science* **126** (1983) 236-244.
[10] http://nobelprize.org/nobel_prizes/physics/laureates/1986/.
[11] R. Wiesendanger, Cambridge University Press. (1998).
[12] E. Meyer, H. Hug Josef, R. Bennewitz, Springer (2004).
[13] H. Arnolds, 2009 CHEM 374: Spectroscopy lecture notes.
[14] H. Ibach, H. Hopster, B. Sexton, Appl. Surf. Sci. 1 (1977) 1-24.
[15] H. Ibach, D. Mills, New York: Academic (1982).
[16] M.E. Pemble, P. Gardener, Wiley. second edition (2007).

Chapter Three:

Co-deposition of Melamine with an Aromatic Dialdehyde on Ni{111}

Part One:

Ordered Growth of Upright Melamine Species on Ni{111}

3.1 Abstract

Melamine (1, 3, 5-triazine-2, 4, 6-triamine) is a common building block used in the construction of 2-D H-bonded architectures at surfaces. Previous work investigating the adsorption of melamine has focussed on relatively unreactive surfaces where intermolecular H-bonding interactions dominate over molecule-surface interactions. In this study, the adsorption of melamine was investigated on the more reactive Ni{111} surface under ultrahigh vacuum conditions. Molecular packing and conformation are investigated with scanning tunnelling microscopy (STM), reflection absorption infrared spectrocopy (RAIRS), and high resolution electron energy loss

spectroscopy (HREELS). The desorption products are investigated by temperature programmed desorption (TPD). The adsorption behaviour was found to be strongly influenced by the substrate, with RAIRS and HREELS indicating that the molecular plane is tilted relative to the surface. Thermally stable one-dimensional chains of partially dehydrogenated melamine are formed on the Ni{111} surface, aligned along the <-211> crystallographic directions.

3.2 Introduction

The self-assembly of small organic building blocks for the creation of two-dimensional nanostructures has been widely studied over recent years. A large variety of structures have been developed so far, incorporating mono- or multi-component molecular assemblies.[1-12] There are advantages to utilising hydrogen-bonding for such structures; mainly, that the relatively high equilibration of intermolecular interactions allows defects within the structure to be minimised, and high diffusion rates of small organic precursors enable the formation of extremely ordered structures on a large scale.

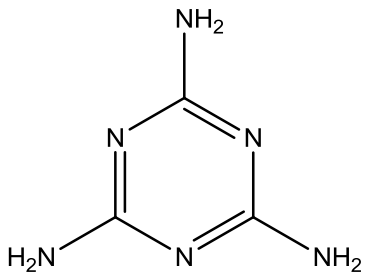

Figure 3.1: Chemical structure of melamine.

Melamine, (1, 3, 5-triazine-2, 4, 6-triamine, see Figure 3.1), is commonly employed as a building block in hydrogen-bonded structures in the literature. The three-fold rotational symmetry, and the ability of the amino group and triazine ring nitrogen atoms to take part in multiple hydrogen bonding interactions make it a desirable molecular unit for nanoscale structures. So far, melamine adsorption has been investigated on the Au{111}[13] and Ag{111}[14] surfaces. In addition, bimolecular hydrogen–bonded systems of melamine have been studied incorporating cyanuric acid,[15, 16] PTCDA,[17] PTCDI,[18-20] and NTCDI.[6] In addition, a tri-molecular system of melamine in combination with PTCDI and uracil has been investigated with scanning tunnelling microscopy by Castell et al.[21] Due to the low thermal stability of hydrogen-bonded structures, research has been conducted into developing covalent structures, which possess higher thermal and mechanical stability. Covalently bonded two-dimensional nanostructures have been fabricated using melamine as the nucleophilic species, reacting with 1,4-phenylene diisocyanate,[22] and with trimesoyl chloride,[23] both on Au{111}, to produce urea and amide linkages, respectively.

The aim in this Chapter is to examine how the ability of melamine to form intermolecular H-bonding interactions is affected by interactions with a relatively reactive surface and to establish the vibrational modes between melamine and the Ni surface; in addition, it is desired to determine the extent of dehydrogenation melamine undergoes upon adsorption.

3.3 Experimental

STM experiments were carried out on an Omicron UHV system with a base pressure of 1 x 10^{-10} mbar. The Ni{111} sample was prepared by cycles of Ar ion bombardment (1.5 kV) and annealing to 893 K until low energy electron diffraction (LEED) and STM indicated the presence of a clean Ni{111} surface. Melamine (Sigma-Aldrich, 99.9 % purity) was deposited onto the Ni{111} surface, held at room temperature, from a glass doser resistively heated to 393 K, separated from the UHV chamber by a gate valve and differentially pumped by a turbomolecular pump. Samples were transferred under UHV conditions to the STM chamber, where images were acquired at room temperature in constant current mode using an electrochemically etched W tip. STM images were processed using WSxM software.[24] RAIRS measurements were carried out using a Nicolet Nexus 860 FTIR spectrometer, fitted with a mercury cadmium telluride (MCT) detector cooled by liquid nitrogen and possessing a spectral range of 800-4000 cm^{-1}. The sample was placed in a UHV chamber, with a base pressure of 1 x 10^{-10} mbar, and the infrared beam (θ_i = 8°) from the spectrometer passed through KBr windows, was reflected off the sample and into the detector. The spectrometer was operated with a resolution of 4cm^{-1}, at 256 scans per spectrum.

HREELS experiments were carried out in a VSW HIB 1000, double pass spectrometer, base pressure of less than 5 x 10^{-10} mbar. The Ni{111} sample was prepared by cycles of Ar ion bombardment (1.5 kV) and annealing to 923 K until low energy electron diffraction (LEED) and HREELS indicated the presence of a clean Ni{111} surface. Melamine (Sigma-Aldrich, 99.9% purity) was deposited onto the Ni{111} surface, held at room temperature, from a glass doser resistively heated to 393 K, separated from

the UHV chamber by a gate valve, and differentially pumped by a turbomolecular pump. Samples were transferred under UHV conditions to the HREELS chamber. Measurements were carried out in the specular direction ($\theta_i = \theta_r = 45°$) with a primary beam energy of 5 eV and a typical elastic peak resolution of ca. 50 cm^{-1}. A maximum likelihood based resolution enhancement method[25, 26] was used to recover the spectra from the instrumental broadening, leading to an improved resolution of ca. 40 cm^{-1} full width at half maximum (FWHM).

Temperature programmed desorption (TPD) experiments were carried out in a UHV system, built by PSP Vacuum Technology Ltd., which, during experiments, was operated at a base pressure of ~ 2 x 10^{-10} mbar. The Ni{111} sample was cleaned as described above and then exposed to melamine sublimed from an identical solid dosing source. For initial TPD experiments, all masses in the range 0-150 amu were monitored to see which peaks increased as a function of sample temperature. These results lead to the monitoring of the following masses at: 2, 27 and 28 atomic mass units (amu) during all TPD experiments. An approximately linear heating rate was used of 2 K s^{-1}. It is noted that, despite the same melamine doser and applied current being used for all experiments, the different positions of the pressure gauges on the experimental UHV chambers resulted in very different melamine pressure readings for the different experimental techniques.

The vibrational modes of melamine were modelled in the ground state using density functional theory (DFT) with the B3LYP[27] hybrid functional and the 6-31G* basis set. Molecular DFT calculations were carried out using the GAUSSIAN 03 program

suite.[28] Gaussview was used to create the input for the simulation and for visualising the optimised molecular structure and the frontier orbitals of melamine.

Geometry and energetics of melamine adsorbed to the Ni surface was simulated using the Vienna Ab Initio Simulation Package (VASP),[29, 30] using the gradient corrected PBE functional,[31] PAW potentials[32, 33] and a plane-wave basis set with VASP's "prec=high" setting, which in this case implies an energy cutoff of 500 eV. DFT calculations were carried out by Dr H. A. Früchtl on the EaStCHEM Research Computing Facility.

3.4 Results

3.4.1 Reflection Absorption Infrared Spectroscopy (RAIRS)

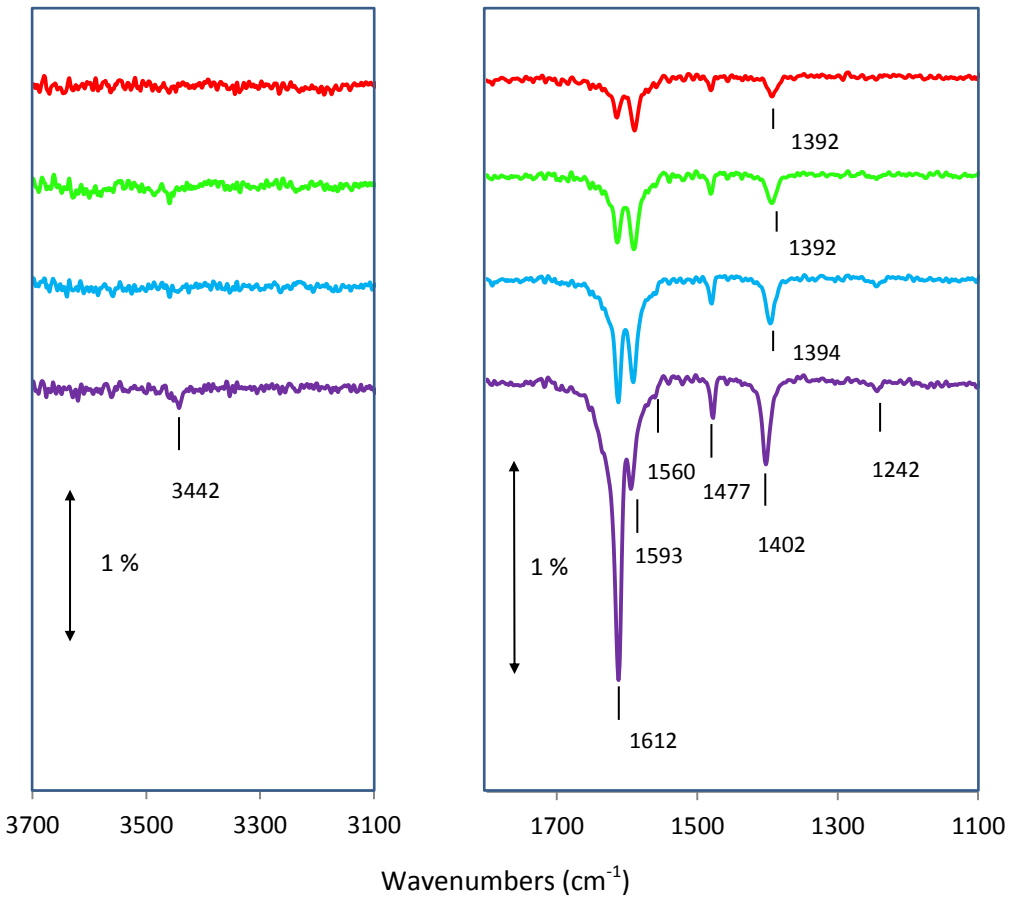

Figure 3.2: RAIR spectra as a function of increasing exposure following melamine adsorption on Ni{111} at 300 K. (Left) high frequency region, (Right) low frequency region. The cumulative coverages are: Red (0.026 L), green (0.052 L), blue (0.076 L) and purple (0.17 L).

The RAIR spectra in Figure 3.2 were acquired following the adsorption of melamine on Ni{111} at 300 K as a function of increasing exposure. At low melamine exposure, bands are observed at 1612, 1593, 1560 (appearing as a shoulder to the 1593 cm^{-1} band), 1477 and 1392 cm^{-1}. As the melamine coverage is increased, the 1392 cm^{-1} band shifts up to 1402 cm^{-1} and there is a change in the relative intensity of the

bands such that at the highest exposures, the 1612 cm^{-1} and 1402 cm^{-1} bands are relatively much more intense than at low melamine exposure. At the highest coverage, additional bands are observed at 3442 and 1242 cm^{-1} which are relatively weak in intensity.

3.4.2 High resolution electron energy loss spectroscopy (HREELS)

The HREEL spectra in Figure 3.3 were acquired following the adsorption of melamine on Ni{111} at 300 K for a range of cumulative coverages. At low melamine exposure, vibrational bands are observed at 3410, 3285, 1575, 1440, 1375, 1215, 1050, 720, 655, 590, 510, and 310 cm^{-1}. Upon increasing melamine exposure, the band intensities increase, and additional bands are observed at 3515, 3435, 1010, 795, and 200 cm^{-1}. At the highest melamine coverage, a shoulder peak is observed adjacent to the 530 cm^{-1} band at 570 cm^{-1}; also, the band at 3435 cm^{-1} is concealed by the adjacent band at 3385 cm^{-1}. The intensities for a number of bands following the highest melamine exposure (red spectra) are lower than for the medium melamine exposure (green spectra); the intensity of the very strong band at 1575 cm^{-1} is significantly diminished, as well as the bands at 1445 and 1395 cm^{-1}. It is believed that this observation can be accounted for by a high deposition flux resulting in multilayer coverage. The insulating effect of the multilayer organic melamine molecules on the Ni{111} surface acts to reduce the signal intensity of some bands, and also accounts for the disappearance of the stated bands. The signal intensity becomes increasingly diminished for higher melamine exposures; hence, spectra for higher melamine coverages have not been included in Figure 3.3.

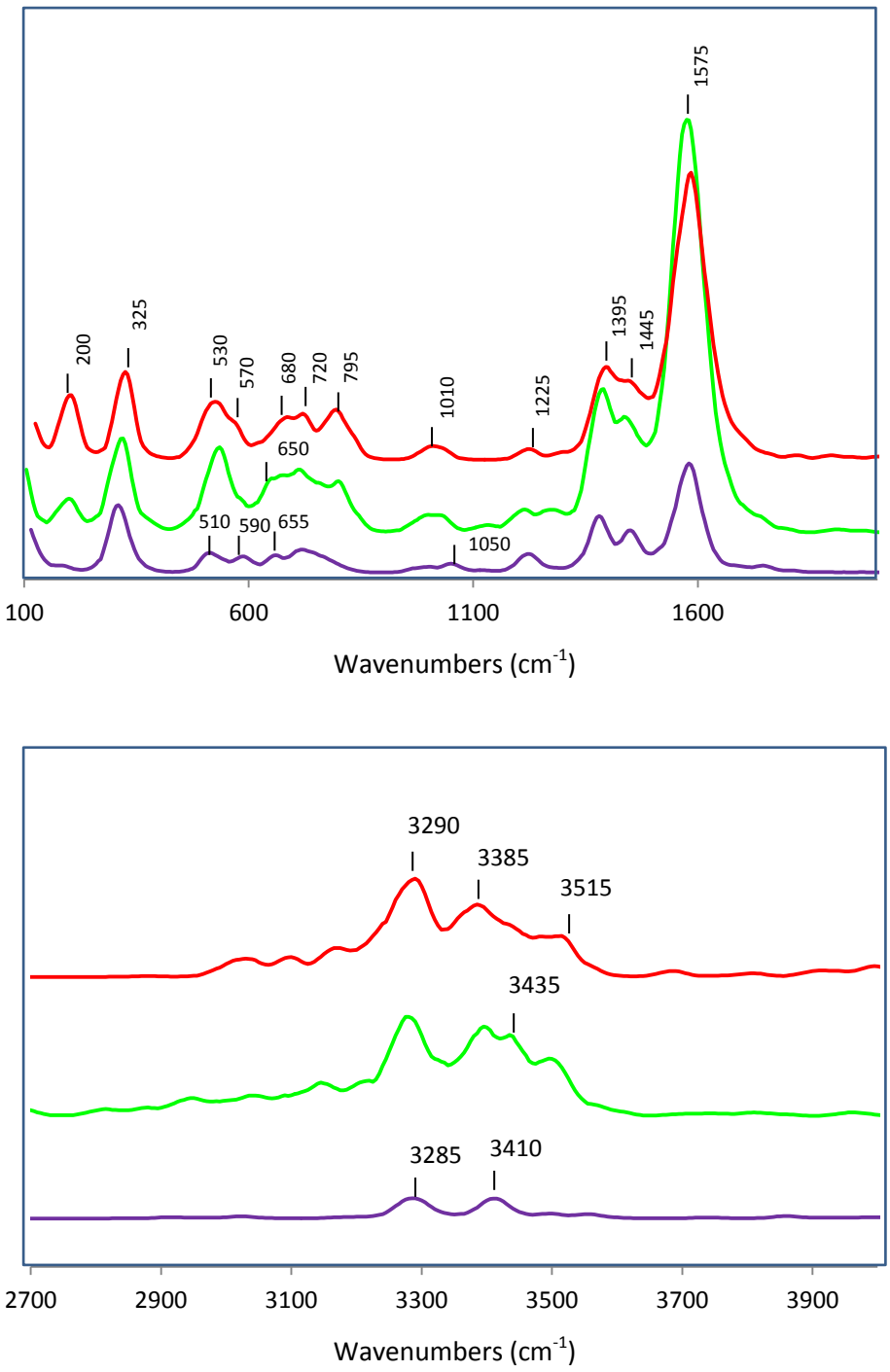

Figure 3.3: HREEL spectra as a function of increasing melamine exposure following melamine adsorption on Ni{111} at 300 K. (Top) Low-frequency region and (Bottom) high-frequency region (the y-axis scale of the high frequency region has been increased by a factor of 1.5 to aid with identifying the bands). The cumulative coverages are: purple (0.2 L), green (0.4 L), and red (0.6 L).

In order to investigate the effect of temperature on the surface melamine structure, HREELS annealing experiments have been performed, see Figure 3.4, for a range of temperatures after saturation coverage of melamine on Ni{111}. After annealing to 423 K, vibrational bands are observed at 192, 312, 532, 697, 757, 987, 1022, 1217, 1382, 1442, and 1577 cm^{-1}. Further up the spectrum, bands are observed at 3272, 3377, 3392, and 3501 cm^{-1}. There is a marginal offset between the vibrational band values between the 0.4 L melamine exposure spectra in Figure 3.3 and that of the melamine spectra after annealing to 423 K in Figure 3.4; however, the vibrational bands maintain a sufficiently similar position in order to be designated with the same assignments.

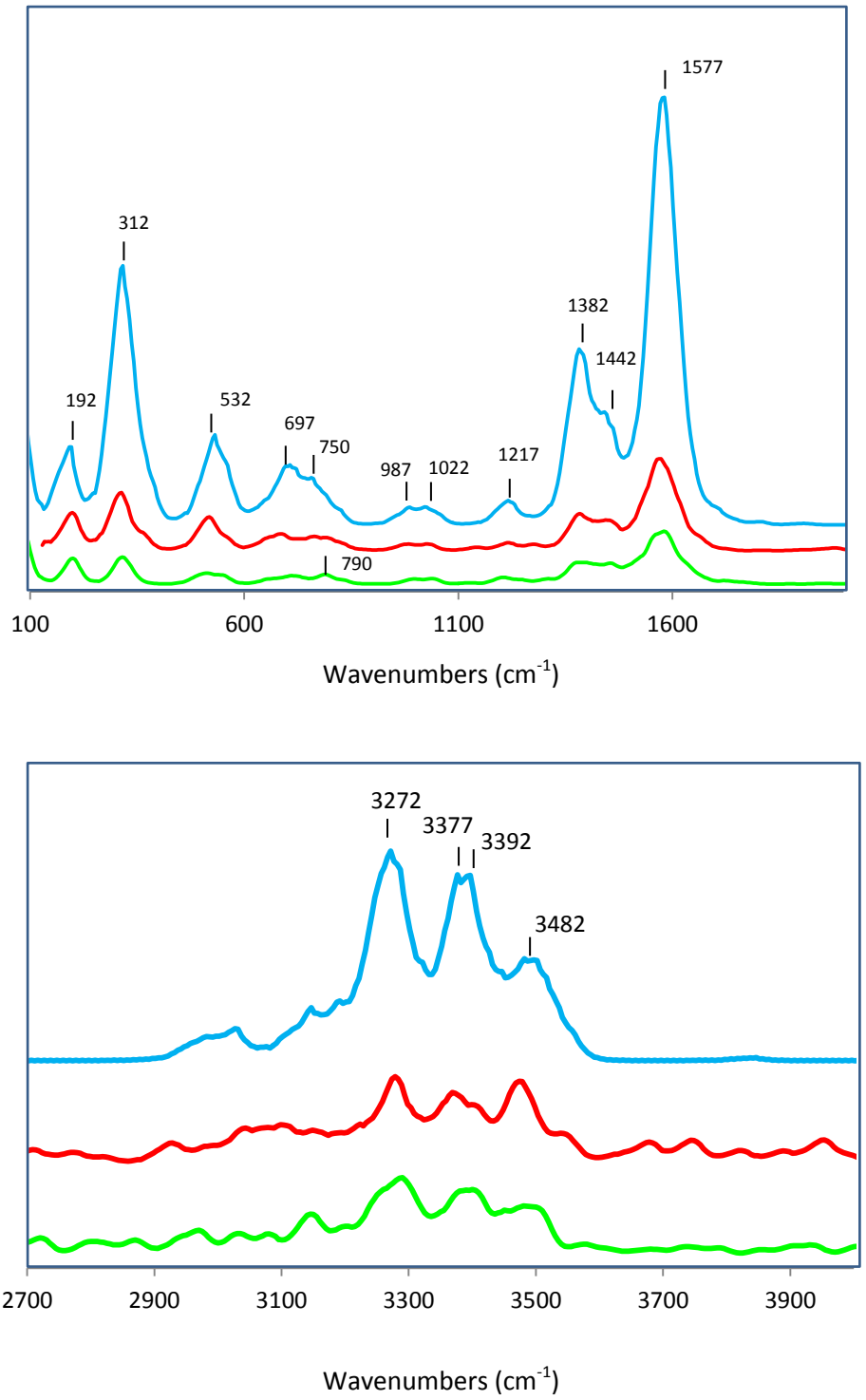

Figure 3.4: HREEL spectra as a function of increasing anneal temperatures following saturation coverage of melamine adsorption on Ni{111} at 300 K. (Top) Low-frequency region and (Bottom) high-frequency region (the y-axis scale of the high frequency region has been increased by a factor of 1.5 to aid with identifying the bands). The anneal temperatures are: green (323 K), red (373 K), and blue (423 K).

3.4.3 Temperature Programmed Desorption (TPD)

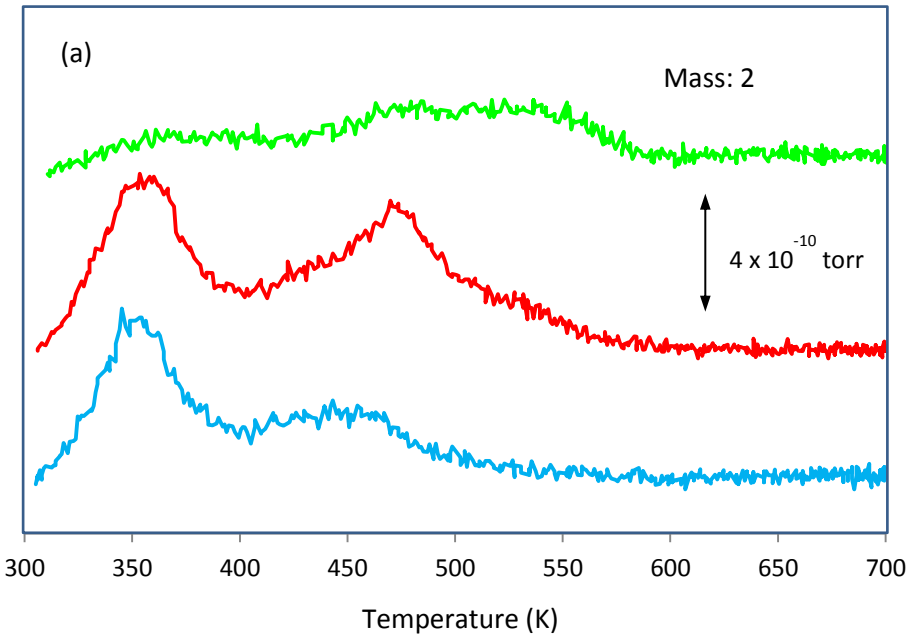

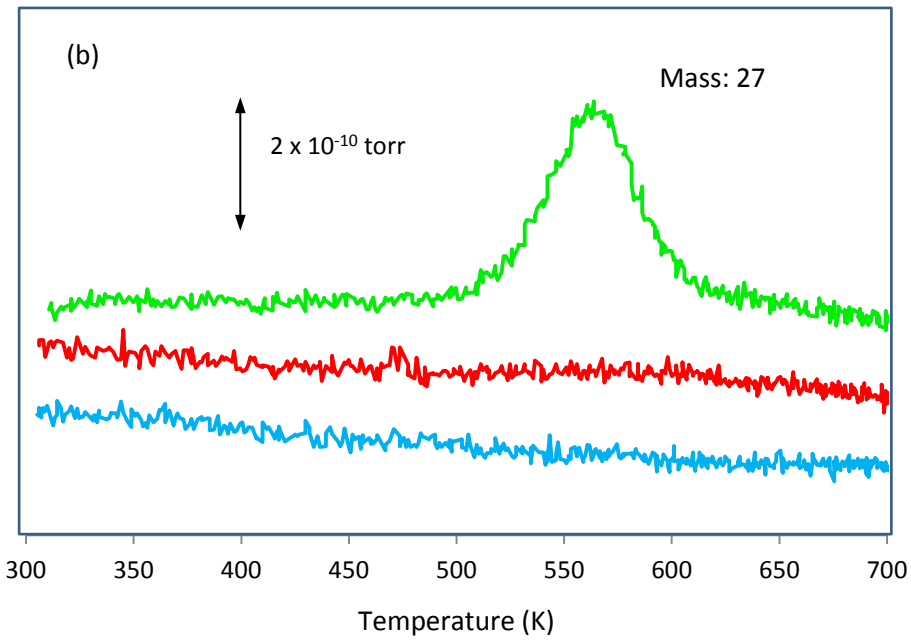

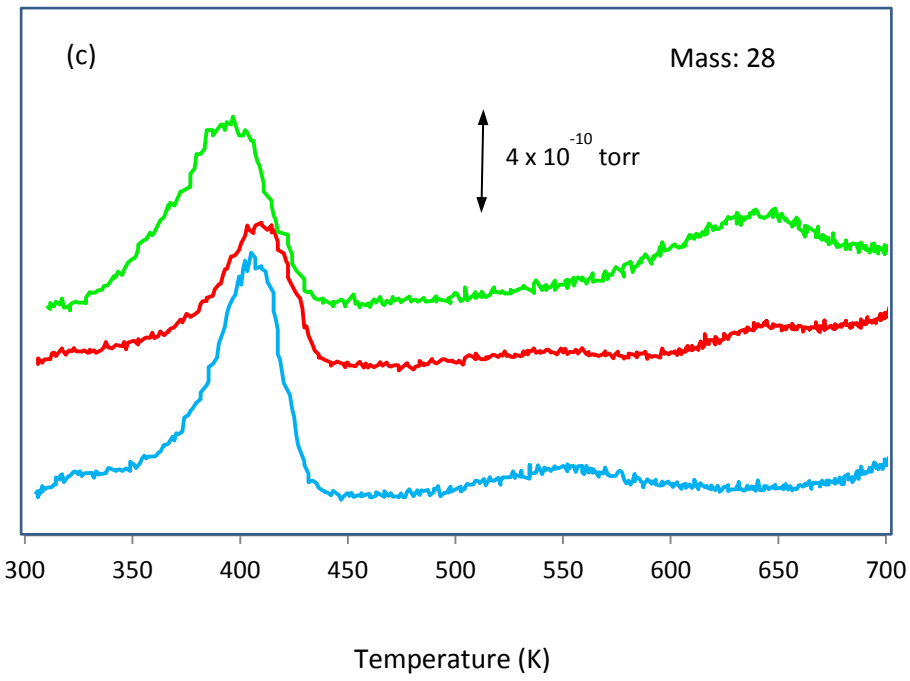

Figure 3.5: TPD spectra for melamine adsorption on Ni{111} at 300 K monitoring masses: a) 2, b) 27, and c) 28. The spectra represent a series of increasing exposures at: 5.4 L (blue), 12 L (red), and 14.4 L (green). Note: The y-axis in all spectra have arbitrary units. The relative intensities of the TPD spectra are represented by the scale bar.

In Figures 3.5 a) – c), TPD data are shown following melamine adsorption onto Ni{111} at 300 K as a function of melamine exposure. For the TPD of the blank Ni sample, not shown, a desorption peak of CO (mass 28) is observed (T_{max} ~ 400 K) which is caused by CO adsorption while the sample cools down to 330 K prior to melamine dosing. The T_{max} value is in good agreement with the desorption temperature for low coverage CO on Ni{111}.[34] In addition, the blank Ni sample TPD also showed a large, broad H_2 peak at T_{max} ~ 500 K, thought to incorporate more than one desorption peak. This desorption temperature is much higher than hydrogen desorption from Ni{111}, and is thought to be desorbed from the heating wires or sample holder. The amount of H_2 desorbing at this temperature appears to decrease upon the highest melamine exposure, and T_{max} shifts to ~ 460 K.

A peak at T_{max} ~ 350 K is observed for hydrogen desorption on Ni{111} after melamine exposure, Figure 3.5 a). The peak integral increases slightly for medium exposure (red spectra). Upon high exposure, the H_2 peak becomes very small (green spectra). A desorption peak for mass 27 is observed, Figure 3.5 b), at T_{max} ~ 560 K following high melamine exposure; however, no peak is observed for low and medium exposure. In Figure 3.5 c), a desorption peak is observed at mass 28 for low exposure at T_{max} ~ 550 K which shifts to T_{max} ~ 650 K for medium and high exposures; the peak integral becoming larger for the higher melamine exposure. It is noted that a desorption tail is observed at ~ 700 K for mass 28 following low exposures (blue and red spectra) of melamine.

Auger electron spectroscopy (AES) spectra taken after TPD runs revealed residual carbon was still present on the Ni{111} surface. This is most likely a decomposition fragment of melamine resulting from the heating treatment.

3.4.4 Scanning Tunnelling Microscopy (STM)

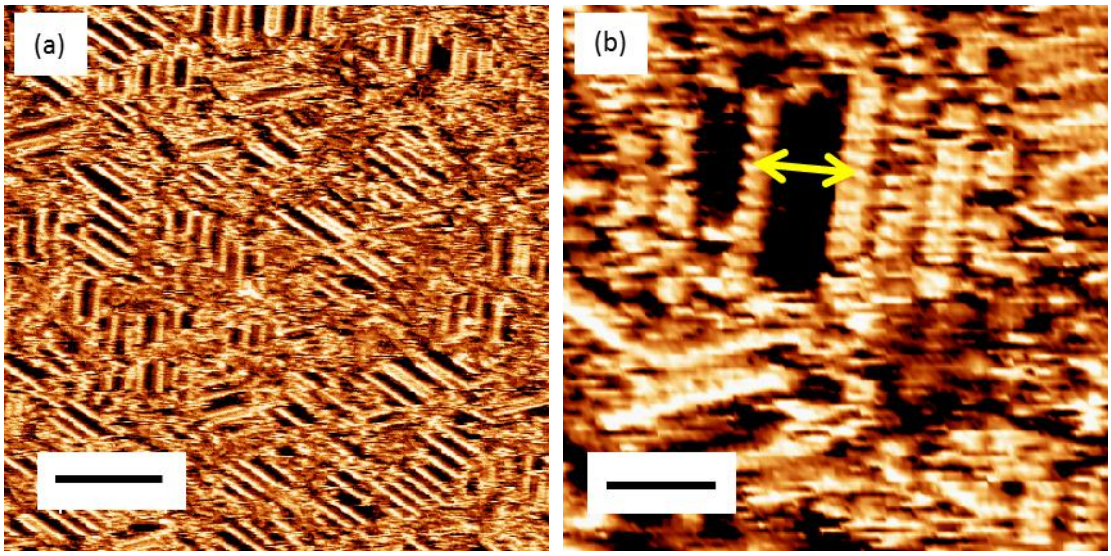

Figure 3.6: (a) STM image of melamine, 0.076 L dose, on Ni{111} at 300 K (scale bar 12 nm; -0.05 V, 1 nA), (b) Close-up STM image of the same surface (scale bar 2.5 nm; -0.05 V, 1.6 nA).

Figure 3.6 a) shows an STM image of the Ni{111} surface following exposure to ~0.1 L melamine at 300 K i.e. approximately corresponding to the blue RAIR spectrum in Figure 3.2. Under these conditions, chains of molecular features are observed aligned along <112> - type surface directions. In between the chains, there is evidence for the presence of relatively mobile species. Figure 3.6 b) is a close-up view of the low coverage melamine chains. The individual melamine molecules are resolvable separated by ~4.5 - 5.0 Å. The spacing between the parallel melamine chains is not constant. One example of this has been highlighted in Figure 3.6 b) by a double headed arrow. In this case, the melamine chains are measured to be separated by approximately 22 Å. The distance of closest approach of melamine chains is found to be 9 Å.

Figure 3.7 a) shows an STM image of a melamine covered Ni{111} surface after an exposure of approximately 0.2 L (i.e. corresponding to the high coverage melamine RAIR spectrum in Figure 3.2). Molecular species are again observed to form one-dimensional chains of molecules that run along the [11-2], [1-21], and [-211] crystallographic directions, related by an angle of 120° to each other. Ordering in 2-D is less pronounced. There are, however, some domains of a few nm in diameter where it is possible to define a 2-D unit cell.

Figure 3.7 b) zooms in on a region of the surface and shows more clearly the 2-D ordering present in the melamine adlayer (a 2-D melamine island has been highlighted by the yellow circle in Figure 3.7 b). The nearest separation between the melamine molecules in adjacent chains is measured to be approximately 9.0 Å and the molecular separation between melamine molecules within the same chain is measured as approximately 4.3 Å. Figures 3.7 c) and d) illustrates the behaviour of the melamine molecules at the step edges. The extent of ordering is less pronounced on the narrower terrace in the centre of Figure 3.7 d).

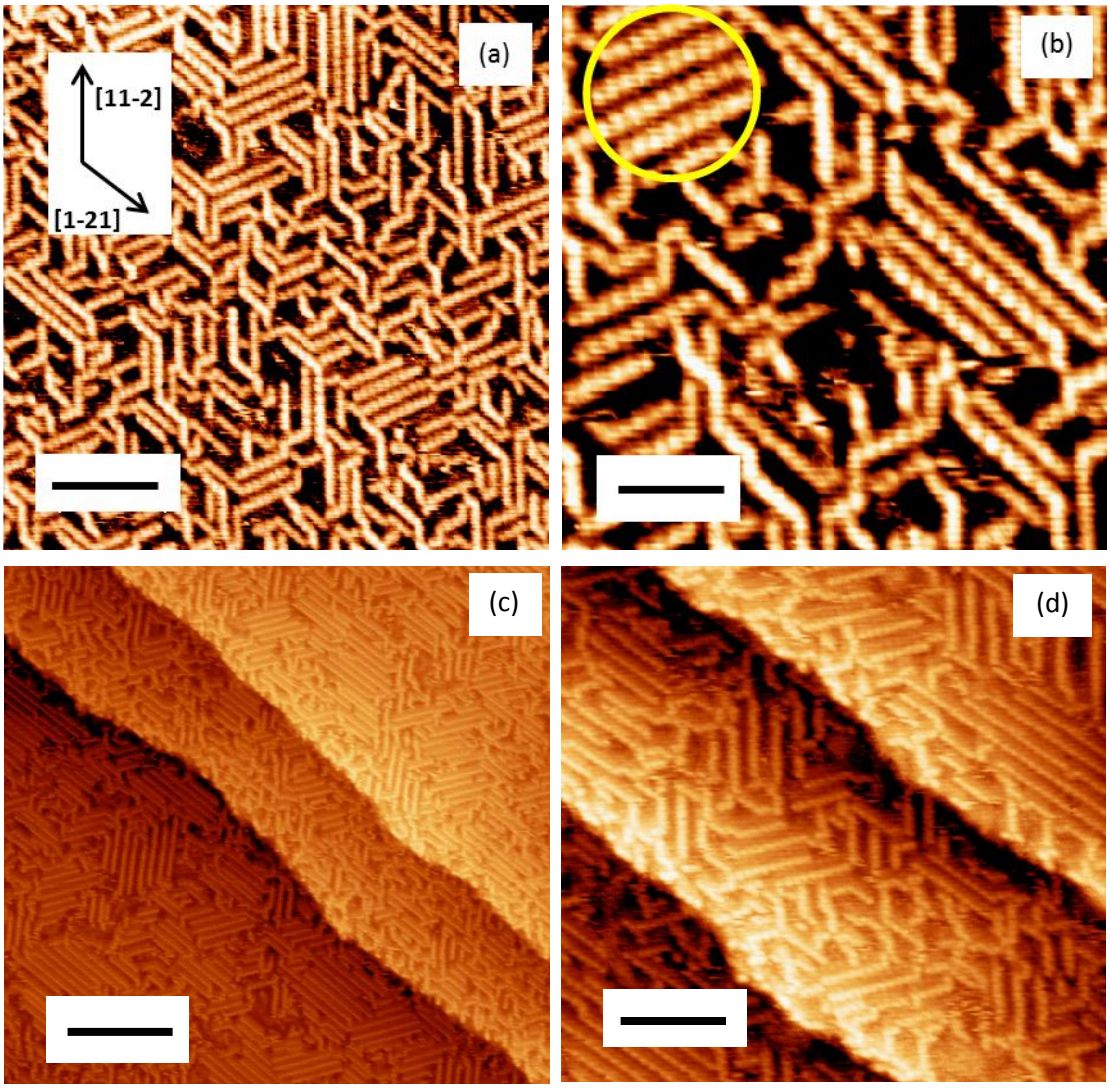

Figure 3.7: a) STM image of melamine, 0.2 L dose, on Ni{111} at 300 K (scale bar 5.6 nm; 0.15 V, 0.45 nA) (b) a zoomed image of the melamine molecules within the chains (scale bar 2.8 nm; -0.15 V, 0.45 nA). A region of 2-D packing is highlighted by the yellow circle (c) showing a comparison of chain growth on Ni{111} terraces versus behaviour at the step edges (scale bar 12 nm; -0.07 V, 1.1 nA). (d) zoomed STM image in the region of a step-edge (scale bar 5.3 nm; -0.3 V, 1.4 nA).

3.5 Discussion

Melamine adsorption on Au{111}[13, 35] and Ag{111}[14] has been investigated by STM. In each case, melamine forms extended 2-D arrays where each molecule adopts a flat lying orientation, due to a favourable aromatic π-electron interaction with the substrate, and has a triangular appearance in STM images. The arrays are stabilised

by intermolecular H-bonding interactions.[13, 14, 35] The experiments on Ni{111} display dramatically different behaviour. Though 2-D islands are observed, growth at 300 K is characterised by the formation of 1-D chains of molecular features separated by ~4.3 Å. In addition, each melamine species is imaged as a cylindrical feature.

In order to interpret the shape of the features observed in STM, DFT calculations were carried out (Gaussian 03, 6-31G*, B3LYP) of the highest occupied molecular orbital (HOMO) and lowest occupied molecular orbital (LUMO) for isolated melamine. Figure 3.8 a) shows the chemical structure of melamine; the numerical labels adjacent to the carbon and nitrogen atoms are referred to in Table 3.1 in order to aid the assignment of the molecular vibrations. Figure 3.8 b) shows each orbital viewed perpendicular and parallel to the plane of the aromatic ring. Though adsorption of melamine on Ni{111} will undoubtedly alter the appearance of the HOMO and LUMO via coupling with the Ni d band, the orbital appearance should still be comparable to the shape of the adsorbed molecules in the STM images. Under the imaging conditions used (i.e., tip biased negatively), one would anticipate that the imaged molecule may resemble the LUMO in appearance, with electrons being transferred from filled tip states to empty sample states. The cylindrical features observed in STM are consistent with the LUMO viewed parallel to the aromatic ring, implying that melamine adsorbs with the aromatic ring either perpendicular to the surface, or at least strongly tilted with respect to the surface.

(a)

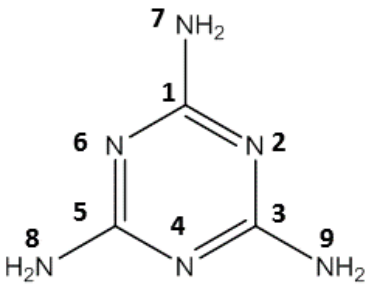

(b)

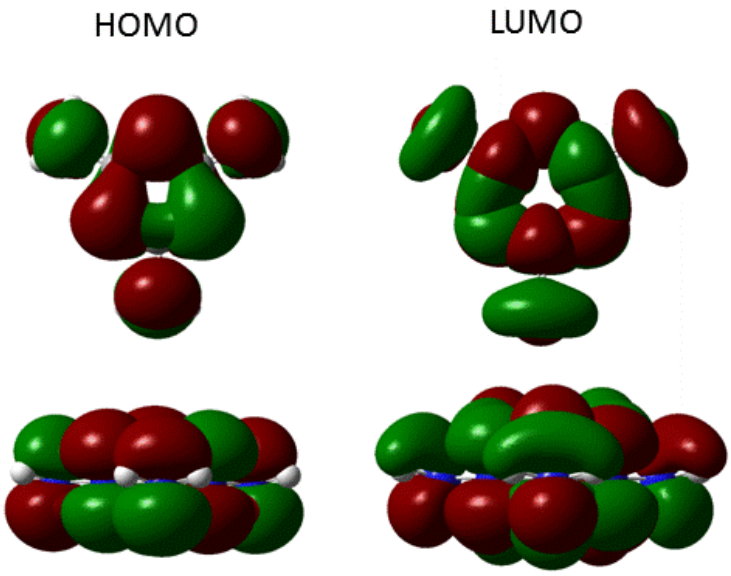

Figure 3.8: (a) Chemical structure of melamine with atom labels to aid explanation of vibrational assignments in Table 3.1 (b) HOMO and LUMO of melamine (Gaussian 03, density functional theory using the B3YLP functional with 6-31G* basis set), showing the front-on view to the left and top-down view to the right for the respective molecular orbitals.

Table 3.1: Vibrational frequencies and assignments for melamine on Ni{111}

Melamine/Ni{111} (HREELS) $\upsilon(cm^{-1})$	Melamine/Ni{111} (RAIRS) $\upsilon(cm^{-1})$	Melamine/gas-phase[36] $\upsilon(cm^{-1})$	Isolated melamine[36] (DFT) $\upsilon(cm^{-1})$	Vibrational mode assignments
		3571 m	3588	$\upsilon\ NH_2^{asym}$
3515				$\upsilon\ NH_2^{sym}$
3435	3442 w	3453 m	3466	$\upsilon\ NH_2^{sym}$
3385				$\upsilon\ N_{(9)}H$, $\upsilon\ N_{(8)}H$
3290				$\upsilon\ N_{(9)}H$, $\upsilon\ N_{(8)}H$
1575	1612 vs	1598 vs	1594	$\beta\ NH_2^{sym}$, $\upsilon\ C_{(1)}N_{(7)}$, aromatic ring breathing
	1593 s			$\beta\ NH_2^{sym}$, $(\upsilon C_{(5)}N_{(6)}, \upsilon C_{(3)}N_{(2)})^{sym}$
	1560 m	1556 m	1565	$\upsilon C_{(1)}N_{(2)}$, $\upsilon C_{(5)}N_{(4)}$
1440	1477 m			ring breathing, $\upsilon N_{(7)}C_{(1)}$
1375	1402 s	1440 s	1433	$(\upsilon C_{(5)}\ N_{(6)}, \upsilon C_{(3)}\ N_{(2)})^{asym}$
1225 m	1240 w			$\beta N_{(8)}H$, $\beta N_{(9)}H$
1010 m		1000 m	982	NH_2 swing
795 s				Ni-H stretch
720 m		752 m	715	Ring deformation (out of plane)
680 m			657	Ring breathing, NH_2 bend
570 m		581 w	565	NH_2 and CNH bend
530 s				Ni-N stretch
325 s			322	$C_{(1)}N_{(7)}H_2$ torsion
200 s			200	Side chain, out of plane bend

Notation: υ- stretch, β- bend. Abbreviations: vs- very strong, s- strong, m- medium, w- weak, sym- symmetric, asym- asymmetric.

There is generally good agreement between the bands observed in the RAIR and HREEL spectra with those of the reported bands observed for gas-phase melamine.[36] There are two regions of the spectra where significant differences are observed. Firstly, in the gas phase melamine spectrum a single band is observed at 1598 cm^{-1} which was assigned to the symmetric scissor mode of the NH_2 functionalities (Table 3.1).[36] In the RAIR spectra of this study, two bands are observed at 1593 and 1612 cm^{-1}. The relative intensities of these bands change with increasing melamine coverage, with the latter band dominating at high coverage. Secondly, in the gas phase melamine spectrum a single band is observed at 1440 cm^{-1} (assigned to a stretching mode comprising motion of the aromatic ring and the C-N bonds of the amine functionality). In the spectra in Figure 3.2, two bands are observed at 1477 and 1402 cm^{-1}. The latter band becomes relatively more intense at higher coverage. The dynamic dipole moments of each of these modes lie in the plane of the aromatic ring. The relatively intense RAIRS bands are therefore consistent with the conclusion that melamine adopts a perpendicular or strongly tilted orientation on Ni{111}.

The HREEL spectra show a very strong band at 1575 cm^{-1}. It is believed that this corresponds to the RAIRS bands at 1612 and 1593 cm^{-1}; since the two bands are separated by ~ 20 cm^{-1}, the resolution of HREELS is insufficient to distinguish the two bands, hence they appear as one band. The HREEL spectra also show two bands at 1445 and 1395 cm^{-1}. These are attributed to the RAIRS bands observed at 1477 and 1402 cm^{-1}, respectively. There is a slight offset between the vibrational frequencies of the RAIRS study and this HREELS study, which have been accounted as due to a

possible asymmetry in the elastic peak of the HREEL sepctra, caused during the tuning process; therefore, leading to a systematic offset of the vibrational mode frequencies. Upon increasing from 0.2 to 0.4 L melamine coverage, the HREEL spectra band intensities increase. There is no observed changes in the relative intensities of the stated vibrational bands upon increasing coverage.

Melamine is closely related in structure to the nucleic acid/base adenine. A RAIRS study of adenine on Cu{110} by McNutt et al.[37] shows an intense band at 1626 cm^{-1} which was concluded to correspond to the scissor mode of the NH_2 functionality oriented with the C-NH_2 bond perpendicular to the Cu{110} surface.

One factor which may be important is the extent to which melamine undergoes dissociative adsorption. The similarity between the RAIR spectra and the gas phase spectra would suggest that the molecule retains much of its integrity, but it could be the case that some dehydrogenation of one or two –NH_2 functionalities occurs on adsorption. The TPD data confirms this claim, showing a hydrogen desorption peak at T_{max} ~ 350 K following low and medium exposure of melamine. The T_{max} value is in good agreement with the desorption temperature for low coverage hydrogen on Ni{111}.[38] However, the H_2 desorption peak becomes very weak for high melamine exposure. It is believed that the high packing density for this exposure regime induces H + H recombination, desorbing as H_2 at room temperature.

Previous investigations of related molecules on Pt and Ni surfaces concluded that some dehydrogenation of the –NH_2 group occurs at and slightly above room temperature. Mudiyanselage and Trenary investigated the adsorption of N-

methylaniline (NMA) on Pt{111}[39] and reported that NMA adsorbs molecularly at 85 K through the nitrogen lone pair, forming a species that is stable up to 300 K. Annealing to temperatures between 300-350 K leads to the partial dehydrogenation of NMA, forming the intermediate N-methyleneaniline (NMEA). Huang et al.[40] investigated the adsorption of aniline on Ni{100} and showed that aniline undergoes partial dehydrogenation of the amine functionality, resulting in reduced steric hindrance for upward reorientation, and, also, increased interaction with the Ni surface. It seems unlikely that melamine would adsorb intact in an upright geometry and be stable up to >500 K as indicated by the STM and TPD experiments.

Given that gas phase melamine exhibits intense bands at 1598 and 1440 cm^{-1}, it is intriguing that two pairs of bands are observed in the 1590-1620 cm^{-1} and 1400-1480 cm^{-1} range and that the relative intensities of each pair of bands are strongly coverage dependent. Wang et al. studied the effect of reducing the symmetry of melamine on the IR spectra.[36] Reducing the symmetry from the gas phase D_{3h} to C_s resulted in the appearance of additional bands of weak intensity. It was found that the most intense bands remained essentially unaltered in intensity and were not split into resolvable doublets. Hence, it seems unlikely that the splitting of the bands observed in Figure 3.2 is associated with a low symmetry melamine adsorption geometry. It is proposed that there are two distinct ‘melamine` species, one which dominates at lower coverage and the second which dominates at higher coverage. In STM, at low coverage the surface is characterised by 1-D ordering, whilst, at high coverage, 2-D islands are relatively much more abundant. It can be concluded that the melamine species contained in the 1-D islands give rise to the bands at 1598 and

1477 cm^{-1}, while the melamine contained in 2-D islands gives rise to the bands at 1612 and 1402 cm^{-1}. The shift in band position could be explained by increased lateral interactions between neighbouring rows of melamine species in the 2-D islands.

Vibrational bands are observed in the HREEL spectra at 3435 (at 0.4 L coverage) and 1225 cm^{-1}, which correspond well to the RAIRS bands observed at 3442 and 1240 cm^{-1}, respectively. It is noted that there are additional bands in the high frequency region for the HREEL spectra than for the RAIR spectra. The much higher scanning exposure time in HREELS compared with RAIRS is the likely explanation for extra bands being detected. At low melamine exposure, a set of two bands are observed at 3410 and 3285 cm^{-1}. For higher exposure to 0.4 L of melamine, there appears another set of two bands at 3490 and 3395 cm^{-1}. This observation agrees with the conclusion that there are two melamine surface species; one at low coverage, and another appearing at higher coverage.

A coverage dependence is observed for certain lower frequency vibrational bands. After increasing the melamine exposure from 0.2 to 0.4 L, vibrational bands appear at 795 and 200 cm^{-1}. These vibrational bands have been simulated by DFT calculations in the study by Wang et al.[36] Therefore, it is not believed they are caused by the high-coverage melamine species. It is likely these observations are on account of the vibrational bands being too weak for detection at low melamine coverage, only appearing at higher melamine exposure.

A weak band is observed at 1050 cm^{-1} for 0.2 L exposure; this subsequently merges with an adjacent band at higher melamine exposure to 0.4 and 0.6 L, forming a band at 1010 cm^{-1}. The gas-phase IR melamine spectrum produced only a single equivalent band at 1000 cm^{-1}.[36] Therefore, the two bands at 1050 and 1010 cm^{-1} are believed to be due to low and high coverage melamine species, respectively.

The TPD spectra also indicate coverage dependent behaviour with regards to the desorption products. The desorption spectra for mass 28 show a desorption tail at T ~ 700 K for low and medium melamine exposure, along with a desorption peak at T_{max} ~ 650 K for medium and high exposures. This mass is believed to correspond to N_2. Ho and Wu undertook a theoretical study of NO_x interaction on Ni{111}.[41] Their findings reveal that the recombination of adsorbed N atoms resulting from the decomposition of NO_x is possible, providing that sufficient thermal energy (E_{act} = 2.34 eV) is supplied to overcome the large energy barriers. Methylamine decomposition on Ni{111} results in nitrogen atom recombination, desorbing as N_2 at T > 700 K.[42] This is a higher temperature than for the main desorption peak observed following high melamine exposure. The shift to a lower desorption temperature is explained by the increased decomposition fragment density and subsequent altered desorption mechanism pathways for higher melamine exposures, resulting in a lower desorption temperature for N_2. It is unlikely that the desorption peak at T_{max} ~ 550 K following low exposure corresponds to N_2 desorption resulting from N recombination. This peak may be due to CO desorption during heating treatment, as CO co-adsorption is common on reactive surfaces such as Ni.

The desorption peak for mass 27 at T_{max} ~ 560 K is observed only following high melamine exposure. This peak is believed to correspond to HCN. No desorption peaks containing carbon are observed for low and medium melamine exposure. It is shown by AES that carbon residue remains on the surface. Residual carbon also remains on the surface following methylamine desorption from Ni{111}.[42] As already discussed, high melamine exposure is thought to alter the desorption mechanism of the decomposition fragments. This is further evidenced by the observation of the HCN peak only following high exposure.

DFT calculations were performed on the adsorption geometry of partially dehydrogenated melamine (i.e. a melamine species which had undergone partial dissociation of two amine functionalities to yield –NH moieties) on a Ni{111} slab in order to identify the optimum adsorption geometry of such a species. In the most stable geometry detected, the N atoms of the NH groups, e.g. atoms 8 and 9 in Figure 3.8 a), and the N of the azide ring located between the NH groups, atom 4 in Figure 3.8 a), are each bound to the surface with the azide N atom in an atop site and the two NH nitrogen atoms in bridge sites. This was found to be at least 23 kJ mol^{-1} more stable than other geometries tested. No Ni-N or Ni-H bands were observed in the RAIRS experiments. The frequency of the former bands is below the range of the RAIRS detector and no new bands were observed in the 700-1100 cm^{-1} range typical of Ni-H.[43]

The HREELS data provide evidence as to the extent of melamine dissociation upon adsorption. Previous studies of analogous molecules on Pt and Ni surfaces concluded that N-H dehydrogenation occurs at temperatures in the vicinity of 300 K. Somorjai

and Gardin,[44] using TPD and HREELS, found that methylamine and ethylamine are both dehydrogenated in the temperature range of 300-400 K; the former is dehydrogenated to HCN at 330 K, while the latter is dehydrogenated to CH_3CN, initially by α-C-H bond scission.

The observed vibrational band at 530 cm^{-1} is believed to correspond to that of the Ni-N stretching mode. The band intensity is seen to increase for increasing melamine exposure. This observation is in close agreement with previous data on Ni-N stretching vibrations at 525 cm^{-1} for methylamine and 500 cm^{-1} for ethylamine, both on Ni{111}.[44] The observed band is also comparable to the Ni-N stretching frequency of NH_3 on Ni{111} at 490 cm^{-1}.[45]

A noticeable alteration after annealing to 423 K is the absence of the vibrational band observed at 795 cm^{-1} for the 0.4 L melamine exposure spectrum at room temperature. An equivalent weak band is observed at 790 cm^{-1} after annealing to 323 K. This vibrational band has been assigned to the Ni-H stretching mode, which has previously been observed in the 700-1100 cm^{-1} frequency range.[46] The disappearance of this band after annealing above 323 K can be attributed to desorption of hydrogen species from the Ni surface. Wedler et al.[38] reported at low H coverage on Ni{111}, desorption occurs at 380 K. This observation is in accordance with the observation in this study of the disappearance of the Ni-H vibrational mode after annealing above 323 K.

The observation of the Ni-H band in this study supports the conclusion of a partially dehydrogenated melamine species on Ni{111}. The second N-H bond of the surface

bound amine groups is likely to be pointing away from the surface to reduce steric interactions; therefore, the Ni surface cannot assist in N-H bond breaking.

It is apparent that after annealing to 423 K, the bands appear more resolved with respect to the bands in the spectra in Figure 3.3. This could be on account of multilayer coverage of melamine after deposition at room temperature decreasing the electron beam interaction with the adsorbed melamine on the Ni{111} surface. After annealing, the physisorbed multilayer species would be desorbed, resulting in the increased signal intensity vibrational bands for the annealed samples.

Figure 3.9 a) shows a molecular model of the proposed structure of partially dehydrogenated melamine in the 2-D domains. The unit cell can be described as being based on a (√3 x 7) rect structure with a molecule at the centre of the unit cell. The measured intermolecular spacing of 4.5 Å is close to the repeat distance along the <-211> directions of 4.3 Å. The spacing between adjacent rows in the model is approximately 9.5 Å – again consistent with the spacing between adjacent rows in STM images. The adsorption mode shown in Figures 3.9 a) and b) would enable anchoring at three points via Ni-N interactions.

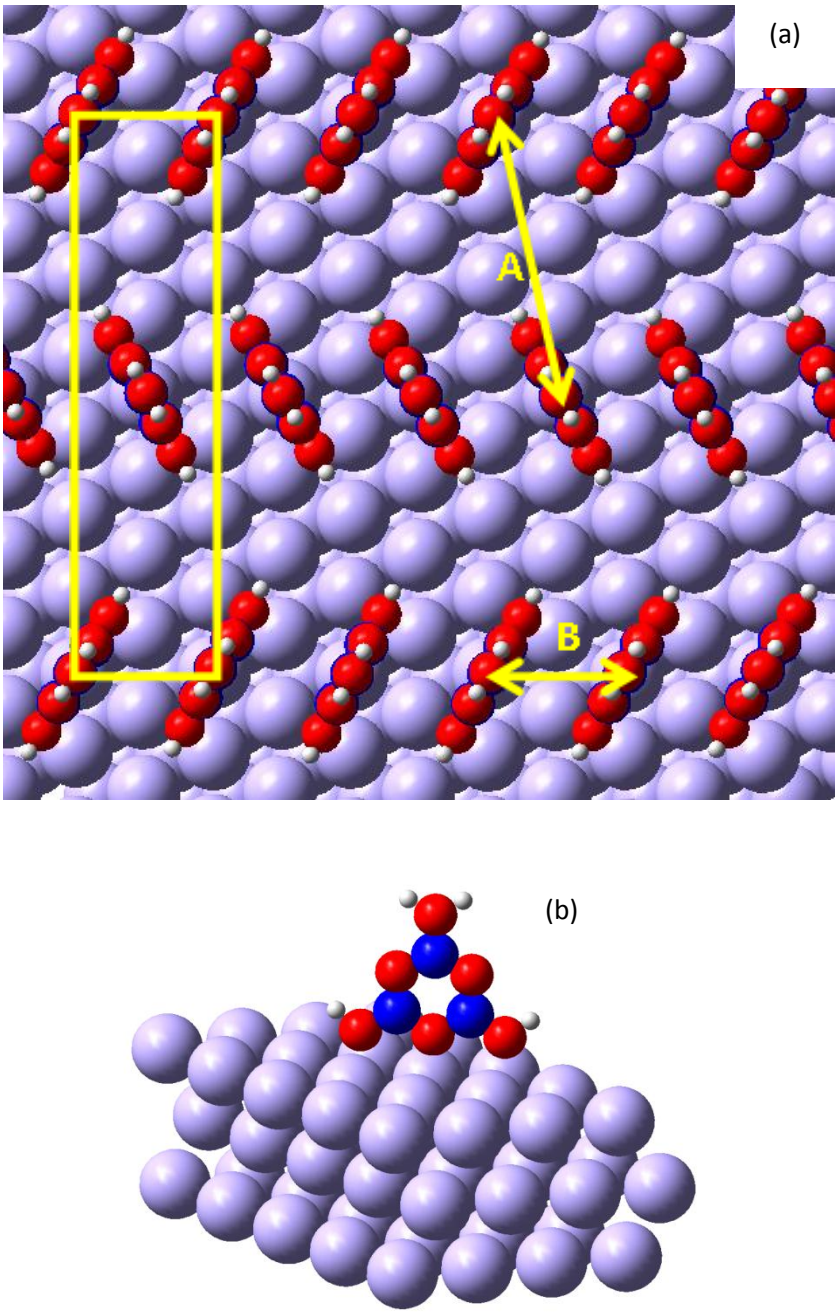

Figure 3.9: Molecular model of melamine chains adsorbed in bridge-top-bridge position, running along the [11-2] vector. The unit cell is represented by the yellow rectangle. (a) Top view: The chain separation distance is highlighted with arrow A (9.0 Å), and the molecular separation distance within a chain is highlighted by arrow B (~4.5 Å). (b) Side view of one molecule in this position. Melamine: carbon-blue, nitrogen-red, hydrogen-grey.

3.6 Conclusions

RAIR and HREEL spectra following the adsorption of melamine on Ni{111} at 300 K exhibit intense bands for in-plane vibrational modes of melamine, suggesting an adsorption geometry with the aromatic ring perpendicular, or close-to perpendicular, to the surface plane at both low and high coverages in the submonolayer regime. Two distinct surface species are detected with RAIRS. These are assigned to melamine species in 1-D chains and melamine species in 2-D domains. The bands associated with the latter species dominate the spectra at high coverage. Previous studies on Au{111}[13, 35] and Ag{111}[14] have shown melamine to adopt a flat-lying orientation, forming extended 2-D arrays via intermolecular hydrogen bonding interactions with each H-bond typically ~0.2 eV in strength.[13] The adsorbed species created on Ni is stable on the surface to at least 500 K indicating an adsorption energy of significanty more than 1 eV. Even though each molecule shares three H-bonds in the melamine arrays, the ability to form a strong adsorbate substrate interaction with Ni is the driving force for the upright orientation adopted by melamine on Ni{111}.

The observed Ni-N stretching mode band at 530 cm^{-1} confirms that melamine adsorbs via σ donation from a triazine nitrogen atom and two amine group nitrogen atoms to the nickel surface. A TPD H_2 desorption peak is observed at T_{max} ~ 350 K, and a Ni-H vibrational band is observed at 795 cm^{-1}, confirming that melamine undergoes partial dehydrogenation at the surface bound amine groups, forming N-H moieties. Annealing of the sample at saturation coverage results in no alteration to the

melamine vibrational bands; however, at 423 K, the Ni-H band disappears due to desorption of surface hydrogen species.

The melamine desorption fragments correspond to masses 2 (H_2), 27 (HCN), and 28 (N_2). The H_2 peak intensity decreases for high exposure due to displacement of hydrogen from the Ni surface by the close-packed melamine species. High melamine exposure leads to an additional peak corresponding to HCN. The increased decomposition fragment density and subsequent altered desorption mechanism pathways for higher melamine exposures results in a lower desorption temperature for N_2.

Melamine adsorption on Ni{111}, at room temperature, occurs with the formation of 1-D structures which propagate along the <-211> crystallographic directions. Bonding to the surface is likely to be via σ-donation to the surface from a triazine nitrogen atom and two amino group nitrogen atoms. The thermal stability of the chains is likely to be consistent with a partially dehydrogenated melamine species bound to the surface via two NH groups and the azide N atom between the two NH groups. DFT calculations support this conclusion and indicate that the favoured adsorption geometry involves the central azide N atom in an atop site and the N atom of the two adjacent NH groups in bridge sites.

The fact that melamine has an amino group pointing away from the surface is an interesting finding. Having a reactive functional group in the form of the nitrogen lone pair leads to the potential for using this system for further reaction with an

electrophile species, for the purpose of developing surface-ordered, three-dimensional systems.

Note: Some of the work presented in Chapter 3 – Part 1 has been published:

Greenwood, J.; Früchtl, H. A.; Baddeley, C. J. J. Phys. Chem. C 2012, 116, 6685. 'Ordered Growth of Upright Melamine Species on Ni{111}: A Study with Scanning Tunnelling Microscopy and Reflection Absorption Infrared Spectroscopy'

3.7 References

[1] T. Kudernac, S.B. Lei, J. Elemans, S. De Feyter, Chem. Soc. Rev. 38 (2009) 3505-3505.

[2] S. De Feyter, A. Miura, S. Yao, Z. Chen, F. Wurthner, P. Jonkheijm, A. Schenning, E.W. Meijer, F.C. De Schryver, Nano Lett. 5 (2005) 77-81.

[3] S. De Feyter, F.C. De Schryver, J. Phys. Chem. B 109 (2005) 4290-4302.

[4] J.V. Barth, J. Weckesser, C.Z. Cai, P. Gunter, L. Burgi, O. Jeandupeux, K. Kern, Angew. Chem.-Int. Edit. 39 (2000) 1230-+.

[5] J.V. Barth, Annu. Rev. Phys. Chem. 58 (2007) 375-407.

[6] D.L. Keeling, N.S. Oxtoby, C. Wilson, M.J. Humphry, N.R. Champness, P.H. Beton, Nano Letters 3 (2003) 9-12.

[7] S. Furukawa, K. Tahara, F.C. De Schryver, M. Van der Auweraer, Y. Tobe, S. De Feyter, Angew. Chem.-Int. Edit. 46 (2007) 2831-2834.

[8] M.C. Blum, E. Cavar, M. Pivetta, F. Patthey, W.D. Schneider, Angew. Chem.-Int. Edit. 44 (2005) 5334-5337.

[9] S. Stepanow, M. Lingenfelder, A. Dmitriev, H. Spillmann, E. Delvigne, N. Lin, X.B. Deng, C.Z. Cai, J.V. Barth, K. Kern, Nat. Mater. 3 (2004) 229-233.

[10] S. Griessl, M. Lackinger, M. Edelwirth, M. Hietschold, W.M. Heckl, Single Mol. 3 (2002) 25-31.

[11] I. Cebula, C. Shen, M. Buck, Angew. Chem.-Int. Edit. 49 (2010) 6220-6223.

[12] N. Lin, S. Stepanow, M. Ruben, J.V. Barth, Templates in Chemistry Iii, Springer-Verlag Berlin, Berlin, 2009, pp. 1-44.

[13] F. Silly, A.Q. Shaw, M.R. Castell, G.A.D. Briggs, M. Mura, N. Martsinovich, L. Kantorovich, J. Phys. Chem. C 112 (2008) 11476-11480.

[14] C.H. Schmitz, J. Ikonomov, M. Sokolowski, Surface Science 605 (2011) 1-6.

[15] H.M. Zhang, Z.X. Xie, L.S. Long, H.P. Zhong, W. Zhao, B.W. Mao, X. Xu, L.S. Zheng, J. Phys. Chem. C 112 (2008) 4209-4218.

[16] H.M. Zhang, Z.K. Pei, Z.X. Xie, L.S. Long, B.W. Mao, X. Xu, L.S. Zheng, J. Phys. Chem. C 113 (2009) 13940-13946.

[17] J.C. Swarbrick, B.L. Rogers, N.R. Champness, P.H. Beton, J. Phys. Chem. B 110 (2006) 6110-6114.

[18] J.A. Theobald, N.S. Oxtoby, M.A. Phillips, N.R. Champness, P.H. Beton, Nature 424 (2003) 1029-1031.

[19] R. Madueno, M.T. Raisanen, C. Silien, M. Buck, Nature 454 (2008) 618-621.

[20] L.M.A. Perdigao, E.W. Perkins, J. Ma, P.A. Staniec, B.L. Rogers, N.R. Champness, P.H. Beton, J. Phys. Chem. B 110 (2006) 12539-12542.

[21] J.A. Gardener, O.Y. Shvarova, G.A.D. Briggs, M.R. Castell, J. Phys. Chem. C 114 (2010) 5859-5866.

[22] S. Jensen, H. Fruchtl, C.J. Baddeley, J. Am. Chem. Soc. 131 (2009) 16706-16713.

[23] S. Jensen, J. Greenwood, H.A. Früchtl, C.J. Baddeley, J. Phys. Chem. C 115 (2011) 8630-8636.

[24] I. Horcas, R. Fernandez, J.M. Gomez-Rodriguez, J. Colchero, J. Gomez-Herrero, A.M. Baro, Rev. Sci. Instrum. 78 (2007) 013705.

[25] B.G. Frederick, G.L. Nyberg, N.V. Richardson, J. Electron Spectrosc. Relat. Phenom. 64-5 (1993) 825-834.

[26] B.G. Frederick, N.V. Richardson, Phys. Rev. Lett. 73 (1994) 772-772.

[27] C.T. Lee, W.T. Yang, R.G. Parr, Phys. Rev. B 37 (1988) 785-789.

[28] M.J. Frisch, G.W. Trucks, H.B. Schlegel, G.E. Scuseria, M.A. Robb, J.R. Cheeseman, J.A. Montgomery, Jr., T. Vreven, K.N. Kudin, J.C. Burant, J.M. Millam, S.S. Iyengar, J.

Tomasi, V. Barone, B. Mennucci, M. Cossi, G. Scalmani, N. Rega, G.A. Petersson, H. Nakatsuji, M. Hada, M. Ehara, K. Toyota, R. Fukuda, J. Hasegawa, M. Ishida, T. Nakajima, Y. Honda, O. Kitao, H. Nakai, M. Klene, X. Li, J.E. Knox, H.P. Hratchian, J.B. Cross, V. Bakken, C. Adamo, J. Jaramillo, R. Gomperts, R.E. Stratmann, O. Yazyev, A.J. Austin, R. Cammi, C. Pomelli, J.W. Ochterski, P.Y. Ayala, K. Morokuma, G.A. Voth, P. Salvador, J.J. Dannenberg, V.G. Zakrzewski, S. Dapprich, A.D. Daniels, M.C. Strain, O. Farkas, D.K. Malick, A.D. Rabuck, K. Raghavachari, J.B. Foresman, J.V. Ortiz, Q. Cui, A.G. Baboul, S. Clifford, J. Cioslowski, B.B. Stefanov, G. Liu, A. Liashenko, P. Piskorz, I. Komaromi, R.L. Martin, D.J. Fox, T. Keith, M.A. Al-Laham, C.Y. Peng, A. Nanayakkara, M. Challacombe, P.M.W. Gill, B. Johnson, W. Chen, M.W. Wong, C. Gonzalez, J.A. Pople, Gaussian 03, revision E.01; Gaussian, Inc.: Wallingford, CT (2004).

[29] G. Kresse, J. Furthmuller, Phys. Rev. B 54 (1996) 11169-11186.

[30] G. Kresse, J. Hafner, Phys. Rev. B 47 (1993) 558-561.

[31] J.P. Perdew, K. Burke, M. Ernzerhof, Phys. Rev. Lett. 77 (1996) 3865-3868.

[32] P.E. Blochl, Phys. Rev. B 50 (1994) 17953-17979.

[33] G. Kresse, D. Joubert, Phys. Rev. B 59 (1999) 1758-1775.

[34] F.T. Netzer, T.E. Madey, J. Chem. Phys 75 (1982) 710.

[35] L.M.A. Perdigao, N.R. Champness, P.H. Beton, Chem. Commun. (2006) 538-540.

[36] Y.L. Wang, A.M. Mebel, C.J. Wu, Y.T. Chen, C.E. Lin, J.C. Jiang, J. Chem. Soc.-Faraday Trans. 93 (1997) 3445-3451.

[37] A. McNutt, S. Haq, R. Raval, Surface Science 531 (2003) 131-144.

[38] G. Wedler, G. Fisch, H. Papp, Berichte Der Bunsen-Gesellschaft Fur Physikalische Chemie 74 (1970) 186-&.

[39] K. Mudiyanselage, M. Trenary, Surf. Sci. 603 (2009) 3215-3221.

[40] S.X. Huang, D.A. Fischer, J.L. Gland, J. Phys. Chem. 100 (1996) 10223-10234.

[41] S.Y. Wu, J.J. Ho, Phys. Chem. Chem. Phys. 12 (2010) 13707-13714.

[42] I. Chorkendorff, J.N. Russell, J.T. Yates, J. Chem. Phys. 86 (1987) 4692-4700.

[43] H. Yanagita, J. Sakai, T. Aruga, N. Takagi, M. Nishijima, Phys. Rev. B 56 (1997) 14952-14955.

[44] D.E. Gardin, G.A. Somorjai, J. Phys. Chem. 96 (1992) 9424-9431.

[45] J.L. Gland, G.B. Fisher, G.E. Mitchell, Chem. Phys. Lett. 119 (1985) 89-92.

[46] H. Yanagita, J. Sakai, T. Aruga, N. Takagi, M. Nishijima, Phys. Rev. B 56 (1997) 14952-14955.

Chapter 3 - Part Two:

Co-deposition of Melamine and Terephthalaldehyde on Ni{111}

3-2.1 Abstract

The co-deposition of melamine and terephthalaldehyde has been investigated on Ni{111} in UHV by STM and RAIRS. Herein, it is shown that no evidence is found for a surface confined reaction to produce oligomers containing imine linkages. Deposition of terephthalaldehyde first results in a self-condensation reaction producing disordered polyester species.

RAIRS indicates that the polymers are adsorbed near parallel to the surface. The polymer species are believed to hinder the propagation of long melamine chains, as were observed on Ni{111}. RAIRS indicates there is no alteration to the terephthalaldehyde or melamine spectra when the species are adsorbed together, suggesting there is no reaction. Terephthalaldehyde is not observed to have any effect on the melamine structures when it is deposited after melamine is deposited first.

3-2.2 Introduction

The condensation reaction between amines and aldehydes holds promise as a means for producing large scale networks of imine polymers. Amines are suitable nucleophilic species on account of the relatively reactive electron lone pair on the nitrogen atom; in addition, aldehydes are ideal electrophilic species due to the

relatively low steric hindrance at the carbonyl group. Amines are ubiquitous nucleophilic species for multicomponent covalent reactions. They have been used in the condensation reaction with aldehydes to form imines, in UHV[1, 2] and in ambient conditions.[3, 4]

In this section, scanning tunnelling microscopy (STM) and reflection absorption infrared spectroscopy (RAIRS) are used to investigate the attempted condensation reaction between melamine (1,3,5-triazine-2,4,6-triamine) and terephthalaldehyde (shown in Figure 3-2.1) on Ni{111}, in ultrahigh vacuum conditions.

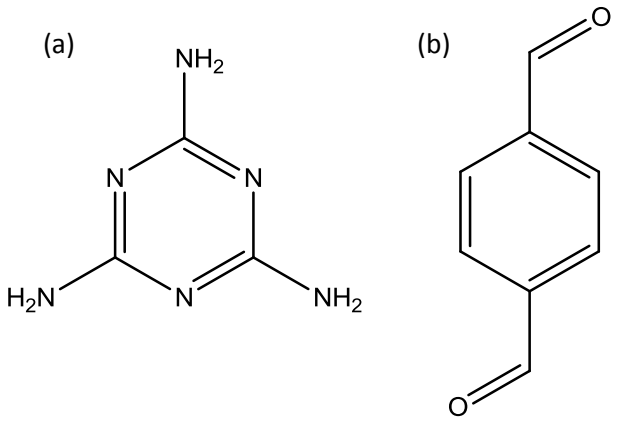

Figure 3-2.1: Chemical structures of: a) melamine, and b) terephthalaldehyde.

3-2.3 Experimental

STM experiments were carried out on an Omicron UHV system with a base pressure of 1 x 10^{-10} mbar. The Ni{111} sample was prepared by cycles of Ar ion bombardment (1.5 kV) and annealing to 893 K until low energy electron diffraction (LEED) and STM indicated the presence of a clean Ni{111} surface. Melamine (Sigma-Aldrich, 99.9 % purity) was deposited onto the Ni{111} surface, held at room temperature, from a

glass doser resistively heated to 393 K, separated from the UHV chamber by a gate valve and differentially pumped by a turbomolecular pump. Terephthalaldehyde (Sigma Aldrich, 99% purity) was deposited onto the Ni{111} surface, held at room temperature, via a precision leak valve. Samples were transferred under UHV conditions to the STM chamber, where images were acquired at room temperature in constant current mode using an electrochemically etched W tip. STM images were processed using WSxM software.[5] RAIRS measurements were carried out using a Nicolet Nexus 860 FTIR spectrometer, fitted with a mercury cadmium telluride (MCT) detector cooled by liquid nitrogen and possessing a spectral range of 800-4000 cm^{-1}. The sample was placed in a UHV chamber, with a base pressure of 1 x 10^{-10} mbar, and the infrared beam (θ_i = 8°) from the spectrometer passed through KBr windows, reflected off the sample and into the detector. The spectrometer was operated with a resolution of 4cm^{-1}, at 256 scans per spectrum.

3-2.4 Results

3-2.4.1 Reflection Absorption Infrared Spectroscopy (RAIRS)

The RAIR spectra in Figure 3-2.2 a) were acquired following the adsorption of terephthalaldehyde on Ni{111} at 300 K as a function of increasing exposure. At low exposure, a single band is observed at ~ 1807 cm^{-1}. Upon increasing coverage, the band shifts to 1786 cm^{-1}. The RAIR spectra in Figure 3-2.2 b) show a series of aldehyde coverages followed by melamine exposure on Ni{111} at 300 K. After melamine deposition, bands are observed at 1614, 1593, 1479, 1410 and 1250 cm^{-1}. The band corresponding to aldehyde deposition is unaltered at 1792 cm^{-1}.

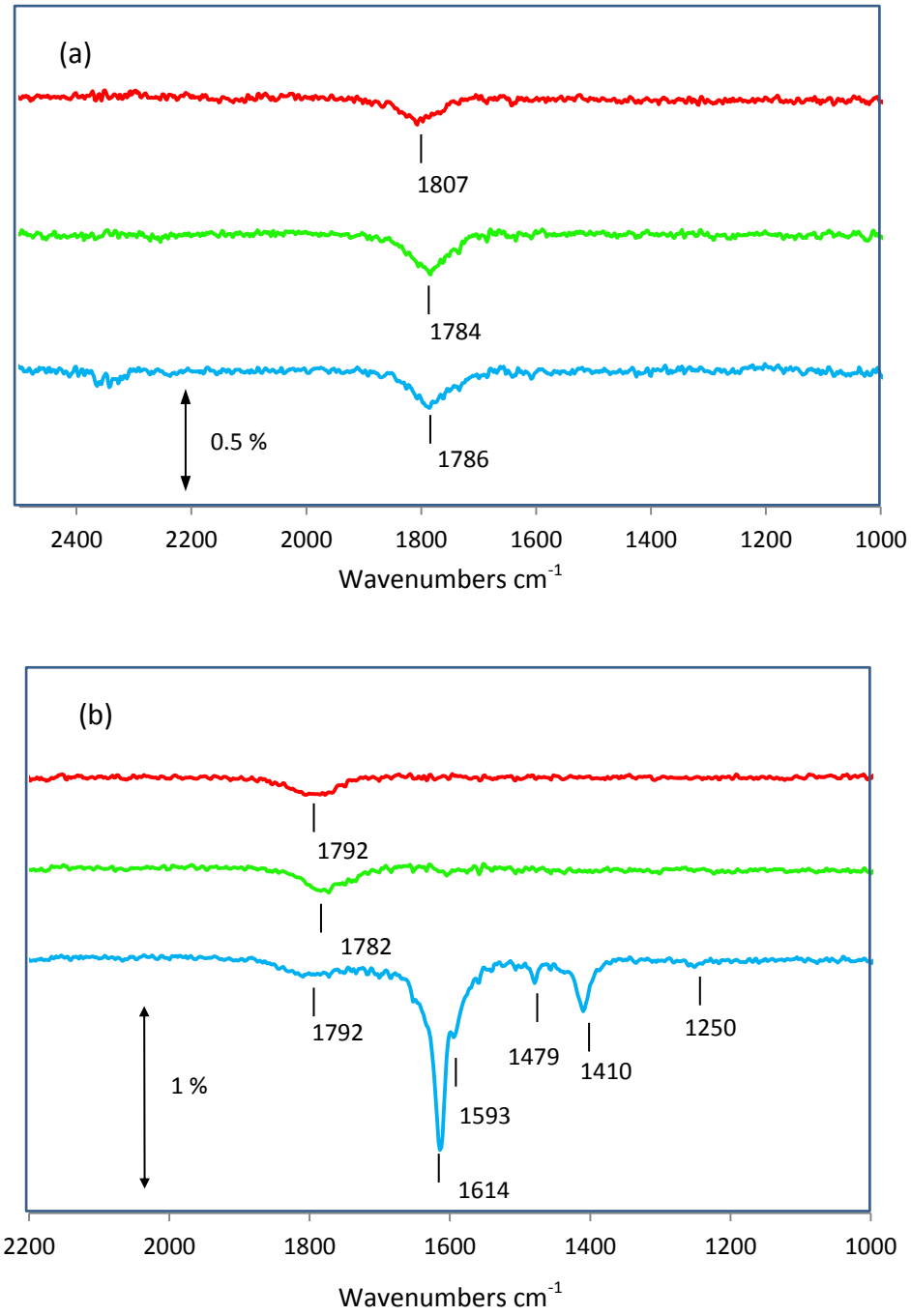

Figure 3-2.2: (a) RAIR spectra as a function of increasing exposure following terephthalaldehyde adsorption on Ni{111} at 300 K. The cumulative coverages are: Red (1.2 L), green (2.4 L), and blue (3 L). (b) RAIR spectra as a function of increasing exposure following terephthalaldehyde adsorption on Ni{111} (red and green spectra) followed by melamine deposition (blue spectra). The cumulative coverages are: Red (1.2 L), green (2.4 L), and blue (0.2 L of melamine).

3-2.4.2 Scanning Tunnelling Microscopy (STM)

Figure 3-2.3 a) shows an STM image of the Ni{111} surface following exposure to 3 L terephthalaldehyde at 300 K. Polymer species of an irregular shape are observed on the surface, and are of a curved appearance. The step edges are covered in bright features; however, no molecular resolution was achieved. In addition, bright clusters are observed on the terraces, of a similar contrast to the step edge features. No evidence of the unreacted dialdehyde species is observed on the surface.

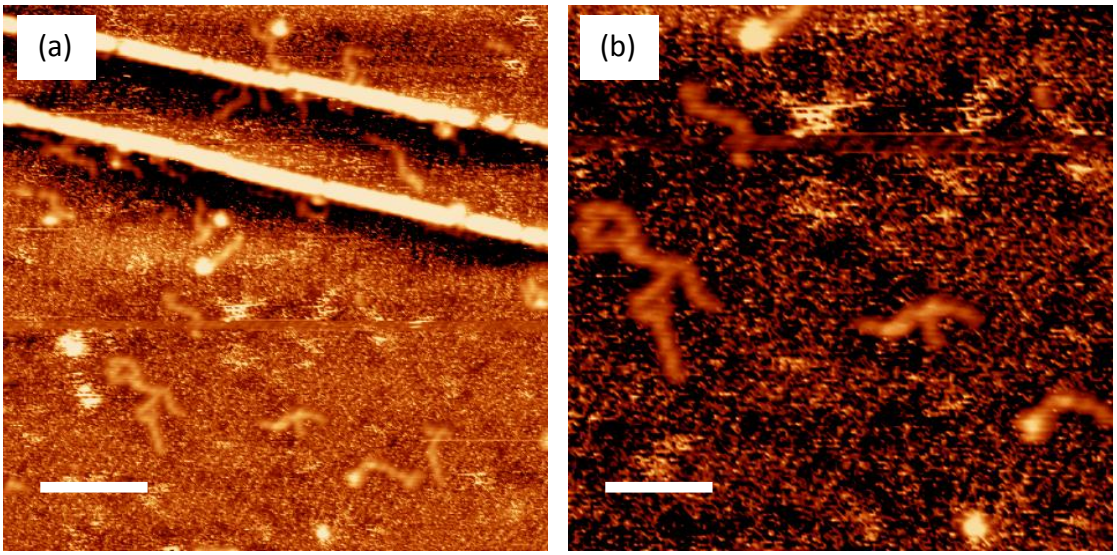

Figure 3-2.3: (a) STM image of terephthalaldehyde (3 L) on Ni{111} at 300 K (I = 0.4 nA, V = -0.6 V, scale bar = 8.6 nm), (b) close-up STM image (I = 0.6 nA, V = -1.1 V, scale bar = 4.7 nm).

Figure 3-2.4 a) shows an STM image following deposition of terephthalaldehyde (2.4 L) prior to deposition of melamine (0.2 L). The image consists of short chain features, arranged haphazardly. Figure 3-2.4 b) shows the image after annealing to 373 K. The molecular features appear to be clustered together, more so than in the room temperature image. The inset is a close-up view of the surface after annealing.

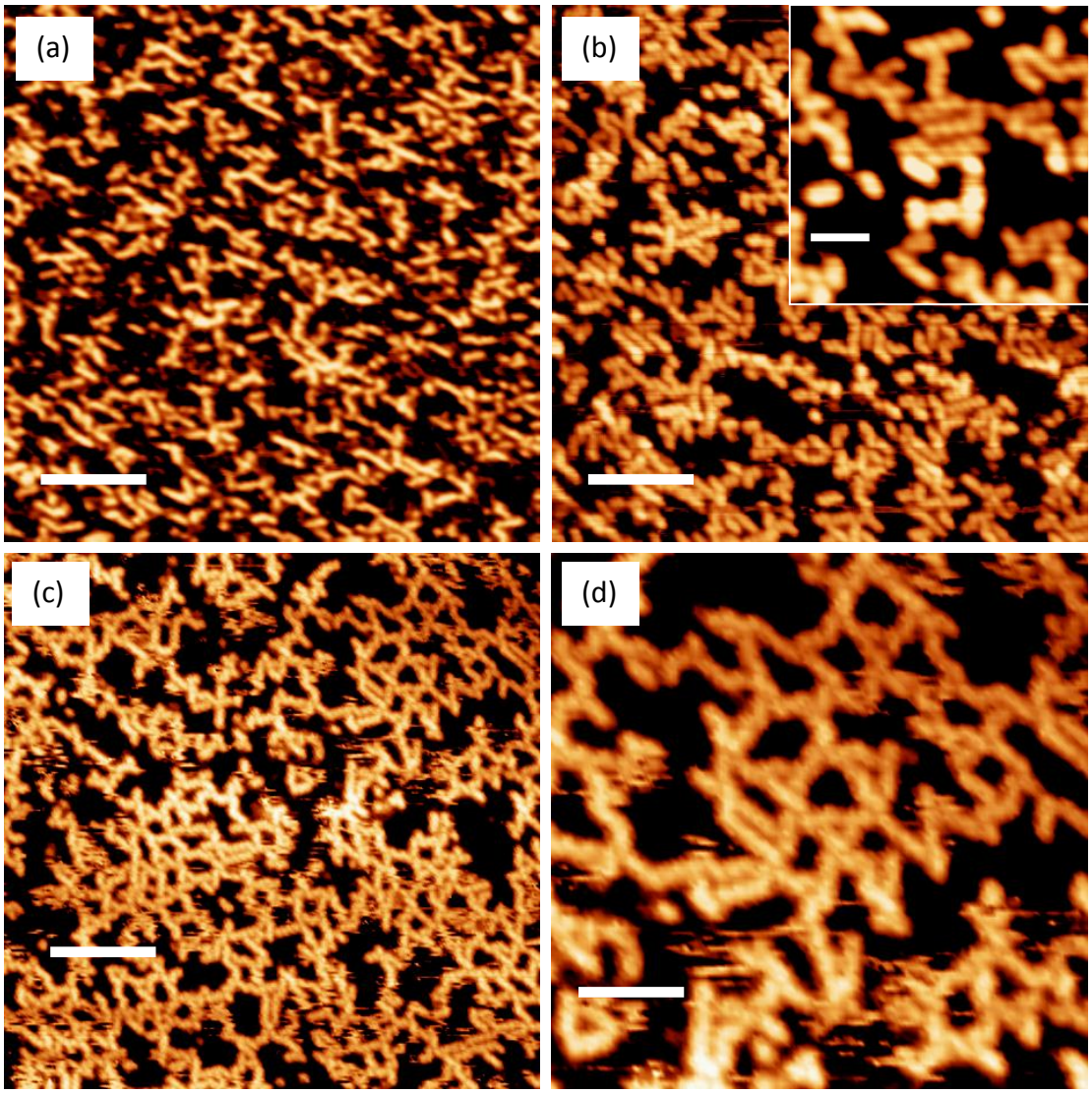

Figure 3-2.4: (a) STM image of terephthalaldehyde (2.4 L) and melamine (0.2 L) on Ni{111} at 300 K (I = 0.3 nA, V = -0.7 V, scale bar = 6.3 nm), (b) annealed to 373 K (I = 0.4 nA, V = -1.2 V, scale bar = 6 nm) [the inset shows an expanded region of this image (scale bar = 1.7 nm)], (c) annealed to 436 K (I = 0.6 nA, V = -1.1 V, scale bar = 7.6 nm), (d) close-up STM image after annealing to 436 K (I = 0.6 nA, V = -1.1 V, scale bar = 3.4 nm).

The individual molecules within the chains are resolvable, measured to be separated by ~ 5 Å. The distance of closest approach of the chains is measured to be ~ 8 Å. Figure 3-2.4 c) is an STM image of the sample after annealing to 436 K. The molecular chains have clustered together to a greater extent, forming islands of interconnected chains. Molecular resolution is achieved for some of the chains; the dimensions are

measured to be approximately the same as the features described in the inset in Figure 3-2.4 b). The pores of the interconnected islands are measured as approximately 1-2 nm across. Figure 3-2.4 d) is a close-up view of the porous structures. The interconnected chains are seen to form shapes of various polygons.

When melamine is deposited prior to terephthalaldehyde, 1-D chains of melamine molecular species are observed to align along the <-211> crystallographic directions, as observed previously for melamine adsorption on Ni{111}, discussed in Chapter 3 – Part 1. Terephthalaldehyde is not observed to have any effect on the melamine structures when it is deposited after melamine is deposited first.

3-2.5 Discussion

The STM images for the deposition of terephthalaldehyde on Ni{111} indicate self-polymerisation occurs on the surface. Deposition of aldehydes and ketones on platinum group metals has resulted in polymerisation in previous studies.[6-9] Lambert et al. observed the self-polymerisation of methyl pyruvate on Pt{111} in the absence of $H_{2(g)}$.[9] The authors concluded that polymerisation occurs by hydrogen elimination from the methyl pyruvate monomer, followed by aldol condensation eliminating methanol. Attard et al. have also studied self-condensation processes on Pt, observing dimeric and aldol intermediates from the self-condensation of ethyl pyruvate.[10] The Tishchenko reaction is well documented, using aluminium alkoxides to catalyse the dimerization of aldehydes bearing an α-hydrogen atom.[11, 12] However, it is unlikely that an aldol type reaction scheme can be applied to the reaction in this study. Terephthalaldehyde is a non-enolizable aldehyde since aromatic aldehydes have no available α-hydrogen atom. Typically, these aldehydes in

solution with stoichiometric amounts of OH^- undergo disproportionation yielding alcohols and carboxylates (Cannizarro reaction).[13] Abaee et al.[14] have reported on ester formation via Tishchenko reactions of aldehydes under LiBr catalysis. Crucially, aromatic aldehydes were successfully used in this reaction scheme. When the aldehyde reactants were mixed with LiBr and Et_3N under solvent-free conditions at room temperature, formation of dimeric esters of the starting substrates was observed in high yields. The authors proposed that the reaction proceeded under a 2:1 ratio of aldehyde to LiBr, in which the aldehyde species coordinated through the carbonyl oxygen atoms to the lithium ion. Such a reacting species is thought to form a six-membered transition state, facilitating 'intramolecular' hydride transfer between the two aldehyde molecules. The reaction conditions will inevitably be different for solution based reactions and those on surfaces in UHV; however, it is believed that the reaction scheme put forward by Abaee et al. is a close approximation to what is happening for ester formation in this study. In this case, the Ni substrate could act to form a transition state between multiple dialdehyde reactant species, facilitating hydride transfer and subsequent ester formation.

The RAIR spectra show a band at ~ 1786 cm^{-1}, corresponding to a carbonyl group stretching mode. The band intensity increases slightly going from low to higher coverage of aldehyde. The most likely product from the self-polymerisation of terephthalaldehyde is an ester species; however, there is no observed band corresponding to the C-O band of the ester species, which would be expected near 1280 cm^{-1} for aryl conjugated esters.[15] Should the molecule lie fairly flat on the surface then the C-O band would not be detected by RAIRS.

RAIRS data in Figure 3-2.2 b) indicate no alteration to the terephthalaldehyde absorption band when melamine is deposited on the Ni{111} surface after terephthalaldehyde exposure. The melamine absorption bands are analogous to those observed for high coverage melamine exposure on Ni{111}, as discussed in Chapter 3 - Part 1. This observation leads to the conclusion that there is no reaction between melamine and terephthalaldehyde on Ni{111} at room temperature for the conditions used.

The STM image in Figure 3-2.4 a) for melamine deposition on a Ni{111} surface at 300 K, pre-covered with terephthalaldehyde (2.4 L), indicate disruption to the growth of the melamine 1-D chains, as described in Chapter 3 – Part 1. The polymers resulting from terephthalaldehyde deposition are undoubtedly hindering the propagation of the melamine chains, resulting in the shorter, more disorganised chains observed. There is no observation of the ester polymers in the image. This can be explained by the lower height profile of the polymers relative to melamine. As described previously, melamine adsorbs upright on the Ni surface via σ-donation to the surface from a triazine nitrogen atom and two amino group nitrogen atoms; whereas, the ester polymers are likely adsorbed parallel or near parallel to the surface, as suggested by the weak RAIRS signal.

There is no evidence of covalent reaction between terephthalaldehyde and melamine on Ni{111}. As already discussed, the aldehyde reactant polymerises upon adsorption on Ni{111}, making it unavailable for further reaction. Also, the upright orientation of melamine renders it unreactive due to the interaction between the surface-bound amine groups and Ni substrate. When terephthalaldehyde is

deposited on the Ni surface pre-covered with melamine there is no evidence of reaction between the aldehyde and the melamine amine group pointing away from the surface. The melamine structures are unaltered, and there is no detectable height variations expected if reaction had occurred.

After annealing the sample to 373 K, shown in Figure 3-2.4 b), the short melamine chains are observed to have clustered together into small islands. The inset in Figure 3-2.4 b) reveals molecular resolution of a 2-D island of melamine. The molecular dimensions, stated in the results section, are analogous to those of melamine on Ni{111}.

Annealing of the sample to 436 K results in the formation of interconnected chains of melamine, producing porous arrays, shown in Figure 3-2.4 c). In their study of methyl pyruvate polymerisation on Pt{111}, Lambert et al. performed temperature programmed reaction (TPR) studies.[9] The main desorption peaks of the decomposition fragments were for CO, H_2, and CO_2; desorbing at 440-470 K, ~ 360 K, and ~ 360 K, respectively. Unfortunately, no TPR studies were performed for the co-deposition of terephthalaldehyde and melamine. The TPR data of Lambert et al. provides a useful comparison to the likely desorption temperature of the polymer fragments in this study. Assuming there is negligible variation in the desorption temperature for the Pt and Ni{111} substrates, it can be proposed that the polymer structures have decomposed and mostly desorbed following annealing to 436 K.

The disappearance of the polymers is the likely reason for the formation of the interconnected melamine chain structures after annealing to 436 K. The formation of the porous melamine chain structures is significant, in that the pore diameters

measure approximately 1-2 nm across. This is ideal for hosting guest molecular species, and is an area of investigation that certainly warrants future study.

3-2.6 Conclusions

STM data reveals a self-condensation reaction occurs following the adsorption of terephthalaldehyde on Ni{111} at 300 K, producing polymer species. RAIR spectra show a single vibrational band corresponding to a carbonyl group stretching mode. It is believed the polymers are ester species adsorbed near-parallel to the surface, accounting for the weak RAIR ester carbonyl signal and lack of C-O band.

When melamine is adsorbed on Ni{111} at 300 K pre-covered with terephthalaldehyde, short and disorganised chains of melamine are observed. This is different to melamine adsorbed on clean Ni{111}, in which 1-D chains of melamine molecular species (~ 5 nm in length) align along the <-211> crystallographic directions.[16] The polymer species are believed to hinder the propagation of the melamine chains. RAIRS indicates there is no alteration to the terephthalaldehyde or melamine spectra when the species are adsorbed together, suggesting there is no reaction. After annealing the sample to 373 K, the short melamine chains are observed to have clustered together into small islands. Further annealing to 436 K reveals the melamine chains form interconnections, producing islands of porous melamine chain structures. This is believed to be caused by the decomposition of the ester polymers and fragment desorption, allowing the melamine chains to interconnect. Terephthalaldehyde is not observed to have any effect on the melamine structures when it is deposited after melamine is deposited first.

3-2.7 References

[1] S. Weigelt, C. Busse, C. Bombis, M.M. Knudsen, K.V. Gothelf, T. Strunskus, C. Woll, M. Dahlbom, B. Hammer, E. Laegsgaard, F. Besenbacher, T.R. Linderoth, Angew. Chem.-Int. Edit. 46 (2007) 9227-9230.

[2] S. Weigelt, C. Bombis, C. Busse, M.M. Knudsen, K.V. Gothelf, E. Laegsgaard, F. Besenbacher, T.R. Linderoth, ACS Nano 2 (2008) 651-660.

[3] Y. Li, J. Wan, K. Deng, X. Han, S. Lei, Y. Yang, Q. Zheng, Q. Zeng, C. Wang, The Journal of Physical Chemistry C 115 (2011) 6540-6544.

[4] R. Tanoue, R. Higuchi, N. Enoki, Y. Miyasato, S. Uemura, N. Kimizuka, A.Z. Stieg, J.K. Gimzewski, M. Kunitake, Acs Nano 5 (2011) 3923-3929.

[5] I. Horcas, R. Fernandez, J.M. Gomez-Rodriguez, J. Colchero, J. Gomez-Herrero, A.M. Baro, Rev. Sci. Instrum. 78 (2007) 013705.

[6] R.J. Madix, T. Yamada, S.W. Johnson, Appl. Surf. Sci. 19 (1984) 43-58.

[7] M.A. Henderson, G.E. Mitchell, J.M. White, Surface Science 188 (1987) 206-218.

[8] M.A. Henderson, Y. Zhou, J.M. White, J. Am. Chem. Soc. 111 (1989) 1185-1193.

[9] J.M. Bonello, F.J. Williams, A.K. Santra, R.M. Lambert, J. Phys. Chem. B 104 (2000) 9696-9703.

[10] N.V. Rees, R.J. Taylor, Y.X. Jiang, I.R. Morgan, D.W. Knight, G.A. Attard, J. Phys. Chem. C 115 (2011) 1163-1170.

[11] W. Tishchenko, *Chem Zentralbl* 77 (1906) 1309 - 1311.

[12] W. Tishchenko, *Chem Zentralbl* 77 (1906) 1552 - 1555.

[13] A. Sorkau, K. Schwarzer, C. Wagner, E. Poetsch, D. Steinborn, J. Mol. Catal. A-Chem. 224 (2004) 105-109.

[14] M.M. Mojtahedi, E. Akbarzadeh, R. Sharifi, M.S. Abaee, Org. Lett. 9 (2007) 2791-2793.

[15] N.B.D. Colthup, L. H; Wiberly, S. B, Academic Press, New York 3rd Edition (1990).

[16] J. Greenwood, H.A. Fruchtl, C.J. Baddeley, J. Phys. Chem. C 116 (2012) 6685-6690.

Chapter Four:

Co-deposition of Melamine with an Aromatic Dialdehyde on Pd{111}

Part One:

Ordered Growth of Upright Melamine Species on Pd{111}

4.1 Abstract

Melamine (1, 3, 5-triazine-2, 4, 6-triamine), was deposited on the Pd{111} surface held at room temperature under ultrahigh vacuum conditions. The overlayer structure formed at saturation coverage was analysed with scanning tunnelling microscopy, and reflection absorption infrared spectroscopy was used to probe the orientation and surface chemistry of adsorbed melamine which was found to adopt an adsorption orientation that is perpendicular, or close to perpendicular, to the {111} surface. The melamine desorption products were analysed with temperature programmed desorption. At low coverage, 1-D chains of partially dehydrogenated melamine are formed on the Pd surface aligned along the <-211> crystallographic directions. At

higher exposure, the linear chains are still present, together with disordered melamine structures.

4.2 Introduction

The fabrication of 2-dimensional nanostructures utilising organic molecular building blocks has been extensively researched. A variety of structures have been realised on a range of surfaces; utilising non-covalent intermolecular forces, such as hydrogen bonds,[1-5] van der Waals forces,[6, 7] and metal-organic coordination,[3, 8, 9] to produce ordered overlayer structures. There are advantages to utilising hydrogen-bonding for such structures; specifically, that the relatively high equilibration of intermolecular-interactions allows defects within the structure to be minimised, and high diffusion rates of small organic precursors enable structures on a large scale. Also, since hydrogen bonds are directional, extremely ordered structures can be created.

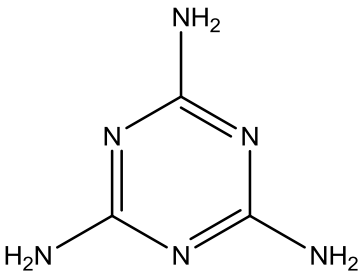

Figure 4.1: Chemical structure of melamine.

Melamine, (1, 3, 5-triazine-2, 4, 6-triamine, see Figure 4.1), is a well-studied molecule amongst hydrogen-bonded structures in the literature. As discussed in Chapter 3 – Part 1, melamine adsorption has been investigated on the Au{111},[10] Ag{111},[11] and Ni{111}[12] surface. Bimolecular hydrogen–bonded systems of melamine have been

studied, incorporating cyanuric acid,[13, 14] PTCDA,[15] PTCDI,[1, 16, 17] and NTCDI.[18] Also, a tri-molecular system of melamine in combination with PTCDI and uracil has been investigated with scanning tunnelling microscopy.[19] However, hydrogen-bonded structures have limited thermal stability; hence, research has been conducted into developing covalent structures which possess higher thermal and mechanical stability. Covalently bonded two-dimensional nanostructures have been fabricated using melamine as the nucleophilic species, reacting with 1,4-phenylene diisocyanate,[20] and with trimesoyl chloride,[21] both on Au{111}, to produce urea and amide linkages, respectively.

Palladium is a catalytically active metal surface for hydrogenation reactions and, with chiral modifier molecules adsorbed on Pd, has a wide range of applications in enantioselective chemistry. For example, with α, β- unsaturated acids (ees up to 72%) and hydroxymethylpyrone (ees up to 94 %), cinchonidine is the preferred modifier on Pd.[22] Cinchona alkaloids are well studied for the use of enantioselective modification of a Pd surface[23, 24] containing a heterocyclic nitrogen atom that plays an important part in the surface orientation of the modifier molecule and, hence, of the reactant molecule. The purpose of using melamine in this study is two-fold: Firstly, to investigate the adsorption behaviour of a molecule with possible analogous substrate-adsorbate interactions as existing chiral modifier molecules; also, to look at the adsorption of a nucleophilic species with the potential for developing 2-dimensional enantioselective networks via covalent bond formation.

Herein, data are presented on the ordering and adsorption orientation of adsorbed melamine on Pd{111} using both scanning tunnelling microscopy and reflection

absorption infrared spectroscopy. Temperature programmed desorption provides information on the desorption fragments and thermal stability of melamine on Pd{111}.

4.3 Experimental

The STM experiments were carried out on an Omicron UHV system with a base pressure of 1 x 10^{-10} mbar. The Pd{111} sample was prepared by cycles of Ar ion bombardment (1.5 kV) and annealed to 893 K until a sharp (1 x 1) LEED pattern was observed and STM indicated the presence of a clean Pd{111} surface. Melamine (Sigma-Aldrich, 99.9 % purity) was deposited onto the Pd{111} surface; held at room temperature, from a glass doser resistively heated to 393 K, separated from the UHV chamber by a gate valve and differentially pumped by a turbomolecular pump. STM images of the surface were acquired by transferring under UHV conditions to the STM chamber, where data were taken in constant current mode using an electrochemically etched W tip. All STM images were acquired at room temperature. STM images were processed using WSxM software.[25]

RAIRS measurements were carried out using a Nicolet Nexus 860 FTIR spectrometer, fitted with a mercury cadmium telluride (MCT) detector cooled by liquid nitrogen and possessing a spectral range of 800-4000 cm^{-1}. The sample was placed in a UHV chamber, with a base pressure of 1 x 10^{-10} mbar, and the infrared beam from the spectrometer (θ_i = 8°) passed through KBr windows, reflected off the sample and into the detector. The spectrometer was operated with a resolution of 4cm^{-1}, at 256 scans per spectrum.

Temperature programmed desorption (TPD) experiments were carried out in a UHV system, built by PSP Vacuum Technology Ltd., operated at a base pressure of ~ 2 x 10^{-10} mbar. The Pd{111} sample was cleaned as described above and then exposed to melamine sublimed from an identical solid dosing source. For initial TPD experiments, all masses in the range 0-150 amu were monitored to see which peaks increased as a function of sample temperature. These results lead to the monitoring of the following masses at: 2, 12, 27 and 28 amu during all TPD experiments. An approximately linear heating rate of 2 K s^{-1} was used. It is noted that, despite the same melamine doser and applied current being used for all experiments, the different positions of the pressure gauges on the experimental UHV chambers resulted in very different melamine pressure readings for the different experimental techniques.

Molecular DFT calculations were carried out using the GAUSSIAN 03 program suite.[26] Gaussview was used to create the input for the simulation and for visualising the optimised molecular structure and the frontier orbitals of melamine. DFT calculations were carried out by Dr H. A. Früchtl on the EaStCHEM Research Computing Facility.

4.4 Results

4.4.1 Reflection Absorption Infrared Spectroscopy (RAIRS)

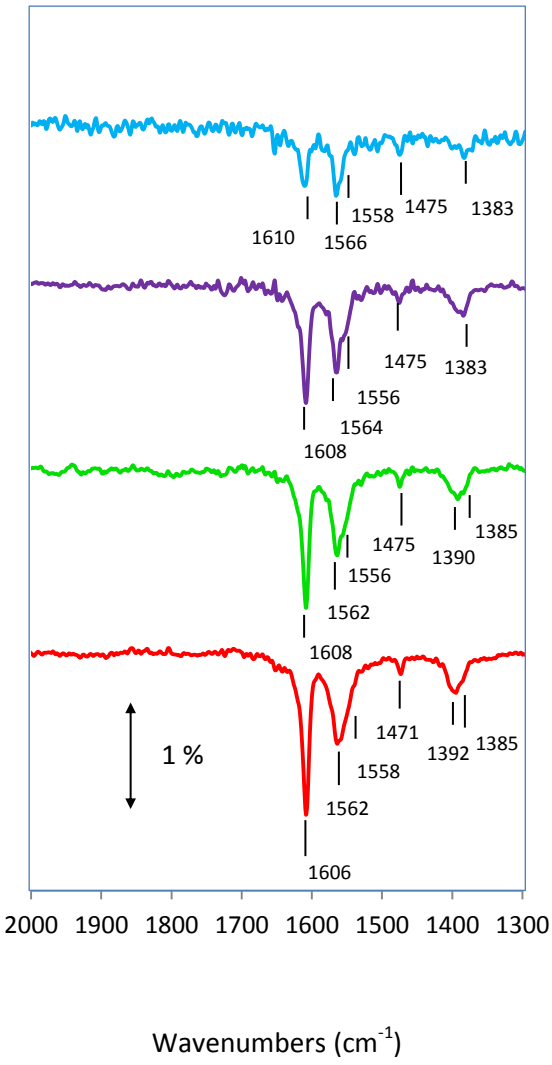

Figure 4.2: RAIR spectra as a function of increasing exposure following melamine adsorption on Pd{111} at 300 K. The cumulative coverages are: Blue (0.036 L), purple (0.072 L), green (0.09 L) and red (0.108 L).

RAIR spectra in Figure 4.2 were acquired following the adsorption of melamine on Pd{111} at 300 K as a function of increasing exposure. At low melamine exposure, bands are observed at 1606, 1566, 1588 (appearing as a shoulder to the 1566 cm^{-1} band), 1475, and 1383 cm^{-1}. At higher coverage, an additional band is observed at

1392 cm^{-1}. As the melamine coverage is increased, there is a change in the relative intensity of the bands such that at the highest exposures the bands at 1606 and 1392 cm^{-1} are relatively much more intense than those at low melamine exposure. Following melamine exposure of 0.09 and 0.108 L, a band at 2339 cm^{-1} is observed, corresponding to gas phase CO_2.

4.4.2 Temperature Programmed Desorption (TPD)

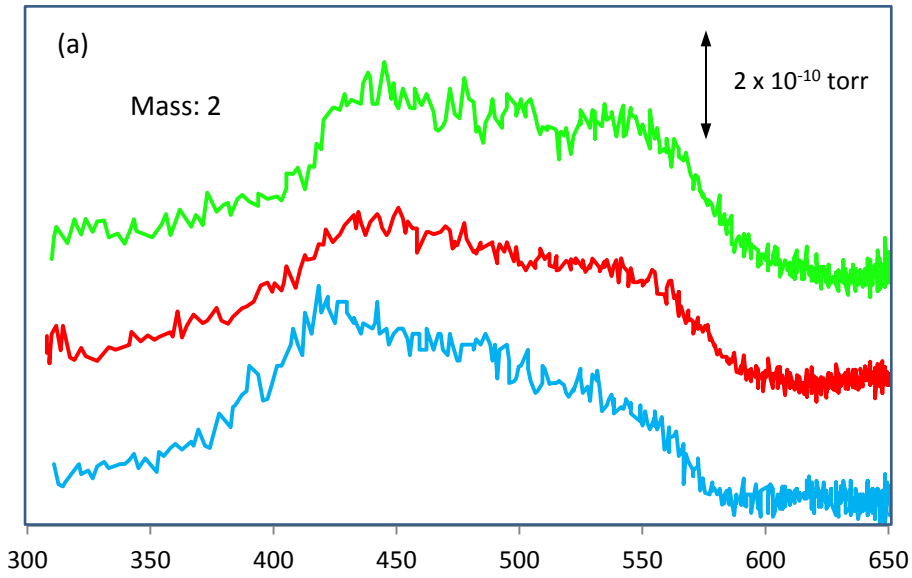

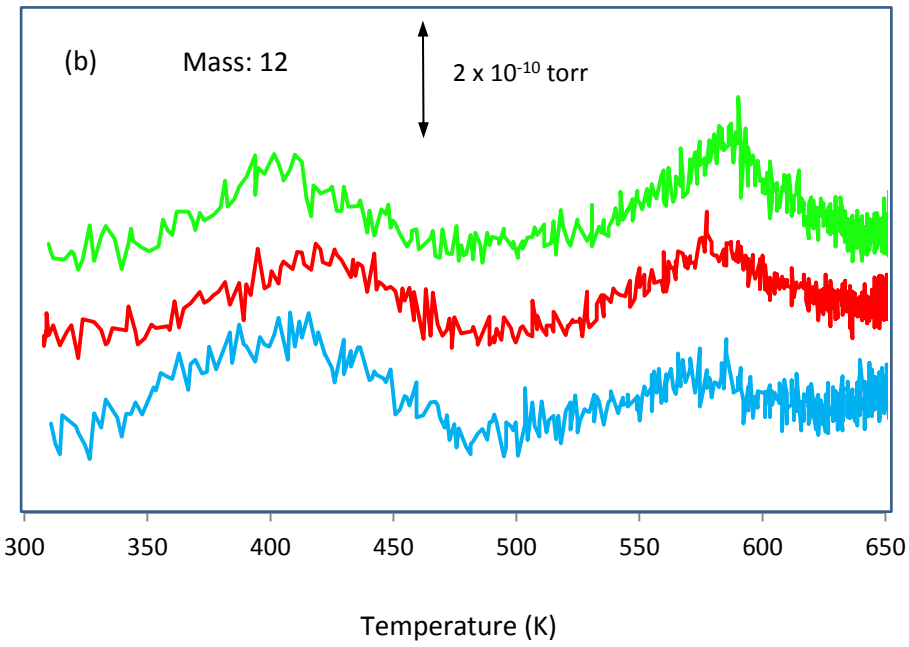
(b)
Mass: 12
2 x 10-10 torr
300
350
400
450
500
550
600
650
Temperature (K)

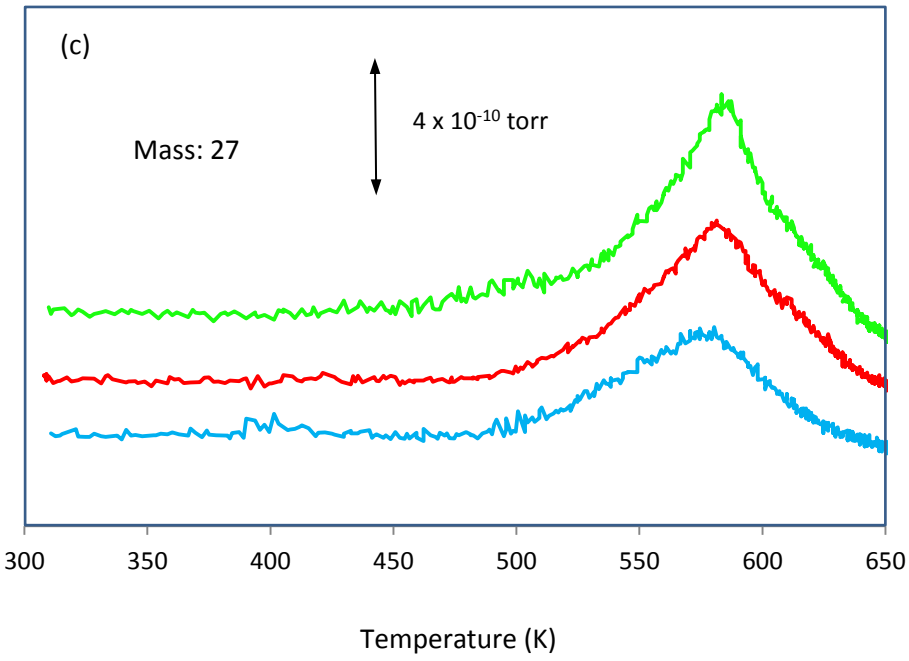
(c)
Mass: 27
4 x 10-10 torr
300
350
400
450
500
550
600
650
Temperature (K)

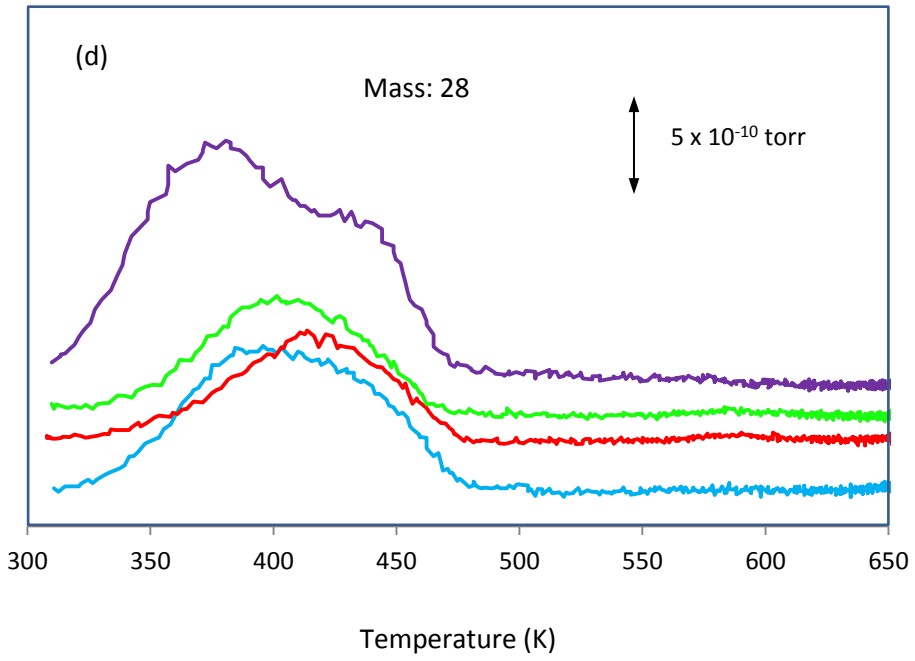

Figure 4.3: TPD spectra for melamine adsorption on Pd{111} at 300 K monitoring masses: a) 2, b) 12, c) 27, and d) 28. The spectra represent a series of increasing exposures at: 6 L (blue), 12 L (red), and 18 L (green). The purple spectra in d) represents the desorption spectra for the blank Pd{111} sample. Note: The y-axis in all spectra have arbitrary units. The relative intensities of the TPD spectra are represented by the scale bar.

In Figures 4.3 a) – d), TPD data are shown following melamine adsorption onto Pd{111} at ~ 300 K as a function of melamine exposure. The TPD of mass 2 (H_2), Figure 4.3 a), shows a large, broad H_2 peak, thought to incorporate more than one desorption peak with T_{max} ~ 420 K and T_{max} ~ 540 K. At low exposure, the relative intensity of the lower temperature desorption peak is greater than the higher temperature desorption peak; however, the relative intensities become the same after higher exposure.

TPD for mass 12 (C), Figure 4.3 b), shows two peaks, at T_{max} ~ 400 K and T_{max} ~ 570 K. The first of these peaks is observed in the TPD of the blank Pd sample, hence is ruled out as a desorption product of melamine decomposition. The higher temperature desorption peak is due to melamine decomposition; the intensity of which increases slightly upon increasing melamine exposure.

The TPD spectra for mass 27 (assigned as HCN) are shown in Figure 4.3 c). A single peak is observed at T_{max} ~ 580 K. The peak intensity increases for increasing melamine exposure.

Figure 4.3 d) shows the TPD spectra for mass 28. The purple spectra represents the desorption spectra from the blank Pd{111} sample. As the mass 28 peak is observed for the blank sample this can be ruled out as a decomposition fragment of melamine. No desorption peaks are observed at higher temperatures, which would correspond to N_2 desorption resulting from N + N recombination, as is the case for melamine desorption from Ni{111}, see Chapter 3 – Part 1.

Auger electron spectroscopy (AES) spectra taken after TPD runs revealed residual carbon was still present on the Pd{111} surface. This is most likely a decomposition fragment of melamine resulting from the heating ramp.

4.4.3 Scanning Tunnelling Microscopy (STM)

Figure 4.4 a) shows an STM image of the Pd{111} surface following exposure to 0.036 L of melamine at 300 K, approximately corresponding to the blue RAIR spectra in Figure 4.2. Under these conditions, chains of molecular features are observed along <112> -type surface directions. Figure 4.4 b) is a close-up view of the low-coverage melamine chains. The individual melamine molecules within each chain are resolvable, separated by 6.4 Å. The distance of closest approach of melamine chains is measured to be 13.1 Å.

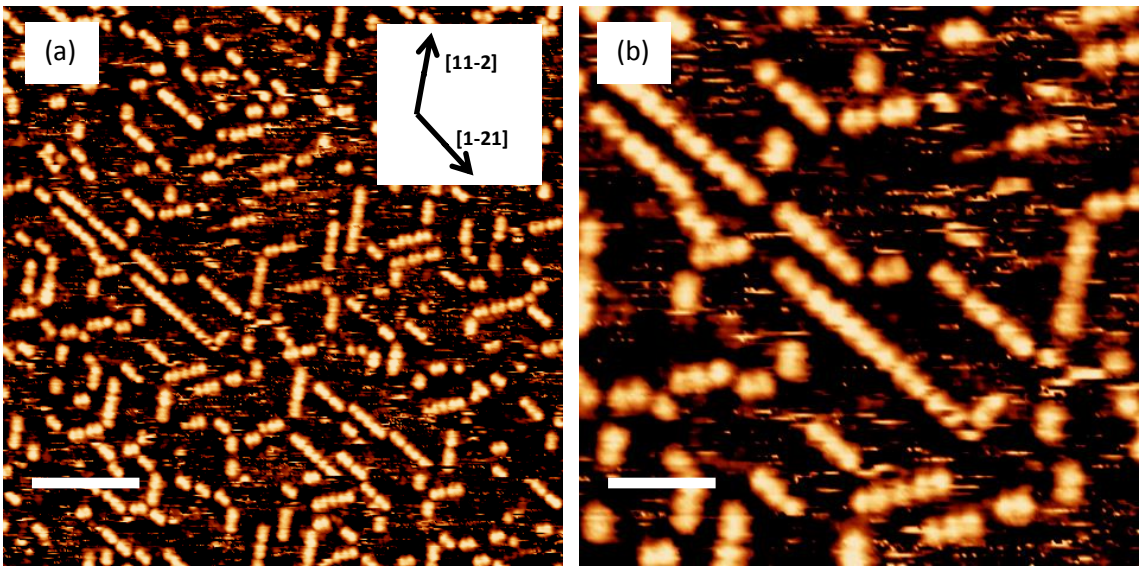

Figure 4.4: (a) STM image of melamine, ~ 0.036 L dose, adsorbed on Pd{111} at 300 K (scale bar 7.5 nm; 0.15 V, 0.3 nA). (b) A close-up image of the same surface (scale bar 3.2 nm).

Figure 4.5 a) shows an STM image of a melamine-covered Pd{111} surface after an exposure of 0.16 L (i.e., corresponding to the high coverage melamine RAIR spectrum in Figure 4.2). There is no apparent long-range order to the melamine overlayer structure that is formed. Melamine is seen to form 2-dimensional filament structures. These filaments interconnect with each other, and are observed to branch off from connection nodes. In a number of cases, the structures consist of a connection node which has branched off in three directions. The angle between the separate branches is close to 120˚, suggesting the structures are partially commensurate. A minority of the filaments are curved over short distances, approximately 5 nm. Figure 4.5 b) represents a close-up view of the surface.

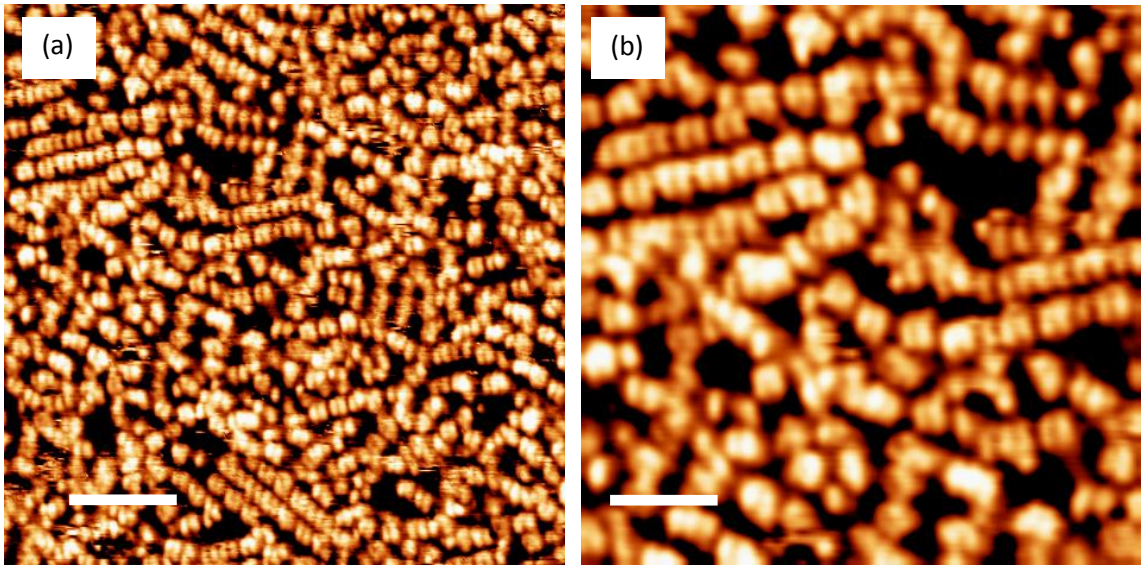

Figure 4.5: (a) STM image of melamine, ~ 0.16 L, adsorbed on Pd{111} at 300 K (scale bar 6.6 nm; 1.5 V, 0.3 nA). (b) A close-up image of the same surface (scale bar 3.4 nm).

4.5 Discussion

The observed melamine overlayer structure on Pd{111} shows there are certain similarities but also key differences to that seen for melamine adsorbed on Ni{111}. Chapter 3 – Part 1 describes melamine adsorbed on Ni{111} occurs with the formation of linear chain structures which propagate along the <-211> crystallographic directions.[12] RAIRS data and DFT calculations confirmed an upright adsorption orientation for melamine on Ni{111}, via σ-donation from the triazine nitrogen atom and two amino group nitrogen atoms. This is conducive for the adsorption of the two surface bound amine groups at bridge sites and the triazine nitrogen atom at an atop site, allowing the melamine molecules to propagate freely in linear chains. The RAIRS data from this study, which will be discussed in further detail later on, confirm that melamine also adopts a tilted adsorption orientation on Pd{111}. The disordered nature of the melamine filament structures means they are less well resolved

compared to those formed on Ni{111}. However, in some cases the filament structures are resolved enough to determine the component molecular features.

It is observed that for both low and high exposure of melamine STM images the molecular features appear to form pairs within the linear chains. The centre-to-centre separation of the paired molecular features is measured as approximately 6.1 Å; whereas, the centre-to-centre separation between separate paired features measures approximately 7.3 Å. If the adjacent paired melamine molecules are tilted towards each other, there is the possibility of intermolecular H-bonding interactions stabilising the features. The intact amino group pointing upwards on adsorbed melamine could potentially form H-bonds with an adjacent amino group. A schematic of the proposed ordering of the melamine molecules on Pd{111} is represented in Figure 4.6. It is noted that the melamine adsorption sites have arbitrarily been chosen.

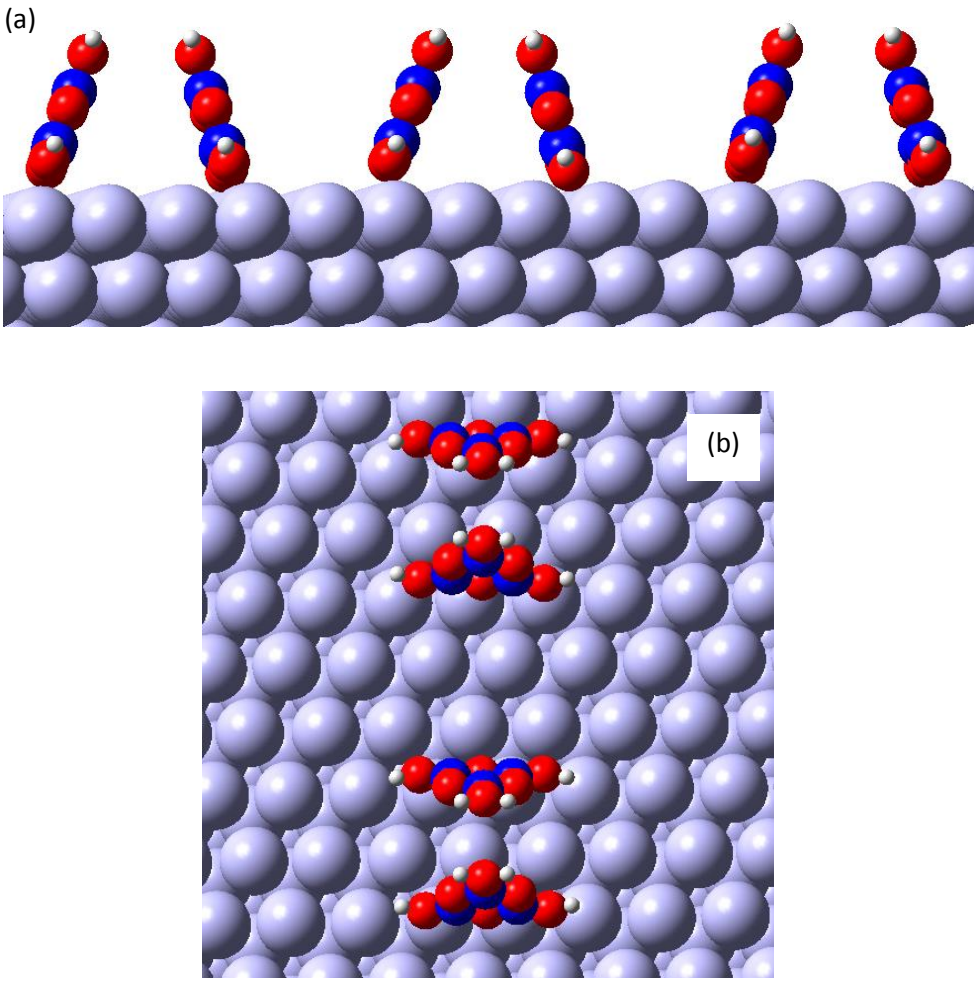

Figure 4.6: Schematic illustration of melamine chains adsorbed on Pd{111}: (a) Side-on view, (b) Top down view. Melamine: carbon-blue, nitrogen-red, hydrogen-grey.

A comparison can be made between the behaviour of melamine adsorption and that of pyridine and quinoline on Pd{111}. Both pyridine and quinoline possess an analogous aromatic ring nitrogen atom which can interact with the Pd substrate. Quinoline is the anchoring chemical moiety of the important chiral modifiers cinchonine and cinchonidine. Lambert et al.[27] investigated the adsorption geometry of quinoline on Pd{111}, characterised by XPS and NEXAFS. The orientation of quinoid chiral modifiers is believed to be essential in forming a modifier-reactant complex. There is a reversal of enantioselectivity and lack of rate enhancement of modified Pd

with respect to the modified Pt system with cinchonine and cinchonidine. However, the findings of Lambert et al. concluded that the measured tilt angle of quinoline is approximately the same on both Pt and Pd{111}, corresponding to an almost flat-lying molecule, and forms disordered networks on both surfaces. NEXAFS for monolayer quinoline on Pd{111} at 295 K indicates the molecule is adsorbed predominately via the aromatic π system. These results suggest the differences in the chirally modified Pt and Pd systems are due to an alteration of the reactant surface chemistry, as opposed to differences in chiral modifier geometry.[27]

Grassian and Muetterties studied the vibrational spectra of pyridine adsorption on Pd{111} using EELS.[28] The results showed that at 310 K, and at saturation coverage, pyridine is chemisorbed to the surface with the aromatic ring plane oriented away from the surface plane. The authors proposed that pyridine behaves as a Lewis acid, donating electron density through the nitrogen electron lone pair into the Pd surface. These results are in agreement with a UPS and EELS study of pyridine on Pd{111} by Netzer and Mach.[29] Pyridine adsorption at 300 K has been shown by EELS[30] and RAIRS[31] to form an α-pyridyl species in an upright configuration when adsorbed on Pt(111), independent of coverage. The osmium complex $HOs_3(CO)_{10}(NC_5H_4)$ provides a good comparison with the adsorbed α-pyridyl species on account of the reduced symmetry. The IR vibrational frequencies observed for the osmium complex correlate with those of the α-pyridyl species on Pt{111}.[30] However, comparison of the EEL spectrum for the pyridine/Pd system with the IR spectra of the osmium complex lacks any relationship, indicating associative adsorption.

It is concluded that melamine adopts a tilted orientation on Pd{111} analogous to that of melamine adsorbed on Ni{111}[12] and to pyridine adsorbed on Pd{111}.[28] Melamine interacts with the Pd surface via the lone pair of electrons on the triazine nitrogen atom and amino group nitrogen atoms. This was also found to be the case for melamine adsorption on Ni{111}. As has already been described, melamine adsorbed on Ni{111} also interacts through σ-donation via the two amino group nitrogen atoms adjacent to the interacting triazine nitrogen atom. The three nitrogen atoms interact with a bride-atop-bridge adsorption site. The Pd interatomic spacing is larger than that of Ni (2.49 Å),[32] measuring 2.75 Å.[33] There are two possible lattice effects influencing the structures: The first relates to the repeat distance between molecules and the other relates to the adsorption site. The greater mismatch in spacing between the Pd surface atoms and the interacting nitrogen atoms on melamine may not conform to melamine propagating in long linear chains, as witnessed on Ni{111}. This is manifested in the larger melamine intermolecular distances (6.4 Å) and the distance of closest approach of melamine chains (13.1 Å) measured in this study, as opposed to the study on Ni{111}, in which the values are measured as ~4.5 to 5 Å, and 9 Å, respectively. In addition, the chains of melamine molecules on Pd{111} are observed to curve in some cases. This is further evidence of the decreased commensurate behaviour of melamine adsorption on Pd{111} with respect to Ni{111}. On Ni, it seems that the bridge-atop-bridge site is not only inherently stable but, also, it is feasible to position melamine molecules in equivalent sites ~ 5 Å apart. On Pd, it appears not to be the case. The preferential melamine adsorption sites on Pd{111} is subject to on-going DFT calculations by Dr H. A. Früchtl.

The TPD data shows coincident desorptions at masses 2, 12 and 27 which are likely to represent the surface reaction rate limited desorption of decomposition products of adsorbed melamine species. There is an absence of lower temperature hydrogen desorption peaks, as observed for Ni{111} in Chapter 3 – Part 1 (T_{max} ~ 350 K), corresponding to H_2 resulting from the dehydrogenation of the surface amino groups. A study of pyrrole adsorption on Pd{111} resulted in the dissociation of N-H and/or C-H bonds and was confirmed by a hydrogen desorption peak at 350 K.[34] However, the onset of the hydrogen desorption begins at ~ 290 K. It is noted that in this study, melamine exposure occurred 10-20 K above room temperature in some cases after sample annealing. The slightly higher sample temperature could have resulted in hydrogen desorption occurring before TPD analysis. In the study of pyrrole adsorption on Pd{111}, a second H_2 desorption peak is observed at ~ 475 K. This was ascribed to the decomposition of CH species. Analogous behaviour was observed in this study, in which hydrogen desorption peaks are observed at temperatures significantly higher than the desorption temperature of hydrogen on Pd{111}. The hydrogen peaks in this study are likely caused by deprotonation of organic decomposition products of melamine. A contribution from background H_2 dissociative adsorption cannot be ruled out.

Methylamine adsorbed on Pd{111} also undergoes dehydrogenation, with a maximum desorption rate of the resulting hydrogen at 325 K.[35] The decomposition products detected by thermal desorption spectrometry (TDS) are H_2 and HCN, with no influence of coverage on the reaction pathway. All adsorbed species were observed to desorb by 500 K. The main desorption peaks for the decomposition products of melamine on

Pd{111} are observed at T_{max} ~ 570/580 K for masses 12 and 27, assigned as C and HCN, respectively. The intensities of these desorption peaks increases for higher exposure of melamine. The mass 12 peak would be due to carbon fragmenting from a higher mass decomposition product, possibly HCN or co-adsorbed CO.

It is proposed that the two surface bound amine groups of melamine are partially dehydrogenated upon adsorption. This was found to be the case for melamine adsorption on Ni{111},[12] in which DFT calculations were performed of partially dehydrogenated melamine (i.e., a melamine species which had undergone partial dissociation of two amine functionalities to yield –NH moieties) adsorbed in an upright orientation on a Ni{111} slab. The dehydrogenated structure was found to be significantly more stable than the fully hydrogenated melamine.

In order to interpret the shape of the features observed in STM, DFT calculations were carried out (Gaussian 03, 6-31G*, B3LYP) of the highest occupied molecular orbital (HOMO) and lowest occupied molecular orbital (LUMO) for isolated melamine. Figure 4.7 a) shows the chemical structure of melamine; the numerical labels adjacent to the carbon and nitrogen atoms are referred to in Table 4.1 in order to aid the assignment of the molecular vibrations. Figure 4.7 b) shows each orbital viewed perpendicular and parallel to the plane of the aromatic ring. [Note: Figure 4.7 is the same as Figure 3.8, used in Chapter – Part 1]. Though adsorption of melamine on Pd{111} will undoubtedly alter the appearance of the HOMO and LUMO via coupling with the Pd d-band, the orbital appearance should still be comparable to the shape of the adsorbed molecules in the STM images. Under the imaging conditions used (i.e., tip biased negatively), one would anticipate that the imaged molecule may resemble the LUMO in appearance,

with electrons being transferred from filled tip states to empty sample states. The cylindrical features observed in STM are consistent with the LUMO viewed parallel to the aromatic ring, implying that melamine adsorbs with the aromatic ring either perpendicular to the surface, or at least strongly tilted with respect to the surface.

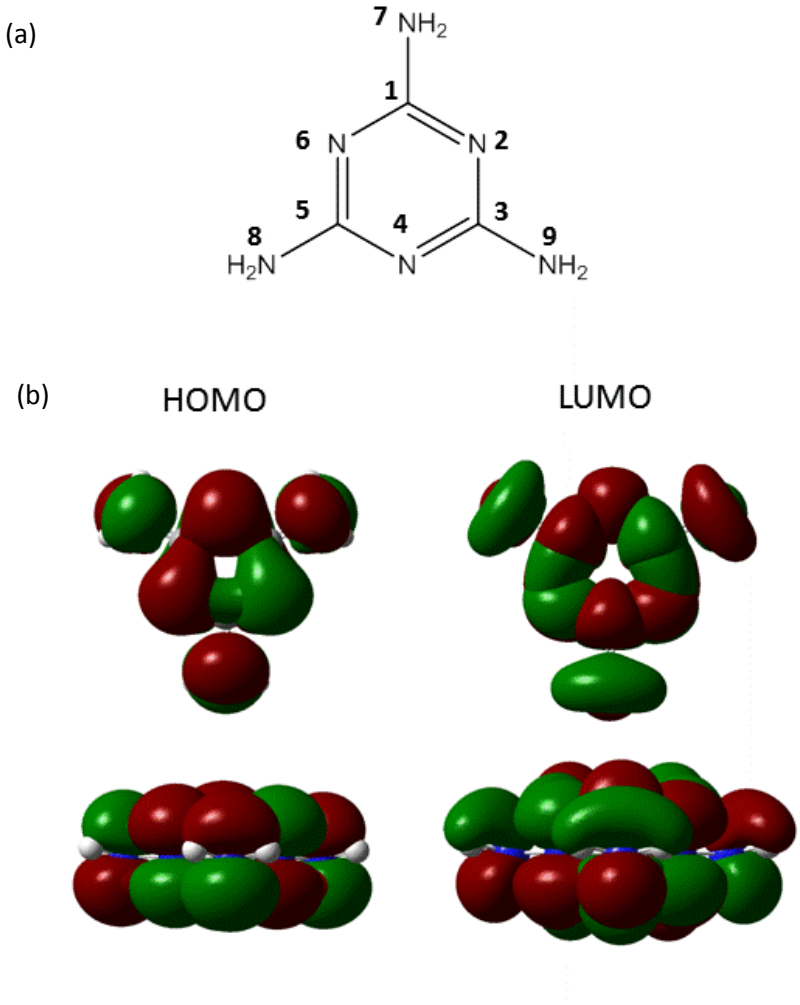

Figure 4.7: (a) Chemical structure of melamine with atom labels to aid explanation of vibrational assignments in Table 4.1 (b) HOMO and LUMO of melamine (Gaussian 03, density functional theory using the B3YLP functional with 6-31G* basis set), showing the front-on view to the left and top-down view to the right for the respective molecular orbitals. Note: The same Figure has been used in Chapter 3 – Part 1.

The RAIR spectra correlates to a good extent with that of gas-phase melamine,[36] which can be used to assist with assigning the vibrational frequencies. In Table 4.1, the IR vibrational frequencies for melamine on Pd{111} and assignments are listed, along with those of the melamine on Ni{111} IR peaks for comparison and the gas-phase melamine for the corresponding frequencies.

Table 4.1: Vibrational frequencies and assignments for Melamine on Pd{111}

Melamine/Pd {111}	Melamine/Ni {111} [12]	Melamine/gas-phase [36]	Vibrational mode assignments
$\upsilon(cm^{-1})$	$\upsilon(cm^{-1})$	$\upsilon(cm^{-1})$	
		3571 m	$\upsilon\ NH_2^{asym}$
	3442 w	3453 m	$\upsilon\ NH_2^{sym}$
1606 vs	1612 vs	1598 vs	$\beta\ NH_2^{sym}$, $\upsilon\ C_{(1)}N_{(7)}$, aromatic ring breathing
1562 s	1593 s		$\beta\ NH_2^{sym}$, $(\upsilon C_{(5)}N_{(6)}, \upsilon C_{(3)}N_{(2)})^{sym}$
1551 m	1560 m	1556 m	$\upsilon C_{(1)}N_{(2)}$, $\upsilon C_{(5)}N_{(4)}$
1471 m	1477 m	1440 s	ring breathing, $\upsilon N_{(7)}C_{(1)}$
	1458 w		In plane aromatic ring stretch
1394 s	1402 s		$(\upsilon C_{(5)}\ N_{(6)}, \upsilon C_{(3)}\ N_{(2)})^{asym}$
	1240 w		$\beta N_{(8)}H$, $\beta N_{(9)}H$

Notation of symbols used: υ- stretch, β- bend. Abbreviations: vs- very strong, s- strong, m-medium, w- weak, sym- symmetrical, asym- asymmetrical.

At saturation coverage, the spectrum of melamine on Pd{111} is dominated by a very intense set of peaks at 1606 and 1562 cm^{-1}. The peak observed at 1606 cm^{-1} is a close correlation with the peak at 1612 cm^{-1} for melamine on Ni{111}.[12] There is also a strong peak observed at 1593 cm^{-1} on Ni{111}, which probably corresponds to the observed peak at 1562 cm^{-1} for the Pd system; however, this peak is offset to a greater extent to the corresponding Ni peak than for the peak at 1606 cm^{-1} is to the Ni peak at 1612 cm^{-1}. There are also three weaker peaks observed at 1551, 1471 and 1394 cm^{-1}

for saturation coverage, which also correlate closely to observed peaks for the Ni system at 1560, 1477 and 1402 cm^{-1}, respectively.

In Chapter 3 – Part 1, the aforementioned vibrational peaks for melamine adsorption on Ni{111} were assigned as follows: 1612 cm^{-1} (vs) - β NH_2^{sym}, υ $C_{(1)}N_{(7)}$, aromatic ring breathing; 1593 cm^{-1} (s) - β NH_2^{sym}, ($υC_{(5)}N_{(6)}$, $υC_{(3)}N_{(2)}$)^{sym}; 1560 cm^{-1} (m) - $υC_{(1)}N_{(2)}$, $υC_{(5)}N_{(4)}$; 1477 cm^{-1} (s) - ring breathing, $υN_{(7)}C_{(1)}$; 1394 cm^{-1} (s) - ($υC_{(5)}$ $N_{(6)}$, $υC_{(3)}$ $N_{(2)}$)^{asym}. The stated atom numbers are the same as those used for the chemical structure of melamine in Figure 4.7 a).

Due to the fact that melamine is adsorbed in a tilted orientation on both Ni and Pd{111}, and that both substrates are chemically similar, it is believed that the vibrational modes for the absorption peaks of melamine adsorbed on Pd{111} are the same as those for the stated corresponding peaks of melamine on Ni{111}. All of the vibrational modes for melamine adsorbed on Pd{111} have been characterised in Table 4.1. In the study of melamine adsorption on Ni{111}, the investigation by McNutt et al.,[37] of adenine adsorption on Cu{110} was referred. There are strong chemical analogies between melamine and adenine on account of the upright amino group and surface bound diazine ring via a nitrogen atom; therefore, the comparison with adenine adsorption on Cu{110} is still valid for the melamine/Pd system. As shown in Table 4.1, the vibrational frequencies in the melamine/Ni study and this present study are in good agreement with those of a gas-phase melamine investigation.[36]

There are, however, significant differences between the two sets of spectra for melamine adsorbed on Ni and Pd{111}. As has already been mentioned, the vibrational frequency offset between the two peaks at 1606 and 1562 cm^{-1} (difference of 44 cm^{-1})

is much greater than for the corresponding peaks of the melamine/Ni system (difference of 19 cm^{-1}). The differences can be rationalised in terms of intermolecular hydrogen bonding interactions between the upright amino groups. This would result in a greater level of tilting towards the surface, increasing the level of interaction between the aromatic ring π orbitals and the Pd substrate. Consequently, the aromatic ring bonds would be weaker due to electron donation into antibonding orbitals, accounting for the shift in vibrational frequencies to lower values. The aromatic ring bond stretches should be affected to a greater extent by the aromatic ring tilting, as opposed to the amino group not interacting with the surface; since the aromatic ring is fully conjugated and bound directly to the substrate via the triazine nitrogen atom. Therefore, an explanation for the higher frequency offset for the aforementioned set of peaks at 1562 and 1593 cm^{-1} could be on account of the greater aromatic ring contribution to the vibrational mode relative to that for the set of peaks at 1606 and 1612 cm^{-1}; which have a greater contribution from the β NH_2^{sym}, υ $C_{(1)}N_{(7)}$ vibrational modes, and are less affected by substrate electronic variations. It is noted that no N-H stretching mode band is observed, as opposed to the study on Ni{111}. This band is intrinsically very weak and if H-bonding is occurring this would act to broaden the band, thereby making it less observable. The reason for this is because there is a superposition of absorption bands due to several different hydrogen bonded species or due to frequency modulation.[37]

The EELS spectra of pyridine adsorbed on Pd{111} at 310 K provides a useful comparison to that of the vibrational spectra of melamine on Pd{111}. Loss peaks, amongst others, were observed in the specular direction at 1340 (w), 1460 (m), and

1570 cm^{-1} (vw); these were assigned as: C-C ring stretch, C-C, C-N stretch, and C-C, C-N stretch, respectively; these values are in good agreement with the observed IR peaks at 1394 s, 1471 m, and 1562 s cm^{-1}, respectively. The stated mode numbers in the paper by Grassian and Muetterties for the loss peaks were taken from ref [38]. The close agreement with the pyridine and melamine vibrational frequencies confirms a tilted adsorption orientation for melamine via donation of electron density through an aromatic ring nitrogen atom, analogous to pyridine adsorption on Pd{111}.

Two pairs of bands are observed in the 1562-1606 and 1392-1471 cm^{-1} range. The relative intensities of each pair of bands are strongly coverage dependent. Similar behaviour was found for the analogous bands of melamine for the study on Ni{111}.[12] The same conclusion of the previous study can be applied in this case: There are two distinct melamine species, one that dominates at lower coverage and the second that dominates at higher coverage. At low coverage, the STM images are characterised by 1-D ordering, whereas at high coverage, the melamine structures are more compact. It is believed that the melamine species contained in the 1-D islands give rise to the bands at 1562 and 1477 cm^{-1}, whereas the melamine contained in the compact structures gives rise to the bands at 1606 and 1392 cm^{-1}.

There is an amino group pointing away from the surface containing a reactive nitrogen electron lone pair. This holds the potential for reaction in three dimensions. Buck et al.[39] have demonstrated depositing Pd nanoparticles on pyridine terminated self-assembled monolayers [40] adsorbed to a gold surface in ambient conditions for the purpose of creating 3-D structures. There is potential for combining this system with that of melamine adsorption on Pd. Alternatively, melamine can be used within the

SAMs to modify the structures as has been demonstrated previously with Cu deposition on SAMs.[16] It would be interesting to determine this procedure utilising Pd nanoparticles grown to functionalise the structures formed via the strong chemisorption interaction with melamine in SAMs.

4.6 Conclusions

Melamine adsorption on Pd{111}, at room temperature, occurs with the formation of 2-dimensional filament structures, which are in some cases curved. The molecule is adsorbed in a tilted orientation, via σ-donation to the surface from a triazine nitrogen atom and two amino group nitrogen atoms. At this stage it is unclear which adsorption site is adopted. It is believed that partial dehydrogenation of the two surface bound amine groups occurs, analogous to the behaviour of melamine adsorption on Ni{111}.

The main desorption peaks for the decomposition products of melamine are observed at T_{max} ~ 570/580 K for masses 12 and 27, assigned as C and HCN, respectively. The intensities of these desorption peaks increases for higher exposure of melamine. The hydrogen desorption peaks observed occur at a much higher temperature than would be expected for adsorbed hydrogen adatoms on the surface, resulting from the partial dehydrogenation of the melamine surface bound amino groups. The hydrogen peaks in this study are likely caused by deprotonation of organic decomposition products of melamine.

RAIRS data give strong signals for in-plane vibrational modes of melamine, suggesting a perpendicular, or close-to perpendicular, adsorption geometry to the surface plane at both low and high coverages. Two distinct surface species are detected with RAIRS.

These are assigned to melamine species in 1-D chains and high coverage 2-D domains. The bands associated with the latter species dominate the spectra at high coverage. There is no shift in the majority of vibrational frequencies for different coverages; hence, this would suggest there is no alteration to the adsorption geometry for varying melamine coverages. Low coverage melamine adsorption on Pd{111}, at room temperature, occurs with the formation of 1-D structures, which propagate along the <211> crystallographic directions. At higher coverage, the 1-D chains are still present, but the structures formed are more disordered. This is in contrast to the high coverage of melamine on Ni{111}, in which the structures are linear, forming 2-D islands of chains. The difference in the high coverage structures formed on Pd and Ni{111} is on account of the variation in the atomic distances. The greater mismatch in spacing between the Pd surface atoms and the interacting nitrogen atoms on melamine does not conform to melamine propagating in long linear chains, as witnessed on Ni{111}. This is manifested in the larger melamine intermolecular distances and the distance of closest approach of melamine chains measured in this study, as opposed to the study on Ni{111}.

4.7 References

[1] J.A. Theobald, N.S. Oxtoby, M.A. Phillips, N.R. Champness, P.H. Beton, Nature 424 (2003) 1029-1031.

[2] T. Kudernac, S.B. Lei, J. Elemans, S. De Feyter, Chem. Soc. Rev. 38 (2009) 3505-3505.

[3] J.V. Barth, Annu. Rev. Phys. Chem. 58 (2007) 375-407.

[4] S. De Feyter, F.C. De Schryver, J. Phys. Chem. B 109 (2005) 4290-4302.

[5] S. De Feyter, A. Miura, S. Yao, Z. Chen, F. Wurthner, P. Jonkheijm, A. Schenning, E.W. Meijer, F.C. De Schryver, Nano Lett. 5 (2005) 77-81.

[6] S. Furukawa, K. Tahara, F.C. De Schryver, M. Van der Auweraer, Y. Tobe, S. De Feyter, Angew. Chem.-Int. Edit. 46 (2007) 2831-2834.

[7] M.C. Blum, E. Cavar, M. Pivetta, F. Patthey, W.D. Schneider, Angew. Chem.-Int. Edit. 44 (2005) 5334-5337.

[8] S. Stepanow, M. Lingenfelder, A. Dmitriev, H. Spillmann, E. Delvigne, N. Lin, X.B. Deng, C.Z. Cai, J.V. Barth, K. Kern, Nat. Mater. 3 (2004) 229-233.

[9] N. Lin, S. Stepanow, M. Ruben, J.V. Barth, Templates in Chemistry Iii, Springer-Verlag Berlin, Berlin, 2009, pp. 1-44.

[10] F. Silly, A.Q. Shaw, M.R. Castell, G.A.D. Briggs, M. Mura, N. Martsinovich, L. Kantorovich, J. Phys. Chem. C 112 (2008) 11476-11480.

[11] C.H. Schmitz, J. Ikonomov, M. Sokolowski, Surface Science 605 (2011) 1-6.

[12] J. Greenwood, H.A. Fruchtl, C.J. Baddeley, J. Phys. Chem. C 116 (2012) 6685-6690.

[13] H.M. Zhang, Z.X. Xie, L.S. Long, H.P. Zhong, W. Zhao, B.W. Mao, X. Xu, L.S. Zheng, J. Phys. Chem. C 112 (2008) 4209-4218.

[14] H.M. Zhang, Z.K. Pei, Z.X. Xie, L.S. Long, B.W. Mao, X. Xu, L.S. Zheng, J. Phys. Chem. C 113 (2009) 13940-13946.

[15] J.C. Swarbrick, B.L. Rogers, N.R. Champness, P.H. Beton, J. Phys. Chem. B 110 (2006) 6110-6114.

[16] R. Madueno, M.T. Raisanen, C. Silien, M. Buck, Nature 454 (2008) 618-621.

[17] L.M.A. Perdigao, E.W. Perkins, J. Ma, P.A. Staniec, B.L. Rogers, N.R. Champness, P.H. Beton, J. Phys. Chem. B 110 (2006) 12539-12542.

[18] D.L. Keeling, N.S. Oxtoby, C. Wilson, M.J. Humphry, N.R. Champness, P.H. Beton, Nano Letters 3 (2003) 9-12.

[19] J.A. Gardener, O.Y. Shvarova, G.A.D. Briggs, M.R. Castell, J. Phys. Chem. C 114 (2010) 5859-5866.

[20] S. Jensen, H. Fruchtl, C.J. Baddeley, J. Am. Chem. Soc. 131 (2009) 16706-16713.

[21] S. Jensen, J. Greenwood, H.A. Fruchtl, C.J. Baddeley, J. Phys. Chem. C 115 (2011) 8630-8636.

[22] M. Studer, H.U. Blaser, C. Exner, Adv. Synth. Catal. 345 (2003) 45-65.

[23] W.R. Huck, T. Mallat, A. Baiker, Catal. Lett. 87 (2003) 241-247.

[24] W.R. Huck, T. Burgi, T. Mallat, A. Baiker, J. Catal. 219 (2003) 41-51.

[25] I. Horcas, R. Fernandez, J.M. Gomez-Rodriguez, J. Colchero, J. Gomez-Herrero, A.M. Baro, Rev. Sci. Instrum. 78 (2007).

[26] M.J. Frisch, G.W. Trucks, H.B. Schlegel, G.E. Scuseria, M.A. Robb, J.R. Cheeseman, J.A. Montgomery, Jr., T. Vreven, K.N. Kudin, J.C. Burant, J.M. Millam, S.S. Iyengar, J. Tomasi, V. Barone, B. Mennucci, M. Cossi, G. Scalmani, N. Rega, G.A. Petersson, H. Nakatsuji, M. Hada, M. Ehara, K. Toyota, R. Fukuda, J. Hasegawa, M. Ishida, T. Nakajima, Y. Honda, O. Kitao, H. Nakai, M. Klene, X. Li, J.E. Knox, H.P. Hratchian, J.B. Cross, V. Bakken, C. Adamo, J. Jaramillo, R. Gomperts, R.E. Stratmann, O. Yazyev, A.J. Austin, R. Cammi, C. Pomelli, J.W. Ochterski, P.Y. Ayala, K. Morokuma, G.A. Voth, P. Salvador, J.J. Dannenberg, V.G. Zakrzewski, S. Dapprich, A.D. Daniels, M.C. Strain, O. Farkas, D.K. Malick, A.D. Rabuck, K. Raghavachari, J.B. Foresman, J.V. Ortiz, Q. Cui, A.G. Baboul, S.

Clifford, J. Cioslowski, B.B. Stefanov, G. Liu, A. Liashenko, P. Piskorz, I. Komaromi, R.L. Martin, D.J. Fox, T. Keith, M.A. Al-Laham, C.Y. Peng, A. Nanayakkara, M. Challacombe, P.M.W. Gill, B. Johnson, W. Chen, M.W. Wong, C. Gonzalez, J.A. Pople, Gaussian 03, revision E.01; Gaussian, Inc.: Wallingford, CT (2004).

[27] J.M. Bonello, R. Lindsay, A.K. Santra, R.M. Lambert, J. Phys. Chem. B 106 (2002) 2672-2679.

[28] V.H. Grassian, E.L. Muetterties, J. Phys. Chem. 91 (1987) 389-396.

[29] F.P. Netzer, J.U. Mack, J. Chem. Phys. 79 (1983) 1017-1025.

[30] V.H. Grassian, E.L. Muetterties, J. Phys. Chem. 90 (1986) 5900-5907.

[31] S. Haq, D.A. King, J. Phys. Chem. 100 (1996) 16957-16965.

[32] F.A. Moller, J. Kintrup, A. Lachenwitzer, O.M. Magnussen, R.J. Behm, Phys. Rev. B 56 (1997) 12506-12518.

[33] Y.M. Savitskii, Hemisphere Publishing Corp (1989).

[34] C.J. Baddeley, C. Hardacre, R.M. Ormerod, R.M. Lambert, Surface Science 369 (1996) 1-8.

[35] J.J. Chen, N. Winograd, Surface Science 326 (1995) 285-300.

[36] Y.L. Wang, A.M. Mebel, C.J. Wu, Y.T. Chen, C.E. Lin, J.C. Jiang, J. Chem. Soc.-Faraday Trans. 93 (1997) 3445-3451.

[37] A. McNutt, S. Haq, R. Raval, Surface Science 531 (2003) 131-144.

[38] E.B. Wilson, *Phys. Rev* 45 (1934) 706.

[39] C. Silien, D. Lahaye, M. Caffio, R. Schaub, N.R. Champness, M. Buck, Langmuir 27 (2011) 2567-2574.

[40] S.N. Patole, C.J. Baddeley, D. O'Hagan, N.V. Richardson, F. Zerbetto, L.A. Zotti, G. Teobaldi, W.A. Hofer, The Journal of Chemical Physics 127 (2007) 024702-024702.

Chapter 4 - Part Two:

Co-deposition of Melamine and Terephthalaldehyde on Pd{111}

4-2.1 Abstract

The co-deposition of melamine and terephthalaldehyde has been investigated on Pd{111} in UHV by STM and RAIRS. Herein, it is shown that there is no reaction between these species to produce oligomers containing imine linkages. Deposition of terephthalaldehyde first results in a self-condensation reaction producing both disordered and ordered honeycomb networks of polyester species. The edges of the ordered networks are observed to align along the <-211> crystallographic directions.

RAIRS indicates that, at low exposure, the polymers are adsorbed near parallel to the surface; however, following higher exposure the polymers adopt a non-parallel orientation to the surface. The polymer species are believed to hinder the propagation of the melamine chains, described in Chapter 4 – Part 1. Similar behaviour was witnessed for the co-deposition of melamine and terephthalaldehyde on the Ni{111} surface, Chapter 3 – Part 2. RAIRS indicates there is no alteration to the terephthalaldehyde or melamine spectra when the species are adsorbed together, suggesting there is no reaction. Terephthalaldehyde is not observed to have any effect on the melamine structures when it is deposited after melamine is deposited first.

4-2.2 Introduction

The condensation reaction between amines and aldehydes holds promise as a means for producing large scale networks of imine polymers. Amines are suitable nucleophilic species on account of the relatively reactive electron lone pair on the nitrogen atom; and, aldehydes are ideal electrophilic species due to the relatively low steric hindrance at the carbonyl group. Amines are ubiquitous nucleophilic species for multicomponent covalent reactions. They have been used in the condensation reaction with aldehydes to form imines, in UHV[1, 2] and in ambient conditions.[3, 4]

In this section, scanning tunnelling microscopy (STM) and reflection absorption infrared spectroscopy (RAIRS) are used to investigate the attempted condensation reaction between melamine (1,3,5-triazine-2,4,6-triamine) and terephthalaldehyde (shown in Figure 4-2.1), in ultrahigh vacuum conditions.

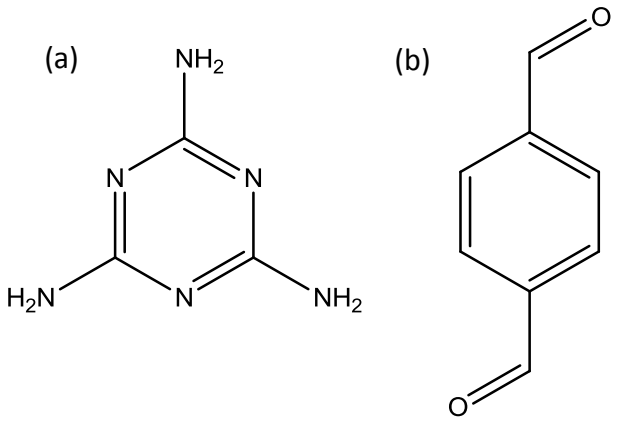

Figure 4-2.1: Chemical structures of: a) melamine, and b) terephthalaldehyde.

4-2.3 Experimental

STM experiments were carried out on an Omicron UHV system with a base pressure of 1 x 10^{-10} mbar. The Pd{111} sample was prepared by cycles of Ar ion bombardment (1.5 kV) and annealing to 893 K until low energy electron diffraction (LEED) and STM indicated the presence of a clean Pd{111} surface. Melamine (Sigma-Aldrich, 99.9 % purity) was deposited onto the Pd{111} surface, held at room temperature, from a glass doser resistively heated to 393 K, separated from the UHV chamber by a gate valve and differentially pumped by a turbomolecular pump. Terephthalaldehyde (Sigma Aldrich, 99% purity) was deposited onto the Pd{111} surface, held at room temperature, via a precision leak valve. Samples were transferred under UHV conditions to the STM chamber, where images were acquired at room temperature in constant current mode using an electrochemically etched W tip. STM images were processed using WSxM software.[5] RAIRS measurements were carried out using a Nicolet Nexus 860 FTIR spectrometer, fitted with a mercury cadmium telluride (MCT) detector cooled by liquid nitrogen and possessing a spectral range of 800-4000 cm^{-1}. The sample was placed in a UHV chamber, with a base pressure of 1 x 10^{-10} mbar, and the infrared beam (θ_i = 8°) from the spectrometer passed through KBr windows, reflected off the sample and into the detector. The spectrometer was operated with a resolution of 4cm^{-1}, at 256 scans per spectrum.

4-2.4 Results

4-2.4.1 Reflection Absorption Infrared Spectroscopy (RAIRS)

The RAIR spectra in Figure 4-2.2 a) were acquired following the adsorption of terephthalaldehyde on Pd{111} at 300 K as a function of increasing exposure. At low exposure, a single band is observed at ~ 1724 cm^{-1}. Upon increasing coverage, additional bands are observed at 1653 and 1255 cm^{-1}. The RAIR spectra in Figure 4-2.2 b) represents an aldehyde coverage followed by melamine exposure on Pd{111} at 300 K. After melamine deposition, bands are observed at 1608, 1551, 1454 and 1408 cm^{-1}. The aldehyde bands are unaltered at 1722 and 1254 cm^{-1}; however, the band at 1649 cm^{-1} is significantly larger after melamine adsorption.

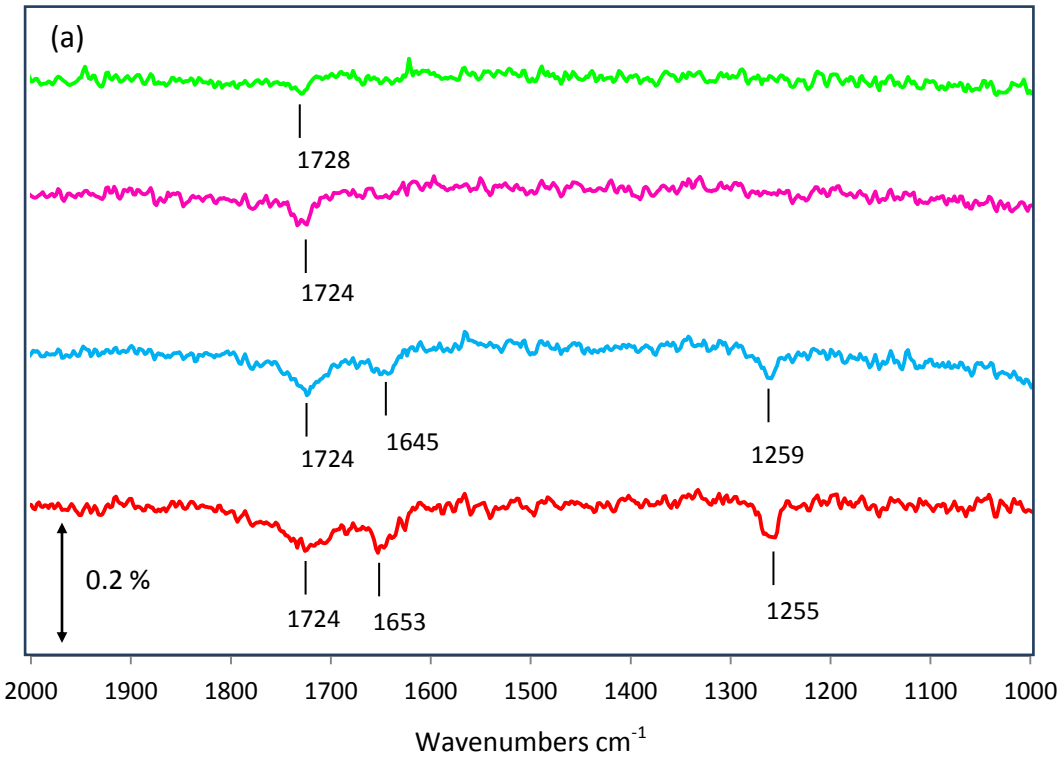

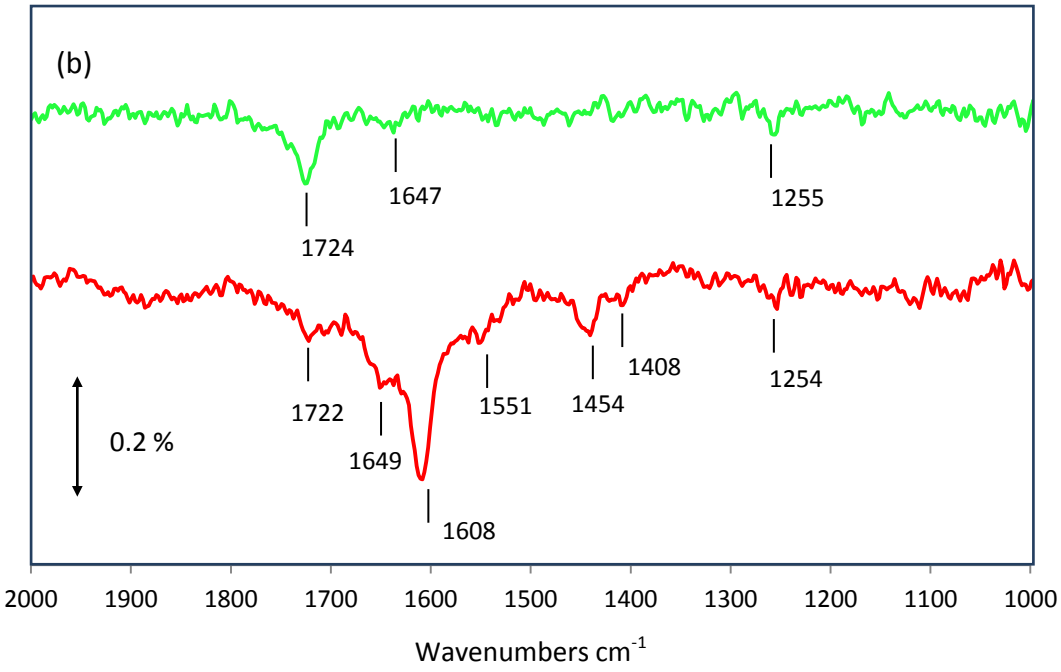

Figure 4-2.2: (a) RAIR spectra as a function of increasing exposure following terephthalaldehyde adsorption on Pd{111} at 300 K. The cumulative coverages are: Green (0.6 L), pink (1.2 L), blue (3 L), and red (4.8 L). (b) RAIR spectra of terephthalaldehyde adsorption on Pd{111} (green spectra, 1.2 L), followed by melamine deposition (red spectra, 0.18 L).

4-2.4.2 Scanning Tunnelling Microscopy (STM)

Figure 4-2.3 a) shows an STM image of the Pd{111} surface following exposure to 4.8 L terephthalaldehyde at 300 K. Polymer species of an irregular, curved shape are observed on the surface, alongside ordered networks of polymers. The ordered arrays extend across a few nanometres and consist of a porous, honeycomb structure. The unit cell of the ordered phase is measured to be ~ 9 x 9 Å, with an angle of 60°. The honeycomb arrays are arranged in either parallelogram or diamond shapes, with the edges aligned along the <-211> crystallographic directions. The image in Figure 4-2.3 b) shows a close-up view of the surface. A diamond shaped

array of the honeycomb phase has been highlighted by the yellow arrow. The STM image in Figure 4-2.3 c) has been highlighted by a yellow arrow, showing a chain of interlocked polymers. This appears to be at the initial stage of the formation of a honeycomb island. Bright clusters are observed on the terraces, of a similar contrast to the step edge features. No evidence of the unreacted dialdehyde species is observed on the surface.

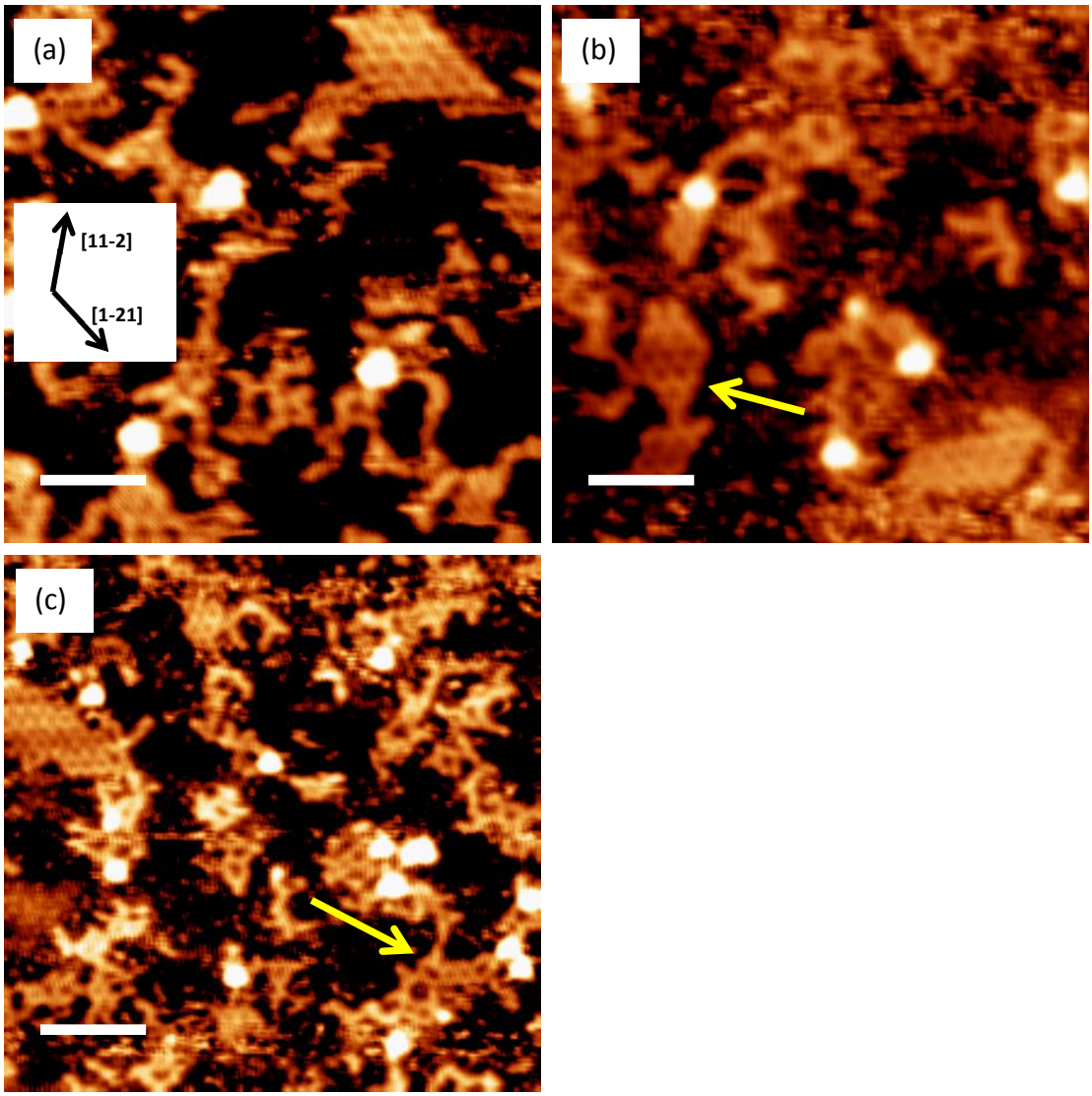

Figure 4-2.3: (a) STM image of terephthalaldehyde (4.8 L) on Pd{111} at 300 K (I = 0.08 nA, V = -0.65 V, scale bar = 3.8 nm), (b) close-up STM image (I = 0.25 nA, V = -0.8 V, scale bar = 4 nm), (c) STM image of different area showing 'horseshoe' and looped polymers, alongside an ordered polymer network (I= 0.25 nA, V = -0.8 V, scale bar = 6.2 nm).

Figure 4-2.4 a) shows an STM image following deposition of terephthalaldehyde (1.2 L) prior to deposition of melamine (0.18 L). The image consists of circular, molecular features, arranged haphazardly. The molecular features are clustered together on the surface; however, a large proportion of the surface is not covered with the molecular features. Figure 4-2.4 b) shows the image after annealing to 380 K. The molecular features are spread across the surface to a greater extent. The resolution of the molecular features is higher relative to those in Figure 4-2.4 a). Further annealing of the sample to 436 K is shown in the STM image in Figure 4-2.4 c). The molecular features are still present on the surface and remain clustered together. Molecular resolution is higher once again, with the molecular features appearing very clear, and of a uniform contrast.

When melamine is deposited prior to terephthalaldehyde, 1-D chains of melamine molecular species are observed to align along the <-211> crystallographic directions, together with disordered melamine structures, as observed previously for melamine adsorption on Pd{111}, shown in Figure 4-2.4 d) for comparison. Terephthalaldehyde is not observed to have any effect on the melamine structures when it is deposited after melamine is deposited first.

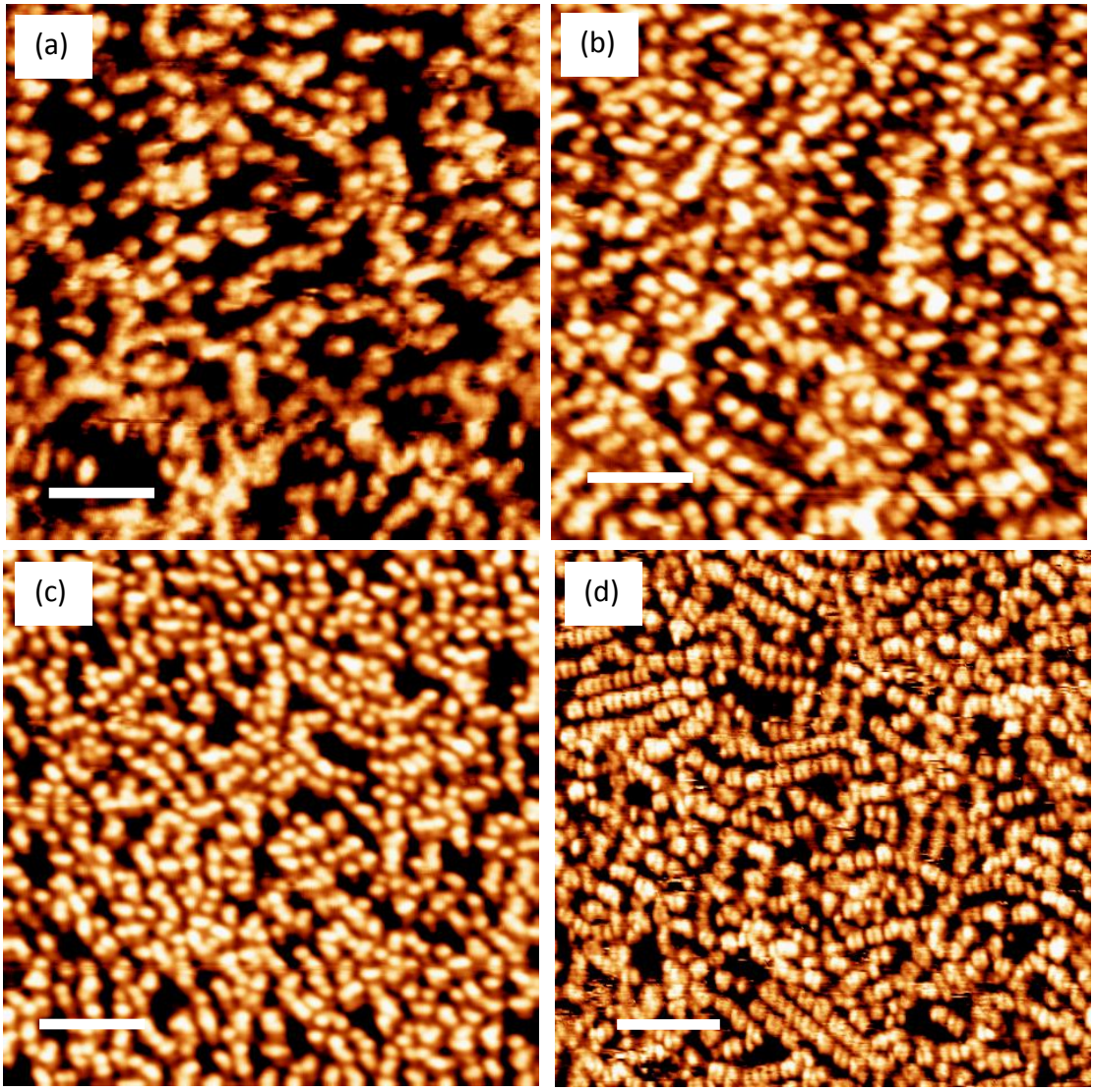

Figure 4-2.4: (a) STM image of terephthalaldehyde (1.2 L) and melamine (0.18 L) on Pd{111} at 300 K (I = 0.5 nA, V = -0.7 V, scale bar = 4.8 nm), (b) annealed to 380 K (I = 0.3 nA, V = -1.2 V, scale bar = 4.8 nm), (c) annealed to 436 K (I = 0.2 nA, V = -0.9 V, scale bar = 5.7 nm), (d) STM image of melamine, ~ 0.16 L, adsorbed on Pd{111} at 300 K, shown as comparison (scale bar 6.6 nm; 1.5 V, 0.3 nA).

4-2.5 Discussion

The RAIR spectra show bands at ~ 1724 and 1653 cm^{-1}, each corresponding to a carbonyl group stretching mode. The band intensities increase slightly going from low to higher coverage of aldehyde. The band at 1255 cm^{-1} is in the same region as would be expected for a C-O stretching mode for aryl conjugated esters.[6] The most

likely product from the self-polymerisation of terephthalaldehyde is an ester species.[7] Should the molecule lie close to flat on the surface then the C-O band would not be detected by RAIRS.

The ordered structures contain pore dimensions which are too small to be consisted of circular, fully interconnected oligomers. Also, the terephthalaldehyde species has only two aldehyde functional groups available for self-polymerisation; this precludes the possibility that the ordered structures are fully covalently linked in 2-dimensions. Consequently, the ordered structures must consist of 1-dimensional linear oligomer species, interconnected by H-bonding and van der Waals interactions. Similar behaviour has been observed for oligourea chains on Au{111},[8] which will be discussed in Chapter 6. The polyester chains must be commensurate with the Pd{111} surface to some degree to account for the edges of the ordered networks aligning along the <-211> directions.

The oligomer structure is determined primarily by the configuration about the ester bond. The two ester linkages at either side of the phenyl ring can be oriented in the same (termed *trans*) or in opposite (termed *cis*) directions. In addition, there is the possibility for each phenyl ring to contain the following: two ester linkages, an ester linkage and a methylene unit, or two methylene units. For the oligomers produced by the reaction of three terephthalaldehyde species, there are sixteen possible configurations of the ester linkages, with six shown in Figures 4-2.5 a) – f). It is noted that only structures are considered where the aromatic ring is parallel to the surface as this is likely to involve a strong metal-molecule interaction. Figure 4-2.5 g) shows the same ester configuration on the central phenyl ring as Figure 4-2.5 d), with the

terminal phenyl rings in close proximity to the carbonyl groups of the ester linkages. This configuration and analogous configurations are likely to be sterically unfavourable, hence can be ruled out as possible structures. Consequently, configurations with ester linkages in the *cis* position, Figures 4-2.5 d) – f), would have a deeper curve structure than those with the ester linkages in the *trans* position, Figures 4-2.5 a) – c). The repeat distances of the curves is represented by the red arrows in Figures 4-2.5 a) and d), for each of the *trans* and *cis* structures, measured as ~9 and ~14 Å, respectively. The former value is comparable to the measured repeat distance of ~9 Å. Therefore, it can be concluded that the oligomer ester linkages adopt the *trans* configuration. A structure of the possible arrangement of the polymer chains is shown in Figure 4-2.6. It is noted that the structure shown is not a fully accurate representation since it does not take into account any rotation about the methylene carbon atoms, or any possible tilted orientation of the polymers. The preferential ester oligomer configurations are subject to on-going DFT calculations by Dr H. A. Früchtl.

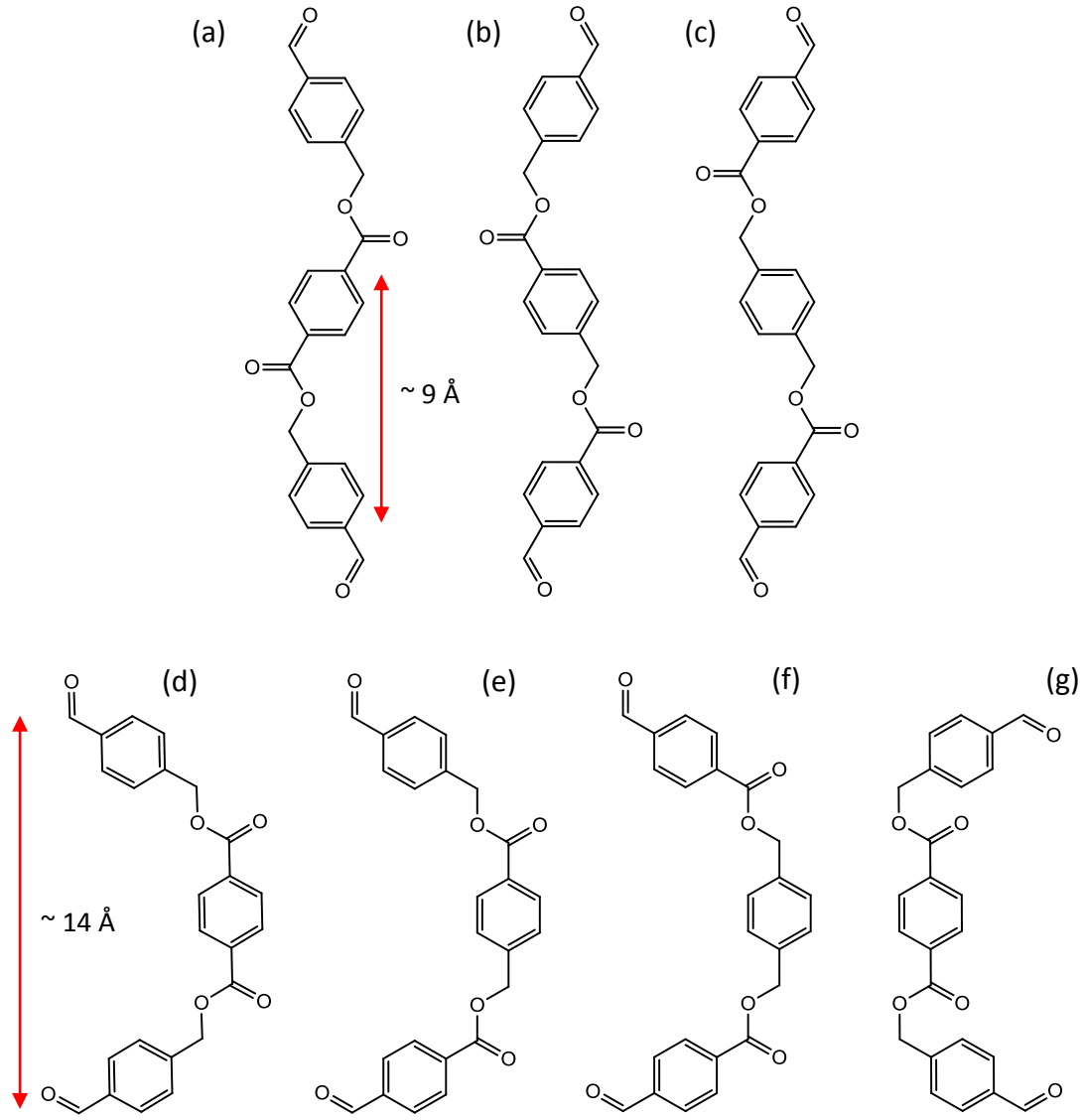

Figure 4-2.5: Chemical structures of likely oligomer structures resulting from the reaction of three dialdehyde species. Ester linkages in the *trans* configuration with the central phenyl ring containing: (a) two ester linkages (b) an ester linkage and a methylene unit (c) two methylene units. Ester linkages in the *cis* configuration with the central phenyl ring containing: (d) two ester linkages (e) an ester linkage and a methylene unit (f) two methylene units. (g) Ester oligomer with the terminal phenyl rings in close proximity to the carbonyl groups of the ester linkages, demonstrating the steric hindrance of such a configuration.

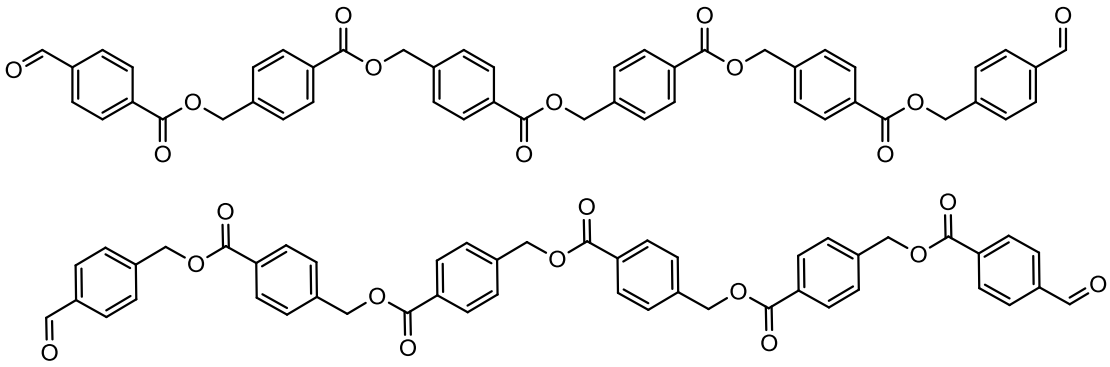

Figure 4-2.6: 2-D representation of the proposed chemical structures of the polyester molecules, resulting from the self-condensation reaction of terephthalaldehyde.

RAIRS data in Figure 4-2.2 b) indicate no alteration to the terephthalaldehyde absorption band when melamine is deposited on the Pd{111} surface after terephthalaldehyde exposure. The melamine absorption bands are analogous to those observed for high coverage melamine exposure on Pd{111}, as discussed in Chapter 4 - Part 1. This observation leads to the conclusion that there is no reaction between melamine and terephthalaldehyde on Pd{111} at room temperature for the conditions used.

The STM images for the deposition of terephthalaldehyde on Pd{111} indicate self-polymerisation occurs on the surface. Deposition of aldehydes and ketones on platinum group metals has resulted in polymerisation in previous studies.[8-11]

The formation of the ordered polymer networks resulting from terephthalaldehyde adsorption on Pd{111} was not observed on Ni{111}, described in Chapter 3 – Part 2. For both the Ni and Pd substrates, it is believed that ester polymers result from the self – condensation reaction of terephthalaldehyde. On Ni{111}, polymers of an irregular shape and curved appearance are observed, measuring as long as 8 nm. In this study, polymers of an irregular shape are also observed; however, a large

proportion form ordered networks. It is noted that the polymers on Pd{111} have a greater tendency to form circular and 'horseshoe' features than on Ni{111}.

Lambert et al. observed the self-polymerisation of methyl pyruvate on Pt{111} in the absence of $H_{2(g)}$.[11] The authors concluded that polymerisation occurs by hydrogen elimination from the methyl pyruvate monomer, followed by aldol condensation eliminating methanol. Attard et al. also studied self-condensation processes on Pt, observing dimeric and aldol intermediates from the self-condensation of ethyl pyruvate.[12] The Tishchenko reaction is well documented, using aluminium alkoxides to catalyse the dimerization of aldehydes bearing an α-hydrogen atom.[13, 14] However, it is unlikely that an aldol type reaction scheme can be applied to the reaction in this study. Terephthalaldehyde is a non-enolizable aldehyde since aromatic aldehydes have no available α-hydrogen atom. Typically, these aldehydes in solution with stoichiometric amounts of OH^- undergo disproportionation yielding alcohols and carboxylates (Cannizarro reaction).[15] Abaee et al.[16] reported on ester formation via Tishchenko reactions of aldehydes under LiBr catalysis. Crucially, aromatic aldehydes were successfully used in this reaction scheme. When the aldehyde reactants were mixed with LiBr and Et_3N under solvent-free conditions at room temperature, formation of dimeric esters of the starting substrates was observed in high yields. The authors proposed that the reaction proceeded under a 2:1 ratio of aldehyde to LiBr, in which the aldehyde species coordinated through the carbonyl oxygen atoms to the lithium ion. Such a reacting species is thought to form a six-membered transition state, facilitating 'intramolecular' hydride transfer between the two aldehyde molecules. The reaction conditions will inevitably be

different for solution based reactions and those on surfaces in UHV; however, it is believed that the reaction scheme put forward by Abaee et al.[16] is a close approximation to what is happening for ester formation in this study. In this case, the Pd substrate could act to form a transition state between multiple dialdehyde reactant species, facilitating hydride transfer and subsequent ester formation.

The deposition of methyl pyruvate has been studied on Pd{111} by Tysoe et al.[17] The authors observed a peak in the RAIR spectrum at ~ 1257 cm^{-1}, due to a ν (C-O) ester mode. They concluded that the methoxy group rotates out of the plane allowing the ester oxygen (C-O-CH_3) to coordinate to the surface. The two peaks observed at 1739 and 1705 cm^{-1} were assigned as free carbonyl and a carbonyl bonded to the surface, respectively. The data implied the molecule is bonded in a trans configuration with its plane perpendicular to the surface. The similarity between the results discussed and those in this study leads to the conclusion that an ester species is formed from the self-condensation reaction of terephthalaldehyde on Pd{111}. The bands observed at 1724, 1653 and 1255 cm^{-1} are assigned as free carbonyl, carbonyl bonded to the surface and an ester group stretching mode, respectively. For the stated bands observed in RAIRS, the ester species must adsorb with the molecular plane tilted to the surface.

At low coverage of the aldehyde reactant, only a single peak at 1724 cm^{-1} is observed. This is analogous to the observation of terephthalaldehyde adsorption on Ni{111}, discussed in Chapter 3 – Part 2. It was concluded that the ester polymers resulting from the self-condensation of terephthalaldehyde, following high exposure, are adsorbed near parallel to the Ni{111} surface. It is believed ester formation

occurs for low exposure in this study, in which the polymers are adsorbed near parallel to the surface. The peak at 1724 cm^{-1} is assigned as a carbonyl stretching mode.

The STM image in Figure 4 a) for melamine deposition on a Pd{111} surface at 300 K, pre-covered with terephthalaldehyde (0.34 L), indicate disruption to the growth of the melamine 1-D chains, as described in Chapter 4 – Part 1. The polymers resulting from terephthalaldehyde deposition are undoubtedly hindering the propagation of the melamine chains, resulting in the disorganised features observed. There is no observation of the ester polymers in the image. The poor resolution of the molecular features in the STM image in Figure 4-2.4 a) makes it difficult to discern the polymer feature from the melamine molecules. However, the bright features observed are of a brighter contrast than the polymers observed in Figure 4-2.3. This can be explained by the possible lower height profile of the polymers relative to melamine. As described previously, melamine adsorbs fully upright on the Pd surface via σ-donation to the surface from a triazine nitrogen atom and two amino group nitrogen atoms; whereas, if the ester polymers are adsorbed at a lower orientation to the surface, as suggested by the RAIRS signal, then they will not be imaged alongside melamine.

There is no evidence of covalent reaction between terephthalaldehyde and melamine on Pd{111}. As already discussed, the aldehyde reactant polymerises upon adsorption on Pd{111}, making it unavailable for further reaction. Also, the upright orientation of melamine renders it unreactive due to the interaction between the surface-bound amine groups and Pd substrate. When terephthalaldehyde is

deposited on the Pd surface pre-covered with melamine there is no evidence of reaction between the aldehyde and the melamine amine group pointing away from the surface. The melamine structures are unaltered, and there is no detectable height variations expected if reaction had occurred.

After annealing the sample to 373 K, shown in Figure 4-2.4 b), the spaces between the melamine clusters are observed to have decreased. Further annealing to 436 K, shown in Figure 4-2.4 c), shows the melamine features to be more resolved and spread out across the surface uniformly. In their study of methyl pyruvate polymerisation on Pt{111}, Lambert et al. performed temperature programmed reaction (TPR) studies[11]. The main desorption peaks of the decomposition fragments were for CO, H_2, and CO_2; desorbing at 440-470 K, ~ 360 K, and ~ 360 K, respectively. Unfortunately, no TPR studies were performed for the co-deposition of terephthalaldehyde and melamine. The TPR data of Lambert et al. provides a useful comparison to the likely desorption temperature of the polymer fragments in this study. Assuming there is negligible variation in the desorption temperature for the Pt and Pd{111} substrates, it can be proposed that the polymer structures have decomposed and mostly desorbed following annealing to 436 K.

4-2.6 Conclusions

STM data reveals a self-condensation reaction occurs following the adsorption of terephthalaldehyde on Pd{111} at 300 K, producing polymer species of an irregular shape, alongside ordered polymer honeycomb networks. The honeycomb networks are shaped as parallelograms or diamonds, with the edges aligned along the <-211> crystallographic directions. At low coverage, RAIR spectra show a single vibrational

band corresponding to a carbonyl group stretching mode. Following higher exposure, additional bands are observed corresponding to a carbonyl interacting with the surface and a C-O stretching mode. It is believed the polymers are ester species adsorbed in a tilted orientation to the surface. This is in contrast to the behaviour observed on Ni{111}, indicating a key chemical difference between the two substrates with regards to the interaction of the ester polymers with the surface.

When melamine is adsorbed on Pd{111} at 300 K pre-covered with terephthalaldehyde, a disorganised arrangement of melamine clusters are observed. This is different to melamine adsorbed on clean Pd{111}, in which 1-D chains of melamine molecular species align along the <-211> crystallographic directions. The polymer species are believed to hinder the propagation of the melamine chains. RAIRS indicates there is no alteration to the terephthalaldehyde or melamine spectra when the species are adsorbed together, suggesting there is no reaction. After annealing the sample to 373 K, the spaces between the melamine clusters are observed to have decreased. Further annealing to 436 K reveals the melamine features are more resolved, with the melamine structures spread across the surface uniformly. This is believed to be caused by the decomposition of the ester polymers and fragment desorption, allowing the melamine features to cluster together. Terephthalaldehyde is not observed to have any effect on the melamine structures when it is deposited after melamine is deposited first.

4-2.7 References

[1] S. Weigelt, C. Busse, C. Bombis, M.M. Knudsen, K.V. Gothelf, T. Strunskus, C. Woll, M. Dahlbom, B. Hammer, E. Laegsgaard, F. Besenbacher, T.R. Linderoth, Angew. Chem.-Int. Edit. 46 (2007) 9227-9230.

[2] S. Weigelt, C. Bombis, C. Busse, M.M. Knudsen, K.V. Gothelf, E. Laegsgaard, F. Besenbacher, T.R. Linderoth, ACS Nano 2 (2008) 651-660.

[3] Y. Li, J. Wan, K. Deng, X. Han, S. Lei, Y. Yang, Q. Zheng, Q. Zeng, C. Wang, The Journal of Physical Chemistry C 115 (2011) 6540-6544.

[4] R. Tanoue, R. Higuchi, N. Enoki, Y. Miyasato, S. Uemura, N. Kimizuka, A.Z. Stieg, J.K. Gimzewski, M. Kunitake, Acs Nano 5 (2011) 3923-3929.

[5] I. Horcas, R. Fernandez, J.M. Gomez-Rodriguez, J. Colchero, J. Gomez-Herrero, A.M. Baro, Rev. Sci. Instrum. 78 (2007) 013705.

[6] N.B.D. Colthup, L. H; Wiberly, S. B, Academic Press, New York 3rd Edition (1990).

[7] Y. Hoshimoto, M. Ohashi, S. Ogoshi, J. Am. Chem. Soc. 133 (2011) 4668-4671.

[8] R.J. Madix, T. Yamada, S.W. Johnson, Appl. Surf. Sci. 19 (1984) 43-58.

[9] M.A. Henderson, G.E. Mitchell, J.M. White, Surface Science 188 (1987) 206-218.

[10] M.A. Henderson, Y. Zhou, J.M. White, J. Am. Chem. Soc. 111 (1989) 1185-1193.

[11] J.M. Bonello, F.J. Williams, A.K. Santra, R.M. Lambert, J. Phys. Chem. B 104 (2000) 9696-9703.

[12] N.V. Rees, R.J. Taylor, Y.X. Jiang, I.R. Morgan, D.W. Knight, G.A. Attard, J. Phys. Chem. C 115 (2011) 1163-1170.

[13] W. Tishchenko, *Chem Zentralbl* 77 (1906) 1309 - 1311.

[14] W. Tishchenko, *Chem Zentralbl* 77 (1906) 1552 - 1555.

[15] A. Sorkau, K. Schwarzer, C. Wagner, E. Poetsch, D. Steinborn, J. Mol. Catal. A-Chem. 224 (2004) 105-109.

[16] M.M. Mojtahedi, E. Akbarzadeh, R. Sharifi, M.S. Abaee, Org. Lett. 9 (2007) 2791-2793.

[17] L. Burkholder, W.T. Tysoe, J. Phys. Chem. C 113 (2009) 15298-15306.

Chapter Five:

Formation of Imine Oligomers on Au under Ambient Conditions

5.1 Abstract

Scanning tunnelling microscopy has been used to investigate the nucleophilic substitution reaction between melamine (1,3,5-triazine-2,4,6-triamine) and terephthalaldehyde on Au/mica following deposition from solution in ambient conditions. The reaction is observed to proceed at room temperature over a timescale of days with the formation of imine oligomers intermixed with melamine islands on the Au surface. The oligomers ultimately self-assemble into a porous arrangement. The mechanism and extent of the surface confined reactions are discussed.

5.2 Introduction

The adsorption of organic precursor molecules for the fabrication of two-dimensional self-organising supramolecular structures has gained prominence over recent years. Numerous structures have been realised on a range of surfaces. Non-covalent

interactions have been utilised, including hydrogen bonding,[1-7] van der Waals interactions,[8, 9] and metal-organic coordination.[3, 10] The intermolecular interactions are relatively weak and the bonds formed are reversible. As such, the surface architectures produced possess a high 2-D order, with a relatively low density of structural defects due to the reversible nature of network growth. However, structures stabilised by the aforementioned intermolecular forces tend to have limited chemical and thermal stability, and, hence, are too weak for applications involving templating or catalysis.

There has been a growing realisation in recent years that the fabrication of covalently bonded surface architectures offers a route to structures with the required stability for practical applications. Amines are ubiquitous nucleophilic species for multicomponent covalent reactions. They have been used in the condensation reaction with aldehydes to form imines, in UHV[11, 12] and in ambient conditions.[13, 14] Amines have also been reacted with anhydrides,[15, 16] forming imides; as well as via the nucleophilic attack of acyl chlorides[17-19] and isocyanates,[20] forming amides and urea functionalities, respectively.

The condensation reaction between amines and aldehydes holds promise as a means for producing large scale networks of imine polymers. Amines are suitable nucleophilic species on account of the relatively reactive electron lone pair on the nitrogen atom; and, aldehydes are ideal electrophilic species due to the relatively low steric hindrance at the carbonyl group. Unlike in nucleophilic substitution reactions resulting in a reactive leaving group which may corrode or poison the surface, e.g. acyl chloride substitution with amines producing a reactive chloride group,

condensation reactions result in a benign water molecule as the product in addition to the imine molecule.

In this Chapter, scanning tunnelling microscopy (STM) is used to investigate the condensation reaction between melamine (1,3,5-triazine-2,4,6-triamine) and terephthalaldehyde (shown in Scheme 5.1), in ambient conditions. Herein, it is shown that the reaction can proceed at room temperature to produce oligomers containing imine linkages.

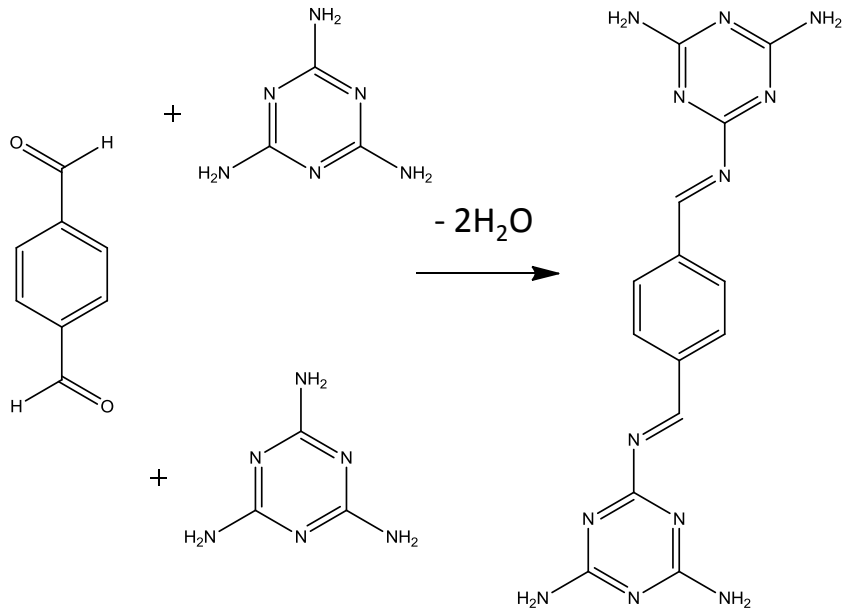

Scheme 5.1: Reaction scheme for the nucleophilic-substitution reaction between melamine and terephthalaldehyde to form an imine oligomer.

5.3 Experimental

300 nm Au films on mica were purchased from Georg Albert PVD. Samples of ~0.5 cm x 1 cm were annealed in a Bunsen flame. Solutions of melamine, 3 mM, (Sigma Aldrich, 99.9%) and terephthalaldehyde, 0.1 mM, (Sigma Aldrich, 99%) in dimethylformamide (DMF) solvent were mixed in a vial and diluted 1:4 in DMF. The

Au sample was introduced to the solution at 300 K for 3 minutes. Prior to STM imaging, the sample was dried in a stream of nitrogen gas. STM data were acquired with a Molecular Imaging Pico STM using Pt/Ir tips (70% Pt: 30% Ir). STM images were processed using WSxM software.[21]

5.4 Results and Discussion

Control experiments were performed to separately investigate the deposition of the reactants terephthalaldehyde and melamine on Au/mica. In the case of terephthalaldehyde, no molecular ordering was observed nor were any disordered molecular features; it is believed this is due to the reactant being too mobile at room temperature to be imaged. Following deposition of melamine at 300 K, domains of the hexagonal melamine phase can clearly be identified on the Au surface. Under conditions of good resolution, each melamine molecule is typically observed as a single triangular feature due to the aromatic ring being parallel to the surface and the shape of the melamine frontier orbitals.[22] In the hexagonal phase, the aromatic rings form the points of a hexagon; each melamine is connected to a neighbouring melamine species via two NH---N hydrogen bonds along the side of the hexagon.[23]

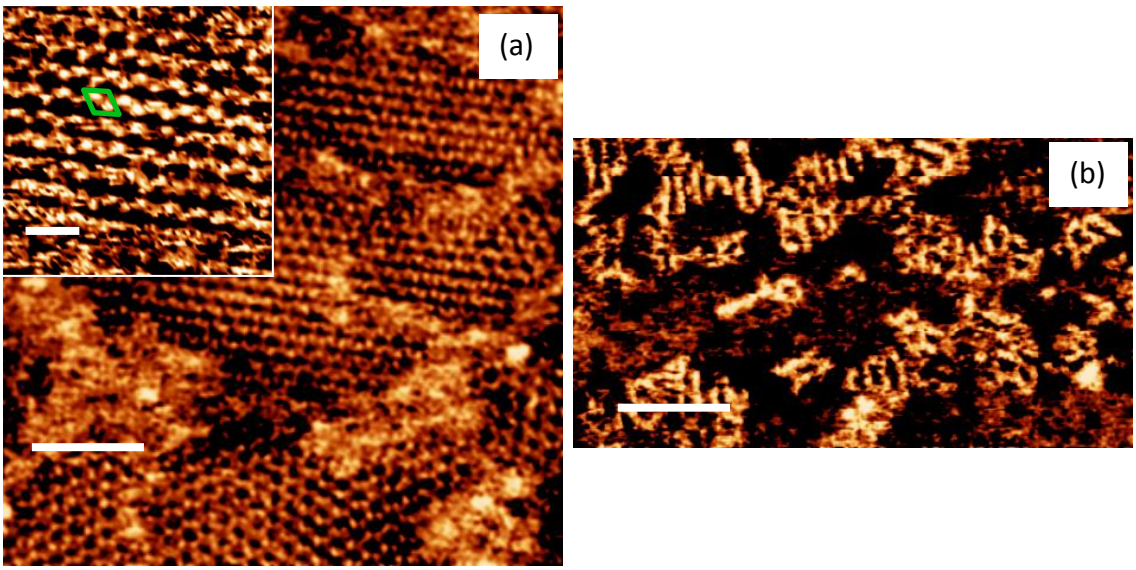

Figure 5.1: (a) STM image of melamine islands, on Au/mica, following co-deposition with terephthalaldehyde (I = 0.03 nA, V = 0.1 V, scale bar = 6.1 nm), the inset shows a close-up image of melamine molecules within an island (I = 0.03 nA, V = 0.1 V, scale bar = 1.8 nm). (b) STM image of imine oligomers in between melamine islands (I = 0.09 nA, V = 0.1 V, scale bar = 6.4 nm).

Over the course of the first 48 hours after sample preparation, there is a gradual change in the appearance of the molecular features in the STM images. The surface coverage of oligomeric features is observed to increase, while the fraction of the surface covered by melamine islands decreases. STM images for the sample within the first few hours of co-deposition of terephthalaldehyde and melamine are shown in Figure 5.1. Hexagonal domains of melamine are clearly visible in Figure 5.1 a), with the inset showing a close-up view, unit cell illustrated in green. The centre to centre separation of adjacent pores surrounded by hexagonal arrangements of melamine is measured to be ~1 nm, which correlates well with previously measured dimensions of melamine on Au{111}.[7, 17] Bright features are observed at the perimeter of the melamine domains and in the space between the melamine islands. Imaging at a slightly higher tunnelling current reveals oligomer species of length between 1.4 and

2.5 nm in regions separating the melamine islands, see Figure 5.1 b). Oligomer formation is attributed to the nucleophilic attack by an amine group of melamine on an aldehyde functionality of terephthalaldehyde.

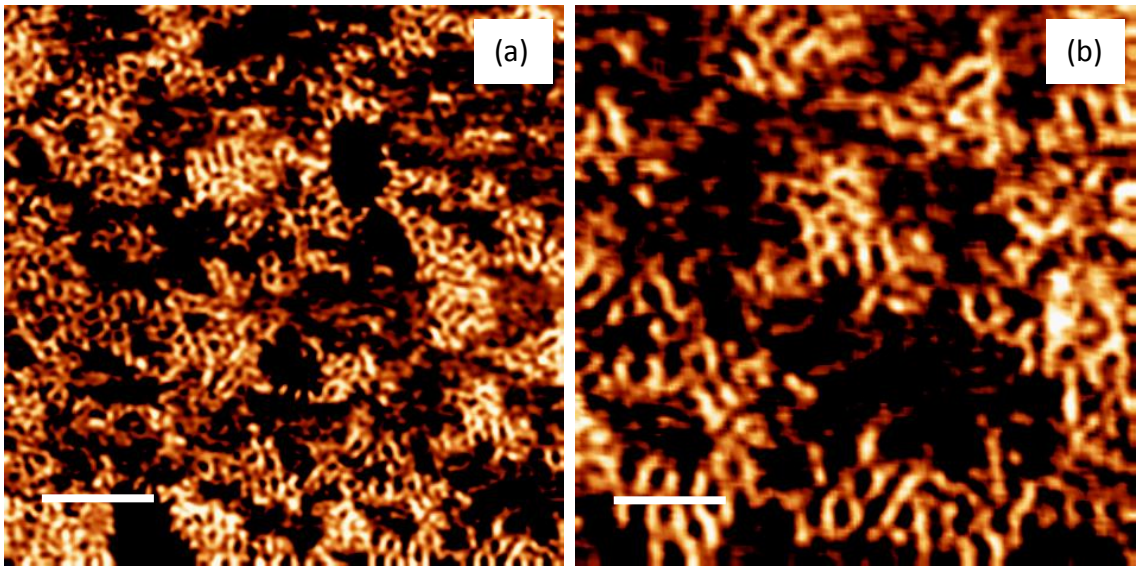

Figure 5.2: (a) STM image of imine oligomers, on Au/mica, ~24 hours after sample preparation (I = 0.15 nA, V = 0.1 V, scale bar= 7.8nm), (b) Close-up STM image of imine oligomers, on Au/mica, ~24 hours after sample preparation (I = 0.15 nA, V = 0.1 V, scale bar= 4nm).

Figure 5.2 a) shows an STM image of the Au on mica sample approximately 24 hours after sample preparation; the sample having been left under ambient conditions in the STM instrument. Figure 5.2 b) shows a close-up view of the sample. The proportion of oligomers has increased, while the number of melamine islands has decreased and the few islands remaining are smaller compared with those imaged in the first few hours after sample preparation.

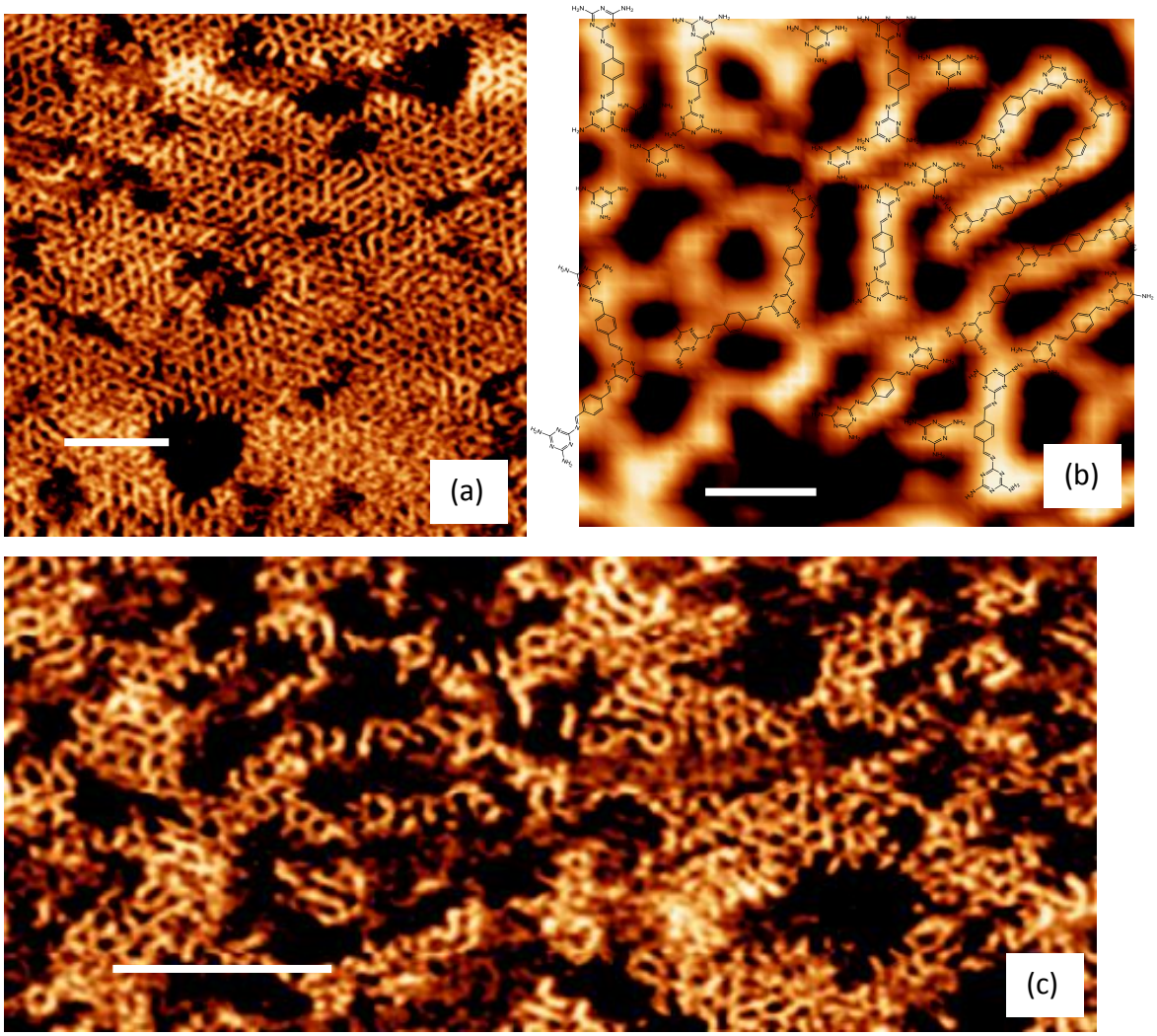

Figure 5.3: (a) STM image of imine oligomers, on Au/mica, approximately 48 hours after sample preparation (I = 0.15 nA, V = 0.1 V, scale bar = 7.3 nm). (b) A close-up image of the oligomer phase. The proposed imine and melamine molecular structures are overlaid on part of the image (I = 0.15 nA, V = 0.1 V, scale bar = 1.2 nm). (c) STM image of imine oligomers separated by regions of (presumably) bare Au surface (I = 0.12 nA, V = 0.1 V, scale bar = 9.5 nm).

Figure 5.3 a) shows STM images of the Au/mica surface approximately 48 hours after sample preparation. Now, the presence of oligomeric species is widespread across the surface, with no indication of the continued presence of melamine domains. The oligomeric features self-assemble to give a porous morphology with relatively uniform pore diameters typically measuring between 0.75 and 1 nm. The oligomeric

components are not of a uniform length, nor are the oligomer structures formed of a uniform topography. The most common features observed have a length of ~1.5 nm and, it is concluded, result from the reaction of the two aldehyde functionalities of terephthalaldehyde with melamine. The structure of the proposed di-imine oligomer is shown in Figure 5.4. The length of this oligomer is approximately 1.45 nm, in close agreement with the length of the features observed in STM. In addition, a smaller number of longer oligomeric features of ~2.5 nm are visible, consistent with the longer oligomeric species shown in Figure 5.4 which require the central melamine molecule to react at two of its three $–NH_2$ functionalities [NB: the length of the longer oligomeric features reported here corresponds to the shortest distance between the two ends of the feature]. The oligomer species coexist with smaller species which often appear with a lower contrast, measuring approximately 0.5 nm in diameter. These are believed to be unreacted melamine species incorporated within the oligomer phase. The presence of unreacted melamine is concluded for a number of reasons. Firstly, the size and appearance of these species is similar to that typically observed for melamine with STM and secondly, the relative position of such features with respect to adjacent oligomers is incompatible with the formation of a stable covalent bond.

The STM image in Figure 5.3 b) illustrates a possible arrangement of oligomers and unreacted melamine species superimposed on self-assembled oligomeric features. The surface is not entirely saturated with oligomer species, as can be seen in Figure 5.3 c), with some areas of bare surface detectable. In the experiments, the terephthalaldehyde concentration was kept constant at 0.1 mM and the

concentration of melamine varied. It was found that extensive oligomer formation was observed over a very narrow range of melamine concentration. At higher melamine concentrations, the surface became saturated with melamine and no reaction was observed, presumably because the adsorption of terephthalaldehyde is blocked. At melamine concentrations lower than 3 mM, no evidence was found for reaction. It can be concluded that a key requirement for surface-confined reaction is sub-monolayer coverage of melamine. Future experiments exploring the effects of terephthaldehyde concentration and adsorption temperature are clearly desirable.

A previous study by Jensen et al.[20] investigated the surface confined reaction between melamine and 1,4-phenylene diisocyanate (1,4-PDI) on Au{111}, in UHV conditions. The authors noted the formation of a range of ordered arrangements of oligomers as a function of annealing temperature. All oligourea species were believed to be terminated in partially reacted melamine units. In each case, ordering was believed to be controlled by intermolecular H-bonding interactions between adjacent terminal triazine moieties. In at least one of the ordered structures, unreacted melamine was found to co-exist with oligourea species. It is believed that similar intermolecular interactions are present in the 2-D structures produced in the current study. Given the greater reactivity of the aldehyde functionality in comparison to the amine functionality of melamine, it is very likely that the oligomers formed in this study are terminated with triazine moieties from reacted melamine. These subsequently self-assemble via intermolecular hydrogen bonding interactions through the unreacted amino groups. Any remaining unreacted melamine would readily be incorporated within these H-bonded structures. The STM

images show both linear and slightly curved, or branched oligomers of a similar length. Assigning the features in the STM images to absolute molecular structures is problematic particularly for the larger oligomers. Figure 5.4 shows some of the possible configurations of oligomers. The structure is determined primarily by the configuration about the newly formed C=N bond. For the oligomers produced by the reaction of one terephthaldehyde molecule with two melamine species, there are two reactively formed C=N bonds each of which can adopt two configurations giving a total of four configurations. Figures 5.4 a) and b) show the two distinguishable configurations of 'gas phase` oligomers. Adsorption of each of these oligomers could occur via either of two mirror equivalent footprints giving, in principle, a total of four distinguishable oligomeric features. Clearly for the larger oligomers formed by the reaction of three melamine molecules with two dialdehyde species, there are four reactively formed C=N bonds each with two possible orientations giving a total of sixteen subtly different molecular structures – some configurations of which are likely to be energetically preferred over others. Consequently, the overlay of oligomeric structures on the STM image of Figure 5.3 b) represents possible configurations of the longer oligomers but should not be taken as an identification of the absolute configuration of each oligomer.

There is no indication of triple branched oligomer structures formed from reaction at all three of the amino groups of a melamine molecule. Previous studies investigating surface confined reactions of melamine have indicated that, upon nucleophilic attack of two of the amino groups, the third amino group becomes deactivated due to withdrawal of electron density.[17, 24] Furthermore, it is found that there are very

few examples of oligomers containing more than two reacted dialdehyde moieties. However, it should be noted that the STM images are not of sufficient quality to distinguish longer branched oligomers from two triazine terminated oligomers connected via intermolecular H-bonds.

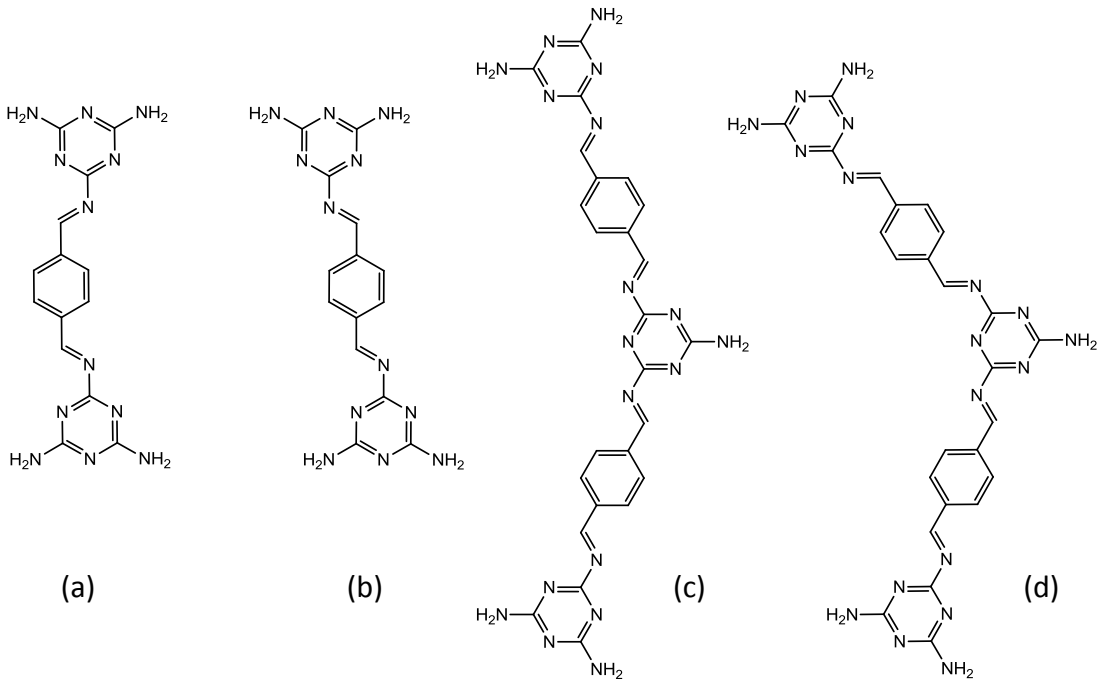

Figure 5.4: Chemical structures of likely oligomer structures resulting from the reaction of one dialdehyde species (a) and (b) and two dialdehyde species (c) and (d).

In previously studied UHV-based investigations of covalent reactions involving melamine on Au{111},[17, 24] melamine species at the centre of ordered domains are essentially inaccessible for reaction. The melamine molecules at the edges of the domain islands are the most weakly bound, forming H-bonds with two adjacent melamine molecules, rather than three as observed for melamine species in the middle of ordered islands. It is likely in the present study that reaction occurs at the island perimeters and that oligomeric species peel off the melamine domains to

allow further reaction with melamine to take place. The dialdehyde reactants must consequently be present on the surface in the space between the melamine islands. The distribution of oligomer lengths is likely to be determined by a combination of factors. Two of the most important factors are the decreased reactivity of melamine after reaction of one $–NH_2$ functionality. This restricts the ability of the di-imine oligomer from further reaction with a dialdehyde. Secondly, altering the stoichiometry of the two reactants may alter the distribution of oligomer lengths. The rate of oligomerisation and the formation of longer oligomers may be enhanced by annealing of the sample as has been the case for other systems studied,[16-18, 24] but annealing in the absence of the solvent is likely to also lead to desorption of reactants rather than oligomer formation. Nevertheless, annealing experiments on the system studied in this Chapter warrant investigation in future studies to determine the effect on the rate of reaction.

Linderoth et al. probed the surface confined reaction between an aldehyde and an amine in UHV conditions.[11] Imine formation from such reactants involves the formation of a hemiaminal tetrahedral intermediate, which, under solution phase conditions, is catalysed by the solvent, acting as a proton-donor/acceptor. Linderoth et al. used an aldehyde group with an adjacent hydroxyl group to act as an intramolecular proton-donor/acceptor for imine formation in the absence of a solvent catalyst. The reaction was observed to occur at room temperature, with all energy barriers of less than 1.17 eV for the reaction pathway.[11] It has been shown that without a proton-donor/acceptor species to catalyse imine formation, the resultant energy barrier is approximately 2.4 eV,[25] ruling out reaction at room

temperature. Despite the absence of an analogous adjacent hydroxyl group to the aldehyde group, the condensation reaction is found to proceed at room temperature in this study. Since the system was investigated in ambient conditions, a likely explanation for the relative ease of reaction is that atmospheric water vapour catalyses the rate limiting step of imine formation from the hemiaminal intermediate. The Au substrate may also contribute towards catalysing the reaction, as has been the case for octylamine coupling on Au{111}.[26]

Wang et al. have also investigated a condensation reaction between an aldehyde and an amine in ambient conditions.[13] The authors highlighted the possibility of the reaction occurring in the solution phase before deposition onto the highly oriented pyrolytic graphite (HOPG) surface, as opposed to a surface confined reaction. The authors also suggested the octanoic acid solvent acted as a catalyst for the rate limiting dehydration of the hemiaminal intermediate. In the present study, it can effectively be ruled out that the condensation reaction occurs in solution due to the length of time elapsed between deposition and formation of the oligomer phase, and the fact that the sample was removed from the solvent prior to imaging.

5.5 Conclusions

The surface-confined condensation reaction between melamine and terephthalaldehyde on Au/mica in ambient conditions has been achieved. Following co-deposition of the reactants at 300 K, ordered domains of pure melamine are observed. Oligomer species are observed to form in the spaces between melamine islands. Over the course of 48 hours after sample preparation, the melamine islands

gradually disappear and the surface becomes covered in self-assembled oligomers which are concluded to be terminated in monosubstituted melamine moieties which connect with neighbouring oligomers via H-bonding interactions. The networks are not ordered but contain pores with a relatively narrow distribution of pore diameters. Some oligomers containing three melamine species and two dialdehyde species are produced, but the formation of longer oligomers is restricted by the relatively low reactivity of monosubstituted melamine.

Note: The work presented in Chapter 5 has been published:

Greenwood, J.; Baddeley, C. J. Langmuir 2013, 29, 653-657. 'Formation of Imine Oligomers on Au under Ambient Conditions Investigated by STM'

5.6 References

[1] J.A. Theobald, N.S. Oxtoby, M.A. Phillips, N.R. Champness, P.H. Beton, Nature 424 (2003) 1029-1031.

[2] T. Kudernac, S. Lei, J.A.A.W. Elemans, S. De Feyter, Chemical Society Reviews 38 (2009) 402-421.

[3] J.V. Barth, Annu. Rev. Phys. Chem. 58 (2007) 375-407.

[4] S. De Feyter, F.C. De Schryver, J. Phys. Chem. B 109 (2005) 4290-4302.

[5] S. De Feyter, A. Miura, S. Yao, Z. Chen, F. Wurthner, P. Jonkheijm, A. Schenning, E.W. Meijer, F.C. De Schryver, Nano Lett. 5 (2005) 77-81.

[6] I. Cebula, C. Shen, M. Buck, Angewandte Chemie International Edition 49 (2010) 6220-6223.

[7] F. Silly, A.Q. Shaw, M.R. Castell, G.A.D. Briggs, M. Mura, N. Martsinovich, L. Kantorovich, J. Phys. Chem. C 112 (2008) 11476-11480.

[8] S. Furukawa, K. Tahara, F.C. De Schryver, M. Van der Auweraer, Y. Tobe, S. De Feyter, Angew. Chem.-Int. Edit. 46 (2007) 2831-2834.

[9] M.C. Blum, E. Cavar, M. Pivetta, F. Patthey, W.D. Schneider, Angew. Chem.-Int. Edit. 44 (2005) 5334-5337.

[10] S. Stepanow, M. Lingenfelder, A. Dmitriev, H. Spillmann, E. Delvigne, N. Lin, X.B. Deng, C.Z. Cai, J.V. Barth, K. Kern, Nat. Mater. 3 (2004) 229-233.

[11] S. Weigelt, C. Busse, C. Bombis, M.M. Knudsen, K.V. Gothelf, T. Strunskus, C. Woll, M. Dahlbom, B. Hammer, E. Laegsgaard, F. Besenbacher, T.R. Linderoth, Angew. Chem.-Int. Edit. 46 (2007) 9227-9230.

[12] S. Weigelt, C. Bombis, C. Busse, M.M. Knudsen, K.V. Gothelf, E. Laegsgaard, F. Besenbacher, T.R. Linderoth, ACS Nano 2 (2008) 651-660.

[13] Y. Li, J. Wan, K. Deng, X. Han, S. Lei, Y. Yang, Q. Zheng, Q. Zeng, C. Wang, The Journal of Physical Chemistry C 115 (2011) 6540-6544.

[14] R. Tanoue, R. Higuchi, N. Enoki, Y. Miyasato, S. Uemura, N. Kimizuka, A.Z. Stieg, J.K. Gimzewski, M. Kunitake, Acs Nano 5 (2011) 3923-3929.

[15] M. Treier, R. Fasel, N.R. Champness, S. Argent, N.V. Richardson, Phys. Chem. Chem. Phys. 11 (2009) 1209-1214.

[16] M. Treier, N.V. Richardson, R. Fasel, J. Am. Chem. Soc. 130 (2008) 14054-+.

[17] S. Jensen, J. Greenwood, H.A. Fruchtl, C.J. Baddeley, J. Phys. Chem. C 115 (2011) 8630-8636.

[18] C.H. Schmitz, J. Ikonomov, M. Sokolowski, The Journal of Physical Chemistry C 113 (2009) 11984-11987.

[19] C.H. Schmitz, M. Schmid, S. Gaertner, H.-P. Steinrueck, J.M. Gottfried, M. Sokolowski, Journal of Physical Chemistry C 115 (2011) 18186-18194.

[20] S. Jensen, H. Fruchtl, C.J. Baddeley, J. Am. Chem. Soc. 131 (2009) 16706-16713.

[21] I. Horcas, R. Fernandez, J.M. Gomez-Rodriguez, J. Colchero, J. Gomez-Herrero, A.M. Baro, Rev. Sci. Instrum. 78 (2007) 013705.

[22] V. Chis, G. Mile, R. Stiufiuc, N. Leopold, M. Oltean, J. Mol. Struct. 924-26 (2009) 47-53.

[23] L.M.A. Perdigao, E.W. Perkins, J. Ma, P.A. Staniec, B.L. Rogers, N.R. Champness, P.H. Beton, J. Phys. Chem. B 110 (2006) 12539-12542.

[24] S. Jensen, H. Früchtl, C.J. Baddeley, Journal of the American Chemical Society 131 (2009) 16706-16713.

[25] N.E. Hall, B.J. Smith, The Journal of Physical Chemistry A 102 (1998) 4930-4938.

[26] S. Weigelt, J. Schnadt, A.K. Tuxen, F. Masini, C. Bombis, C. Busse, C. Isvoranu, E. Ataman, E. Laegsgaard, F. Besenbacher, T.R. Linderoth, J. Am. Chem. Soc. 130 (2008) 5388-+.

Chapter Six:

Reaction of an Aliphatic Diamine with Aromatic Diisocyanates on Au{111}

6.1 Abstract

The surface-confined reaction of 1,4-diaminobutane with 1,3- and 1,4-phenylene diisocyanate on Au{111} was investigated by scanning tunnelling microscopy in ultrahigh vacuum. For both the meta and para diisocyanates, the nucleophilic addition reaction to form oligourea species occurred at, or slightly above, 300 K. Subsequent annealing allows oligomers to form extended ordered assemblies which density functional theory reveals are stabilised by intermolecular H-bonding interactions.

6.2 Introduction

Surface confined covalent assembly on metallic surfaces provides a means of preparing thermally stable 2-D molecular architectures with potential application in templating and catalysis. In recent years, much research has focused on the construction of surface confined covalent networks utilising a range of chemical reactions in ultrahigh vacuum (UHV)[1-22] and under ambient conditions via deposition from solution.[23-25] A key motivation of this thesis has been the fabrication of networks possessing well defined chemical functionality for potential use as docking sites for catalytic reagents. Previous work[12] has investigated the nucleophilic attack by melamine (an aromatic tri-amine) on 1,4-phenylene diisocyanate producing oligomers containing urea linkages (-NH-CO-NH-). Oligomeric species were found to produce a number of ordered structures as a function of annealing temperature with the structures being stabilized by intermolecular H-bonding interactions.[12] The isocyanate group is advantageous for covalent reactions since it is particularly electrophilic at the linear (sp-hybridised) carbon atom.

In this study, the reaction of 1,4-diaminobutane (1,4-DAB) with 1,3- and 1,4-phenylene diisocyanate (PDI) on Au{111} in UHV (Scheme 6.1) is reported. The use of an aliphatic diamine is an important advance in this thesis, as it allows the possibility to functionalize the sp^3 hybridized methylene backbone as a means of incorporating chirality into the oligomeric structures. Herein, it is shown that urea oligomers are formed at room temperature for each isocyanate isomer. Following incremental annealing treatments, the oligomer chains increase in length as the reaction proceeds and eventually form extended ordered domains of oligomers. Significant

differences are observed in the topological arrangement of the ordered and disordered oligomer arrays depending on which isomer of diisocyanate is used. The oligomer domains are stable on the Au surface up to 523 K. The synthesis and structure of ordered oligomer domains is examined with scanning tunnelling microscopy (STM) and density functional theory (DFT) calculations.

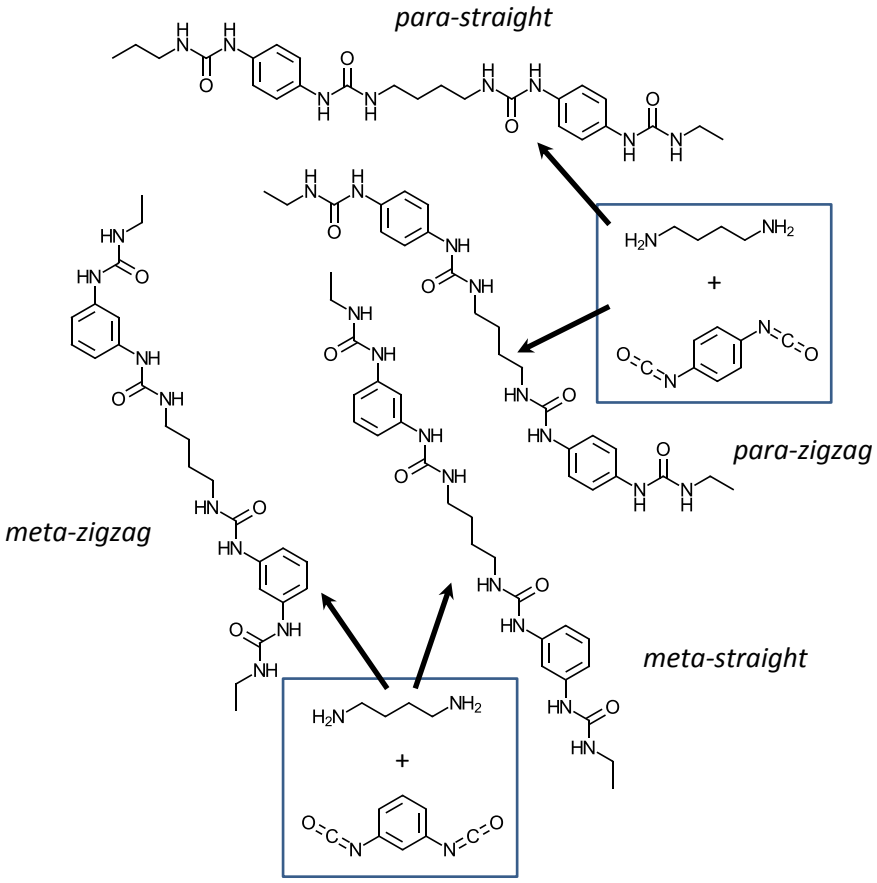

Scheme 6.1: Showing the *straight* and *zigzag* arrangements of the oligomeric products of the reaction between 1,4-diaminobutane and 1,3 (*meta*)- and 1,4 (*para*)-phenylene diisocyanate.

6.3 Experimental

STM experiments were carried out on an Omicron UHV system with a base pressure of 1 x 10^{-10} mbar. The Au{111} sample was prepared by cycles of Ar ion bombardment (0.9 kV) and annealing to 893 K until low energy electron diffraction

(LEED) and STM indicated the presence of a clean Au{111} surface. 1,4-diaminobutane, 1,3- and 1,4-phenylene diisocyanate (all supplied by Sigma Aldrich) were deposited onto the Au{111} surface, held at room temperature, via a precision leak valve. Samples were transferred under UHV conditions to the STM chamber, where images were acquired at room temperature in constant current mode using an electrochemically etched W tip. STM images were processed using WSxM software.[26]

6.4 DFT Calculations

Periodic calculations were carried out using the VASP program.[27-29] The PAW[30] method using the VASP-supplied pseudopotentials and a plane-wave basis set with an energy cut-off of 400 eV was used. Energies and forces were calculated using the PBE-D method, consisting of the Perdew-Burke-Ernzerhof functional[31] and the empirical van der Waals correction of Grimme.[32] A two-dimensional network of polymer chains, without supporting metal surface, was created and optimised. This allowed us to relax the unit cell dimensions, as well as the positions of the atoms within the unit cell. The height of the unit cell was set to 12 Å, to provide a vacuum slab sufficient to prevent interactions between different images of the polymer layer. The optimisation was carried out with constant cell volume to prevent large changes in the thickness of the vacuum slab. DFT calculations were carried out by Dr H. A. Früchtl on the EaStCHEM Research Computing Facility.

6.5 Results and Discussion

Assuming that the aliphatic chains remain fully extended, when two DAB molecules react with a single diisocyanate species, the two urea linkages at either side of the phenyl ring can be oriented in the same or in opposite directions (Scheme 6.1). In

both the meta and para isomers of the polymer, one of these arrangements leads to a more or less linear continuation of the chain, while the other shows a bend of the chain at the phenyl ring. The geometries of the four resulting polymer networks were optimised, and the nomenclature *meta-straight*, *meta-zigzag*, *para-straight* and *para-zigzag* will be used in discussing the DFT calculations. Note that the notation is based on idealised structures of planar chains with all angles 120^{o} or 109.5^{o}. After optimisation, the meta-straight chain will display a small bend at the phenyl group, see Figure 6.4 c). A second *meta-zigzag* arrangement can be formed where two carbonyl oxygens come into close proximity (analogous to the *para-zigzag* conformation). This configuration is likely to be sterically unfavourable and would induce a much sharper bend in the zigzag than was observed experimentally (see below), so this configuration was ignored.

Control experiments were carried out to separately investigate the deposition of 1,4-DAB, 1,3- and 1,4-PDI onto Au{111}. In each case, no ordered molecular arrangements were observed by STM. Jensen et al.[12] reported that 1,4-PDI was too mobile on Au{111} to be imaged by STM at 300 K . This is found also to be the case for 1,3-PDI and 1,4-DAB on Au{111}.

6.5.1 1,4-DAB + 1,4-PDI on Au{111}

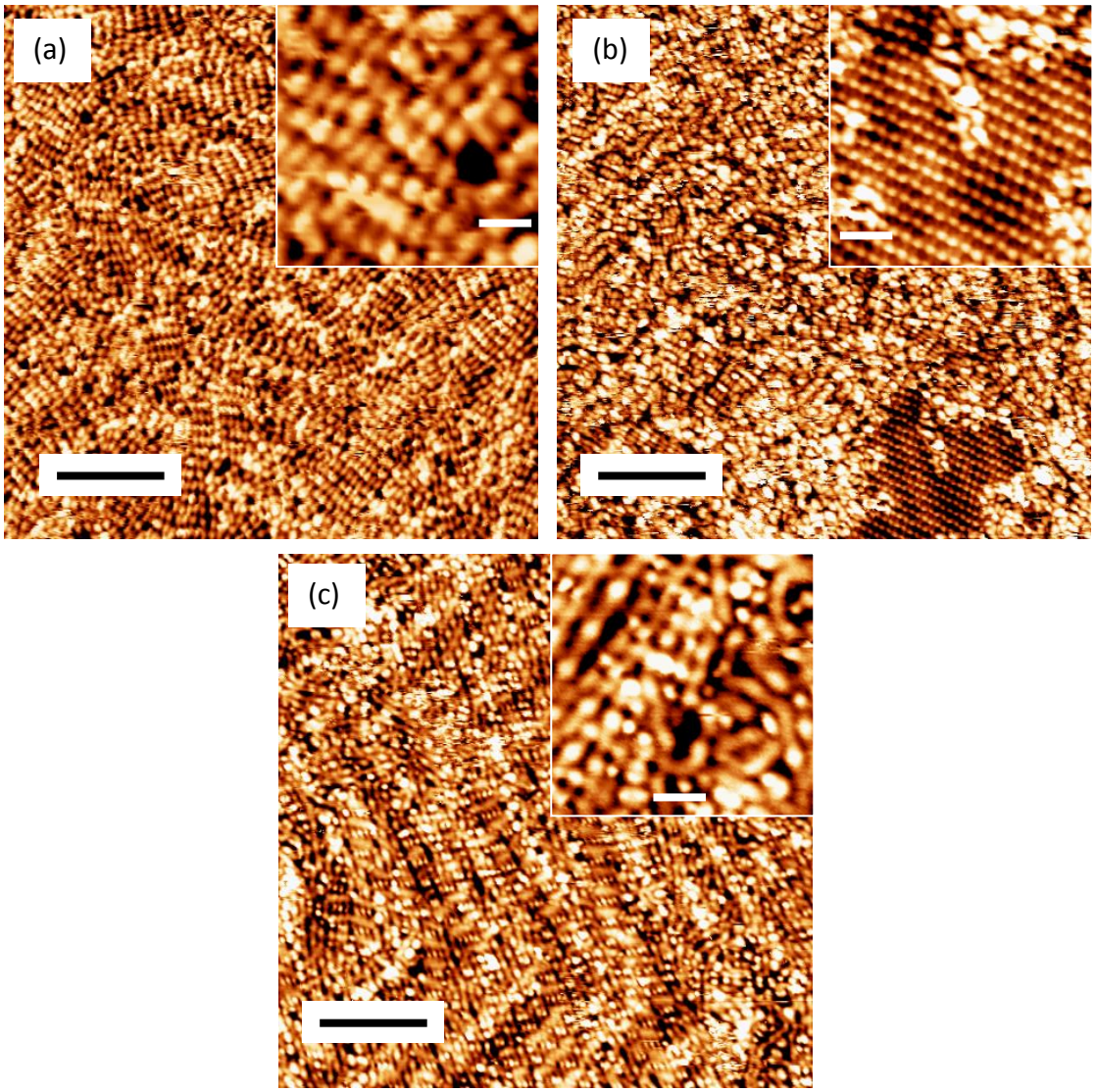

Figure 6.1: STM images following the co-adsorption of 1,4 PDI and 1,4 DAB at 300 K and subsequent anneal to (a) 323 K (I=0.2 nA, V=0.15 V, Scale bar = 8.4 nm). Inset shows an expanded region of this image (Scale bar = 1.3 nm). (b) 373 K. (I = 0.2 nA, V = 0.35 V, Scale bar = 10 nm). Inset shows an expanded region of this image (Scale bar = 2.6 nm) (c) 423 K (I = 0.2 nA, V = 0.05 V, Scale bar = 8.8nm). Inset shows an expanded region of this image (Scale bar = 1.7 nm)

Following co-deposition of 1,4-DAB and 1,4-PDI at room temperature, indications of the presence of diffusing mobile species was observed, but no evidence of reaction was found in the STM images. Figure 6.1 a) shows that after annealing the sample to 323 K, the surface became covered with features whose dimensions are consistent

with the formation of oligomer species via the reaction of 1,4-DAB with 1,4-PDI (see DFT calculations below). As the annealing temperature was increased, the formation of domains of oligomeric species became more extensive, see Figure 6.1 b) and c). Regions of ordered oligomeric species were found to co-exist with more randomly organized one-dimensional oligomer chains. A small domain of ordered molecular features is observed in the lower right hand corner of Figure 6.1 b). The herringbone reconstruction is clearly visible beneath this domain. The nearest neighbour separation between the bright features within the rows is 6.6 ± 0.2 Å, and the row separation is 8.5 ± 0.3 Å. Very few domains of this type were observed and only after annealing the sample to 373 K. The intermolecular dimensions are not consistent with the formation of oligomeric species. The most likely explanation is that these domains consist of unreacted 1,4-PDI molecules which have approximate dimensions of ~ 7.7 Å x ~ 4.3 Å. This phase was not observed in the STM images following higher temperature annealing. The domain is surrounded by oligomer species which may allow 1,4-PDI to be imaged by restricting its ability to diffuse across the surface. 1,4-PDI species has never been resolved when this has been deposited alone at 300 K.

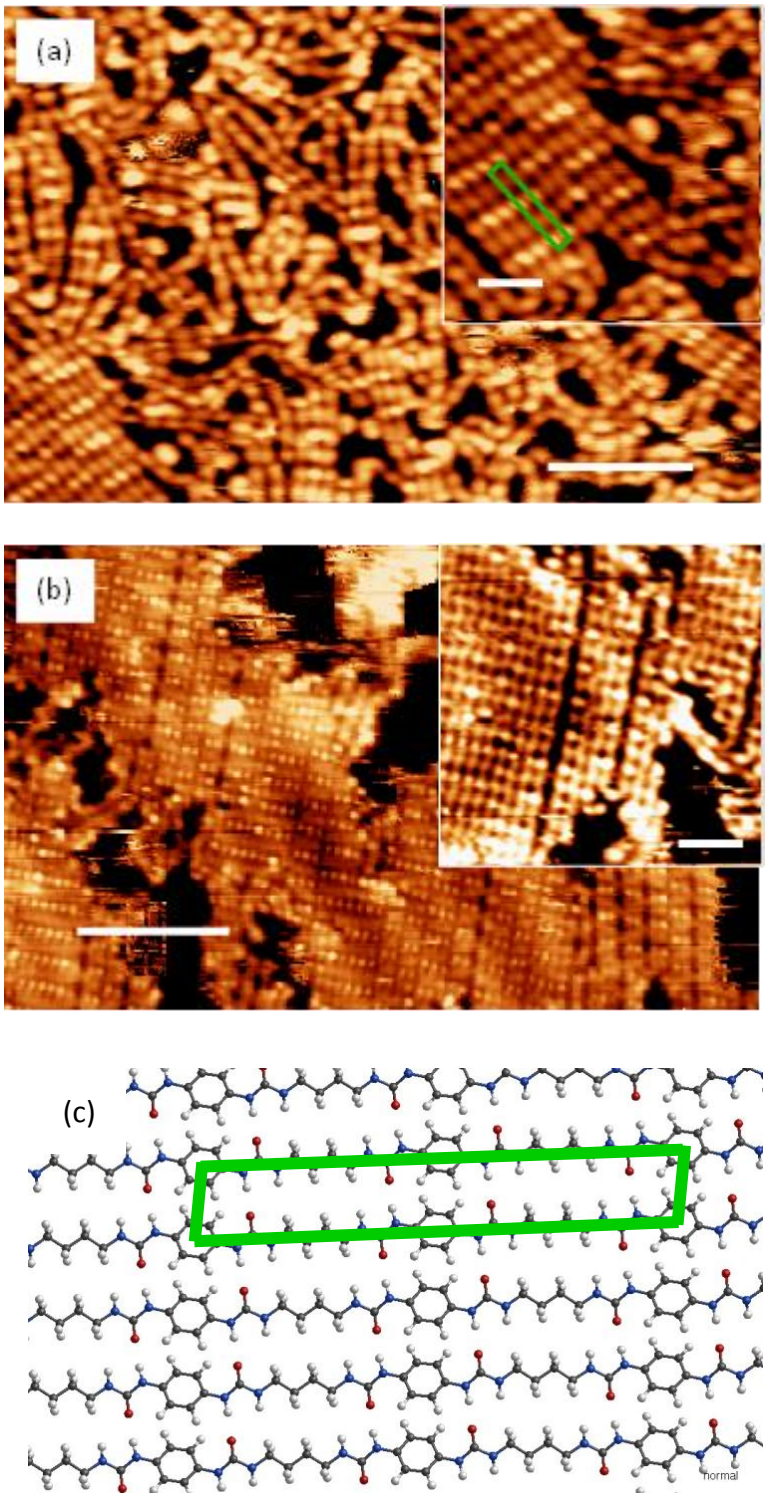

Figure 6.2: (a) STM image of covalently coupled 1,4-PDI with 1,4-DAB on Au{111}, after annealing to 473 K (I = 0.25 nA, V = 0.6 V, scale bar = 6 nm) . Inset shows an ordered array of urea polymers (scale bar = 2 nm), the unit cell is shown in green, with dimensions of 5.5 ± 0.2 Å x 33.0 ± 1.0 Å (b) STM image of ordered polyurea network after annealing to 523 K (I = 0.1 nA, V = - 0.3 V, scale bar = 8.3 nm) Inset shows an expanded region of this image (Scale bar = 2.6 nm). (c) DFT model of an ordered assembly of oligomers in the *para-straight* conformation; the unit cell is shown in green, with dimensions of 5.1 Å x 32.6 Å.

Figure 6.2 a) shows STM images of the Au surface after annealing to 473 K, the inset representing a close-up view. Within the ordered domains, a unit cell of dimensions 5.5 Å x 33 Å can be defined. Figure 6.2 b) shows an STM image of the sample after annealing to 523 K. Arrays of linear ordered oligomeric species remain on the surface. A few curved oligomer features are seen at the island perimeters, seeming to interconnect the ordered island arrays. The ordered oligomers typically contain ~9 bright features which are attributed to the aromatic rings.

6.5.2 1,4-DAB + 1,3-PDI on Au{111}

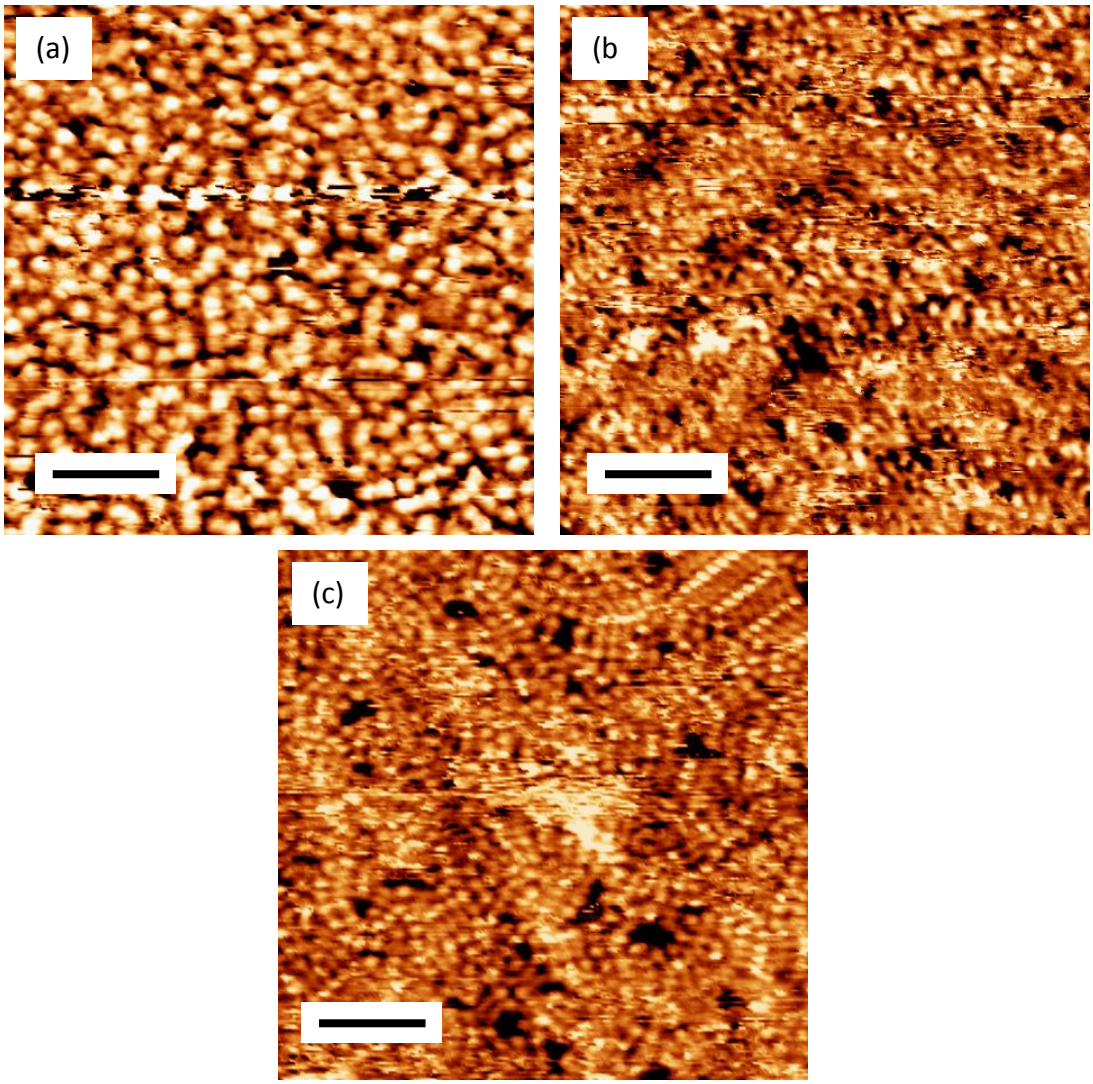

Figure 6.3: (a) STM image of covalently coupled 1,3-PDI with 1,4-DAB, on Au{111}, at room temperature (I=0.2 nA, V=1.1 V, scale bar = 5.3 nm), (b) annealed to 336 K (I=0.1 nA, V=1.2 V), scale bar = 6.8 nm), (c) annealed to 473 K (I=0.15 nA, V=-0.1 V, scale bar = 4.5 nm).

In order to examine the influence of the relative position of the isocyanate substituents around the aromatic ring, the co-deposition of 1,3-PDI with 1,4-DAB was studied on Au{111} at 300 K. After co-deposition, STM revealed a disordered array of bright circular features, each measuring approximately 1 nm in diameter, see Figure 6.3 a). Such features were not observed after the separate deposition of each reagent onto Au{111}. The features are similar in appearance to those imaged following the adsorption of 1,4-PDI with 1,4-DAB and subsequent annealing to 323 K, see Figure 6.1 a), and these features may correspond to urea oligomers resulting from reactions between adsorbed amines and diisocyanates. If this is the case, there is STM evidence that the addition reaction occurs at room temperature which may reflect a difference in reactivity between the 1,3- and 1,4-PDI molecules. No significant changes are observed on annealing the sample to 427 K. However, after annealing to 473 K, small patches of ordered structures are imaged amongst the disordered species, see Figure 6.3 c).

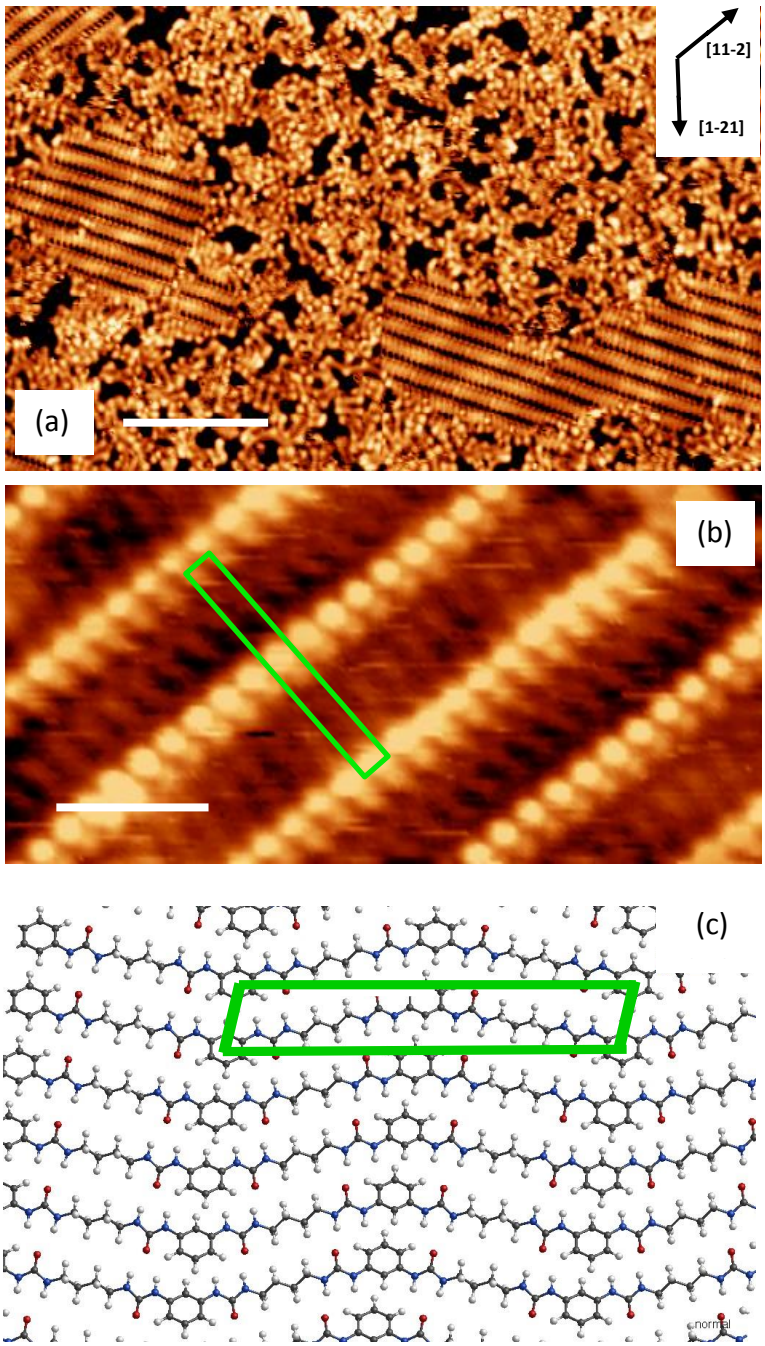

Figure 6.4: (a) STM image of covalently coupled 1,3-PDI with 1,4-DAB, on Au{111}, after annealing to 523 K (I = 0.25 nA, V = 0.6 V, scale bar = 13 nm) . (b) STM image of ordered polyurea network after annealing to 523 K (I = 0.15 nA, V = 0.75 V, scale bar = 1.9 nm); the unit cell is shown in green, with dimensions of 5.5 ± 0.2 Å x 30.5 ± 1.0 Å (c) DFT model of an ordered assembly of oligomers in the *meta-straight* conformation; the unit cell is shown in green, with dimensions of 5.2 Å x 31.2 Å.

STM images of the Au surface after annealing to 523 K are shown in Figures 6.4 a) - b). Islands of ordered oligomers are observed, which are separated by regions of disordered oligomeric structures. The aromatic rings are aligned along the high

symmetry <-211> crystallographic directions. The aromatic ring moieties are not well resolved in Figure 6.4 a), especially along the [1-21] direction; this is most likely due to a tip effect as this reverse contrast was not observed on other occasions even using similar tunneling parameters. In Figure 6.4 b), both the aromatic ring moieties and aliphatic chain backbone of the urea oligomers in the ordered structure are clearly resolved. Neighbouring aromatic rings are separated by ~5.5 Å and adjacent rows of aromatic rings are separated by 15.0 – 15.5 Å.

6.5.3 DFT Investigations

		Unit cell dimensions		
	Relative Energy per unit cell /kJ mol^{-1}	Length /Å	Width /Å	Angle
Meta-straight	0	31.2	5.2	81°
Meta-zigzag	34.3	28.3	5.1	91°
Para-straight	18.8	32.6	5.1	83°
Para-zigzag	52.9	28.0	5.6	88°

Table 6.1: The unit cell dimensions of the ordered structures predicted by DFT for the oligomers derived from *meta* and *para* PDI taking into account the *straight* and *zigzag* conformations.

In order to identify the structures of the oligomers within the ordered domains, periodic calculations on 2D-periodic domains of each structure were carried out. In forming ordered domains of oligomers there are a number of degrees of freedom. Firstly, there is considerable flexibility in the $-(CH_2)_4-$ backbone of DAB. However, for long chain hydrocarbons on unreactive surfaces such as HOPG, there is a strong tendency for such aliphatic backbones to adopt the all-trans configuration typically with an optimum interchain distance of 4.0-4.4 Å to optimize van der Waals interactions.[33] As summarized in Scheme 6.1, there is also the possibility that the urea functionalities can be oriented in the *straight* or *zigzag* configurations. Though it

is clear that many other configurations could exist as evidenced by the disordered regions of the surface, the ordered domains consist of oligomers possessing high symmetry. Consequently, the DFT calculations focused on a narrow range of possible regularly repeating structures. Domains of each structure were tested in order to determine their optimum dimensions and to compare their relative energies. Figures 6.2 c) and 6.4 c) show the preferred structures for each oligomer type. For each isomer of PDI, a strong energetic preference was observed for the *straight* configuration. For 1,4-PDI, the *straight* configuration was lower in energy by 34.1 $kJmol^{-1}$ per unit cell while for 1,3-PDI, a similar difference (34.3 $kJmol^{-1}$ per unit cell) was calculated. For the *meta-straight* configuration, the dimensions of the optimized unit cell were 5.2 Å x 31.2 Å, with the unit cell vectors separated by an angle of 81^{o}. The longer dimension corresponds to the spacing between alternate aromatic rings along the oligomer. Overall, these dimensions are in excellent agreement with the dimensions of 5.5 Å x 30-31 Å measured by STM. For the *para-straight* configuration, the optimized unit cell dimension is measured to be 5.1 Å x 32.6 Å with the unit cell vectors separated by an angle of 83^{o}, in very good agreement with the dimensions measured by STM of 5.5 Å x 33.0 Å. [It should be noted here that the true unit cell for the *para-straight* configuration has a long dimension of exactly half this value. For consistency between alternating, e.g. Figure 6.2 c), and symmetric, e.g. Figure 6.4 c), side chain orientations, the larger unit cell was used.] It was estimated that dimensions could be measured to within ~ 3 % using the WSxM software; this also applies to all of the STM scale bars stated throughout this thesis. The driving force underpinning the ordering of the molecular arrays is likely to be the formation of intermolecular H-bonds between neighbouring urea functionalities. The spacing

between adjacent -$(CH_2)_4$- units is approximately 1 Å larger than the optimum van der Waals spacing for adjacent methylene units. In order to avoid repulsive interactions between adjacent oligomers, the DFT calculations show that the aromatic rings rotate out of the plane of the oligomers by 31^o (*para-straight*) and 32^o (*meta-straight*). This allows NH---O bonds to be produced for each carbonyl group in the *para-straight* configuration. In the *meta-straight* configuration, the nature of the H-bonding is asymmetric about a given aromatic ring. The carbonyl group on one side of the ring is equidistant from two N-H functionalities. On the opposite side of the aromatic ring, the NH—O bond is more similar in nature to those in the *para-straight* configuration. The *meta-straight* configuration is calculated to have a lower energy by 18.8 $kJmol^{-1}$ per unit cell, compared to the *para-straight* configuration – the difference is likely to be related to the fact that the former H-bonding orientation is energetically more favourable. From simple geometric arguments, the dramatic tilting of the aromatic rings presumably contributes significantly to the enhanced contrast observed in STM images. It should be noted that the unit cells were optimized without including the Au surface in the calculations. The excellent agreement of the dimensions of the DFT calculations with those of the STM images coupled with the relatively unreactive nature of the Au surface is believed to justify this approach. For example, any reorientation of the aromatic rings induced by the Au surface would likely result in a significant modification of the intermolecular distances and unit cell dimensions.

The cumulative inductive effect of the two nitrogen atoms in the urea group is greater than the orbital overlap of the nitrogen electron lone pairs into the carbonyl π^* orbital, thereby increasing the electrophilicity of the urea carbonyl group relative

to an amide carbonyl, favouring stronger intermolecular H-bonding interactions. This would be expected to result in the oligourea arrays being more thermally stable than analogous amide oligomers. STM suggests that oligomers are formed at, or slightly above, room temperature. 1,4-PDI has been shown to undergo surface-confined reactions with aromatic amines at room temperature.[12] It is unlikely that oligomer length increases significantly as a function of annealing temperature since any unreacted isocyanate species desorb at relatively low temperature depleting the supply of isocyanate. The effect of temperature is primarily to enable restructuring and diffusion of existing oligomers allowing the healing of defects within the chains and facilitating the formation of ordered oligomer arrangements. It was not tested for the possibility that repeated dosing of either component could lead to increases in the observed chain lengths and the size of ordered oligomer domains.

Apart from the topological variation in the reacted structures, one would predict reactivity differences between the two diisocyanate monomers. The nucleophilic addition reaction leads to a negative charge being localized on the oxygen atom of the isocyanate group. Proton transfer between the nitrogen atoms leads to the urea group formation; however, the negative charge can be delocalised onto the isocyanate group in the *para* position, thereby stabilising the intermediate. For 1,3-diisocyanate, the negative charge bypasses the *meta* position, therefore the stabilisation of delocalising the negative charge over the other isocyanate group is not available for the 1,3-diisocyanate reagent. The experimental observations would suggest that the difference in reactivity of the isocyanate derivatives has little effect on the extent of reaction, with surface mobility being the dominant factor in surface reactivity.

The extent of ordering is greater for the oligomeric species derived from 1,4-PDI. After annealing to 523 K, only ordered arrays of oligomers remain resulting from reaction from 1,4-PDI, interspersed by bare surface; whereas relatively smaller domains of ordered oligomers are formed from 1,3-PDI , interspersed by disordered oligomers. Though DFT predicts that the arrays formed from 1,3-PDI are slightly lower in energy, it is likely that the strongly linear nature of the former oligomers enables them to diffuse more readily; whereas the more zig-zag arrangement of the oligomers derived from 1,3-PDI provides them with a greater tendency to lock into more disordered arrangements.

6.6 Conclusions

STM data and DFT calculations provide strong evidence that both 1,3- and 1,4-phenylene diisocyanate undergo a nucleophilic addition reaction with 1,4-diaminobutane on Au{111} in UHV at, or slightly above, room temperature. Upon annealing to higher temperatures, both diisocyanate derivatives react with 1,4-diaminobutane to form urea oligomers. At sufficiently high temperatures, the urea oligomers form ordered networks, held together by intermolecular H-bonding via the urea linkages. The ordered oligomer structures are thermally stable up to at least 523 K. DFT predicts that the *para-straight* and *meta-straight* configurations are favoured over the *zigzag* analogues. In each case, the aromatic rings are strongly tilted out of the plane of the surface to minimize lateral repulsions and to enable intermolecular H-bonding interactions. The topographical arrangement of the ordered oligomer networks differs for the two diisocyanate derivatives; the *para-straight* oligomers form strongly linear oligomer networks, whereas the *meta-straight* oligomers have a slight zig-zag configuration. These subtle differences are believed to influence the

relative ability to form long-range ordered domains. For applications in templating, catalysis, biosensing etc., it is desirable to produce porous structures. In this study of simple amine and isocyanate building blocks, structures are formed which are densely packed and do not possess the desired porosity. Enhancement of porosity is likely to be achieved by the use of tri-isocyanates or tri-amine building blocks. The ease of reactivity coupled with the thermal stability of the structures reported in this study leads to the conclusion that isocyanate/amine systems may be ideally suited for application in templating and catalysis.

Note: The work presented in Chapter 6 has been published:

Greenwood, J.; Früchtl, H. A.; Baddeley, C. J. J. Phys. Chem. C 2013, 117, 4515-4520. 'Surface-Confined Reaction of Aliphatic Diamines with Aromatic Diisocyanates on Au{111} Leads to Ordered Oligomer Assemblies'

6.7 References

[1] L. Grill, M. Dyer, L. Lafferentz, M. Persson, M.V. Peters, S. Hecht, Nat. Nanotechnol. 2 (2007) 687-691.

[2] S. Weigelt, C. Busse, C. Bombis, M.M. Knudsen, K.V. Gothelf, T. Strunskus, C. Woll, M. Dahlbom, B. Hammer, E. Laegsgaard, F. Besenbacher, T.R. Linderoth, Angew. Chem., Int. Ed. 46 (2007) 9227-9230.

[3] S. Weigelt, C. Bombis, C. Busse, M.M. Knudsen, K.V. Gothelf, E. Laegsgaard, F. Besenbacher, T.R. Linderoth, ACS Nano 2 (2008) 651-660.

[4] S. Weigelt, J. Schnadt, A.K. Tuxen, F. Masini, C. Bombis, C. Busse, C. Isvoranu, E. Ataman, E. Laegsgaard, F. Besenbacher, T.R. Linderoth, J. Am. Chem. Soc. 130 (2008) 5388-5389.

[5] S. Weigelt, C. Busse, C. Bombis, M.M. Knudsen, K.V. Gothelf, E. Laegsgaard, F. Besenbacher, T.R. Linderoth, Angew. Chem., Int. Ed. 47 (2008) 4406-4410.

[6] M.I.t. Veld, P. Iavicoli, S. Haq, D.B. Amabilino, R. Raval, Chem. Commun. (2008) 1536-1538.

[7] N.A.A. Zwaneveld, R. Pawlak, M. Abel, D. Catalin, D. Gigmes, D. Bertin, L. Porte, J. Am. Chem. Soc. 130 (2008) 6678-6679.

[8] M. Treier, N.V. Richardson, R. Fasel, J. Am. Chem. Soc. 130 (2008) 14054-14055.

[9] J.A. Lipton-Duffin, O. Ivasenko, D.F. Perepichka, F. Rosei, Small 5 (2009) 592-597.

[10] M. Treier, R. Fasel, N.R. Champness, S. Argent, N.V. Richardson, Phys. Chem. Chem. Phys. 11 (2009) 1209-1214.

[11] R. Gutzler, H. Walch, G. Eder, S. Kloft, W.M. Heckl, M. Lackinger, Chem. Commun. (2009) 4456-4458.

[12] S. Jensen, H.A. Früchtl, C.J. Baddeley, J. Am. Chem. Soc. 131 (2009) 16706-16713.

[13] D. Heim, D. Ecija, K. Seutert, W. Auwaerter, C. Aurisicchio, C. Fabbro, D. Bonifazi, J.V. Barth, J. Am. Chem. Soc. 132 (2010) 6783-6790.

[14] M.O. Blunt, J.C. Russell, N.R. Champness, P.H. Beton, Chem. Commun. 46 (2010) 7157-7159.

[15] F. Sedona, M. Di Marino, M. Sambi, T. Carofiglio, E. Lubian, M. Casarin, E. Tondello, ACS Nano 4 (2010) 5147-5154.

[16] J.F. Dienstmaier, A.M. Gigler, A.J. Goetz, P. Knochel, T. Bein, A. Lyapin, S. Reichlmaier, W.M. Heckl, M. Lackinger, ACS Nano 5 (2011) 9737-9745.

[17] G. Franc, A. Gourdon, Phys. Chem. Chem. Phys. 13 (2011) 14283-14292.

[18] S.A. Krasnikov, C.M. Doyle, N.N. Sergeeva, A.B. Preobrajenski, N.A. Vinogradov, Y.N. Sergeeva, A.A. Zakharov, M.O. Senge, A.A. Cafolla, Nano Research 4 (2011) 376-384.

[19] C.H. Schmitz, M. Schmid, S. Gaertner, H.-P. Steinrueck, J.M. Gottfried, M. Sokolowski, J. Phys. Chem. C 115 (2011) 18186-18194.

[20] C.H. Schmitz, J. Ikonomov, M. Sokolowski, J. Phys. Chem. C 115 (2011) 7270-7278.

[21] S. Jensen, J. Greenwood, H.A. Früchtl, C.J. Baddeley, J. Phys. Chem. C 115 (2011) 8630-8636.

[22] T. Faury, S. Clair, M. Abel, F. Dumur, D. Gigmes, L. Porte, Journal of Physical Chemistry C 116 (2012) 4819-4823.

[23] J.C. Russell, M.O. Blunt, J.M. Garfitt, D.J. Scurr, M. Alexander, N.R. Champness, P.H. Beton, J. Am. Chem. Soc. 133 (2011) 4220-4223.

[24] Y. Li, J. Wan, K. Deng, X. Han, S. Lei, Y. Yang, Q. Zheng, Q. Zeng, C. Wang, J. Phys. Chem. C 115 (2011) 6540-6544.

[25] J. Greenwood, C.J. Baddeley, Langmuir (2012) 10.1021/la304506s.

[26] I. Horcas, R. Fernandez, J.M. Gomez-Rodriguez, J. Colchero, J. Gomez-Herrero, A.M. Baro, Rev. Sci. Instrum. 78 (2007) 013705.

[27] G. Kresse, J. Furthmuller, Phys. Rev. B 54 (1996) 11169-11186.

[28] G. Kresse, J. Hafner, Phys. Rev. B 47 (1993) 558-561.
[29] G. Kresse, J. Hafner, Phys. Rev. B 49 (1994) 14251-14269.
[30] P.E. Blochl, Phys. Rev. B 50 (1994) 17953-17979.
[31] J.P. Perdew, K. Burke, M. Ernzerhof, Phys. Rev. Lett. 77 (1996) 3865-3868.
[32] S. Grimme, J. Comput. Chem. 27 (2006) 1787-1799.
[33] F. Tao, Y.G. Cai, S.L. Bernasek, Langmuir 21 (2005) 1269-1276.

Chapter Seven:

Formation of Porous, Chiral Arrays of Cyanuric Acid following Deposition of 1,4-Phenylene Diisocyanate on Au{111}

7.1 Abstract

The surface-confined interaction between cyanuric acid (CA) and 1,4-phenylene diisocyanate (1,4-PDI) has been investigated on Au{111} in UHV by scanning tunnelling microscopy (STM) and high resolution electron energy loss spectroscopy (HREELS). No covalent bond forming surface confined reaction is observed between co-adsorbed CA and PDI. The results suggest that 1,4-PDI does not stick to the surface after a monolayer of CA is deposited; instead, it partially extracts pre-adsorbed cyanuric acid from the surface. Cyanuric acid undergoes a phase transition from a hexagonally close-packed structure to a hexagonal porous phase. Two cyanuric acid porous phases are observed amongst the close-packed structures, which adopt a flat-lying orientation with respect to the surface. Upon annealing,

large domains of the porous phases are observed. The factors which may affect the formation of these phases are discussed.

7.2 Introduction

The formation of two-dimensional nanostructures based on supramolecular chemistry holds promise for the formation of nanostructure architectures. Highly complex arrays can be fabricated via the self-assembly of precursor species utilising directional and reversible hydrogen bonding. Advances in this field in recent years have enabled the creation of a range of ordered two-dimensional supramolecular structures on surfaces.[1-12] Modified surfaces such as these are important for the development of applications exhibiting molecular recognition for chemical sensors and heterogeneous catalysis.

Cyanuric acid (CA) has been intensively studied as a molecular building block for hydrogen-bonded structures. The ability of the hydroxyl groups and the triazine nitrogen atoms of the enol structure of CA allow it to participate in multiple hydrogen bonding interactions, therefore making it a desirable molecular unit for nanoscale structures. In particular, supramolecular networks of cyanuric acid and melamine have been studied by a number of groups investigating the structures and energetics of the networks formed on different surfaces.[13-17]

Structures stabilised by hydrogen bonds are of limited thermal stability. In recent years, a range of surface-supported 2D nanostructures have been fabricated by employing covalent reactions. Ideally, fully covalent structures would offer improved

thermal and mechanical durability. Isocyanate species have been shown to be effective electrophiles for surface-confined covalent reactions.[18, 19]

It is shown that the covalent reaction between cyanuric acid and 1,4-phenylene diisocyanate (PDI), chemical structures are shown in Figure 7.1, on Au{111} in UHV does not proceed under the conditions tested. The proposed reaction scheme is shown in scheme 7.1. However, following deposition of 1,4-PDI, the saturated hexagonal close-packed structure of cyanuric acid is observed to undergo a phase transition to a form two separate chiral porous phases.

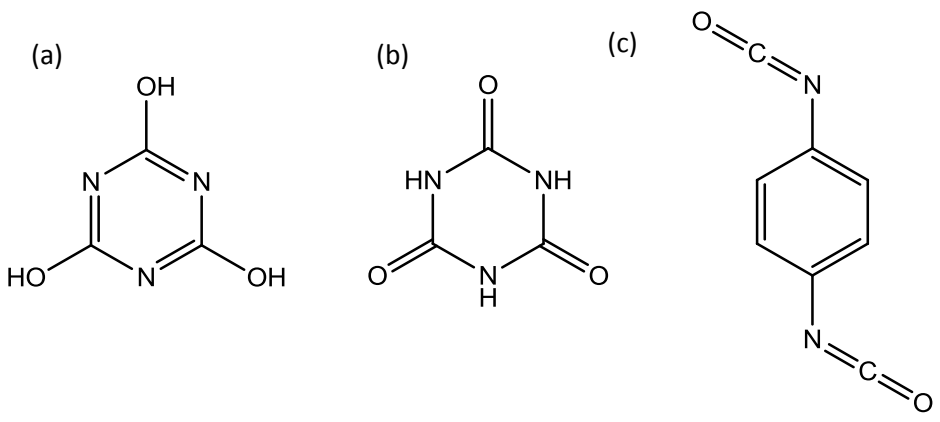

Figure 7.1: Chemical structures of: a) cyanuric acid (hydroxyl tautomer), b) cyanuric acid (ketone tautomer), and c) 1,4-phenylene diisocyanate.

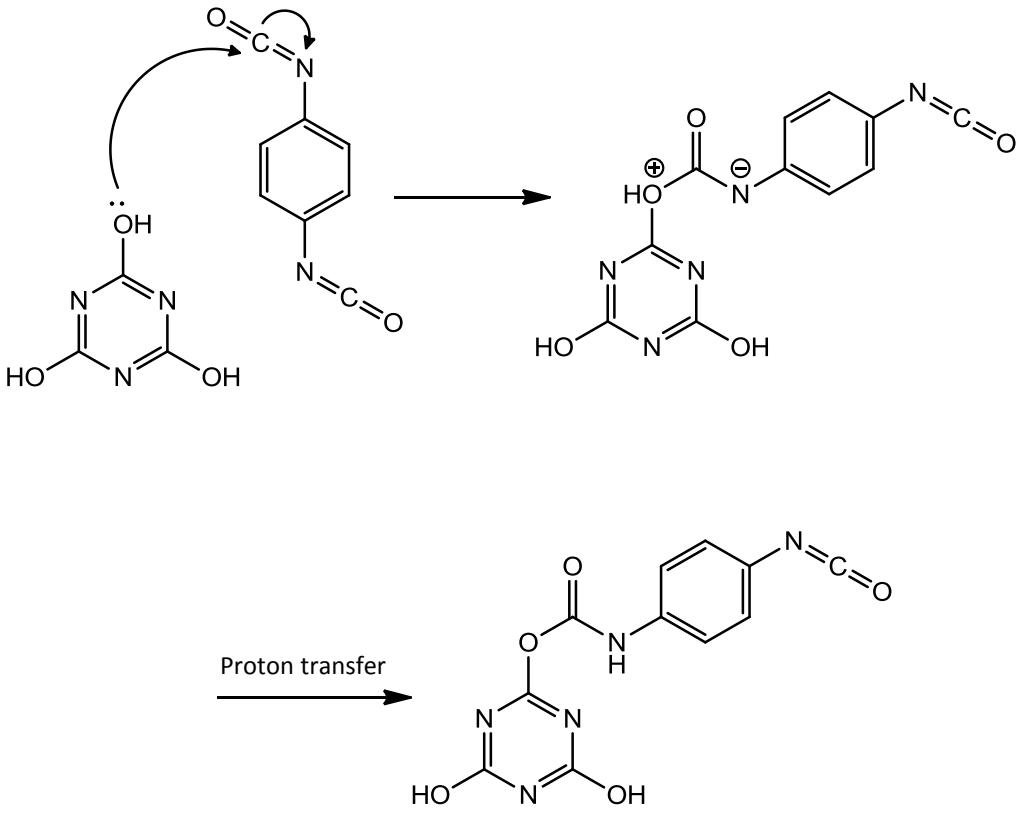

Scheme 7.1: Proposed reaction scheme between hydroxyl tautomer of cyanuric and 1,4-phenylene diisocyanate to produce a urethane linkage.

7.3 Experimental

The STM experiments were carried out in an Omicron UHV system with a base pressure of 1 x 10^{-10} mbar. The Au{111} sample was prepared by cycles of argon ion bombardment (0.8 kV) and annealing to 893 K until low-energy electron diffraction (LEED) and STM indicated the presence of a clean Au{111} surface exhibiting the characteristic (√3 x 22) herringbone reconstruction. Cyanuric acid (Sigma-Aldrich) was heated to 393 K and sublimed onto the Au{111} substrate which was held at 300 K. 1,4-phenylene diisocyanate (Sigma Aldrich) was deposited onto Au{111} in UHV via a precision leak valve. Images of the surface were acquired by transferring under UHV conditions to the STM chamber where data were acquired in constant current

mode using an electrochemically etched W tip with the sample at room temperature. STM images were processed using WSxM software.[20]

HREELS experiments were carried out in a VSW HIB 1000, double pass spectrometer, base pressure of less than 5 x 10^{-10} mbar. The Au{111} sample was prepared by cycles of Ar ion bombardment (0.8 kV) and annealing to 893 K until low energy electron diffraction (LEED) and HREELS indicated the presence of a clean Au{111} surface. Cyanuric acid (Sigma-Aldrich) was deposited onto the Au{111} surface, held at room temperature, from a glass doser resistively heated to 393 K, separated from the UHV chamber by a gate valve, and differentially pumped by a turbomolecular pump. Samples were transferred under UHV conditions to the HREELS chamber. Measurements were carried out in the specular direction ($\theta_i = \theta_r = 45°$) with a primary beam energy of 5 eV and a typical elastic peak resolution of ca. 50 cm^{-1}. A maximum likelihood based resolution enhancement method[21, 22] was used to recover the spectra from the instrumental broadening, leading to an improved resolution of ca. 40 cm^{-1} full width at half maximum (FWHM).

The vibrational modes of melamine were modelled in the ground state using density functional theory (DFT) with the B3LYP[23] hybrid functional and the 6-31G* basis set. Molecular DFT calculations were carried out using the GAUSSIAN 03 program suite.[24] Gaussview was used to create the input for the simulation and for visualising the optimised molecular structure and the frontier orbitals of melamine.

7.4 Results

7.4.1 High Resolution Electron Energy Loss Spectroscopy (HREELS)

The HREEL spectra in Figure 7.2 were acquired following the adsorption of a saturation coverage of CA on Au{111} at 300 K. The CA/Au{111} sample was subsequently exposed to 1,4-PDI and annealed over a range of temperatures. Following CA adsorption, vibrational bands are observed at: 226, 396, 446, 466, 581, 731, 781, 811, 1366, and 1431 cm^{-1}. There is a slight increase in some of the vibrational band intensities upon deposition of 1,4-PDI; these include the bands at: 226, 396, 446, and 781 cm^{-1}. After annealing to 323 and 373 K, there is a significant increase in the vibrational band intensities at: 226, 446, 581, 731, 811, 1366, and 1431 cm^{-1}.

Assignment of the low intensity bands is challenging due to the low resolution associated with HREELS, and the noise in the spectrum. A second set of HREEL spectra, not shown, were taken for repeat experiments. The corresponding low intensity vibrational bands were compared with those in the spectra in Figure 7.2. The bands with the strongest correlation in the two set of spectra were assigned as vibrational modes. The signal intensity becomes increasingly diminished in the spectra for higher temperature annealing; hence, spectra for annealing beyond 373 K have not been included in Figure 7.2.

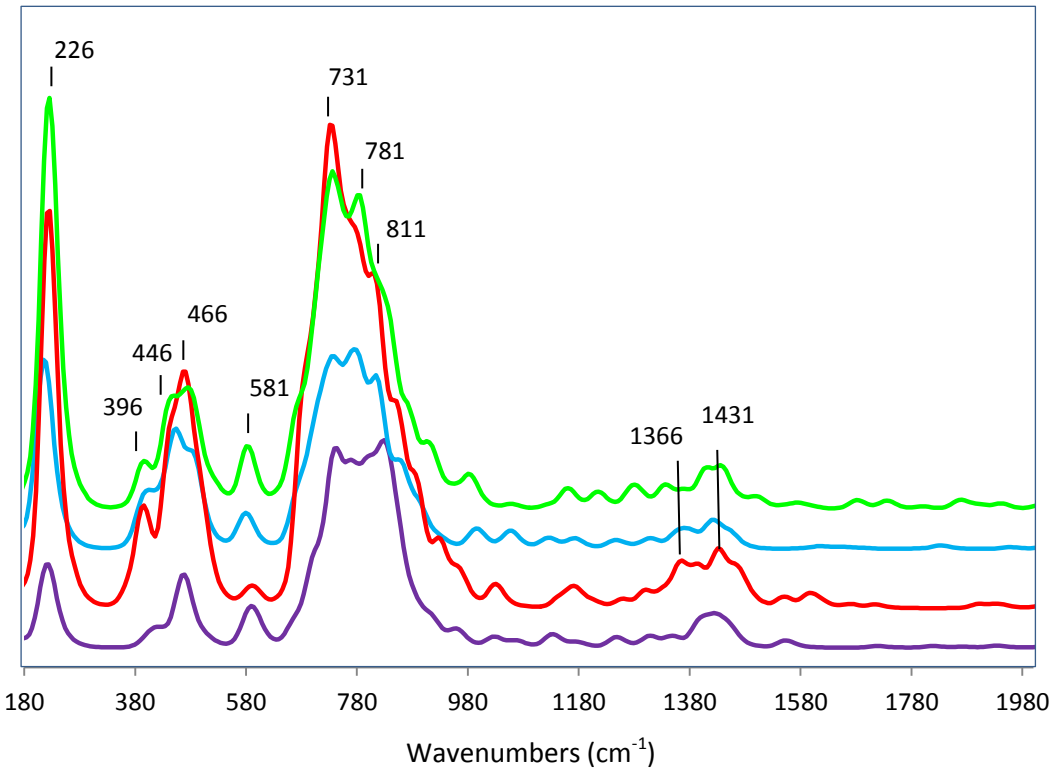

Figure 7.2: HREEL spectra of cyanuric acid on Au{111}. The spectra are represented as: purple (CA, saturation coverage), blue (CA and 1,4-PDI), red (CA and 1,4-PDI annealed to 323 K), green (CA and 1,4-PDI annealed to 373 K). The y-axis represents the intensity (arbitrary units). For clarity, a y-axis offset has been applied to each spectrum.

7.4.2 Scanning Tunnelling Microscopy (STM)

The Au{111} surface, held at 300K, was dosed with cyanuric acid (CA) (6 L) forming monolayer coverage. The characteristic hexagonal close-packed structure of CA is observed, shown in Figure 7.3 a). The CA unit cell is shown in the inset of Figure 7.3 a), measured as ~ 0.74 x 0.7 nm for vectors *a* and *b*, respectively. This structure has been reported on Au{111} in the literature.[17] The Au herringbone reconstruction is visible underneath the overlaying CA monolayer, which has been reported as demonstrating a weak molecule-substrate interaction.[15, 25] The STM image in Figure 7.3 b) shows CA under a different set of tunnelling conditions. In this case, CA appears as three-spoke molecular features, with each spoke attributed to the

position of a hydroxyl group. According to the literature, this three-spoke appearance of CA has not been reported previously.

Upon deposition of 1, 4-PDI (26.4 L), domains of a porous phase are observed within the close-packed phase of CA, shown in Figure 7.3 c). A close-up view is shown in Figure 7.3 d). The unit cell is represented by the white parallelogram. The nearest-neighbour pore separation is measured as 1.2 nm and 1 nm along vectors ‘a` and ‘b`, respectively, with an angle of γ = 120°.

It is noted that there are two alignments of the porous phase, highlighted by the yellow arrows in Figure 7.3 c). These are separated by approximately 33° to each other. The measured angle is slightly greater than that of the high symmetry crystal angle of 30°; however, this offset is believed to be due to thermal drift during scanning. The porous structures are likely to be commensurate with respect to the surface.

The STM image in Figure 7.3 e) shows a different type of hexagonal porous phase, referred to as phase B from hereon. The nearest-neighbour pore separation is measured as 2 nm. The distance between the two nearest neighbour bright features is measured as 0.72 nm. In this case, the hexagons of the CA molecules are separated from each other. The area of each molecular feature is measured as approximately 0.45 nm^2. Some of the pores appear to be filled with bright features which are likely to be trapped CA molecules within or on top of the pore. Other pores have features of a slightly lower contrast at the centre.

Control experiments were carried out to investigate the deposition of 1,4-PDI onto Au{111}. No ordered molecular arrangements were observed by STM. Jensen et al.[18] reported that 1,4-PDI was too mobile on Au{111} to be imaged by STM at 300 K .

It is noted that deposition of 1,4-PDI first, followed by CA deposition resulted in a monolayer coverage of CA. No observations of porous phases were observed, nor were there any signs of covalent reaction between the reactant species. The relatively strong intramolecular H-bonding interactions of the CA molecules are the likely cause for displacement of 1,4-PDI from the surface.

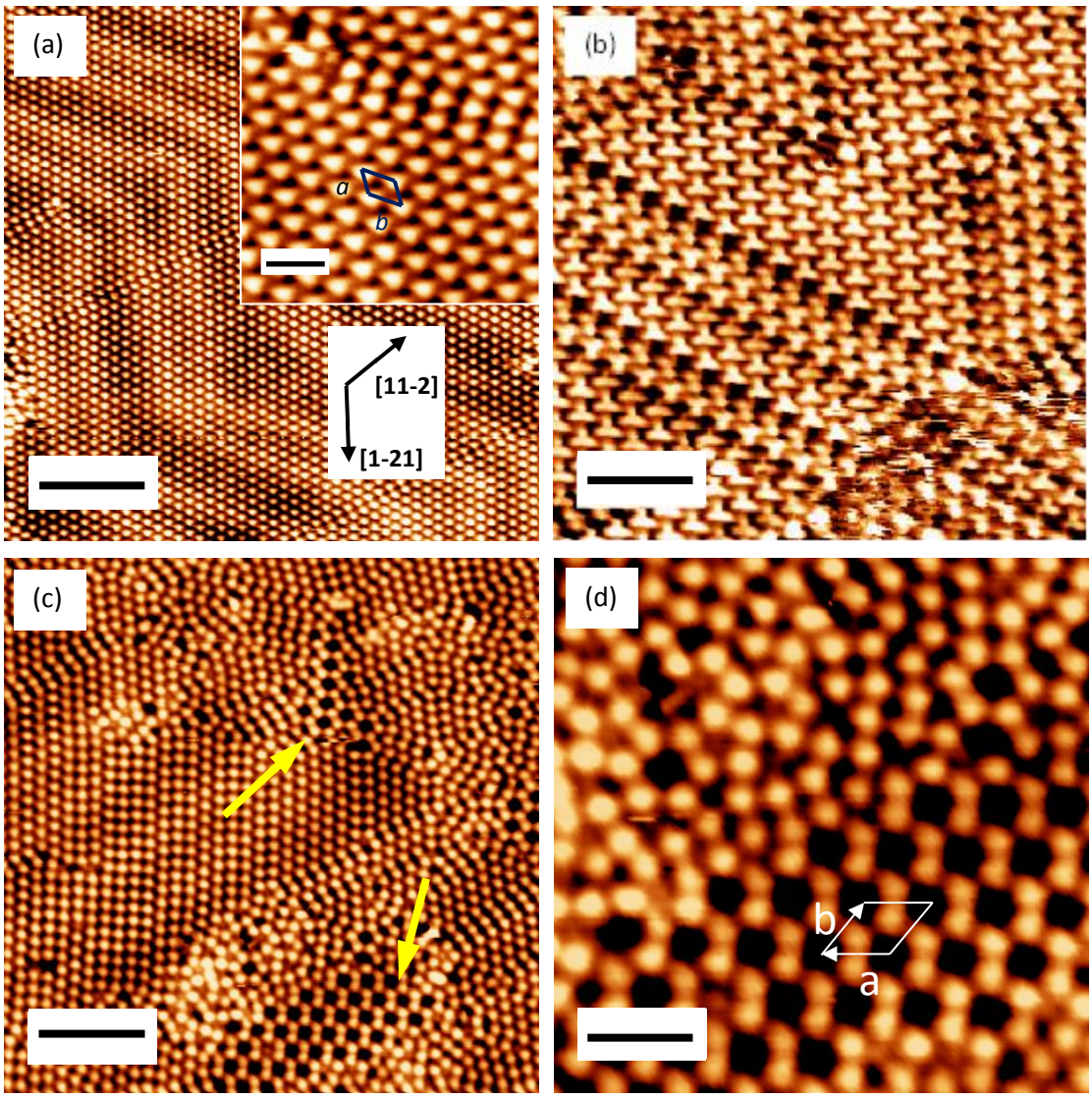

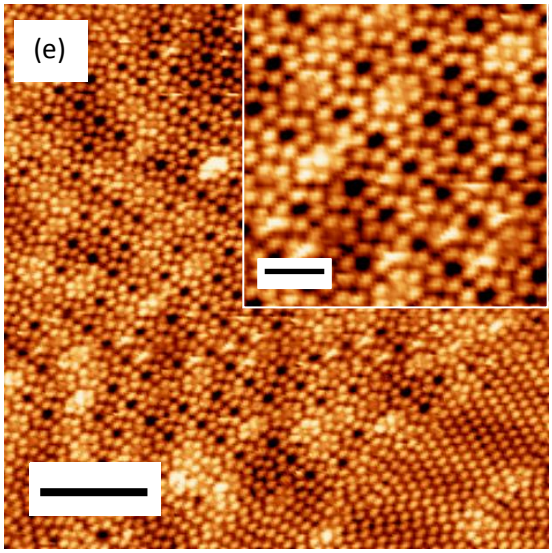

Figure 7.3: a) STM image of cyanuric acid on Au{111} at 300 K following saturation coverage (6 L) (scale bar = 6.6 nm, I = 0.4 nA, V = 0.8 V). Inset shows a close-up view (scale bar = 1.4 nm); b) STM image showing three-spoked appearance of cyanuric acid (scale bar = 2.8 nm, I = 0.2 nA, V = 0.85 V); c) STM image showing CA phase A following deposition of 1,4-PDI (26.4 L) (scale bar = 5.2 nm, I = 0.2 nA, V = 1.1 V); d) close-up view of phase A, unit cell represented by white parallelogram; e) STM image of CA phase B (scale bar = 6.8 nm, I = 0.3 nA, V = 0.75 V). Inset shows close-up view of phase B (scale bar = 2.2 nm).

The STM image in Figure 7.4 shows a unique structure which was observed only in one location on the sample. It is analogous to the porous phase already described, possessing the same dimensions; however, there are parallel lines within the structure of a high contrast. The spacing between these lines is consistent and measured to be 4 nm. The CA molecules within the striped porous phase are adjacent to a step edge. Unfortunately, the STM image does not include the left hand side of the domain where it meets the step edge. Other domains of the porous phase adjacent to step edges do not have the same appearance as this case. Therefore, a possible explanation for the appearance of this unique structure is that the step edge is a surface screw dislocation. The variation in the electronic structure of such a feature could account for the periodic contrast alterations observed.

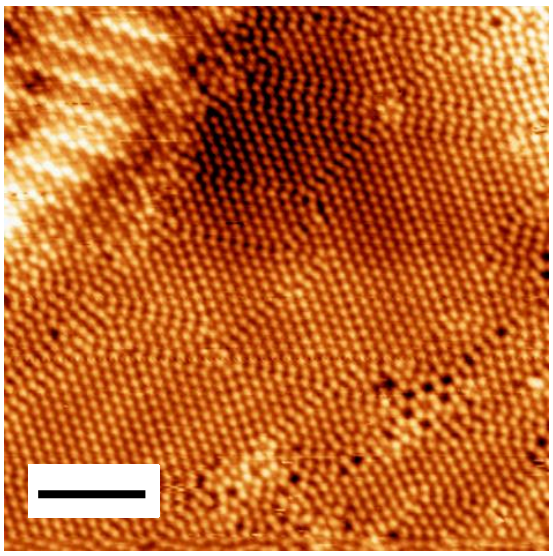

Figure 7.4: STM image of striped porous phase of cyanuric acid on Au{111} adjacent to a step edge (scale bar = 6.1 nm, I = 0.2 nA, V = 0.95 V).

Following annealing to 323 K, there is a significant alteration to the proportion of the CA structures formed. The majority of the surface is still covered in the close-packed phase of CA. Patches of bare Au surface are present, indicating partial desorption of some CA. A large amount of CA is present as island domains of either phase A or B, shown in Figure 7.5 a); a close-up view of phases A and B after annealing to 323 K is shown in Figure 7.5 b) and c), respectively. There is no alteration to the structure or dimensions of either phase following annealing. The unit cell for phase A, shown in Figure 7.5 b), has cell parameters of: a = 1.1 nm, b = 1.2 nm and angle γ = 120°. Also, the unit cell for phase B is illustrated in Figure 7.5 c). The cell parameters are: a = 1.9 nm, b = 1.8 nm and angle γ = 120°.

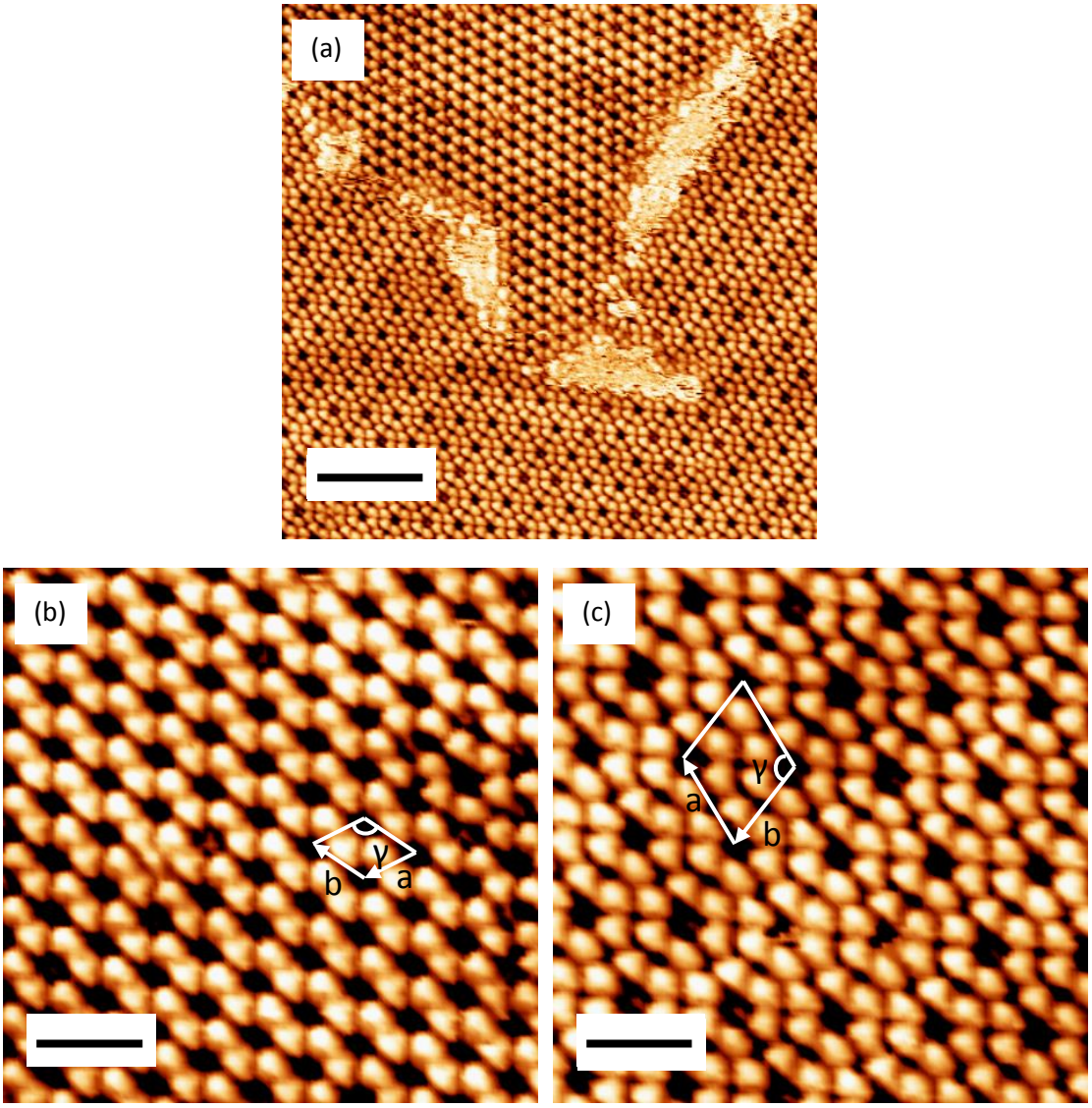

Figure 7.5: a) STM image of island domains of phases A and B of cyanuric acid on Au{111} after annealing to 323 K (scale bar = 6.5 nm, I = 0.35 nA, V = 0.05 V); b) close-up view of phase A of cyanuric acid after annealing to 323 K (scale bar = 2.1 nm); c) close-up view of phase B of cyanuric acid after annealing to 323 K (scale bar = 2.1 nm).

After annealing to 373 K, most of the CA has desorbed, leaving only small islands on the surface, shown in Figure 7.6. Within these islands, CA consists of the close-packed phase, phase B and a disordered arrangement. Phase A was not observed amongst the CA islands after annealing to 373 K.

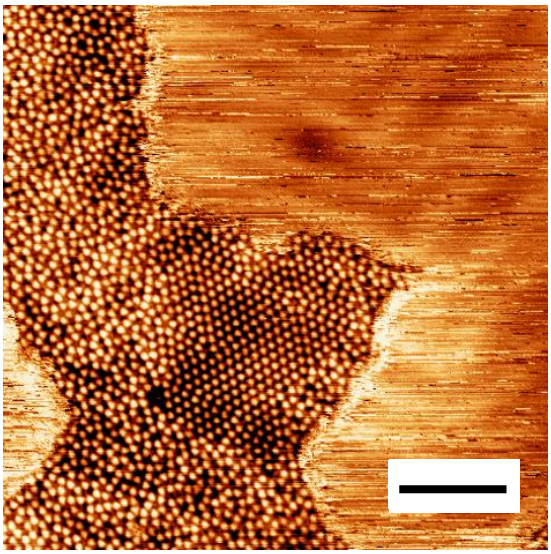

Figure 7.6: STM image of island domain of cyanuric acid on Au{111} after annealing to 373 K (scale bar = 8 nm, I = 0.25 nA, V = -0.08 V).

7.5 Discussion

Cyanuric acid adsorption on Ag/Si{111},[16] Au{111},[15, 17] and HOPG[26] has been investigated by STM. In all cases, CA forms extended 2D arrays, where each molecule adopts a flat-lying orientation and has a circular appearance in STM images. The arrays are stabilised by intermolecular H-bonding interactions. An exception to this observation was made by Zhang et al.[14] studying the self-assembly of CA molecules on Au{111} in ambient conditions. The authors observed a porous phase with a primitive unit cell composed of six bright dots forming a six fold ring. In their study, the CA nearest neighbour separation was measured as 0.5 nm, and the average area of each molecule as 0.19 nm². The authors concluded that since the area measured was less than the maximum area of a CA molecule, ~0.44 nm², the CA molecules must adsorb perpendicular to the Au surface, via either the ketone or N-H group.

The CA arrangement observed by Zhang et al.[14] is identical to phase B following deposition of 1,4-PDI, described in this study. The authors concluded that the upright

orientation of the CA self-assembled monolayers was a consequence of H-bonding interactions between CA and the water solvent molecules. The appearance of the porous phase described by Zhang et al.[14] in ambient conditions has not until now been observed in studies of CA in UHV. Both phases A and B observed in this study are only formed following deposition of 1,4-PDI. The surface coverage of CA molecules within both of the porous phases is less than in the close-packed phase of CA. The CA network is calculated to have a binding energy of 0.65 eV/molecule for the close-packed phase.[17] This indicates that CA is stable on Au{111} at room temperature, and would rule out CA naturally desorbing over time to produce a less dense structure. Therefore, deposition of 1,4-PDI must result in partial extraction of CA from the substrate. This is also the likely cause for the transition of CA from the close-packed phase to the porous structures of phases A and B. The interaction between the surface bound CA and sublimed 1,4-PDI is believed to be analogous to the interaction between CA and water observed by Zhang et al.[14]

Zhang et al.[14] observed two homochiral domains of pure enantiomers. The angle between the long axis of the unit cell of each domain was measured as 22 ± 2°, in which a (√21 x √21)R ± 11° structure is established. For the same phase in this study, phase B, only the one homochiral domain is observed in the STM images. It is noted that all of the images were taken for the same area of the sample; hence, statistically speaking, this is insufficient to suggest there is only a single homochiral domain of phase B. It is believed there are two homochiral domains of phase B, analogous to those observed by Zhang et al.[14] with the same (√21 x √21)R ± 11° structure. After annealing to 323 K, only a single homochiral domain of phase A is observed,

although, as discussed in the results section, two homochiral structures of Phase A are observed in Figures 7.3 c) and d).

There is no evidence in any of the STM images of reaction between CA and 1,4-PDI to form urethane oligomers. Liang et al.[27] have performed DFT calculations of the relative energies of the tautomeric forms of cyanuric acid. Their results predicted the ketone form to be more stable than the hydroxyl form by as much as 116.8 kJ mol^{-1}. Such a high energetic difference in stabilities between the two possible tautomers would suggest CA adsorbs on Au{111} predominantly as the triketone form. Consequently, this rules out a nucleophilic addition reaction between CA and 1,4-PDI. To interpret the shape of the features observed in STM, DFT calculations were carried out (Gaussian 03, 6-311G, B3LYP) of the highest occupied molecular orbital (HOMO) and lowest unoccupied molecular orbital (LUMO) for isolated cyanuric acid. Figure 7.7 shows each orbital viewed perpendicular and parallel to the plane of the aromatic ring. Since adsorption of cyanuric acid is weak on Au{111}, the appearance of the HOMO and LUMO orbitals should still be comparable to the shape of the adsorbed molecules in the STM images.

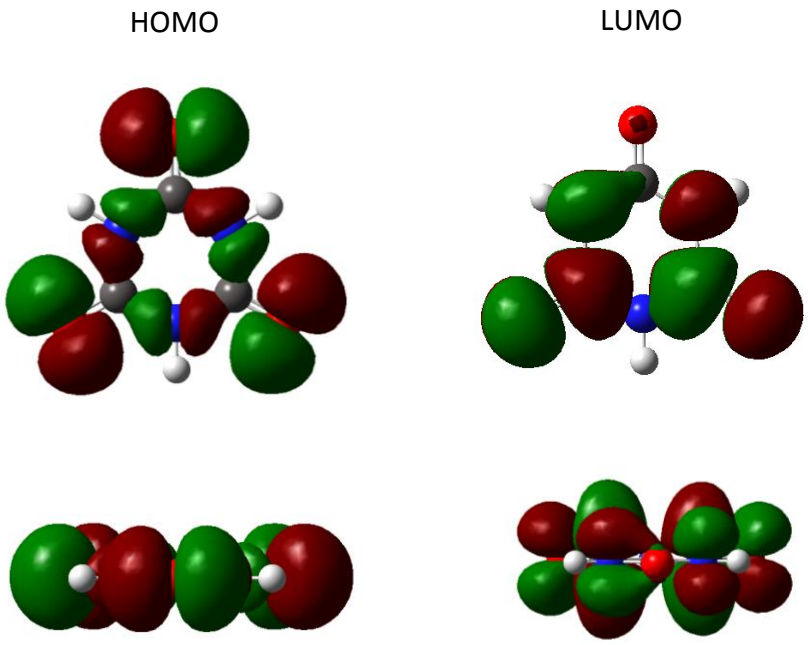

Figure 7.7: HOMO and LUMO of cyanuric acid (Gaussian 03, density functional theory using the B3YLP functional with 6-311G basis set), showing the front-on view to the left and top-down view to the right for the respective molecular orbitals.

Table 7.1: Vibrational frequencies and assignments for cyanuric acid on Au{111}

CA/Au{111} (this work) υ(cm^{-1})	CA/gas phase υ(cm^{-1})[28]	isolated CA (DFT) υ(cm^{-1}) [28]	vibrational mode assignments
	3458, 3456, 3438	3547	ν NH
	1778	1778	ν CO, δ NH
1431 m	1451, 1447	1425	ν ring, ν CO, δ NH
1366 m	1409, 1395, 1393, 1389	1377	δ NH, ν ring, δ CO
811 vs, 781 vs, 731 vs	750, 748	719	γ CO
581 m	638, 632, 621, 618	629	γ NH
466 s, 446 s, 396 m			ν Au-O, ν Au-ring
226 vs			γ ring

Notation: υ- stretch, δ-in plane bend, γ-out of plane bend. Abbreviations: vs- very strong, s-strong, m- medium, w- weak. Underlined values are those of the highest intensity.[28]

Under the imaging conditions used (i.e., tip biased positively), with the exception of Figure 7.6, it would be expected that the imaged molecule may resemble the HOMO in appearance, with electrons being transferred from filled sample states to empty tip states. The triangular and three-spoked appearance of cyanuric acid in the STM images of Figures 7.3 a) and b), respectively, are consistent with the HOMO viewed parallel to the Au substrate. Therefore, the apices of the triangular and three-spoked structures correspond to the carbonyl group of CA. The STM images in Figures 7.5 b) and c) also show CA to be triangular in appearance, indicating CA is parallel to the Au substrate in both phases A and B. This finding is in contrast to the conclusion of Zhang et al.[14] suggesting CA adopts an upright orientation. The authors based their conclusion of an upright orientation of CA on the basis that the measured average area was too small to be adsorbed flat. In this study, the average area of each CA molecule in phase B is measured as ~ 0.45 nm^2, which corresponds very well to the maximum area of CA (~ 0.44 nm^2). This measurement is further evidence that CA adsorbs parallel to the surface in phase B.

A model of the molecular arrangement of phases A and B is represented in Figure 7.8, with the unit cell vectors from Figures 7.5 b) and c) included for phases A and B, respectively. In both cases, the CA molecules are arranged in a formation which optimises the hydrogen bonding interactions between the carbonyl and N-H groups of adjacent molecules. As phase B is the only remaining one of the two porous phases after annealing to 373 K, this indicates it is the most thermodynamically stable. The model in Figure 7.8 for phase B shows that each CA molecule is

surrounded by more molecules compared to those in phase A, increasing the relative H-bonding interactions.

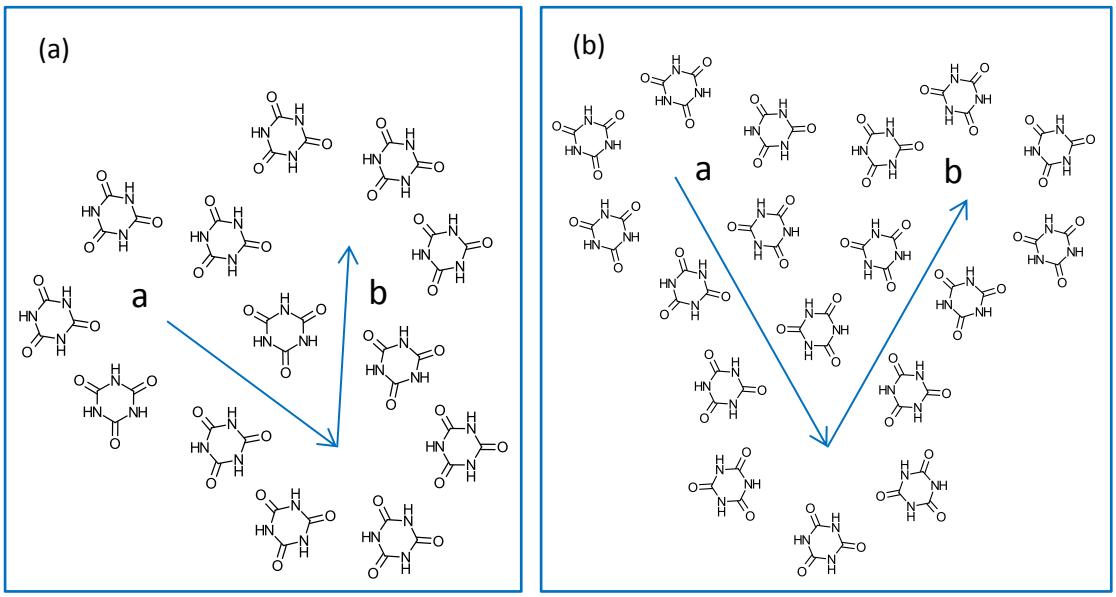

Figure 7.8: Molecular model of CA molecule arrangement in: a) Phase A (a = 1.1 nm, b = 1.2 nm) and b) Phase B (a = 1.9 nm, b = 1.8 nm).

Rostkowska et al.[28] investigated the infrared spectrum of cyanuric acid isolated in a low temperature Ar matrix. The authors performed DFT calculations of the normal modes of cyanuric acid, the results of which were used to assign the vibrational modes of the experimental spectrum. There is generally good correlation between the bands observed in our HREEL spectra and the reported bands observed for gas-phase cyanuric acid.[28]

There are more vibrational bands in the HREEL spectra than would be expected for CA. Since CA is a 12-atomic molecule of D_{3h} symmetry, there should be only 10 bands at different frequencies.[28] The higher number of vibrational bands observed can be explained by the loss of symmetry of CA upon adsorption on Au{111}. This would

result in the splitting of some of the vibrational mode bands. Analogous behaviour was observed in the IR spectrum of matrix-isolated cyanuric acid[28] and trithiocyanuric acid.[29] It is worth noting that in our HREEL spectra, or in the IR bands observed by Rostkowska et al.[28], no bands are detected in the frequency range of 3500 cm^{-1}, which is the characteristic range of OH group stretching vibrations. The lack of vibrational modes in our HREEL spectra at the stated range confirms CA adsorbs as the tri-ketone tautomer on Au{111}.

A major discrepancy in the HREEL spectra is the lack of a carbonyl vibrational band corresponding to the ketone groups of cyanuric acid. The IR spectra obtained by Rostkowska et al.[28] detected multiple carbonyl peaks, the most intense band is observed at 1778 cm^{-1}. The DFT calculations of the authors also simulated a carbonyl stretching mode at 1778 cm^{-1}. The dipole moment for the carbonyl stretching mode is within the plane of the molecule for CA. The surface selection rule would render this vibrational mode undetectable when CA is adsorbed parallel to the surface. Therefore, the HREEL spectra indicate the plane of the CA molecule is adsorbed parallel to the Au surface. In addition, no vibrational bands are observed associated with N-H stretching modes, for which the dipole moment is in the plane of the molecule.

The strongest vibrational modes in the HREEL spectra for CA, observed at 811, 781 and 731 cm^{-1}, are assigned to the out-of-plane bending mode of the carbonyl group. Sexton investigating pyrrole adsorption on Cu{100} observed a strong vibrational band in EELS at 600 cm^{-1}, assigned as the out-of-plane NH bending mode.[30] This

corresponds well to the band observed in our HREEL spectra at 581 cm^{-1}, which has also been assigned as the out-of-plane NH bending mode.

Whelan et al.[31] investigated the adsorption of a benzylic macrocycle on Au{111}. The authors observed a vibrational band at ~ 470 cm^{-1} attributed to a Au-O stretch due to the interaction between the Au substrate and carbonyl group. This is closely related to the set of vibrational bands observed at 466, 446 and 396 cm^{-1}, which have also been assigned to the Au-O stretching mode.

The small vibrational bands observed at 1431 and 1366 cm^{-1} cannot be due to the vibrational modes of flat-lying CA. The gas phase IR study by Rostkowska et al.[28] found IR bands of corresponding values to the stated observed bands in this study, values and assignments are listed in Table 7.1. In order for the carbonyl stretch and in-plane N-H bending mode to be detectable in HREELS a small proportion of CA must adopt an upright geometry. Similar behaviour has been observed for melamine adsorption on Au{111} following reaction with trimesoyl chloride.[32] Typically, melamine adopts a flat-lying orientation on Au{111} in a honeycomb phase.[16, 33] However, the melamine honeycomb phase is observed to undergo a compression to a close-packed structure, after reaction with trimesoyl chloride, which is thought to incorporate guest melamine molecules in the existing hexagonal arrangement. The central feature was assigned as an upright melamine molecule, as the pore size is too small to accommodate a flat-lying species.

As described in the results section, the STM image in Figure 7.3 e) indicates there are bright features at the centres of some of the pores in phase B. This is most likely caused by trapped CA molecules which, if adsorbed in an upright orientation, would

account for the HREELS bands at 1431 and 1366 cm^{-1}. It is noted that the vibrational bands are observed for CA before 1,4-PDI deposition, in which phase B is not present. However, there are still disordered regions along with the close-packed phase of CA. In these cases, it is possible for some CA to be present in an upright geometry in order to minimise steric repulsion. The bands at 1431 and 1366 cm^{-1} are relatively weak for a very strong dipole moment; hence, the proportion of CA in an upright geometry must be very small.

7.6 Conclusions

HREELS and STM data indicate that cyanuric acid adsorbs parallel to the Au surface in the ketone tautomeric form. Upon deposition of 1,4-phenylendiisocyanate, no covalent reaction between the two species is observed to occur. As CA adsorbs in the ketone tautomer, and not the hydroxyl form, the electron lone pairs on the carbonyl oxygen atoms are too low in energy to be available for nucleophilic attack.

It is noted that deposition of 1,4-PDI first, followed by CA deposition resulted in displacement of 1,4-PDI and a monolayer coverage of CA. No observations of porous phases were observed, nor were there any signs of covalent reaction between the reactant species. The relatively strong intramolecular H-bonding interactions of the CA molecules are the likely cause for displacement of 1,4-PDI from the surface.

There is no evidence of 1,4-PDI sticking to the surface after CA is adsorbed first. The results suggest that 1,4-PDI partially extracts pre-adsorbed CA from the surface. This leads to the formation of two porous phases of CA amongst the close-packed phase. Upon annealing, the proportion of the two porous phases increases, forming large domains of homochiral arrays. The finding that 1,4-PDI extracts CA from the surface

is an interesting result. This could lead to novel ways of forming ordered, porous structures on surfaces for the purpose of hosting guest molecular species. Further study of this class of system is desirable.

7.7 References

[1] T. Kudernac, S.B. Lei, J. Elemans, S. De Feyter, Chem. Soc. Rev. 38 (2009) 3505-3505.

[2] S. De Feyter, A. Miura, S. Yao, Z. Chen, F. Wurthner, P. Jonkheijm, A. Schenning, E.W. Meijer, F.C. De Schryver, Nano Lett. 5 (2005) 77-81.

[3] S. De Feyter, F.C. De Schryver, J. Phys. Chem. B 109 (2005) 4290-4302.

[4] J.V. Barth, J. Weckesser, C.Z. Cai, P. Gunter, L. Burgi, O. Jeandupeux, K. Kern, Angew. Chem.-Int. Edit. 39 (2000) 1230-+.

[5] J.V. Barth, Annu. Rev. Phys. Chem. 58 (2007) 375-407.

[6] D.L. Keeling, N.S. Oxtoby, C. Wilson, M.J. Humphry, N.R. Champness, P.H. Beton, Nano Letters 3 (2003) 9-12.

[7] S. Furukawa, K. Tahara, F.C. De Schryver, M. Van der Auweraer, Y. Tobe, S. De Feyter, Angew. Chem.-Int. Edit. 46 (2007) 2831-2834.

[8] M.C. Blum, E. Cavar, M. Pivetta, F. Patthey, W.D. Schneider, Angew. Chem.-Int. Edit. 44 (2005) 5334-5337.

[9] S. Stepanow, M. Lingenfelder, A. Dmitriev, H. Spillmann, E. Delvigne, N. Lin, X.B. Deng, C.Z. Cai, J.V. Barth, K. Kern, Nat. Mater. 3 (2004) 229-233.

[10] S. Griessl, M. Lackinger, M. Edelwirth, M. Hietschold, W.M. Heckl, Single Mol. 3 (2002) 25-31.

[11] I. Cebula, C. Shen, M. Buck, Angew. Chem.-Int. Edit. 49 (2010) 6220-6223.

[12] N. Lin, S. Stepanow, M. Ruben, J.V. Barth, Templates in Chemistry Iii, Springer-Verlag Berlin, Berlin, 2009, pp. 1-44.

[13] H.M. Zhang, Z.K. Pei, Z.X. Xie, L.S. Long, B.W. Mao, X. Xu, L.S. Zheng, J. Phys. Chem. C 113 (2009) 13940-13946.

[14] H.M. Zhang, Z.X. Xie, L.S. Long, H.P. Zhong, W. Zhao, B.W. Mao, X. Xu, L.S. Zheng, J. Phys. Chem. C 112 (2008) 4209-4218.

[15] P.A. Staniec, L.M.A. Perdigao, B.L. Rogers, N.R. Champness, P.H. Beton, J. Phys. Chem. C 111 (2007) 886-893.

[16] L.M.A. Perdigao, N.R. Champness, P.H. Beton, Chem. Commun. (2006) 538-540.

[17] W. Xu, M.D. Dong, H. Gersen, E. Rauls, S. Vazquez-Campos, M. Crego-Calama, D.N. Reinhoudt, I. Stensgaard, E. Laegsgaard, T.R. Linderoth, F. Besenbacher, Small 3 (2007) 854-858.

[18] S. Jensen, H. Fruchtl, C.J. Baddeley, J. Am. Chem. Soc. 131 (2009) 16706-16713.

[19] J. Greenwood, H.A. Fruchtl, C.J. Baddeley, The Journal of Physical Chemistry C 117 (2013) 4515-4520.

[20] I. Horcas, R. Fernandez, J.M. Gomez-Rodriguez, J. Colchero, J. Gomez-Herrero, A.M. Baro, Rev. Sci. Instrum. 78 (2007) 013705.

[21] B.G. Frederick, G.L. Nyberg, N.V. Richardson, J. Electron Spectrosc. Relat. Phenom. 64-5 (1993) 825-834.

[22] B.G. Frederick, N.V. Richardson, Phys. Rev. Lett. 73 (1994) 772-772.

[23] C.T. Lee, W.T. Yang, R.G. Parr, Phys. Rev. B 37 (1988) 785-789.

[24] M.J. Frisch, G.W. Trucks, H.B. Schlegel, G.E. Scuseria, M.A. Robb, J.R. Cheeseman, J.A. Montgomery, Jr., T. Vreven, K.N. Kudin, J.C. Burant, J.M. Millam, S.S. Iyengar, J. Tomasi, V. Barone, B. Mennucci, M. Cossi, G. Scalmani, N. Rega, G.A. Petersson, H. Nakatsuji, M. Hada, M. Ehara, K. Toyota, R. Fukuda, J. Hasegawa, M. Ishida, T. Nakajima, Y. Honda, O. Kitao, H. Nakai, M. Klene, X. Li, J.E. Knox, H.P. Hratchian, J.B. Cross, V. Bakken, C. Adamo, J. Jaramillo, R. Gomperts, R.E. Stratmann, O. Yazyev, A.J. Austin, R. Cammi, C. Pomelli, J.W. Ochterski, P.Y. Ayala, K. Morokuma, G.A. Voth, P. Salvador, J.J. Dannenberg, V.G. Zakrzewski, S. Dapprich, A.D. Daniels, M.C. Strain, O. Farkas, D.K. Malick, A.D. Rabuck, K. Raghavachari, J.B. Foresman, J.V. Ortiz, Q. Cui, A.G. Baboul, S. Clifford, J. Cioslowski, B.B. Stefanov, G. Liu, A. Liashenko, P. Piskorz, I.

Komaromi, R.L. Martin, D.J. Fox, T. Keith, M.A. Al-Laham, C.Y. Peng, A. Nanayakkara, M. Challacombe, P.M.W. Gill, B. Johnson, W. Chen, M.W. Wong, C. Gonzalez, J.A. Pople, Gaussian 03, revision E.01; Gaussian, Inc.: Wallingford, CT (2004).

[25] S. Clair, S. Pons, A.P. Seitsonen, H. Brune, K. Kern, J.V. Barth, J. Phys. Chem. B 108 (2004) 14585-14590.

[26] X. Zhang, T. Chen, Q. Chen, L. Wang, L.J. Wan, Phys. Chem. Chem. Phys. 11 (2009) 7708-7712.

[27] X.Q. Liang, W.X. Zheng, N.B. Wong, J.S. Li, A.M. Tian, Theochem-J. Mol. Struct. 672 (2004) 151-159.

[28] H. Rostkowska, L. Lapinski, M.J. Nowak, Vib. Spectrosc. 49 (2009) 43-51.

[29] H. Rostkowska, L. Lapinski, A. Khvorostov, M.J. Nowak, J. Phys. Chem. A 109 (2005) 2160-2166.

[30] B.A. Sexton, Surface Science 163 (1985) 99-113.

[31] C.M. Whelan, F. Cecchet, R. Baxter, F. Zerbetto, G.J. Clarkson, D.A. Leigh, P. Rudolf, J. Phys. Chem. B 106 (2002) 8739-8746.

[32] S. Jensen, J. Greenwood, H.A. Fruchtl, C.J. Baddeley, J. Phys. Chem. C 115 (2011) 8630-8636.

[33] F. Silly, A.Q. Shaw, M.R. Castell, G.A.D. Briggs, M. Mura, N. Martsinovich, L. Kantorovich, J. Phys. Chem. C 112 (2008) 11476-11480.

Chapter Eight: Summary

8.1 Overview

The main goal throughout this project has been the investigation of surface-confined covalent reactions. The ultimate motivation of this research is to develop enantioselective heterogeneous catalysis; covalent networks are believed to infer the necessary thermal and chemical stability required to chirally modify catalytic surfaces for docking interactions with reactant species. Covalent organic frameworks (COFs) on surfaces hold potential for a number of chemical applications, and not just in the field of heterogeneous catalysis; for example in areas such as molecular electronics and templating. This is evidenced by the large number of publications and reviews into this area of research in a relatively short space of time.[1-4]

8.2 Conclusions

This thesis documents a number of chemical reaction systems towards developing covalent organic frameworks. The system most studied has been between

melamine and terephthalaldehyde, an aromatic triamine and aromatic dialdehyde, respectively. The reaction was first looked at on Au/mica under ambient conditions, described in Chapter 5. Over a period of three days, covalent reaction occurs between the reactants forming imine oligomer species which form an intermolecular H-bonded porous array. The network pores could potentially host guest molecular species. There is no indication of triple branched oligomer structures formed from reaction at all three of the amino groups of a melamine molecule. Melamine does not react beyond the second amino group, upon nucleophilic attack of two of the amino groups the third amino group becomes deactivated due to withdrawal of electron density, as has previously been reported by Jensen et al.[5, 6]

Following on from the successful reaction of melamine with terephthalaldehyde on Au/mica, the reaction was attempted in UHV on Ni{111} and Pd{111}, described in Chapters 3 and 4, respectively. The first part of each of these Chapters focussed on melamine adsorption on the respective substrate. This provided a detailed comparison study of the interaction behaviour of melamine on the two catalytically active surfaces. In both cases, melamine adsorbs in an upright orientation on the surface, through the three surface bound nitrogen atoms via electron donation form the electron lone pairs to the surface. This is contrary to previous studies of melamine on Au{111} and Ag{111}, which have shown melamine to adopt a flat-lying orientation.[7, 8] Each molecule can potentially share three H-bonds with adjacent melamine species while adsorbed parallel to the surface; however, the ability to form a strong adsorbate-substrate interaction is the driving force for the

upright orientation adopted by melamine on Ni{111} and Pd{111}. The surface bound amine groups are partially dehydrogenated. The fact that melamine has an amino group pointing away from the surface is significant. The reactive nitrogen electron lone pair can potentially be used for further reaction with an electrophile species, for the purpose of developing surface ordered, three-dimensional systems. On both Ni and Pd, melamine is observed to form linear, molecular chains aligned along the high symmetry crystal directions. The linear structures formed on Ni are longer and more ordered than those on Pd. There are two possible lattice effects influencing the structures: The first relates to the repeat distance between molecules and the other relates to the adsorption site. The greater mismatch in spacing between the Pd surface atoms and the interacting nitrogen atoms on melamine may not conform to melamine propagating in long linear chains, as witnessed on Ni{111}. In addition, melamine on Pd{111} forms pairs within the molecular chains. If the adjacent paired melamine molecules are tilted towards each other, there is the possibility of intermolecular H-bonding interactions stabilising the features.

The second parts of Chapters 3 and 4 expand on the co-deposition of melamine with terepthalaldehyde on Ni{111} and Pd{111}, respectively. The findings suggest that the dialdehyde reactant self-polymerises on both surfaces, forming a polyester species. On both substrates, no covalent reaction between melamine and terephthalaldehyde was observed to occur. The reasons for this are believed to be as follows. Firstly, the self-polymerisation of the aldehyde reactant deactivates it to

further reaction with melamine. Secondly, the upright orientation of melamine results in the amino groups being sterically unavailable for reaction.

Despite the reaction between melamine and terephthalaldehyde not occurring, co-deposition of the species produced useful results on Ni{111}. The polyester species resulting from the self-condensation of the aldehyde reactant disrupted the adsorbed melamine structures. Annealing of the sample results in the decomposition of the polyester species and, consequently, allows the melamine chains to form an interconnected, porous array. The porous melamine chain structures are an interesting finding. The pore diameters measure approximately 1-2 nm across, which is complimentary to hosting guest molecular species. The structures are thermally stable up to at least 436 K, at which they are formed. Also, the Ni substrate on which they are formed is catalytically active for hydrogenation reactions. The polyester species formed on Pd{111} were observed to form ordered, porous networks. Again, this result is significant in that porous networks on a catalytically active surface can potentially be chirally functionalised and host reactant species. The systems studied on Ni{111} and Pd{111} are an area of investigation that warrant further study.

The reaction of 1,4-diaminobutane with 1,3- and 1,4-phenylene diisocyanate on Au{111} in UHV is reported on in Chapter 6. This builds on previous work carried out by Jensen et al.[5] which investigated the surface-confined covalent reaction between melamine and 1,4-phenylene diisocyanate. The isocyanate group is advantageous for covalent reactions since it is particularly electrophilic at the linear (sp-hybridised) carbon atom. The use of an aliphatic diamine is an important

advance, as it allows the possibility to functionalise the sp^3 hybridised methylene backbone as a means of incorporating chirality into the oligomeric structures. STM data and DFT calculations provide strong evidence that both 1,3- and 1,4-phenylene diisocyanate undergo a nucleophilic addition reaction with 1,4-diaminobutane on Au{111} in UHV at, or slightly above, room temperature. Upon annealing to higher temperatures, both diisocyanate derivatives react with 1,4-diaminobutane to form urea oligomers. At sufficiently high temperatures, the urea oligomers form ordered networks, held together by intermolecular H-bonding via the urea linkages. The ordered oligomer structures are thermally stable up to at least 523 K. For applications in templating, catalysis, biosensing etc., it is desirable to produce porous structures. In this study of simple amine and isocyanate building blocks, structures are formed which are densely packed and do not possess the desired porosity. Enhancement of porosity is likely to be achieved by the use of tri-isocyanates or tri-amine building blocks. The ease of reactivity coupled with the thermal stability of the structures reported in this study leads to the conclusion that isocyanate/amine systems may be ideally suited for application in templating and catalysis.

Chapter 7 describes the surface-confined interaction between cyanuric acid and 1,4-phenylene diisocyanate, investigated on Au{111} in UHV. No covalent reaction is observed between the reactants. The results suggest that the isocyanate reactant does not stick to the surface after cyanuric acid is deposited; instead, it partially extracts pre-adsorbed cyanuric acid from the surface. Cyanuric acid undergoes a phase transition from a hexagonally close-packed structure to a hexagonal porous phase. Two cyanuric acid porous phases are observed amongst the close-packed

structures, which adopt a flat-lying orientation with respect to the surface. Upon annealing, large domains of the porous phase are observed. As cyanuric acid adsorbs in the ketone tautomer, and not the hydroxyl form, the electron lone pairs on the carbonyl oxygen atoms are too low in energy to be available for nucleophilic attack. The finding that 1,4-phenylene diisocyanate extracts cyanuric acid from the surface is an interesting result. This could lead to novel ways of forming ordered, porous structures on surfaces. Further study of this class of system is desirable.

8.3 Future Work

It is concluded that the most successful systems studied in this thesis are: melamine reacted with terephthalaldehyde on Au/mica under ambient conditions, and the reaction of 1,4-diaminobutane with 1,3- and 1,4-phenylene diisocyanate. Both reactions resulted in covalent bond formation at room temperature. These systems can be modified by the selective use of the respective reactants with tri-substituted functional groups, which is believed to produce greater interconnectivity of covalent networks. As already stated, the use of aliphatic reactant species is advantageous to allow for the incorporation of chiral functional groups into the structures. Consequently, docking interactions with host guest molecular species could result in enantioselective behaviour.

It is found that the use of reactant species which form domains of interconnected H-bonding interactions, such as melamine and cyanuric acid, are generally undesirable for the purpose of forming covalent networks. The reactant species at the centre of such ordered domains are essentially inaccessible for reaction. In studies of covalent reactions on surfaces utilising melamine, the reaction occurs at

the island perimeters. This is because the melamine molecules at the edges of the domain islands are the most weakly bound, forming H-bonds with two adjacent melamine molecules, rather than three as observed for melamine species in the middle of ordered islands, and that oligomeric species peel off the melamine domains to allow further reaction with melamine to take place. The electrophilic reactants must consequently be present on the surface in the space between the melamine islands. This necessitates that sub-monolayer coverage of melamine is adsorbed on the surface for the electrophile reactant to be adsorbed. It is preferable for the reactants to be intermixed to allow a widespread reaction to occur, as in the case of the 1,4-diaminobutane with 1,4- and 1,3-phenylene diisocyanate.

The use of Au as a substrate in this thesis has been necessary for the covalent reaction between two species. The inert behaviour of Au allows the reactants to diffuse across the surface in order to react together. The drawback is that Au does not possess catalytic behaviour for potential hydrogenation reactions. Deposition of the reactants directly onto catalytic surfaces, such as Ni{111} and Pd{111}, results in the adsorbate-substrate interactions dominating, not allowing diffusion of the reactant species to occur for covalent reaction formation. Performing covalent reactions on metal alloy surfaces might offer a solution by incorporating the desired properties of two metals. In particular, Au/Pd surface alloys may hold potential in this regard. Alloying is widely used to alter the chemical properties of metal surfaces.[9-12] The theory proposed is thus: Forming a Au layer on a Pd substrate would allow covalent reactions to occur directly on the surface. Applied annealing

results in Au deposited on Pd to segregate into the bulk,[13] thus exposing the catalytic Pd surface to the covalent network. Future work on covalent organic frameworks is likely to involve studies on surface alloys, and holds great promise in the field of enantioselective heterogeneous catalysis.

8.4 References

[1] A. Gourdon, Angew. Chem.-Int. Edit. 47 (2008) 6950-6953.
[2] G. Franc, A. Gourdon, Physical Chemistry Chemical Physics 13 (2011) 14283-14292.
[3] M. Lackinger, W.M. Heckl, J. Phys. D-Appl. Phys. 44 (2011).
[4] H. Liang, Y. He, Y.C. Ye, X.G. Xu, F. Cheng, W. Sun, X. Shao, Y.F. Wang, J.L. Li, K. Wu, Coord. Chem. Rev. 253 (2009) 2959-2979.
[5] S. Jensen, H. Fruchtl, C.J. Baddeley, J. Am. Chem. Soc. 131 (2009) 16706-16713.
[6] S. Jensen, J. Greenwood, H.A. Fruchtl, C.J. Baddeley, J. Phys. Chem. C 115 (2011) 8630-8636.
[7] F. Silly, A.Q. Shaw, M.R. Castell, G.A.D. Briggs, M. Mura, N. Martsinovich, L. Kantorovich, J. Phys. Chem. C 112 (2008) 11476-11480.
[8] C.H. Schmitz, J. Ikonomov, M. Sokolowski, Surface Science 605 (2011) 1-6.
[9] T. Wei, J. Wang, D.W. Goodman, J. Phys. Chem. C 111 (2007) 8781-8788.
[10] J. Xu, T. White, P. Li, C.H. He, J.G. Yu, W.K. Yuan, Y.F. Han, J. Am. Chem. Soc. 132 (2010) 10398-10406.
[11] A.F. Lee, S.F.J. Hackett, G.J. Hutchings, S. Lizzit, J. Naughton, K. Wilson, Catal. Today 145 (2009) 251-257.
[12] F. Calaza, Z. Li, F. Gao, J. Boscoboinik, W.T. Tysoe, Surface Science 602 (2008) 3523-3530.
[13] C.J. Baddeley, M. Tikhov, C. Hardacre, J.R. Lomas, R.M. Lambert, J. Phys. Chem. 100 (1996) 2189-2194.